

Atomic scale investigations of fracture in metal alloys

Présentée le 15 octobre 2021

Faculté des sciences et techniques de l'ingénieur
Laboratoire de modélisation mécanique multi-échelle
Programme doctoral en mécanique

pour l'obtention du grade de Docteur ès Sciences

par

Eleanor Yi Kei MAK

Acceptée sur proposition du jury

Prof. J.-F. Molinari, président du jury
Prof. W. Curtin, directeur de thèse
Prof. L. Qi, rapporteur
Prof. R. Janisch, rapporteuse
Prof. J. Kolinski, rapporteur

To my loving family...

Acknowledgements

This thesis represents four years of my scientific endeavors as a member of the Laboratory for Multiscale Mechanics Modeling (LAMMM) at EPFL. Financial support for the research work contained in this thesis was provided by the Swiss National Science Foundation as part of project 200021_18198/1 entitled “Harnessing atomic-scale randomness: design and optimization of mechanical performance in High Entropy Alloys.” This thesis would not have been possible without the support, encouragement, and guidance from many colleagues, friends, and family. So, at the conclusion of this journey, I would like to express a few words of grateful thanks.

First and foremost, I would like to extend my sincere thanks to my thesis advisor, Professor Curtin, for his scientific nurturing. I am grateful for his challenging but supportive direction, for the freedom I had to explore and self-direct, and especially his patience at every step along the way. I am particularly thankful for his guidance in matters of writing and technical communication, which will certainly be valuable for the rest of my career. I also thank my jury committee for the productive discussion and constructive comments during my thesis defense.

I have had the great pleasure of working in a scientifically stimulating environment fostered by my colleagues in LAMMM – in no particular order: Till Junge, Binglun Yin, Francesco Maresca, Nikolaos Bouklas, Mostafa Khosrownejad, Ali Teranchi, Markus Stricker, Predrag Andric, Shankha Nag, Wolfram Nöhring, Max Hodapp, Yi Hu, Daniel Marchand, Ali Falsafi, Alireza Ghafarollahi, Ankit Gupta, Xiao Zhou, Abhinav Jain, Carolina Baruffi, Manura Liyanage, Ekin Kubilay, You Rao, Xin Liu, Masoud Rahbarniazi, Terrence Moran, and also visiting Professor Derek Warner. Many thanks as well to LAMMM secretary Géraldine Palaj for her timely assistance in daily matters big or small and for her help with the French translation of the abstract. I am very proud to be a part of the LAMMM family.

I am deeply grateful to Till, especially for taking me under his wing the first few months, to Markus for his always generous assistance, and to Francesco for his thoughtful insights. I owe a great deal of my know-how to their expertise and I sincerely thank them for their many encouraging words at challenging moments. I thank Predrag for starting me off in atomistic simulations and the discussions on fracture mechanics, and Alireza

Acknowledgements

for his always calm troubleshooting and brainstorming help with technical problems. I would also like to thank Rasool and Yi for their efforts and solidarity as part of our solid mechanics teaching assistant team.

Many thanks to the regular “crew” for their steady camaraderie and the many fun activities punctuating the serious scientific work (hiking in the mountains, barbecues by the lake, sampling the culinary offerings in Lausanne, etc. ...). Special thanks go to Daniel, fellow Canadian, for the stimulating conversations over numerous dinners of spicy fish and crispy beef, and to Carolina, for her inspirational (but tangential) thoughts and for enlightening me on the finer aspects of spritz. I am very grateful to have supportive women in my life and my sincere thanks go to Endrina Rivas, Alina Walch, and Emma Källstig who were always willing to lend an ear.

My husband, Ernst, has been a constant source of support at every step along the way despite the long physical distance between Switzerland and the Netherlands – I am endlessly grateful for his love and encouragement. I am also thankful for the unwavering support and confidence from my Dutch family, Ton, Marianne, Frank, and Cecile, and the extended Remij and Verheijen families.

Last but not least, I thank my father, Yu Fai, my mother, Freda, and my brother, Jason. They have always encouraged me to freely pursue my interests wherever they may take me and I thank them for their unconditional love.

Lausanne, September 30, 2021

E. M.

Abstract

The demand for metal alloys with superior structural performance in industrial applications continues to increase, as does the need for more-energy efficient materials and methods. Many materials that are otherwise attractive for structural applications are limited by poor fracture properties at low and moderate temperatures, and these properties limit their formability and suitability for fracture-critical/energy-absorption applications.

Attractive fracture properties, namely ductility and high fracture toughness, are connected to a competition between brittle cleavage and ductile dislocation emission mechanisms at an atomistic crack tip in crystalline metals. Dislocation emission from a crack tip is the necessary precursor to blunting and toughening leading to subsequent ductile mechanisms for macroscopic ductility. The intrinsic capacity for dislocation emission is the intrinsic ductility which, under mode I loading, occurs if the critical stress intensity for dislocation emission K_{Ie} is lower than the critical stress intensity for cleavage K_{Ic} . The competing crack tip mechanisms are studied here using atomistic simulations. The current methods are constrained by the accuracy of the interatomic potentials representing the materials, as fracture is an especially challenging simulation environment, and this is particularly the case for complex alloys.

Pure magnesium (Mg) is an attractive metal for structural applications due to its low density, but also has low ductility and low fracture toughness. Alloying of Mg with rare earth elements, e.g. yttrium (Y), in small amounts improves the ductility. Dilute alloying (3at%Y) slightly improves the overall ductility of a crack as the overall fracture toughness is improved due to local solute-induced deformation phenomena at the crack tip. However, the local fluctuations of the random solutes enable emission rather than cleavage in crack orientations only where the differences in the critical load for cleavage and emission are small. Basal-plane cleavage remains strongly preferred, as in pure Mg. Dilute alloying is unable to fundamentally change the brittle nature of the base material.

Multicomponent, single-phase, polycrystalline High Entropy Alloys (HEAs) have recently emerged as a new class of metal alloys, and some refractory bcc HEAs composed mainly of Nb, V, Ta, Cr, Mo, and/or W show excellent strength retention up to very high temperatures but low ductility at room temperature (RT). A RT ductility crite-

Abstract

rion based on K_{Ie}/K_{Ic} for critical crack orientations is proposed based on the elemental metals and is then applied to HEAs. Agreement with experimental trends in ductility vs. composition across a range of existing HEAs is demonstrated. The analysis is then extended across large composition spaces of the Mo-Nb-Ta-V-W and Mo-Nb-Ti alloy families, identifying new compositions with the potential for RT ductility.

The cleavage and dislocation emission crack tip mechanisms are thermally-activated processes and are each associated with an energy barrier connected to the critical stress intensity. Ductilization at RT is possible only if the intrinsic cleavage and emission energy barriers are comparable, but many bcc HEAs have emission barriers that are very large and insurmountable on average compared to the cleavage barriers. Significantly reduced local emission energy in a random system is demonstrated with a model equiatomic MoNbTi random alloy, signifying the potential for local crossover from brittle to ductile behavior even if a material is brittle on average. The average theory connects the energy barrier, stress intensity, and material properties for emission but the same connections are not translated to the scale of the atomic fluctuations. The interaction of the atomic misfit volume and the crack fields is a critical energetic contribution to the emission process and introduces large variations to the emission energy. Ongoing work involves quantifying the connection between the stochastic compositional disorder with variations in the energy contributions for emission, which is necessary to develop an analytic theory. In the meantime, large average misfit volume is a potential supplementary criterion to improve broad screening for ductility in HEAs.

Keywords: atomistic simulations, fracture, random alloy, magnesium, high entropy alloys, intrinsic ductility, dislocation emission

Résumé

Dans l'industrie, la demande d'alliages métalliques avec des performances structurales supérieures continue d'augmenter, ainsi que le besoin de matériaux et de méthodes efficaces d'un point de vue énergétique. De nombreux matériaux, en principe attractifs dans des applications structurales, sont limités par leurs mauvaises propriétés de rupture à températures basses et modérées, car ces propriétés limitent leur formabilité ainsi que leur utilisation dans des applications où le risque de rupture et la résilience du matériau sont critiques.

Dans les métaux cristallins, les propriétés de rupture intéressantes, à savoir à ductilité et à haute résistance, sont liées à une compétition entre le mécanisme fragile de clivage et le mécanisme ductile d'émission de dislocations de la pointe de la fissure. L'émission de dislocations de la pointe de la fissure est le précurseur nécessaire à l'émoussement et au durcissement conduisant aux mécanismes ductiles ultérieurs de la ductilité macroscopique. La capacité intrinsèque de l'émissions de dislocations est la ductilité intrinsèque qui, sous chargement en mode I, survient si l'intensité de la contrainte critique de l'émission de dislocations K_{Ie} est inférieure à l'intensité de la contrainte critique du clivage K_{Ic} . Dans cette thèse, ces différents mécanismes concurrents de la pointe de fissure sont étudiés à l'aide de simulations atomiques. Les méthodes atomiques actuelles sont limitées par la précision des potentiels interatomiques utilisés pour les matériaux, car la fracture est un domaine de simulation particulièrement compliqué, surtout dans le cas d'alliages complexes.

Le magnésium pur (Mg) est un métal intéressant pour les applications structurales en raison de sa faible densité. Toutefois, sa ductilité et sa résistance à la rupture sont faibles. Les alliages de Mg, obtenus par ajout de petites quantités de terres rares, par ex. l'yttrium (Y), améliorent la ductilité. L'ajout d'une quantité modérée d'éléments d'alliage (3at%Y) améliore légèrement la ductilité globale ainsi que la résistance globale, en raison des phénomènes locaux de déformation induits par la présence des solutés à la pointe de la fissure. Cependant, les fluctuations locales des solutés aléatoires activent l'émission de dislocations plutôt que le clivage dans l'orientations de la fissure seulement où les différences des charges critiques de clivage et d'émission de dislocations sont faibles. Le clivage le long du plan basal reste fortement préférable, comme dans le Mg pur. Au

final, l'ajout d'une quantité modérée d'éléments d'alliage ne modifie pas radicalement la nature fragile du matériau de base.

Les alliages à haute entropie (HEA) polycristalline, multicomposés, monophasés, sont apparus récemment comme une nouvelle classe d'alliages métalliques. Certains HEAs réfractaires avec structure cubique à corps centré (ccc), composés principalement de Nb, V, Ta, Cr, Mo et/ou W, présentent une excellente résistance à des températures très élevées mais, en revanche, montrent une faible ductilité à température ambiante (TA). Basé sur l'étude des matériaux élémentaires, nous proposons un critère de ductilité à température ambiante basé sur K_{Ic}/K_{Ic} pour les orientations critiques des fissures. Le critère est ensuite appliqué aux HEAs. L'accord entre les résultats obtenus avec le critère proposé et les tendances expérimentales sur la ductilité des HEAs en fonction de leur composition est démontré. Ensuite, nous appliquons notre analyse à toutes les compositions possibles des alliages Mo-Nb-Ta-V-W et Mo-Nb-Ti, en identifiant ainsi des nouvelles compositions avec le potentiel de la ductilité à température ambiante.

Les mécanismes de clivage et d'émission de dislocations de la pointe de la fissure sont des processus thermiquement activés, donc associés à une barrière énergétique liée à l'intensité de la contrainte critique. La ductilité à température ambiante n'est possible que si les barrières énergétiques intrinsèques pour le clivage et l'émission sont comparables. Cependant, plusieurs HEAs ccc ont des barrières d'émission très élevées, au point d'être infranchissables par rapport aux barrières associées au clivage. Ici, nous montrons dans un modèle d'alliage aléatoire MoNbTi équiatomique que la barrière énergétique de l'émission est localement réduite, ce qui signifie localement une potentielle transition entre comportement fragile et ductile, même si les propriétés moyennes du matériau suggèrent un comportement fragile.

La théorie appliquée aux propriétés moyennes est en connexion avec la barrière énergétique de l'émission, l'intensité de la contrainte et les propriétés du matériau, mais les mêmes connexions ne sont pas valables à l'échelle des fluctuations atomiques. L'interaction entre la distorsion induite par les solutés et le champ de contrainte à la pointe de la fissure est une contribution énergétique critique pour le processus d'émission et introduit de grandes variations dans la barrière énergétique associée. Les travaux en cours consistent à quantifier le lien entre le désordre stochastique dans la composition et les variations de la barrière énergétique de l'émission, ce qui est nécessaire pour développer une théorie analytique. En attendant, une haute distorsion induite par les solutés est, potentiellement, un critère supplémentaire pour améliorer la présélection de HEAs avec ductilité élevée.

Mots-clés: simulation atomique, rupture, alliage aléatoire, magnésium, alliages à haute entropie, ductilité intrinsèque, émission de dislocations

Contents

Acknowledgements	i
Abstract (English/Français)	iii
List of Figures	xi
List of Tables	xv
Introduction	1
I Background: theory and simulation of atomistic fracture	5
1 Linear Elastic Fracture Mechanics (LEFM)	7
1.1 Plane strain crack stress fields	8
1.2 Plane strain asymptotic crack tip fields	10
1.3 Fracture process zone and small scale yielding	12
1.4 Energetics of crack extension	13
2 Atomistic crack-tip processes	15
2.1 Fracture toughness and macroscopic ductility	16
2.2 Dislocation emission and surface step creation	17
2.2.1 Crack tip shielding by dislocations	20
2.3 Intrinsic ductility criterion	22
2.4 Activation of crack tip processes	23
3 Atomistic simulation methods	25
3.1 Elements of Molecular Dynamics/Statics simulations	25
3.2 Transition state theory and the Nudged Elastic Band (NEB) method . .	28
3.2.1 Transition state theory	28
3.2.2 Nudged Elastic Band method	31
3.3 <i>K</i> -controlled atomistic simulation framework	33
3.4 Validation of LEFM using atomistic simulations	35
3.4.1 Emission and cleavage pathways using NEB	36

4	Interatomic potentials for atomistic simulations of fracture	41
4.1	Semi-empirical potentials for Mg and Mg-Y	42
4.1.1	EAM/MEAM potentials for Mg	43
4.1.2	MEAM potential for Mg-Y	44
4.2	EAM potentials for bcc elements and alloys	45
4.3	Average-atom approximation of random alloys	46
4.4	Machine learning potentials	50
4.4.1	Gaussian approximation potentials for bcc Fe and W	51
4.4.2	Neural network potentials for Mg	53
II	Atomistic fracture in alloys	59
5	Intrinsic fracture behavior of dilute Mg-Y alloys	61
5.1	Material properties and simulation details	62
5.2	Intrinsic ductility and fracture toughness	65
5.2.1	Basal	67
5.2.2	Prismatic	67
5.2.3	Pyramidal	69
5.2.4	Tensile twin	72
5.3	Structural disorder of the crack tip	73
5.4	LEFM as a predictor of crack tip behavior	77
5.5	Summary	78
6	A ductility criterion for bcc high entropy alloys	81
6.1	Intrinsic ductility in bcc crystals: cleavage vs dislocation emission	84
6.2	Ductility criterion based on intrinsic fracture of bcc elements	86
6.3	Ductility in High Entropy Alloys	90
6.3.1	Ductility of MoNbTaVW, MoNbTaW, and MoNbTi using first-principles inputs	90
6.3.2	Ductility using scaled inputs from interatomic potentials	91
6.4	Identifying new ductile HEA compositions	94
6.5	Discussion	96
6.6	Summary	98
7	Randomness and intrinsic ductility in bcc high entropy alloys	99
7.1	Activated crack tip mechanisms in random environments	101
7.2	Dislocation emission in random environments	103
7.2.1	Local emission energy barrier	104
7.2.2	Local environments on the slip plane	106
7.3	Energy of emission in the atomistic system	111
7.3.1	Misfit volume/crack interaction	118
7.4	Discussion	120

7.5 Summary	122
8 Conclusion	123
Appendix	127
A.1 Material properties and anisotropic elastic parameters of Mg and Mg-Y	127
A.2 Material parameters of bcc refractory elements and alloys	128
A.3 DFT methodology for bcc HEAs	130
A.4 Mixed-mode ductility criterion	131
A.5 Atomistic energy in rigid block shear	132
A.6 Local material properties in random alloys	136
Bibliography	139
Curriculum Vitae	155

List of Figures

1.1	A finite crack of length $2a$ centered on an infinite plate under biaxial σ^{app} stress.	9
2.1	Schematic of crack geometry and coordinate system.	19
3.1	Schematic of a thermally activated process between two metastable states.	29
3.2	Schematic of the chain of replicas (images) Q^i of the nudged elastic band (NEB) (in green) connecting states A and B on a 2d potential energy surface.	32
3.3	Schematic of the K -controlled simulation setup in the x - y plane.	35
3.4	2d cleavage energy profile of the NbTiZr (110) $[\bar{1}\bar{1}0]$ crack orientation from NEB simulation at various K_I as labeled (in units of $\text{MPa}\sqrt{\text{m}}$).	37
3.5	NEB simulation of the cleavage process in NbTiZr for the (110) $[\bar{1}\bar{1}0]$ crack orientation.	38
3.6	NEB simulation of the dislocation emission process in NbTiZr for the (110) $[\bar{1}\bar{1}0]$ crack orientation.	39
3.7	Energy barriers for cleavage and dislocation emission in the (110) $[\bar{1}\bar{1}0]$ crack orientation as a function of the applied load K_I	40
4.1	A -alloy vs. true random alloy material properties.	48
4.2	Crack tip behavior from direct K -test simulation for a random (R) and equivalent A -alloy (A) in the model $\text{Mo}_{20}\text{Nb}_{20}\text{Ta}_{20}\text{V}_{20}\text{W}_{20}$ system (Zhou potential [1]) for four crack orientations.	49
4.3	Examples of crack tip behavior obtained from GAP.	53
4.4	Cross sectional view of crack tips post fracture for prismatic I, prismatic II, and pyramidal II crack planes, as observed in simulations for MEAM [2] and NNP.	55
5.1	The resistance curve (R-curve) of the applied load K_I versus crack extension Δa	66
5.2	A basal I (0001) $[\bar{1}\bar{2}10]$ orientation crack in a random Mg-Y alloy under mode I loading.	67
5.3	A basal II (0001) $[\bar{1}010]$ orientation crack in a random Mg-Y alloy under mode I loading.	68

List of Figures

5.4	A prismatic I ($\bar{1}010$)[$\bar{1}2\bar{1}0$] orientation crack in a random Mg-Y alloy under mode I loading.	69
5.5	A prismatic II ($\bar{1}2\bar{1}0$)[$\bar{1}010$] orientation crack in a random Mg-Y alloy under mode I loading.	70
5.6	A pyramidal I ($\bar{1}011$)[$\bar{1}2\bar{1}0$] orientation crack in a random Mg-Y alloy under mode I loading.	71
5.7	A pyramidal II ($\bar{1}2\bar{1}2$)[$\bar{1}010$] orientation crack in a random Mg-Y alloy under mode I loading.	72
5.8	A tensile twin I ($\bar{1}01\bar{2}$)[$\bar{1}2\bar{1}0$] orientation crack in a random Mg-Y alloy under mode I loading.	73
5.9	A tensile twin II ($10\bar{1}2$)[$\bar{1}2\bar{1}0$] orientation crack in a random Mg-Y alloy under mode I loading.	74
5.10	Plane projection (x - y) of crack tip configurations in Mg-Y around the intrinsic stress intensity K_{Ic}, K_{Ie}	74
5.11	Plastic lattice disorder in the vicinity of the crack tip grows over $\Delta K_I = 0.20K_{Ie}$ ($K_{Ie} = 0.255 \text{ MPa}\sqrt{\text{m}}$) for a Mg-Y crack in the prismatic I ($\bar{1}010$)[$\bar{1}2\bar{1}0$] orientation.	75
5.12	Evolution of the crack tip environment in a basal I (0001)[$\bar{1}2\bar{1}0$] orientation over an increment of $\Delta K_I = 0.04K_{Ic}$ ($K_{Ic} = 0.262 \text{ MPa}\sqrt{\text{m}}$) illustrated using 12Å thick slices centered at 6, 18, 20, and 42Å along the crack front.	76
5.13	Dislocation emission from the disordered crack tip in a prismatic II ($\bar{1}2\bar{1}0$)[$\bar{1}010$] orientation ($K_{Ic} = 0.272 \text{ MPa}\sqrt{\text{m}}$).	77
5.14	Response of a partially pinned dislocation nucleated from disordered crack tips in the Mg-Y alloy.	78
6.1	Geometry of crack orientations (\mathbf{n})[\mathbf{l}] favoring edge dislocation nucleation on the $a/2\langle 111 \rangle$ planes in mode I fracture.	85
6.2	LEFM predictions of stress intensity and intrinsic ductility for 5 bcc elements and four crack orientations.	88
6.3	Mixed-mode isotropic ductility index normalized by the pure mode I ductility index for the various possible dislocation emission slip planes studied here (see Equation (6.1)).	90
6.4	Fully-relaxed EAM material properties compared to fully-relaxed DFT material properties.	92
6.5	Predicted intrinsic ductility index $D = K_{Ie}/K_{Ic}$ and measured RT compression ductilities for selected HEA compositions.	93
6.6	Ductility for three HEA families discretized at intervals of 10% concentration of each alloy constituent, using scaled EAM properties ($\beta = 1.04$).	95
6.7	Ductility index $D = K_{Ie}/K_{Ic}$ versus the average valence electron count (VEC) per atom for three HEA families corresponding to Fig. 6.6, with the ductility criteria indicated, for each orientation.	97

7.1	Schematic of local vs. average quantities in a random material.	102
7.2	Model MoNbTi <i>A</i> -alloy emission energy along the NEB chain of replicas.	104
7.3	Creation of a set of starting chain of replicas for a random environment.	104
7.4	Emission energy barriers from 9 random environments, ordered approximately from lowest to highest energy overall.	105
7.5	Expansion of an incipient dislocation in random environment 5.	106
7.6	Schematic of a dislocation loop on its emission plane.	107
7.7	Saddle point dislocation slip contours and local unstable stacking fault (USF) energy of the slip plane atoms.	108
7.8	Saddle point dislocation slip contours and shear stress of the slip plane atoms.	109
7.9	Similar variation of the unstable stacking fault (USF) energy γ_{usf} and stiffness μ' with composition in the <i>A</i> -alloy representation of the model Mo-Nb-Ti space of alloys.	110
7.10	Variations of local USF energy γ_{usf}^* vs. variations of local energy barrier ΔE_e^* for the set of random environments.	111
7.11	Emission energy contributions along NEB chain of replicas in the model MoNbTi <i>A</i> -alloy.	114
7.12	The misfit energy ΔU_{mis} of the <i>A</i> -atom emission pathway with random configurations of atomic misfit volume.	119
A.1	Brittle fracture toughness K_I versus temperature of W in the $\{100\}\langle 001 \rangle$ crack orientation at varying strain rates [3].	130
A.2	Rigid shift of one half-block relative to another by Δ forming a stacking fault at the slip plane.	134
A.3	Local USF energy of a slip plane atom.	137

List of Tables

4.1	Stress intensity factors K_I for cleavage and emission for various crack orientations as computed and simulated using Mg NNP and its material properties.	55
5.1	Crack tip cleavage and emission competition in Mg and Mg-3at%Y as predicted from linear elastic fracture mechanics.	64
6.1	Material parameters of bcc refractory elements used in the LEFM analysis: the elastic constants C_{ij} , the relaxed surface energies γ_s and unstable stacking fault energies γ_{usf}	87
7.1	Misfit volume following Vegard's law for the model MoNbTi HEA. . . .	118
A.1	Elastic constants calculated for Mg and Mg-Y.	127
A.2	Anisotropic elastic properties for Mg and Mg-Y.	128
A.3	Elastic moduli and the Zener anisotropy of selected bcc refractory elements obtained from the EAM potential, and selected First-principles/Density Functional Theory (FP/DFT) and experimental (Expt.) literature. . . .	129
A.4	Elastic moduli and the Zener anisotropy of the selected HEAs obtained from the EAM potential and selected First-principles/Density Functional Theory (FP/DFT) literature.	129
A.5	Surface energies γ_s and USF energies γ_{usf} used in the LEFM analysis of four equiatomic HEAs.	131

Introduction

The creation and use of metal alloys can be traced back to the earliest of human history. The earliest alloys from copper ore containing natural traces of arsenic were unintentional. As we understand now, arsenic lowers the melting point, which makes the alloy an easier material to cast and work with, and increases the strength, so more durable weapons and tools could be created – these properties would certainly have been advantageous for early humans. Later on, alloying became deliberate – tin alloyed with copper, for example, yielded the mechanically superior bronze, giving birth to the Bronze Age and sparking a long history of metallurgical discovery. Metals in modern industry are rarely used in their pure native form since alloying can dramatically improve physical, mechanical, and processing properties.

Alloy development and discovery have generally come hand-in-hand with the technological advances over time. Taking the last century for example, the development of aluminum alloys exploded around the First World War, driven by the need to create strong but lightweight airframes for the suddenly booming aerospace industry. Alloyed steels (e.g. high speed steels, carbides, and stainless steels) quickly followed, improving cutting tools and mechanical components with higher strength and improved temperature resistance. Conventional alloying, such as the examples above, involves the addition of one or more elements to a base metal forming an alloy family based on the principal element. This methodology has been very successful as history shows, but the alloy families which can be developed are fundamentally limited by the number of base elements. Today, the demand for metal alloys with increasingly superior structural and functional performance for industrial applications continues to increase and drives the need for innovation in alloy design.

A new class of metal alloys has emerged relatively recently, the High Entropy Alloys (HEAs) [4–6], which represent a paradigm shift in alloy development toward multiple principal components combined in almost equiatomic concentrations. HEAs have gained research traction due to their potential for very desirable mechanical properties, e.g. high strength and exceptional strength retention at high temperatures; excellent resistance to wear, corrosion, and oxidation; and also their ability to be fabricated with established

techniques and equipment which would ease an eventual transition from laboratory research to mass production [7].

As we see, these complex alloys are teeming with unexplored potential. However, our current understanding of these novel materials is limited and preliminary, based only on a few alloys families that have been fabricated to date. The equilibrium phases and phase diagrams beyond binary and ternary systems are mostly unknown, for instance, but that knowledge is important for fabrication. Understanding of mechanical properties is also limited, usually to hardness and compressive properties, although tensile properties and ductility are very important for design [7]. From an engineering design perspective, brittle material failure from unrestrained crack growth is generally catastrophic for a structural component. The fracture properties of a structural material are therefore a critical consideration. While new theoretical advances are starting to provide quantitative understanding of the connections between strength, composition, and temperature in HEA systems [8–10], there is yet no clear understanding of similar connections between composition, temperature, and ductility. Identification of alloys with high strength and good ductility is a goal driving current alloy development. High fracture toughness, which is a material’s inherent ability to resist fracture, is a particularly valuable trait.

The problem of fracture can be addressed at many length scales. We can treat it from a macroscopic perspective and utilize the stresses, strains, and energies from continuum fracture mechanics for engineering design without delving into the microscopic intricacies of defects and microstructure (e.g. grain boundaries, dislocations, voids, ...). Alternatively, we can consider the basic microscopic constituent of the material, the atom, and address fracture as the decohesion of atomic bonds between two layers of atoms. The attractive fracture properties of high ductility and high fracture toughness in metals and their alloys are connected to a competition between brittle cleavage and ductile dislocation emission mechanisms at an atomistic crack tip. Dislocations are well-known carriers of plasticity in crystalline metals [11], and thus a fundamental capacity to emit dislocations – an intrinsic ductility – is a necessary precursor to truly ductile macroscopic behavior. The alloy environment, especially HEAs, is complex due to the multiple constituent elements and inherent stochasticity, so naturally the connection between intrinsic ductility and mechanical behavior will be more complex than elemental systems. In this thesis, we are interested in investigating how the inherent randomness of an alloy affects the ductility of an atomistic crack tip.

Together with improving the materials themselves, another part of alloy design is improving the cost- and energy-efficiency of the development methods. With modern computing power, computationally-guided design using atomistic simulation methods have become an invaluable part of the alloy design process, and we use these methods to study the complex and nonlinear behavior around an atomistic crack tip. Simulations can be used to test hypotheses and study the underlying physics and mechanisms controlling

the material behavior beyond what can be studied with physical experiments. Molecular Dynamics/Statics methods enable us capture the evolution of atoms at length- and time-scales suitable to study, for example, dislocation plasticity and defect-crack interactions. Simulations can also be used more broadly to probe relationships between composition, structure, and properties to identify over-arching trends in material properties, or to conduct exploratory screening over large sets of candidate materials. In the later part of this thesis, we try to draw connections between composition and ductility over the composition space of several HEA families.

Overall, we can generally accomplish computational studies at broader scope, higher resolution, faster speed, and lower cost than to iteratively fabricate and test a comparable set of physical specimens, even considering the very expensive computational cost of first-principles methods. The development of quantitatively predictive models will greatly increase the efficiency and cost of alloy design and supplement physical experiments. At present, there are still many underlying challenges in simulating random alloy systems due their inherent complexity. Fracture is a particularly challenging simulation environment, which becomes evident as a common theme throughout this thesis. Nonetheless, while the atomistic methods continue to be improved, we must find useful ways to press forward with the existing resources.

The goal of this thesis is to provide atomistic insight into simulating fracture and the nature of the fracture behavior in random alloys. This thesis is divided into two parts as follows. The first part introduces the relevant background behind the theory and simulation methods of atomistic fracture in crystalline metals and metal alloys and is the necessary backdrop for the computational studies and discussion presented in Part II. We first begin with theoretical framework of Linear Elastic Fracture Mechanics (LEFM) in Chapter 1, which introduces the asymptotic crack tip fields and the concept of stress intensity. The atomistic crack tip mechanisms of cleavage and dislocation emission – and from their competition, intrinsic ductility – are characterized within the LEFM framework and are discussed in Chapter 2. Following in Chapter 3, we briefly review the atomistic simulation methods used in the computational studies in Part II, including Molecular Dynamics/Statics and the Nudged Elastic Band method based on transition state theory. We review the LEFM-compliant K -controlled simulation framework, which allows for quantitative comparisons between theory and atomistic simulations using these methods, and validate the theory for the complex HEAs.

A critical component of atomistic simulations is the interatomic potential representing the material, and the fracture environment is often very challenging for any interatomic potential. Consequently, in Chapter 4, we introduce several semi-empirical interatomic potentials, focusing on those used in the simulations in Part II. Here we highlight some of the problematic aspects of their fracture performance that motivate the interest in machine learning potentials. We also briefly introduce the “Average atom” interatomic potential to represent the average behavior of a true random material, which we use

extensively to study the complex HEA system.

Part II presents several atomistic fracture studies which aim to extend our current understanding of fracture and intrinsic ductility in random alloy systems. These studies are presented chronologically, which is also in the order of increasing system complexity. In Chapter 5, we first look at a model magnesium-yttrium (Mg-Y) dilute alloy. The base material, magnesium (Mg) has significant technological potential and its intrinsic ductility is well-documented. The mechanical properties of Mg are enhanced by small amounts of rare earth elements such as Y. We find that solutes at the dilute limit can provide some mild toughening effect but cannot fundamentally convert the intrinsic nature of the brittle base material thus highlighting a significant constraint of conventional alloying.

Turning our interest to HEAs, their multiple principal components produce superior mechanical properties but generally poor ductility connected to fracture phenomena. The random alloy crack tip is significantly more complex to study so in Chapter 6 we first investigate the activated crack tip behavior in several averaged model refractory HEAs in order to establish a reference against which we can later distinguish the random effect. We propose a room temperature (RT) screening criterion for ductility and apply it to brittle HEAs to identify new compositions with potential for RT ductility.

Dislocation emission is by nature a nucleation event and perceives a local environment in a random system rather than the global average properties. Consequently, following in Chapter 7 we compare the deviations of emission behavior in a random system vs. its average behavior coming from variations in the material properties due to compositional disorder and inherent “microdistortions” from atomic misfit volume. The inherent randomness in an alloy improves the ductility overall. Significant reductions to the local emission energy signify the potential for local crossover from brittle to ductile behavior even if a material is brittle on average. We continue to refine the strategy for broad screening for ductility, which remains a pressing challenge in alloy design.

Background: theory and simulation of atomistic fracture

Part I

1 Linear Elastic Fracture Mechanics (LEFM)

Structural materials are found in a wide range of industrial applications, for example, in aerospace applications, in the energy (e.g. nuclear) sector, in infrastructure, and in biomedical components to name just a few [12]. In these applications, brittle material failure by fracture can be catastrophic, often resulting in loss of life. One popular example is the case of the Liberty ships which were designed and produced during the Second World War and suffered from severe brittle fracture – some incidents involved the complete fracture of ships into two [13]. The Liberty disaster was due to a lack of understanding of fracture at the time, for example low temperature embrittlement and the properties of fracture initiation, and is credited to prompting the practical research giving birth to modern fracture mechanics.

The emergence of fracture mechanics is credited to the work of Griffith [14] and his formulations of fracture as a energetic concept in the beginning of the 20th century, but it was the subsequent analysis by Irwin [15, 16] who introduced the concept of stress intensity, Orowan [17], Westergaard [18], and later Rice [19] in the mid-century that brought the theoretical framework to its essential form. Today, in the framework of Linear Elastic Fracture Mechanics (LEFM), we can describe and predict a variety of fracture phenomena (e.g. brittle fracture, fracture toughness, fatigue crack growth, stress-corrosion crack growth, ...) in terms of stress and crack parameters. Incidents such as the Liberty disaster are not resigned to the history books, however, since we create increasingly complex structures and components in the present day. We require theoretical and practical methods to understand and design for fracture properties and LEFM is thus an invaluable analysis tool to this end.

In engineering we want to predict and design against fracture. We treat a material as a continuum and analyze the stress, strain, and energy – this chapter focuses on the continuum approach. The fracture problem can also be approached at smaller scales, and the features across different length scales together determine the ultimate physical nature of the failure. For instance, we can consider the interactions of a crack with

microstructure, e.g. grains and their boundaries in polycrystalline metals, or defects, e.g. dislocations, solutes, precipitates, voids. The basic microscopic constituents of materials are atoms, and fracture at the atomic level is a separation of atomic planes. We focus on the atomistic crack-tip processes in later in Chapter 2.

LEFM is considered a mature topic with numerous comprehensive texts (e.g. [20–22]), but we revisit some key points in this chapter. A crack in a solid body consists of a plane discontinuity between an upper and lower crack face; the joint of the two faces forms the crack front. Any fracture mode in a cracked body can be decomposed into three fundamental fracture modes: mode I, perpendicular tensile opening; mode II, shear sliding; and mode III, anti-plane “tearing” strain [16]. The discussion in this thesis is generally framed around mode I fracture. Fracture criteria is established via two approaches, and we discuss both in the following. The first approach is through local crack-tip stress fields, where linear analysis yields asymptotic fields which can be expressed in terms of the stress intensity factor K . The second approach is by considering a global energy balance of the potential energy and the rate of energy release of crack extension. The energy release rate and stress intensity are unique related in linear elastic materials.

1.1 Plane strain crack stress fields

To illustrate the concept of the stress intensity factor (SIF) and the near-tip stress and displacement fields, consider a large plate (planar dimensions $-L/2 < x_1 < L/2$, $-L/2 < x_2 < L/2$) subjected to a remotely-applied symmetric bi-axial stress σ^{app} (Fig. 1.1). The plate contains a centered line crack of length $2a$, which is defined by imposing traction-free conditions on the upper and lower surface crack surfaces. Applying the conditions of a plane-strain approximation, the results are independent of the out-of-plane x_3 dimension and reduces to a 2d problem.

For a very small crack $a \ll L$ and at the limit $L \rightarrow \infty$, this configuration can be treated mathematically as an infinite plate with a finite crack. The boundary conditions at $x_1^2 + x_2^2 \rightarrow \infty$ are $\sigma_{11} = \sigma_{22} = \sigma^{\text{app}}$ and $\sigma_{12} = 0$. The crack surfaces are traction free, so there the boundary conditions are $\sigma_{12} = \sigma_{22} = 0$ at $|x_1| = a, y = 0$. This far-field loading scenario corresponds to mode I since the loads are symmetric with respect to the line of the crack.

The complex potential functions of Kolosov and Muskhelishvili [24] is a powerful general method to treat plane elasticity problems. The function method of Westergaard [18, 25] further exploits the symmetry/anti-symmetry of the fundamental fracture modes, and the solution of this boundary value problem is given by Westergaard [18] as

$$Z_I(z) = \frac{\sigma^{\text{app}} z}{\sqrt{z^2 - a^2}} \quad (1.1)$$

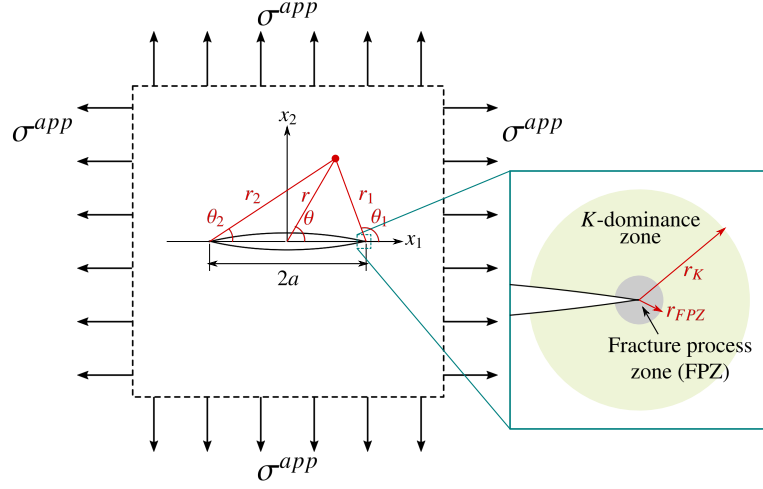


Figure 1.1: A finite crack of length $2a$ centered on an infinite plate under biaxial σ^{app} stress. Stresses far away from the crack are influenced by the boundary conditions and the sample geometry. In the vicinity of the crack tip, the K -dominance zone ($r_K \ll a$), where the asymptotic fields are accurate, contains a small nonlinear fracture process zone (FPZ). Adapted from [21, 23].

where Z_I is the so-called Westergaard function for mode I problems. Using polar coordinates and the following relations (see Fig. 1.1),

$$\begin{aligned} z &= re^{i\theta} \\ z - a &= r_1 e^{i\theta_1} \\ z + a &= r_2 e^{i\theta_2} \end{aligned} \quad (1.2)$$

Eq. (1.1) is conveniently expressed as

$$Z_I = \frac{\sigma^{app} r}{\sqrt{r_1 r_2}} \exp i \left(\theta - \frac{\theta_1}{2} - \frac{\theta_2}{2} \right) \quad (1.3)$$

and its derivative is

$$Z'_I = -\frac{\sigma^{app} a^2}{(r_1 r_2)^{3/2}} \exp \left(i \frac{3}{2} (\theta_1 + \theta_2) \right) \quad (1.4)$$

from which we explicitly obtain the stress fields

$$\begin{aligned} \sigma_{11} &= \frac{\sigma^{app} r}{\sqrt{r_1 r_2}} \left[\cos \left(\theta - \frac{\theta_1}{2} - \frac{\theta_2}{2} \right) - \frac{a^2}{r_1 r_2} \sin \theta \sin \frac{3}{2} (\theta_1 + \theta_2) \right] \\ \sigma_{22} &= \frac{\sigma^{app} r}{\sqrt{r_1 r_2}} \left[\cos \left(\theta - \frac{\theta_1}{2} - \frac{\theta_2}{2} \right) + \frac{a^2}{r_1 r_2} \sin \theta \sin \frac{3}{2} (\theta_1 + \theta_2) \right] \\ \sigma_{12} &= \frac{\sigma^{app} r}{\sqrt{r_1 r_2}} \left[\frac{a^2}{r_1 r_2} \sin \theta \sin \frac{3}{2} (\theta_1 + \theta_2) \right] \end{aligned} \quad (1.5)$$

At far distances, $r_1 \approx r_2 \approx r \rightarrow \infty$ and $\theta_1 \approx \theta_2 \approx \theta$ such that $\sigma_{11} = \sigma_{22} = \sigma^a$ and $\sigma_{12} = 0$.

1.2 Plane strain asymptotic crack tip fields

The stress fields in the vicinity of a crack tip control crack growth. In the vicinity of a crack tip, e.g. taking the right crack tip in Fig. 1.1, we have $r_1/a \ll 1$, $\theta \approx 0$, $\theta_2 \approx 0$, $r \approx a$, and $r_2 \approx 2a$. The various terms in Eq. (1.5) reduce to

$$\begin{aligned} \sin \theta &\approx \frac{r_1}{a} \sin \theta_1 \\ \sin \frac{3}{2}(\theta_1 + \theta_2) &\approx \sin \frac{3}{2}\theta_1 \\ \cos \left(\theta - \frac{\theta_1}{2} - \frac{\theta_2}{2} \right) &\approx \cos \frac{\theta_1}{2} \\ \cos \frac{3}{2}(\theta_1 + \theta_2) &\approx \cos \frac{3}{2}\theta_1 \end{aligned} \tag{1.6}$$

The mode I stress intensity factor K_I for this problem is [16]

$$K_I = \sigma^{\text{app}} \sqrt{\pi a} \tag{1.7}$$

Further rewriting Eq. (1.5) so that the origin is centered on the crack tip ($r, \theta_1 \equiv \theta$), the stress field near the crack tip written in terms of the mode I stress intensity is

$$\begin{aligned} \sigma_{11} &= \frac{K_I}{\sqrt{2\pi r}} \cos \frac{\theta}{2} \left(1 - \sin \frac{\theta}{2} \sin \frac{3\theta}{2} \right) \\ \sigma_{22} &= \frac{K_I}{\sqrt{2\pi r}} \cos \frac{\theta}{2} \left(1 + \sin \frac{\theta}{2} \sin \frac{3\theta}{2} \right) \\ \sigma_{12} &= \frac{K_I}{\sqrt{2\pi r}} \sin \frac{\theta}{2} \cos \frac{\theta}{2} \cos \frac{3\theta}{2} \end{aligned} \tag{1.8}$$

The displacement around the crack tip can be derived in a similar fashion and the fields are

$$\begin{aligned} u_1 &= \frac{K_I}{2\mu} \sqrt{\frac{r}{2\pi}} \cos(\theta/2) \left[\kappa - 1 + 2 \sin^2(\theta/2) \right] \\ u_2 &= \frac{K_I}{2\mu} \sqrt{\frac{r}{2\pi}} \sin(\theta/2) \left[\kappa + 1 - 2 \cos^2(\theta/2) \right] \end{aligned} \tag{1.9}$$

where $\kappa = 3 - 4\nu$ for plane strain.

From the crack tip stress fields in Eq. (1.8) we can make several observations. The stresses contain the well-known $1/\sqrt{r}$ singularity at the crack tip, and these fields do not depend on the material properties. The geometry of the cracked body (e.g. crack length) and the loading condition (e.g. particulars of σ^{app} at the boundaries) influence the singular crack tip fields only through the mode I stress intensity factor K_I . Any

1.2. Plane strain asymptotic crack tip fields

crack tip phenomena can thus be elegantly characterized solely in terms of a value of critical stress intensity. For more complex configurations, the crack tip fields depend on a combination of the stress intensities of the three modes, i.e. K_I , K_{II} , and K_{III} . However, we mainly focus on K_I since it is usually a dominant contribution. The low compressive ductility in many bcc elements and HEAs may be related to an intrinsic lack of resistance to tensile (mode I) failure [26].

Many materials are anisotropic, so their material properties and fracture behavior show directional dependence. For cubic materials, the Zener ratio a_r is a typical measure of the amount of anisotropy and is the expression

$$a_r = \frac{2C_{44}}{C_{11} - C_{12}} \quad (1.10)$$

where C_{ij} are the components of the elastic tensor in the contracted Voigt notation; $a_r = 1$ for an isotropic material.

The sextic Stroh [27] formalism is a powerful tool for the analysis of 2d deformations of anisotropic linear elastic solids. We direct the reader to [20] where the Stroh formalism is presented in its detailed entirety. The anisotropic singular near-tip stress fields are

$$\begin{aligned} [\sigma_{11}, \sigma_{21}, \sigma_{31}]^T &= -\frac{K_I}{\sqrt{2\pi r}} \operatorname{Re} \left\{ \mathbf{B} \left\langle \frac{v_\alpha}{\sqrt{\cos \theta + v_\alpha \sin \theta}} \right\rangle \mathbf{B}^{-1} \right\} \\ [\sigma_{12}, \sigma_{22}, \sigma_{32}]^T &= -\frac{K_I}{\sqrt{2\pi r}} \operatorname{Re} \left\{ \mathbf{B} \left\langle \frac{1}{\sqrt{\cos \theta + v_\alpha \sin \theta}} \right\rangle \mathbf{B}^{-1} \right\} \end{aligned} \quad (1.11)$$

and the displacements are

$$\mathbf{u} = \frac{K_I \sqrt{2r}}{\sqrt{\pi}} \operatorname{Re} \left\{ \mathbf{A} \left\langle \sqrt{\cos \theta + v_\alpha \sin \theta} \right\rangle \mathbf{B}^{-1} \right\} \quad (1.12)$$

where the angle brackets represent the elements of a diagonal matrix. In the above, $\mathbf{A} = [\mathbf{a}_1, \mathbf{a}_2, \mathbf{a}_3]$ and $\mathbf{B} = [\mathbf{b}_1, \mathbf{b}_2, \mathbf{b}_3]$, which are the complex matrices, and $\mathbf{v} = \langle v_\alpha \rangle$, the eigenvalues, satisfy the eigenvalue relationship of

$$\mathbf{N} \begin{bmatrix} \mathbf{A} \\ \mathbf{B} \end{bmatrix} = \mathbf{v} \begin{bmatrix} \mathbf{A} \\ \mathbf{B} \end{bmatrix} \quad (1.13)$$

In Eq. (1.13), the fundamental elasticity matrix \mathbf{N} can be partitioned into a 2×2 block [20], i.e.

$$\begin{aligned} \mathbf{N} &= \begin{bmatrix} \mathbf{N}_1 & \mathbf{N}_2 \\ \mathbf{N}_3 & \mathbf{N}_1^T \end{bmatrix} \\ \mathbf{N}_1 &= -\mathbf{T}^{-1} \mathbf{R}^T, \quad \mathbf{N}_2 = \mathbf{T}^{-1}, \quad \mathbf{N}_3 = \mathbf{R} \mathbf{T}^{-1} \mathbf{R}^T - \mathbf{Q} \end{aligned} \quad (1.14)$$

where $\mathbf{Q}_{ik} = C_{i1k1}$, $\mathbf{R}_{ik} = C_{i1k2}$, $\mathbf{T}_{ik} = C_{i2k2}$, and C_{ijkl} is the material stiffness tensor.

Given an orientation where the material properties are symmetric about the crack line, the closed-form analytical solutions are provided by [28]. We can write the near-tip stress fields for mode I loading in this case as

$$\begin{aligned}\sigma_{11} &= \frac{K_I}{\sqrt{2\pi r}} \operatorname{Re} \left[\frac{a_1 a_2}{a_1 - a_2} \left(\frac{a_2}{\sqrt{\cos \theta + a_2 \sin \theta}} - \frac{a_1}{\sqrt{\cos \theta + a_1 \sin \theta}} \right) \right] \\ \sigma_{22} &= \frac{K_I}{\sqrt{2\pi r}} \operatorname{Re} \left[\frac{1}{a_1 - a_2} \left(\frac{a_1}{\sqrt{\cos \theta + a_2 \sin \theta}} - \frac{a_2}{\sqrt{\cos \theta + a_1 \sin \theta}} \right) \right] \\ \sigma_{12} &= \frac{K_I}{\sqrt{2\pi r}} \operatorname{Re} \left[\frac{a_1 a_2}{a_1 - a_2} \left(\frac{1}{\sqrt{\cos \theta + a_1 \sin \theta}} - \frac{1}{\sqrt{\cos \theta + a_2 \sin \theta}} \right) \right]\end{aligned}\quad (1.15)$$

which still contain the inverse square-root singularity in r . The corresponding displacements are written as

$$\begin{aligned}u_1 &= K_I \sqrt{\frac{2r}{\pi}} \operatorname{Re} \left[\frac{1}{a_1 - a_2} \left(a_1 p_2 \sqrt{\cos \theta + a_2 \sin \theta} - a_2 p_1 \sqrt{\cos \theta + a_1 \sin \theta} \right) \right] \\ u_2 &= K_I \sqrt{\frac{2r}{\pi}} \operatorname{Re} \left[\frac{1}{a_1 - a_2} \left(a_1 q_2 \sqrt{\cos \theta + a_2 \sin \theta} - a_2 q_1 \sqrt{\cos \theta + a_1 \sin \theta} \right) \right]\end{aligned}\quad (1.16)$$

The angular distribution of the displacements depends on the constants p_1 , p_2 , q_1 , and q_2 , and they are obtained from

$$\begin{aligned}p_1 &= S_{11}^p a_1^2 + S_{12}^p - S_{16}^p a_1 \\ p_2 &= S_{11}^p a_2^2 + S_{12}^p - S_{16}^p a_2 \\ q_1 &= S_{12}^p a_1 + S_{22}^p / a_1 - S_{26}^p \\ q_2 &= S_{12}^p a_2 + S_{22}^p / a_2 - S_{26}^p\end{aligned}\quad (1.17)$$

where a_1 and a_2 are the roots of the characteristic equation

$$S_{11}^p a^4 - 2S_{16}^p a^3 + (2S_{12}^p + S_{66}^p) a^2 - 2S_{26}^p a + S_{22}^p = 0 \quad (1.18)$$

where $S_{ij}^p = S_{ij} - S_{i3}S_{3j}/S_{33}$ are the components of the material compliance tensor for the plane-strain approximation in the contracted Voigt notation, and $\mathbf{S} = \mathbf{C}^{-1}$ is the material compliance tensor. The displacement fields for mode II, etc., are derived in a similar fashion (see [29]). In Chapter 3 we discuss the K -controlled simulation framework. There, a simulated atomistic crack is loaded to exactly some stress intensity by imposing the displacement boundary conditions of the LEFM displacement solution, e.g. Eq. (1.16).

1.3 Fracture process zone and small scale yielding

LEFM predicts diverging stresses at the crack tip which are, in fact, finite due to the nonlinear response of the real material under very high stresses. Material failure (e.g. plastic flow, micro-cracks, void growth) begins in the so-called “fracture process zone”

(FPZ) in the region ahead of the crack (schematically shown in Fig. 1.1). The degree of K -dominance Λ is defined as the proportion of the singular stresses, i.e. the inverse square-root fields, to the total stress, and $\Lambda \leq 1$. In the region of K -dominance, the stress is effectively described by the inverse square-root singular fields, and thus by the stress intensity factor. The small scale yielding (SSY) assumption requires that the FPZ is confined to a very small region close to the crack tip relative to the size of the crack and well within the K -dominance zone. i.e. for a half-crack size a , the size of the regions r must satisfy a “length-scale” hierarchy of $r_{FPZ} \ll r_K \ll a$. The complex fracture processes and nonlinear deformation inside the FPZ are ignored using the singular fields.

For a center crack contained in a finite plate, the size of the K -dominance region is very sensitive to the size of the plate (for examples see [21, 23]). The size of the K -dominance zone decreases with decreasing plate dimensions such that the region in which the singular fields/stress intensity is an effective descriptor of the crack tip fields becomes very small so K does not account for entire force driving fracture. The required minimum size of the finite plate containing a center crack satisfying SSY is thus generally quite large which can become problematic in atomistic simulations. We return to this point in Chapter 3.

1.4 Energetics of crack extension

It is convenient to formulate the fracture problem in an energetic framework, i.e. as a variation in the global energy of a system during crack extension. Neglecting dynamic effects, the total potential energy Π of a system contains the internal strain energy U stored in a loaded body Ω and the external work of tractions V , and is written for the linear system as

$$\Pi = U + V = \frac{1}{2} \int_{\Omega} \sigma_{ij} \varepsilon_{ij} d\Omega - \int_{\Gamma_t} T_i u_i d\Gamma \quad (1.19)$$

where T_i are the tractions on boundaries Γ_t corresponding to displacements u_i , but in a traction-free elastic body $\Pi = U$. Consider the change in the total mechanical energy of the system that would occur if a crack were to extend by an increment of da . The energy release rate G per unit of crack extension da is defined as

$$G = -\frac{d\Pi}{da} \quad (1.20)$$

The mechanical energy release rate G represents the amount of available energy in the body providing the energy to drive the crack and pay the cost of dissipative processes.

In elastic materials, the energy and stress approaches for fracture are equivalent. This can be shown by relating the strain energy and the energy release rate associated with an increment of crack extension (da). The energy release rate G and the stress intensity

K are uniquely related. For mixed-mode loading with a plane strain approximation, the energy release rate for an isotropic material is written as [30]

$$G = \frac{1}{2\mu} \left[(1 - \nu) (K_I^2 + K_{II}^2) + K_{III}^2 \right] \quad (1.21)$$

where μ is the isotropic shear modulus. On a related note, Rice [19, 31] derives the path-independent J -integral from the variation of the potential energy with crack extension which applies to non-linear elastic materials as well. In elastic materials, the J -integral is also equivalent to the energy release rate, so G , J , and K are uniquely related.

Eq. (1.21), when generalized to anisotropic elasticity [32], becomes

$$G = \mathbf{K}^\top \mathbf{\Lambda} \mathbf{K} \quad (1.22)$$

where $\mathbf{K}^\top = [K_{II}, K_I, K_{III}]$ is the external loading and $\mathbf{\Lambda}$ is the Stroh energy tensor [20, 27]. For an atomically sharp, semi-infinite crack in homogeneous media,

$$\mathbf{\Lambda} = \frac{1}{2} \text{Re} \left(i \mathbf{A} \mathbf{B}^{-1} \right) \quad (1.23)$$

where \mathbf{A} and \mathbf{B} are the same complex matrices as above.

The fracture criterion in the energy approach is $G = G_c$ – a crack will extend if the energy release rate is equal to a critical rate G_c , where G_c is the energetic cost of the energy-dissipating processes per increment of crack extension [15]. In a purely brittle material under quasi-static loading, energy dissipation is solely due to the creation of new surface corresponding to the crack extension. The critical energy release rate is then twice the surface (creation) energy of the crack plane γ_s which is a property of the material, i.e. $G_c = 2\gamma_s$ is the Griffith [14] criterion for brittle fracture. The mode I anisotropic fracture criteria is written as

$$K_{Ic} = \sqrt{\frac{2\gamma_s}{\Lambda_{22}}} \quad (1.24)$$

A critical fracture property for design is the effective fracture toughness, i.e. a material's resistance to crack growth, and is equal to the critical stress intensity at which the crack grows, e.g. K_{Ic} in mode I. The fracture toughness includes the possible energy-dissipating processes contained in the near-crack tip FPZ. K_{Ic} can evolve and increase – or “toughens” – with crack extension due to the evolving size of the FPZ and the associated increase in energy dissipation via FPZ processes. The crack resistance curve (R -curve), which is the relationship of K_{Ic} vs. crack growth Δa , captures the notion of toughening. Later in Chapter 5, local solute-induced phenomena in a dilute alloy provide an additional source of energy dissipation that improves the fracture toughness as observed from atomistic R -curves.

2 Atomistic crack-tip processes

This chapter is in part extracted from the following publications

1. Mak, E., & Curtin, W. A. (2020). Intrinsic fracture behavior of Mg–Y alloys. *Modelling and Simulation in Materials Science and Engineering*, 28(3), 035012
2. Mak, E., Yin, B., & Curtin, W. A. (2021). A ductility criterion for bcc high entropy alloys. *Journal of the Mechanics and Physics of Solids*, 152, 104389

One tenet in materials science, often called the structure-property paradigm, is that the mechanical properties of a material are a function of the underlying structure at the atomic/nanoscale. A crack interacts with the defects and the microstructure (e.g. dislocations, solute and precipitates, voids, grain boundaries, ...) in its vicinity, and these basic interactions at the microscopic level determine the fracture behavior at the macroscopic scale, which are the phenomenon of interest for industrial applications. Metals and metal alloys are widely used as structural materials across a wide range of applications (aerospace, infrastructure, biomedical industry, etc.). Especially for structural applications, failure by fracture can be catastrophic, so fracture toughness, i.e. the resistance to fracture, is a vital material design property for performance and reliability. Hydrogen embrittlement [34] is a prime example: the atomic-scale interactions of diffusible hydrogen with a crack translates to low macroscopic fracture toughness and catastrophic consequences and remains a current problem (e.g. the 2013 failure of Oakland Bay Bridge [35] due to embrittlement in structural steels).

Fracture toughness in crystalline metals depends on the intrinsically brittle or ductile nature of the crack tip [14, 30, 36] depending on a competition between the atomistic crack tip mechanisms of cleavage and dislocation emission. In the previous chapter, we presented the critical mode I stress intensity for Griffith cleavage K_{Ic} , above which a sharp crack in a continuum becomes unstable to extension. At loads below K_{Ic} , a crack

is thermodynamically precluded from cleavage and is instead unstable to closure. Due to the discrete character of the atomistic lattice, lattice trapping [37, 38] of a crack tip leads to a range of stress above and below K_{Ic} where the crack remains stable. This is a well-observed phenomenon in simulation [39, 40] and is generally modest in crystalline metals.

Dislocation emission has practical importance for ductility which has motivated a number of approximate continuum models [36, 41–44] to predict a comparable mode I stress intensity for dislocation emission K_{Ie} . The process of emission, in addition to producing a dislocation, blunts the crack tip which changes the crack tip singularity. The most widely-used emission model by Rice [30] and a correction for the surface step creation of crack tip blunting is presented following. We also discuss the mechanism of “dislocation shielding” [45–47] where a dislocation in the vicinity of the crack tip shields the crack tip from the far-field loading.

We can capture the crack tip competition of intrinsic ductility by a simple ductility index D that compares the stress intensities for the competing mechanisms. Both crack tip mechanisms are thermally activated processes, so the critical stress intensities for cleavage and emission, K_{Ic} and K_{Ie} , are lower and upper limits, respectively, and are further connected to a load-dependent energy barrier.

2.1 Fracture toughness and macroscopic ductility

A commonly accepted definition of fracture toughness is a material’s resistance to the growth of a pre-existing crack. Fracture toughness is related to the energy dissipation processes in the vicinity of a crack tip. The fracture toughness in the very early stages of crack growth are controlled by (i) the nanoscale process of atomic decohesion of the crack tip, and (ii) plastic deformation surrounding a crack tip. Dislocations are the main carriers of plasticity in crystalline metals [11]. Metals and metal alloys develop toughness via crack tip plasticity through the intrinsically ductile mechanism of dislocation emission, which blunts the crack tip and changes the crack tip singularity [12]. The emitted dislocations move away from the crack tip and generate far-field plasticity. Dislocation emission is a necessary precursor to blunting and toughening and is thus the enabling mechanism for the subsequent onset of ductile failure mechanisms (void nucleation, growth, and coalescence ahead of the crack) that provide the means for large energy dissipation.

In contrast, an intrinsically brittle material is unable to emit dislocations from a crack tip. In very brittle materials, e.g. ceramics, fracture is controlled almost entirely by the local decohesion of the atomic bonds between two layers of atoms at the crack tip. Take for example a single-crystal containing pre-existing dislocations and a pre-existing atomically sharp crack. A sharp crack remains sharp and propagates easily

through the material by brittle cleavage. Although the material can be deforming due to dislocation plasticity zone around the crack tip, and this provides some energy dissipation higher than the Griffith cleavage value, the fracture toughness remains far lower than the toughness achievable by ductile failure mechanisms. From a continuum perspective, macroscopic crack extension encompasses the complex microscale failure processes, e.g. the accumulation of microcracks in brittle materials, and void nucleation, growth, and coalescence in ductile materials. Consequently, a fundamental requirement for achieving macroscopic high fracture toughness in crystalline materials is thus intrinsic ductility representing a material's capacity to emit a dislocation [48].

2.2 Dislocation emission and surface step creation

The cohesive-type model of Rice [30] (hereafter called “Rice theory”) is based on the Peierls concept [49] and was formulated for the problem of 2d dislocation emission ahead of a semi-infinite crack under pure mode II loading. The cohesive model eliminates the elastic stress singularity at the crack tip and instead the cohesive response ahead of the crack tip is described by a shear resistance τ as a periodic function of the slip plane displacement δ , where δ is along the plane of displacement discontinuity in a continuum.

For a discrete lattice in the atomistic system, lattice planes are separated by a distance h . The relative slip between two lattice planes is denoted by Rice as Δ , where $\Delta = \delta + h\tau/\mu$ includes an additional amount of elastic shearing ($h\tau/\mu$) in the lattice. A simple form of the τ vs Δ relationship is approximated by the Frenkel sinusoid, which has the form

$$\tau = \frac{\mu b}{2\pi h} \sin\left(\frac{2\pi\Delta}{b}\right) \quad (2.1)$$

where b is the Burgers vector of the emitted dislocation. A functional for the energy of slip (per unit area) is

$$\Psi(\Delta) = \int \tau d\Delta = \frac{\mu b^2}{2\pi^2 h} \sin^2\left(\frac{2\pi\Delta}{b}\right) = \gamma_{usf} \sin^2\left(\frac{2\pi\Delta}{b}\right) \quad (2.2)$$

which is the area under the τ - Δ curve. This energy is the so-called generalized stacking fault (GSF) energy. Its maximum at $\Delta = b/2$ is the unstable stacking fault (USF) energy γ_{usf} and is the energy barrier to shear one half of a block of perfect lattice relative to another along a slip plane.

A corresponding energy functional $\Phi(\delta)$ obtained from τ - δ shares a common maximum γ_{usf} with $\Psi(\Delta)$. The path-independent J -integral [19] applied along the contour of the crack around the cohesive zone is equivalent to Φ [30], i.e.

$$J = - \int_0^\infty \tau \frac{\partial \delta}{\partial x} dx = \int_0^{\delta_{tip}} \tau(\delta) d\delta \equiv \Phi(\delta_{tip}) \quad (2.3)$$

Chapter 2. Atomistic crack-tip processes

The J -integral is equivalent to the energy release rate G , so for the isotropic elastic case we have

$$G \equiv (1 - \nu) \frac{K_{II}^2}{2\mu} = \Phi(\delta_{tip}) \quad (2.4)$$

An incipient dislocation is a distribution of partial slip across the slip plane and reaches a critical point of instability at the position of the USF, i.e. where $\Phi = \Psi = \gamma_{usf}$ is a maximum. The energy release rate is also a maximum corresponding to the point of the dislocation. Rice gives the critical stress intensity for mode II loading as

$$K_{IIe} = \sqrt{\frac{2\mu\gamma_{usf}}{1 - \nu}} \quad (2.5)$$

for an isotropic elastic material assuming that the relative motion along the slip plane is in pure shear (“constrained-path” approximation).

In mode I loading, the slip plane is inclined at an angle θ from the crack plane. Rice proposed that the distribution of shear slip along the slip plane is the same for modes I and II, so the result for mode I emission can be estimated by computing an effective mode II loading along the slip plane giving the result

$$K_{Ie} = \sqrt{\frac{2\mu\gamma_{usf}}{1 - \nu}} \left[\cos^2 \left(\frac{\theta}{2} \right) \sin \left(\frac{\theta}{2} \right) \right]^{-1} \quad (2.6)$$

with the emission occurring also at the Δ of the USF. The full anisotropic analysis was presented in [32], and the anisotropic counterpart to the isotropic results for mode II (Eq. (2.5)) and mode I (Eq. (2.6)) are

$$\begin{aligned} K_{IIe} &= \sqrt{\gamma_{usf} o(\theta, \phi)} \\ K_{Ie} &= \sqrt{\gamma_{usf} o(\theta, \phi) / F_{12}(\theta)} \end{aligned} \quad (2.7)$$

The anisotropic elastic parameter $o(\theta, \phi)$ from the Stroh formalism is

$$o(\theta, \phi) = s_i(\phi) \Lambda_{ij}^{(\theta)-1} s_j(\phi) \quad (2.8)$$

where θ and ϕ are the inclinations of the slip plane and the dislocation Burgers vector, respectively (see Fig. 2.1), and $\mathbf{s}(\phi)$ is the slip vector in the constrained path approximation, and

$$\Lambda_{ij}^{(\theta)} = \Omega_{ik} \Omega_{lj} \Lambda_{kl} \quad (2.9)$$

2.2. Dislocation emission and surface step creation

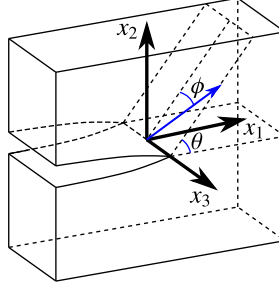


Figure 2.1: Schematic of crack geometry and coordinate system. A crack extends along its plane (x_1 - x_3) in the x_1 direction. The crack front is defined along the x_3 axis. Dislocation emission occurs on a slip plane intersecting the crack plane at an angle θ . The dislocation Burgers vector is inclined at an angle ϕ with respect to the crack front normal on the slip plane.

is the rotated matrix of $\mathbf{\Lambda}$ (Eq. (1.23)) for a crack orientation. The rotation matrix given by

$$\Omega_{ij} = \begin{bmatrix} \cos \theta & \sin \theta & 0 \\ -\sin \theta & \cos \theta & 0 \\ 0 & 0 & 1 \end{bmatrix} \quad (2.10)$$

A notable result of the Rice theory is that the major material parameter determining K_{Ie} is the USF energy γ_{usf} of the emission plane.

Recent work by [48] identify an absence of a maximum in the slip energy at the crack tip in mode I emission of a partial dislocation. This immediately precludes the direct application of the mode II Rice theory for mode I since the Rice theory is based on an energy maximum (i.e. γ_{usf}). The additional creation of new surface due to slip can make a non-negligible contribution to the energy changes at the crack tip. The Rice concept of an instability of the energy is shifted to a mechanical instability at the crack tip. Emission is instead controlled by reaching a critical crack tip displacement associated with a mechanical instability associated with the formation of a surface step. Deviations from the Rice theory arise, but the critical stress intensity for emission takes a form which resembles the Rice criterion, i.e.

$$K_{Ie} = \sqrt{G_{Ie} o(\theta, \varphi) / |F_{12}(\theta)|} \quad (2.11)$$

F_{ij} resolves the applied K field into an effective shear along the dislocation slip plane, i.e.

$$K_{(i)}^{\text{eff}} = F_{ij} K_{(j)} \quad (2.12)$$

where components $F_{ij} = D_{i2}^{(j)}$ relate the angular asymptotic crack tip stress distribution to the mode of loading as

$$\sigma_{kl}(r, \theta) = \frac{K_{(j)}}{\sqrt{2\pi r}} D_{kl}^{(j)}(\theta) \quad (2.13)$$

and the bracketed indices, i.e. (\bullet) , indicate loading modes $\{1, 2\} = \{\text{II}, \text{I}\}$. $F_{12}(\theta)$ is a

geometric parameter accounting for the inclination of the slip plane θ with respect to the crack plane.

Across a wide range of fcc materials, Andric and Curtin [48] devise a good analytic estimate of the critical energy release rate as

$$G_{Ie} = \begin{cases} 0.145\gamma_s^e + 0.5\gamma_{usf}^e & , \gamma_s^e > 3.45\gamma_{usf}^e \\ \gamma_{usf}^e & , \text{otherwise} \end{cases} \quad (2.14)$$

where γ_s^e and γ_{usf}^e are the surface energy and unstable stacking fault energy of the emission plane, respectively. No aspect of the analysis in [30, 48] relies specifically on the crystal structure, so the theory is not limited to, for example, the fcc materials studied by [48]. However, Eq. (2.14) was never compared to atomistic simulations in non-fcc metals, but we do so later in this thesis (e.g. in Chapter 3.4 and 4.4.2). Eq. (2.14) reduces to the Rice relationship when γ_s^e is small, which is in general the case for most of the bcc metals and HEAs, so the simpler Rice condition can generally be used in studies of bcc materials.

2.2.1 Crack tip shielding by dislocations

Dislocations are a well-known source of crack-tip shielding, whereby the stress singularity at a crack tip is reduced due to the dislocations in its neighborhood [45–47]. The opposite, where the singularity is enhanced (anti-shielding), is also possible. The magnitude of shielding/anti-shielding depends on the magnitude and sign of the Burgers vector and the position and orientation of the dislocation and emission plane relative to the crack tip and plane. A full dislocation, once emitted, moves far away from the crack tip generating far-field plasticity and its shielding effect subsides. In fatigue for instance, accumulated crack tip shielding can become a potent source of extrinsic toughening impeding crack extension [50].

In fcc and hcp crystals, where dislocations dissociate into two partial dislocations, the first emission event is that of a partial dislocation. The partial emission then leaves a stacking fault extending from the crack tip to the equilibrium position of the emitted partial. The second event can then be the emission of (i) a second partial but on an adjacent plane, starting the formation of a twin-like structure at the crack tip, or (ii) a trailing partial dislocation on the same plane as the original partial, annihilating the stacking fault and creating a full dislocation. A full dislocation can glide far away from the crack tip. The analysis of Ref. [51] extends the original instability-based emission theory to include the second partial dislocation emission. For the case where a full dislocation is formed, an analytic estimate of the stress intensity for the emission of the

trailing partial is

$$K_{Ie}^{\text{trail}} = \sqrt{G_{Ie}^{\text{trail}} o(\theta, \varphi_{\text{trail}})} / (|F_{12}(\theta)| \cos(\varphi_{\text{trail}}))$$

$$G_{Ie}^{\text{trail}} = \begin{cases} 0.0725\gamma_s^e + 0.5(\gamma_{usf}^e - \gamma_{ssf}^e) & , \gamma_s^e > 6.9(\gamma_{usf}^e - \gamma_{ssf}^e) \\ \gamma_{usf}^e - \gamma_{ssf}^e & , \text{otherwise} \end{cases} \quad (2.15)$$

where γ_{ssf}^e is the stable stacking fault energy of the emission plane, and φ_{trail} is the inclination of the trailing dislocation Burgers vector with respect to the crack front normal on the emission plane.

Note that the macroscopic applied stress intensity factor K_I^{app} is generally not the same as the local stress intensity factor at the crack tip K_I^{tip} . Dislocation plasticity surrounding the crack tip, generated by dislocation motion and multiplication as driven by the crack tip stress fields, leads to additional contributions to K_I^{tip} . These contributions are usually negative, i.e. the crack tip is shielded from the full macroscopic applied load K_I^{app} by the fields of the dislocations that have evolved due to the crack tip stress fields. The LEFM analysis of dislocation/crack interactions is well-established [32, 36, 47, 52]. A dislocation at position (r_i, ϕ_i) with respect to the crack tip generates additional mode I and mode II stress intensity factors $k_I^{\text{d}}(r_i, \phi_i)$ and $k_{II}^{\text{d}}(r_i, \phi_i)$, respectively; and, by superposition, the effects of an array of dislocations are additive. In the presence of N^{d} dislocations at positions (r_i, ϕ_i) , the stress intensity at the crack tip is then

$$K_I^{\text{tip}} = K_I^{\text{app}} - \sum_{i=1}^{N^{\text{d}}} k_I^{\text{d}}(r_i, \phi_i) \quad (2.16)$$

In simulations, we apply K_I^{app} on the system but observe the crack tip behavior due to K_I^{tip} , which includes the shielding of emitted dislocations (there are no other dislocations included in these atomistic simulations). The crack tip behavior and brittle/ductile competition are defined in terms of the critical stress intensities,

$$K_{Ic}^{\text{tip}} = K_{Ic} + \sum_{i=1}^{N^{\text{d}}} k_I^{\text{d}}$$

$$K_{Ie}^{\text{tip}} = K_{Ie} + \sum_{i=1}^{N^{\text{d}}} \left(k_I^{\text{d}} + \frac{|F_{11}(\theta)|}{|F_{12}(\theta)|} k_{II}^{\text{d}} \right) \quad (2.17)$$

$$K_{Ie, \text{trail}}^{\text{tip}} = K_{Ie, \text{trail}} + \sum_{i=1}^{N^{\text{d}}} \left(k_I^{\text{d}} + \frac{|F_{11}(\theta)|}{|F_{12}(\theta)|} k_{II}^{\text{d}} \right)$$

with the mode I and mode II shielding contribution from each dislocation given as

$$\begin{aligned} k_I^d &= \frac{1}{2\sqrt{2\pi r}} \Lambda_{2j}^{-1} b_k^I D_{k2}^{(j)} \\ k_{II}^d &= \frac{1}{2\sqrt{2\pi r}} \Lambda_{1j}^{-1} b_k^{II} D_{k2}^{(j)} \end{aligned} \quad (2.18)$$

where $\mathbf{b}^{(i)}$ is the Burgers vector, indices j, k are summed from 1 to 3, and bracketed indices indicate the mode of loading.

2.3 Intrinsic ductility criterion

The intrinsic fracture behavior of a material is dictated by the behavior of an atomistically sharp crack tip. A material is intrinsically ductile if the crack emits dislocations, and thus blunts, rather than cleaving and remaining sharp. The dislocation emission starts the process of blunting the crack tip, enabling increased loads, increased far-field plasticity and energy dissipation, and thus increasing the macroscopic fracture toughness. In complex crystal structures, there are multiple crack orientations, each with specific cleavage planes and associated dislocation slip systems for emission. Intrinsic ductility thus requires that all, or nearly all, of the cleavage/slip geometries in the material be intrinsically ductile and emit dislocations.

Intrinsic ductility is thus a competition between brittle crack cleavage and ductile dislocation emission and can be characterized within the framework of LEFM by the critical intensities for cleavage K_{Ic} and emission K_{Ie} . The critical SIFs depend solely on the underlying material energies and crystallographic orientation. A material is intrinsically ductile if $K_{Ie} < K_{Ic}$ such that, under increasing applied loading, the applied stress intensity at the crack tip K_I^{tip} first reaches the value K_{Ie} , leading to emission and blunting, and preventing the crack tip from reaching the (higher) value of K_{Ic} .

The intrinsic ductility criterion is then the ratio of the emission and cleavage stress intensities, and a material is *intrinsically* ductile if the ductility index D satisfies

$$D = \frac{K_{Ie}}{K_{Ic}} = \chi \bar{\gamma} < 1 \quad (2.19)$$

where the two quantities

$$\begin{aligned} \chi &= \frac{\Lambda_{22} o(\varphi, \theta)}{\sqrt{2} \cos(\varphi) F_{12}(\theta)} \\ \bar{\gamma} &= \sqrt{\frac{\gamma_{usf}}{\gamma_s}} \end{aligned} \quad (2.20)$$

separate the anisotropic elastic geometric effects from the material energetic effects. The LEFM analysis requires only a few material parameters which include the elastic moduli C_{ij} , surface energy of the cleavage planes γ_s , unstable stacking fault energy

of the emission planes γ_{usf} , and the fracture geometry. These material parameters are relatively straightforward to obtain from atomistic simulations, and can also be obtained relatively accurately (e.g. with DFT), so the relative simple D criterion is well-suited for broad screening.

2.4 Activation of crack tip processes

Both cleavage (above K_{Ic}) and emission are thermally-activated events. Lattice trapping, which has been well-established theoretically [37, 38] and in atomistic simulations [39, 40], creates a finite energy barrier for cleavage at the Griffith K_{Ic} . Thermal activation is then relevant above K_{Ic} , which is a *lower* bound since ideal brittle fracture is governed by thermodynamics. In contrast, emission can occur below K_{Ie} if thermal activation provides sufficient energy to overcome some energy barrier. K_{Ie} is an *upper* bound for instantaneous (athermal) 2d dislocation emission. The operative thermally-activated cleavage and emission stress intensities can thus be closer than the values of K_{Ie} and K_{Ic} computed at $T = 0$ K in LEFM. We remark that the values of both K_{Ic} and K_{Ie} are expected to decrease with increasing temperature since elastic constants, surface, and fault energies are all temperature dependent. The intrinsic ductility D (Eq. (2.19)) is thus expected to be minimally dependent on temperature, especially at RT for materials with high melting points, e.g. the high-melting-point refractory HEAs studied in the later chapters.

The emission mechanism involves a local instability of a nucleating dislocation corresponding to an energy saddle point and is inherently a 3d problem. Analysis of the nucleation problem is often focused on identifying the activation energy barrier ΔE as a function of load. Knowledge of the temperature-dependent energy barrier allows the prediction of the nucleation rate (e.g. Eq. (3.7)).

The theory and modeling of dislocation nucleation has a rich history. Computation of ΔE through atomistic simulation with the NEB approach (e.g. [53–55]) has been a relatively recent development but earlier theoretical analysis date to the 1990s. We discuss the NEB method and its application to fracture further in Chapter 3. The widely-cited model by Rice [30] incorporates atomic-scale effects using the Peierls framework in LEFM and confine the nonlinearity associated with the dislocation slip to a plane of zero-thickness within a linear elastic continuum. For the simplified 2d scenario, closed-form analytic expressions relating the critical load for dislocation emission and material parameters were obtained, although in some cases with some geometric constraints [30, 44, 56]. More realistic 3d nucleation analysis is possible still within the Peierls framework using numerical analysis [57–60], e.g. by means of numerical shape functions extending the 2d analysis [30].

Xu and coworkers [59, 60] solve the 3d nucleation more generally for dislocation loops

with arbitrary geometry in a linear elastic solid as a variational problem. They separate the inelastic displacements δ from the elastic displacements $\bar{\mathbf{u}}$ so the crack opening displacement is expressed as $\mathbf{u} = \bar{\mathbf{u}} + \delta$. The potential energy Π of the system is partitioned into an elastic part W and an inelastic part V , which are further separated into $\bar{\mathbf{u}}$ and δ contributions, i.e.

$$\Pi[\bar{\mathbf{u}} + \delta] = W[\bar{\mathbf{u}} + \delta] + V[\delta] = W_1[\bar{\mathbf{u}}] + W_1[\delta] + V[\delta] - W_2[\bar{\mathbf{u}}, \delta] \quad (2.21)$$

In Eq. (2.21), $W_1[\bar{\mathbf{u}}]$ is the elastic strain energy of the unslipped system, i.e. from the standard K -field. Due to the δ , several inelastic modifications arise in the system. The inelastic displacement along the displacement and the opening displacement of the crack is treated as a continuous distribution of dislocations loops confined to the crack and slip plane surfaces. $W_1[\delta]$ is the self-interaction energy of this distributed dislocation, based on general expressions for the strain energy [11, 59]. An interplanar slip energy $V[\delta]$, obtained over the slip plane surface, has the form

$$V[\delta] = \int \Phi[\delta] dS \quad (2.22)$$

and depends on the shear potential $\Phi = \int \tau d\delta$ which can be approximated, for example, with the Frenkel sinusoid connected to the γ_{usf} (Eq. (2.1)). Finally, the interaction between the elastic $\bar{\mathbf{u}}$ and inelastic δ is given as

$$W_2[\bar{\mathbf{u}}, \delta] = K_I \int \mathbf{n} \cdot \sigma_I \cdot \delta dS \quad (2.23)$$

where σ_I are the mode I stresses corresponding to a K_I -field with unit magnitude. A numerical solution for δ , e.g. by Newton-Raphson iteration, is obtained by rendering $\Pi[\bar{\mathbf{u}} + \delta]$ stationary. The reader is directed to [59, 60] for the full expressions and derivations. The continuum formulation above does not directly translate to the atomistic system, but we can draw some understanding of the major energetic contributions to the emission problem overall, for example, an energy of slip related to V (Eq. (2.22)) or a change in the elastic stress field due to slip. Later in Chapter 7, we draw on the continuum theory in order to semi-analytically partition the energy contributions of emission in an atomistic system.

The activation energy for emission ΔE is defined as the difference in Π between two configurations: a stable equilibrium configuration and a critical saddle point instability configuration with displacements δ_0 and δ_{sp} , respectively [60]. This is written as

$$\Delta E = \Pi[\delta_{sp}] - \Pi[\delta_0] \quad (2.24)$$

In mode I, the (3d) emission energy barrier becomes zero-valued approaching the 2d limit when the load reaches the critical energy release rate $G_{Ie} = \gamma_{usf}$ at K_{Ie} [58, 60, 61].

3 Atomistic simulation methods

In this chapter we briefly discuss several computational methods used in conducting the atomistic simulations presented in Part II. The choice of the computational tool should reflect the length- and time-scale of the mechanism(s) of interest [62]. We study the atomistic crack tip behavior, specifically the static competition between cleavage and dislocation emission crack tip mechanisms controlling intrinsic ductility. These mechanisms are at a length-scale well-suited to atomistic simulations but beyond DFT due to the need to preserve a certain “length-scale hierarchy” between the fracture process zone, K -dominance, and simulation size. We extensively employ Molecular Statics (MS), the static variant of Molecular Dynamics (MD), in studying atomistic fracture. Both cleavage and dislocation emission are thermally-activated processes (Chapter 2.4). Transition state theory provides a framework to characterize a thermally activated process, and we use the Nudged Elastic Band (NEB) method to obtain the energy barrier and transition path of the crack tip mechanisms.

The MD/MS and NEB methods are used in conjunction with the K -controlled atomistic simulation framework, allowing for accurate LEFM-compliant modeling of a semi-infinite crack tip. Andric and Curtin [23] comprehensively review and validate various aspects of the K -controlled framework, but since that discussion underlies the computational setup of the studies in Part II we revisit some of the major points and subtleties here. LEFM-compliance enables quantitative comparisons between simulation and continuum theory, so it is important to validate the predictions as best as possible using direct incrementally-loaded simulations, or indirectly, by studying the relationship between load and activation barriers.

3.1 Elements of Molecular Dynamics/Statics simulations

Molecular dynamics (MD) is a well-established simulation method to model the motion of individual particles in a system under prescribed conditions. At its core, atoms are

treated as classical Newtonian particles, and the equations of motion are numerically integrated to solve for the physical configuration of the system. Suppose at some time t_n a system with N atoms, treated as point masses, have positions $(\mathbf{r}_1^n, \mathbf{r}_2^n, \dots, \mathbf{r}_N^n)$ and velocities $(\mathbf{v}_1^n, \mathbf{v}_2^n, \dots, \mathbf{v}_N^n)$. The MD algorithm following enables the computation of the position and velocity of the system of atoms at time $t^{n+1} = t^n + \Delta t$, i.e. after a time step of Δt .

The interaction between the atoms is described by an underlying interatomic potential energy function $U(\mathbf{r}_1, \mathbf{r}_2, \dots, \mathbf{r}_N)$ that depends on the positions of all of the atoms. Given the potential U , the force acting on each atom i at time n is determined by

$$\mathbf{F}_i = - \frac{\partial U(\mathbf{r}_1^n, \mathbf{r}_2^n, \dots, \mathbf{r}_N^n)}{\partial \mathbf{r}_i^n} \quad (3.1)$$

The force of an atom, regardless of the interatomic potential, can always be written as a sum of central forces which depend only on the distances between atoms. Eq. (3.1) can alternatively be written as

$$\mathbf{F}_i = \sum_{j \neq i} \mathbf{F}_{ij} = \sum_{j \neq i} \frac{\partial U(\mathbf{r}_{12}^n, \mathbf{r}_{13}^n, \dots)}{\partial \mathbf{r}_{ij}^n} \frac{\mathbf{r}_{ij}^n}{r_{ij}^n} \quad (3.2)$$

where \mathbf{r}_{ij} is the distance between atoms i and j , \mathbf{F}_{ij} is generally the contribution to the force on atom i due to atom j , and $\mathbf{F}_{ij} = -\mathbf{F}_{ji}$ satisfies the strong law of action and reaction. Following Eq. (3.1), the acceleration \mathbf{a}_i^n of each atom i at t^n is

$$\mathbf{a}_i^n = \frac{\mathbf{F}_i^n}{m_i} \quad (3.3)$$

where m_i is the mass of atom i .

The position and velocity of each atom at time t^{n+1} can be obtained using a simple velocity Verlet algorithm as

$$\mathbf{r}_i^{n+1} = \mathbf{r}_i^n + \mathbf{v}_i^n \Delta t + \frac{1}{2} \mathbf{a}_i^n \Delta t^2 \quad (3.4a)$$

$$\mathbf{v}_i^{n+1} = \mathbf{v}_i^n + \left(\frac{\mathbf{a}_i^n + \mathbf{a}_i^{n+1}}{2} \right) \Delta t \quad (3.4b)$$

From Equation (3.3) it is evident that the accelerations at time t^{n+1} , i.e. \mathbf{a}_i^{n+1} , are required to update the velocities. Consequently, the positions of the atoms are first updated according to Equation (3.4a) so that the forces can be obtained using Equation (3.1) and the updated accelerations can be computed using Equation (3.3), finally allowing for the velocity to be updated via Equation (3.4b). This process is iterated over a number of specified increments to obtain the evolution of the system forward in time.

The above describes the basic machinery of the MD method, which has been extended to different ensembles, for example, constant temperature (canonical) and constant pressure (isothermal-isobaric).

In the above, we consider N -atoms in 3-dimensional (3d) coordinate space with the positions $\mathbf{R} = (\mathbf{r}_1, \mathbf{r}_2, \dots, \mathbf{r}_N)$. We refer to all possible configurations of \mathbf{R} , i.e. $\{\mathbf{R}\}$, as the configurational space. As we shall see in the following, it becomes useful to represent the N -atom system as a point in the $3N$ -dimensional configuration space, rather than N points in the 3d coordinate space. Any arbitrary configuration \mathbf{R} has its potential energy given by $U(\mathbf{R})$, so the configuration space is a potential energy surface (PES) with some topography.

Molecular statics (MS) simulations employ an energy minimization, termed relaxation, in order to identify the local minima (the “relaxed” states) of the potential energy surface starting from an initial (“unrelaxed”) guess of the equilibrium structure. The local minima represent energetically metastable configurations which are likely physically relevant [63]. Commonly implemented minimization algorithms include gradient methods (e.g. steepest descent, conjugate gradient) and damped dynamics methods (e.g. FIRE) which iteratively update the atomic positions until reaching a specified force or energy tolerance. Using MS, we can compute intrinsic $T = 0$ K material properties (lattice parameter, elastic constants, surface energies, generalized stacking fault curves and unstable stacking fault energies, etc.) and identify the configuration and energetics of crystalline defects, e.g. cracks and dislocations.

The interatomic potential function $U(\mathbf{r}_1, \mathbf{r}_2, \dots, \mathbf{r}_N)$ is clearly one, if not the most, critical component in MD/MS simulations since it is a functional representation of the material behavior. The interatomic potential employed in a simulation controls the accuracy of the resulting simulation results. Although the potential energy of any atomistic configuration could, in theory, be accurately determined using first-principles methods, e.g. Density Function Theory (DFT), DFT calculations are highly computationally intensive even for a small number of atoms and thus cannot be feasibly used for studies at the scales typical to many mechanics problems. In particular, the large-scale studies employed to study mechanisms of plasticity in fracture is significantly beyond the limits of DFT at present.

A large effort in computational research is as a result devoted to the development of empirical interatomic potentials, which are functions that map the configuration of atom positions to a corresponding energy. An empirical/semi-empirical potential takes on a fixed functional form containing several free parameters fit to experiments and/or first-principles calculations such that specific material properties are reproduced in simulation [63, 64]. The design of these potentials can be tailored for specific applications, such as studying fracture, by optimizing the fitting process to reproduce key problem-specific material properties.

The embedded-atom method (EAM) [65] and modified embedded-atom method (MEAM) [66] are two widely-used types of empirical interatomic potentials for MD/MS simulations of metals. There is also interest in developing DFT-accurate interatomic potentials that are fit to and reproduce first-principles-accurate material parameters and defect properties. More recently is an avid interest in machine learning interatomic potentials which have the potential for excellent accuracy owing to high flexibility from non-fixed functional forms. In Chapter 4, we discuss several EAM/MEAM-type potentials, DFT-accurate interatomic potentials, and machine learning potentials which have been used to simulate atomistic fracture in various crystalline metals to varying degrees of success.

All MD/MS results presented in this thesis were conducted with the open-source Large-scale Atomic/Molecular Parallel Simulator (LAMMPS) [67] and the resulting atomic configurations were visualized with the Open Visualization Tool (OVTIO) [68] utilizing the Common Neighbor Analysis (CNA) [69] functionality to identify the crystal structures.

3.2 Transition state theory and the Nudged Elastic Band (NEB) method

The potential energy surface $U(\mathbf{R})$ for a real N -atom system as introduced above is a non-convex hypersurface containing an exponentially large number of local minima to N [70]. The landscape of the potential energy surface can be imagined as consisting of many basins containing local energy minima, which represent metastable states, separated by ridges. Many important material deformation processes, e.g. dislocation motion, diffusion, and fracture to name just a few, involve a rearrangement of atoms from one metastable configuration to another. These processes are described as “thermally-activated”, since random thermal fluctuations play a critical role in facilitating these transformations [71, 72].

The process of transformation can be represented as a pathway along the energy landscape from one metastable state to another. The minimum energy path (MEP) is the lowest energy trajectory that exits a basin and enters into another, crossing the ridge in-between at the saddle point [63] (see Fig. 3.1). The saddle point is thus the point of maximum potential energy along the MEP and corresponds to the transition state. The energy barrier or activation energy of the transformation is the difference in energy between the initial and transition state and controls the rate of the transformation.

3.2.1 Transition state theory

A real system can often exist in multiple metastable states, and it spends most of its time in any one such state undergoing small uninteresting thermal fluctuations. In

3.2. Transition state theory and the Nudged Elastic Band (NEB) method

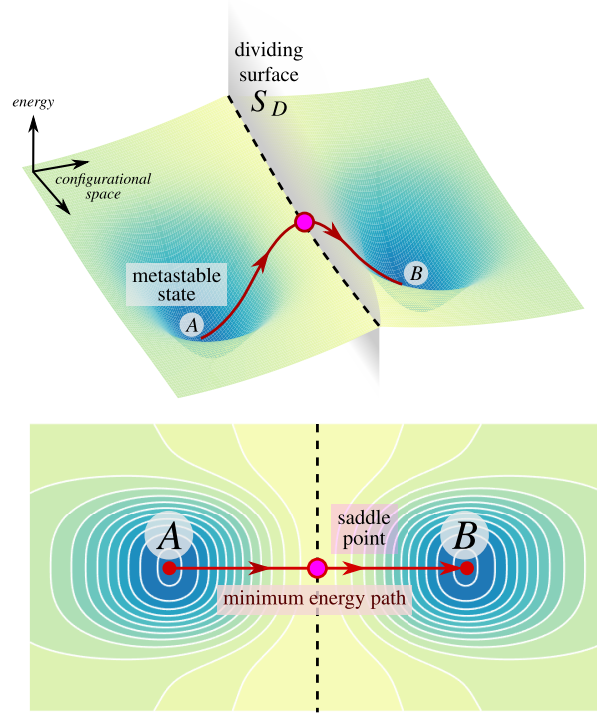


Figure 3.1: Schematic of a thermally activated process between two metastable states. (top) A 3d representation of the potential energy surface is divided by the surface S_D (dashed line) into two regions corresponding to metastable states A and B . (bottom) The minimum energy path (MEP) connects the two states. The highest point of the MEP is the saddle point corresponding to the transition state. Adapted from [73].

contrast, the transition between two states requires a rare, sufficiently large fluctuation in the energy; the time scale of such a transition is also very fast and typically several orders of magnitude smaller than the time between transitions. Consequently, extracting information about the transition directly from a MD trajectory is challenging if not intractable, and motivates alternative techniques to study the transition event.

Transition state theory (TST) [71, 74] uses equilibrium statistical mechanics to determine the rate of a thermally-activated transition between two metastable states in the $3N$ -configuration space of an N -atom system. Suppose a system is in thermal equilibrium at temperature T . Two metastable states A and B are identified by the vectors \mathbf{r}_A and \mathbf{r}_B in configurational space, respectively. TST assumes that a (hyper)surface S_D , which lies perpendicular to the contour of the potential energy, partitions the PES into two regions of the basins corresponding to A and B and passes through the transition state P (Fig. 3.1). The system is assumed to spend all of its time in either region A or B – in state A or B , respectively – with an occasional jump between the two states with the aid of thermal fluctuations. The time scale of the transition is assumed to be much longer than the time period of atomic vibration, enabling the equilibration of the system after each transition. The transition will occur if the system makes it to

the transition state and has velocity pointing away from the initial state. TST further assumes that the system will not pass through the surface \mathcal{S}_D again without having been first transformed; this assumption is often called the “no-crossing” assumption leading to an upper bound of the transition rate.

For the NVT (canonical) distribution of states, the rate at which the system transitions from A to B is exactly expressed by

$$\nu_{A \rightarrow B}^{TST} = \sqrt{\frac{k_B T}{2\pi m}} \frac{\int_{\mathcal{S}_D} e^{-U(\mathbf{R})/k_B T} dS}{\int_A e^{-U(\mathbf{R})/k_B T} d\mathbf{R}} \quad (3.5)$$

where k_B is the Boltzmann constant, m is the atomic mass, and $U(\mathbf{R})$ is the potential energy of the system in configuration \mathbf{R} [71]. The numerator is an integral over the dividing surface \mathcal{S}_D , and the denominator is the configurational partition function over region A .

Computation of the quantity in Eq. (3.5) requires knowledge of the shape of \mathcal{S}_D , but the representation and optimization of \mathcal{S}_D is challenging. Consequently, in order to avoid evaluation of the integrals in Eq. (3.5), the energy surface can be assumed to be locally quadratic and approximated by an expansion of the energies in the normal vibrational modes at the initial state A and saddle point P . The resulting approximation to the reaction rate ν , referred to as harmonic TST (HTST) [71], is

$$\nu_{A \rightarrow B}^{HTST} = \frac{\prod_{j=1}^{3N} \nu_j^A}{\prod_{j=1}^{3N-1} \nu_j^P} \exp\left(-\frac{U(\mathbf{R}_P) - U(\mathbf{R}_A)}{k_B T}\right) \quad (3.6)$$

where ν_i^A and ν_i^P are the normal vibrational frequencies at A and P , respectively. However, direct computation of the N normal frequencies can quickly become intractable as the system size N becomes large.

A further simplification of Eq. (3.5) as an Arrhenius-type dependence of the rate constant with temperature and an energy barrier and is written as

$$\nu_{A \rightarrow B} = \nu_0 \exp(-\Delta E/k_B T) \quad (3.7)$$

where the prefactor in Eq. (3.5) is condensed to an “trial” frequency ν_0 in the direction of the reaction coordinate at the initial state [53, 55, 75, 76], and ΔE is the (free) energy barrier associated with the transition. The simplified ν_0 is not an intrinsic property of the system [77]. For thermally-activated transitions in crystalline materials ν_0 is typically on the order of 10^{13} s^{-1} [75, 78, 79] although the Debye frequency is sometimes used. Some dislocation mechanisms including dislocation nucleation involve significant changes in atomic arrangement and a large entropic barrier with non-negligible anharmonic effects [77, 80, 81], so the HTST and the Arrhenius-type dependence for example can yield very poor predictions of the expectation time (i.e. ν^{-1}). For dislocation nucleation, ν_0 is

3.2. Transition state theory and the Nudged Elastic Band (NEB) method

often approximated as $6 \times 10^{11} \text{ s}^{-1}$ [30, 55, 82, 83].

3.2.2 Nudged Elastic Band method

The energy barrier ΔE , which depends on the initial metastable state and the transition state, is a critical quantity for determining the transition rate of a thermally-activated process, e.g. in Eqs. (3.5) and (3.6). We are, however, generally only in possession of knowledge of the two metastable end-states of the process while the transition state is unknown. By identifying the MEP connecting the two end-states, we can identify the transition state and thus the energy barrier of the transition.

The Nudged Elastic Band (NEB) method, following the work of Jónsson and coworkers [84, 85], and more recently string methods [86], are widely-used computational techniques for computing the MEP using known initial and final metastable states. In this thesis, we use the NEB method as implemented in the `replica` package in LAMMPS and we review some of the main points following. The MEP connects an initial and a final metastable state in a transition that are two local energy minima in the configurational space for a system of N atoms. The MEP is first discretized into a chain of \mathcal{R} number of intermediate states, termed replicas or images and denoted here by Q , by linear interpolation for example. The first and last replicas (Q^0 and $Q^{\mathcal{R}}$, respectively) are the initial and final end-states and are normally kept fixed. The remaining $\mathcal{R}-2$ intermediate replicas are the discrete degrees of freedom.

The intermediate replicas are not in equilibrium and thus subject to a force from the underlying potential energy according to the interatomic potential, i.e. a force on each replica i is

$$\mathbf{F}_{pot}^i = -\nabla U(Q^i) \quad (3.8)$$

which acting alone simply moves each replica to one of the end-states. For this reason, the replicas are joined by a spring of zero unstretched length and spring constant k so that the chain of replicas are constrained to remain spread out along the MEP. The spring force on each replica i is

$$\mathbf{F}_k^i = k(Q^{i+1} - Q^i) - k(Q^i - Q^{i-1}) \quad (3.9)$$

The intermediate replicas evolve toward the MEP under a combination of forces from the potential energy and the springs. Simply adding these contributions, e.g.

$$\mathbf{F}^i = \mathbf{F}_{pot}^i + \mathbf{F}_k^i \quad (3.10)$$

generally will not yield the MEP since the chain is very sensitive to the spring stiffness k . If k is too low, all of the replicas fall toward a minimum; and if too high, the stiff elastic band cut corners and travels along a higher energy part of the PES thus overestimating

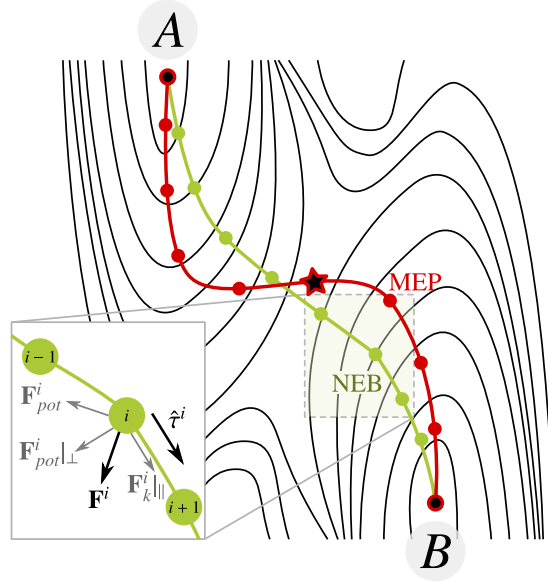


Figure 3.2: Schematic of the chain of replicas (images) Q^i of the nudged elastic band (NEB) (in green) connecting states A and B on a 2d potential energy surface. In the inset, the i^{th} image has tangent $\hat{\tau}^i$ and the total force \mathbf{F}^i acting on the replica consists of the component of the potential force \mathbf{F}_{pot}^i acting perpendicular to $\hat{\tau}^i$, $\mathbf{F}_{pot}^i|_{\perp}$, and the parallel-acting spring force $\mathbf{F}_k^i|_{\parallel}$. The images converge to the minimum energy path (MEP) (in red) of the transition with an image at the saddle point (star) using CI-NEB. Adapted from [73, 87].

the saddle point.

Instead, only certain components of each force contribution are used, i.e. instead of Eq. (3.10) we use

$$\mathbf{F}^i = \mathbf{F}_{pot}^i|_{\perp} + \mathbf{F}_k^i|_{\parallel} \quad (3.11)$$

where $\mathbf{F}_{pot}^i|_{\perp} = \mathbf{F}_{pot}^i - (\mathbf{F}_{pot}^i \cdot \hat{\tau})\hat{\tau}^i$ and $\mathbf{F}_k^i|_{\parallel} = k(|Q^{i+1} - Q^i| - |Q^i - Q^{i-1}|)\hat{\tau}^i$ (see Fig. 3.2). The tangent to the path at replica i , $\hat{\tau}^i$, is well-estimated by bisecting two unit vectors, i.e.

$$\hat{\tau} = \frac{Q^i - Q^{i-1}}{|Q^i - Q^{i-1}|} + \frac{Q^{i+1} - Q^i}{|Q^{i+1} - Q^i|} \quad (3.12)$$

which ensures equispacing of the images along the MEP [88]. The MEP is the converged chain of replicas obtained by simultaneous force-based minimization of replicas in parallel (Fig. 3.2). The Climbing Image (CI-NEB) method [89] is a modification to the original NEB method that rigorously converges a replica to a saddle point without significantly adding to the computational cost.

The activation of many 3d processes of dislocations and cracks involve the collective motion of a large group of atoms and a long reaction path. When the energy landscape is skewed by a large applied load, the saddle point is skewed closer to the initial state [90]. Such is the case for dislocation emission from a crack tip – most of the transition

path is downhill energy, but only the uphill part of the transition before the nucleation instability is interesting to study. Increasing resolution of the MEP in the short segment before the transition state alone is not possible, and increasing resolution everywhere along the MEP is exceedingly computationally inefficient. The free-end NEB method [91] improves the computational efficiency for this situation. The MEP is first converged over the entire transition path as is conventional. The elastic band is then cut short, and the cut end is allowed to move freely on an energy iso-surface in a second NEB calculation. We primarily use the free-end NEB method to compute the $T = 0$ K energy barriers of the cleavage and dislocation emission crack tip mechanisms.

3.3 K -controlled atomistic simulation framework

MD/MS and NEB methods are general simulation methods, and we use them to simulate the behavior of an atomistic crack tip in order to gain qualitative and, if possible, quantitative understanding of mechanisms at play. The atomistic crack can be simulated in several ways, but the various methodologies are not equally faithful to the principles of fracture mechanics so not all methods can be used for extracting quantitatively accurate information. In many cases the simulation method can strongly influence the simulation results, often leading to inaccurate/misleading results and conclusions about fracture phenomenon. We direct the reader to Andric and Curtin [23] for a comprehensive review of the pitfalls of different simulation methods prevalent in body of literature simulating atomistic fracture but review several key points in the following.

Finite-sized center cracks appear in many fracture studies and have the advantage of (i) being easy to construct, and (ii) having similar geometry as macroscopic test specimens, but the design of the simulation setup and application of LEFM must be undertaken with care. In order to satisfy K -dominance and the “length-scale hierarchy” (see Chapter 1.3), the minimum simulation size scales with the size of the finite crack, i.e. for the half crack size a , $r_{FPZ} \ll r_K \ll a$. For more complex problems, the required minimum size can become quite large and quickly becomes very computationally demanding. As well, since most of the atoms are outside of the asymptotic region, the finite crack setup is not very efficient for studying the crack tip region.

More problematically, the far-field applied stress required to drive crack tip phenomena are generally very large for finite-cracks, e.g. an applied stress of $\sigma^{app} = K_I/\sqrt{\pi a}$ is required to generate a stress intensity of K_I . The stresses in the asymptotic region can thus be at or even higher than the applied stress, so the entire material may no longer be linear elastic, and this violates the basic premise of LEFM and invalidates any LEFM-based predictions. High stresses ahead of the crack can drive non-linear behavior and damage phenomena outside of the intended FPZ, so $r_{FPZ} > r_K$, which again violates LEFM. This is particularly problematic for studies of crack-defect interactions (e.g. with dislocations and grain boundaries) since defects at some distance away from the crack

can still detect and respond to the spurious non-asymptotic fields.

As Andric and Curtin [23] note, these issues stemming from finite-sized cracks can be resolved by simply using a semi-infinite crack with K -controlled loading, termed the K -test simulation framework, to explicitly study the asymptotic crack tip region. An edge crack is centered in the simulation cell; the traction-free surface extends from the boundary to the middle of the specimen. Along the boundary of the simulation cell, the boundary conditions are the asymptotic near-crack tip displacement fields with respect to the crack tip position. Thus, by construction, the entire simulation domain is the asymptotic crack tip region for an essentially infinite-sized crack, and this maximizes the number of atoms in the FPZ which is good for computational efficiency. The only requirement is that the size of the FPZ (r_{FPZ}), which is generally well within ~ 10 nm of crack tip, is much smaller than the smallest simulation cell dimension. The loading is precisely the stress intensity K_I corresponding to the prescribed displacements in Eq. (1.16). There are no artificially high stresses ahead of the crack tip as in the finite-crack simulations. Although the K -test framework is relatively established for continuum-scale fracture studies, its presence in atomistic-scale studies is generally not as consistent [23].

The setup of the K -test framework in atomistic simulations is quite systematic. The simulation cell can be of any shape, and a boundary region is defined as the region of atoms within some distance from the edges of the cell, typically within $2r_{cut}$, where r_{cut} is the cut-off distance of the interatomic potential. The initial sharp semi-infinite crack is created starting from a perfect lattice by imposing the atomistic displacements according to the anisotropic LEFM solution at a far-field load K_I (or in general it can be any desired K). For a plane-strain problem, we use a planar specimen periodic in the out-of-plane direction along the crack front (Fig. 3.3a). The system is then relaxed while holding the boundary atoms fixed. The far-field load is increased incrementally, i.e. via displacements corresponding to some ΔK_I , the system is minimized after each load increment with the boundaries held fixed and the behavior of the crack tip is observed. Since the K -test setup satisfies the concept of LEFM, the observed crack tip mechanisms quantitatively correspond with LEFM predictions – this has been demonstrated for various fcc [48, 51, 92], hcp [33, 93, 94], and bcc [26] materials. One main disadvantage of the K -test framework is thus the need for the asymptotic displacement fields which can be troublesome to obtain for more complex geometries. A second disadvantage is that the boundary conditions are displacement fields with respect to a *specific* crack tip position, so to remain accurate for an extending crack they must be updated to reflect the moving crack tip (e.g. [23, 33, 95, 96]).

An atomically sharp crack is theoretically unstable to closure at loads below the Griffith K_{Ic} , and unstable to extension above K_{Ic} . Due to the discrete nature of the atomistic system, sharp brittle cracks (where no emission occurs before K_{Ic}) remain stable around K_{Ic} in simulation due to a small amount of lattice trapping [37, 38]. In order to ex-

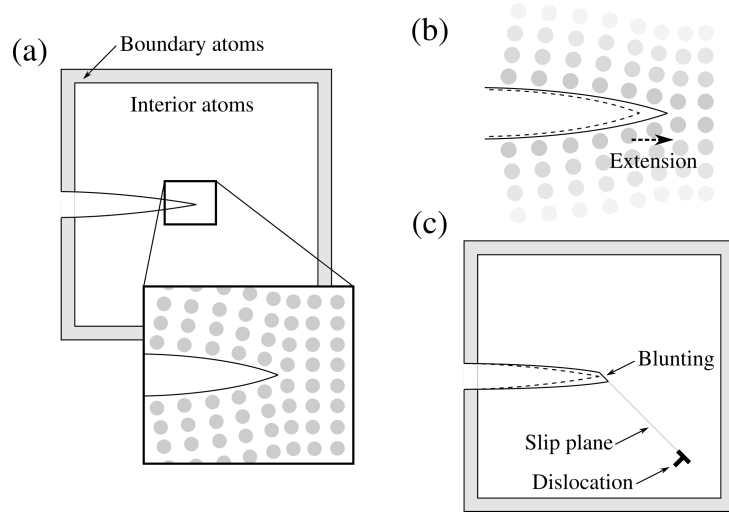


Figure 3.3: Schematic of the K -controlled simulation setup in the x - y plane. The specimen has periodic boundary conditions along the crack front in the out-of-plane direction. (a) Initial configuration of the semi-infinite crack tip (b) Uncracked (dashed line) and cracked configurations of the crack for the cleavage NEB simulations; the crack tip remains sharp after cleavage. (c) Sharp crack before emission (dashed line) and blunted crack after emission configurations for the dislocation emission NEB simulations.

to explore the crack tip behavior below K_{Ic} , we can use “screening” and “blunting” methods to approximate a traction-free crack. A crack is screened by artificially deleting the interactions between the atoms across the crack surface, noting that this can change the interactions of the atoms at/near the crack tip somewhat when using many-body potentials. Blunting involves the deletion of one more multiple layers of atoms to create a slightly geometrically-blunted crack tip such that the finite distance separating the crack surfaces prevents atomistic interactions. We generally apply screening in ductile cases (i.e. loading below K_{Ic}) to maintain crack tip stability since blunting can notably change the singularity at the crack tip [97].

3.4 Validation of LEFM using atomistic simulations

The LEFM Griffith theory for the cleavage K_{Ic} is based on an exact thermodynamic statement. The LEFM prediction for the emission K_{Ie} is, however, an estimate and so it is important to validate that prediction as best as possible. The theory for K_{Ie} has been compared very carefully to simulations of emission in fcc and hcp metals described by EAM potentials, and has been shown to be generally good [33, 48]. These validation studies are encouraging but the accuracy of the theory as applied to bcc crystals as well should nonetheless be demonstrated.

The standard atomistic simulation method for testing fracture theories is the K -test framework. Unfortunately, direct K -test simulations of atomistic fracture commonly

display unphysical behavior at the sharp crack tip due to problems with the interatomic potential. For example, a sharp crack will commonly undergo accumulated structural distortions, not unlike amorphization, rather than cleavage; any fracture behavior is then essentially fictitious. Similarly, a ductile crack should emit a dislocation since emission is well-known to be strongly downhill in energy beyond a finite energy barrier, but is often accompanied by structural distortions and/or other planar faults, or occurring ahead-/behind the crack tip, or not occurring at all. These behaviors are likely initially locally downhill in energy on the PES on an alternative path from a “standard” mechanism, but ultimately lead to much higher energy paths overall corresponding to unphysical configurations.

This is due to problems within the interatomic potentials despite producing reasonable and artifact-free material properties (e.g. elastic constants, USF energy, surface energy) that control the crack tip phenomena of interest. This is particularly true for bcc crystals, with bcc Fe well-studied in particular [98] and our own studies showing similar problems for the Zhou et al. [1] family of potentials for both the bcc elements and their random alloys. In Chapter 4 we discuss several interatomic potentials at greater depth. The direct K -test method is susceptible to artifacts arising from the interatomic potential since the crack tip configuration is incrementally evolved and unguided, i.e. no pre-established configuration is provided for the evolution.

3.4.1 Emission and cleavage pathways using NEB

The combination of the standard K -test with transition state methods is a creative way to circumvent some of the problems with the interatomic potentials in direct fracture simulations. Using the NEB method we can find the transition path and energy barrier between an initial sharp crack and a well-defined final state (either cleavage or dislocation emission) at an applied load K_I . The NEB is a form of constraint on the system preventing completely free evolution of the system, e.g. the incremental free evolution in direct K -test simulations. The following results show that over some range of applied K_I the transition paths for both cleavage and emission are qualitatively sound and are not influenced by the spurious crack tip behavior. The evolving emission of a dislocation loop is very similar to that observed in other systems where there are no artifacts in the potentials. Thus, the physical cleavage and emission paths are separated from the spurious lower-energy paths by some energetic barriers, and the physical path can be studied without artifacts with these potentials.

For cleavage, the final state corresponds to a sharp crack that has advanced one periodic distance along the crack growth direction at the same applied load K_I with boundary conditions determined by the initial state crack position (Fig. 3.3b). Cracks are created following the standard K -test methodology. There is a small error in the elastic energy (1 – 3%) due to the finite simulation size that leads to a small increase in the simulated

3.4. Validation of LEFM using atomistic simulations

value of K_{Ic} . Normally, the boundary conditions are different for the initial and cleaved crack configurations, which are both for K_I but have different crack tip positions. However, the pair of cleavage NEB end-states require identical boundary conditions for K_I , but with the crack tip in two different positions. Consequently, the relaxed energies in the two discrete systems are not exactly equal due to the constraint of the boundary condition. The model NbTiZr system using the EAM-type Zhou et al. interatomic potential [1] is used to illustrate – we study the same system in Chapter 6. In Fig. 3.4 a small residual energy at K_{Ic} is observed in the cleavage NEB simulations for the 2d case, i.e. $\delta E = E(x_R = 1) - E(x_R = 0) > 0$, where x_R is the reaction coordinate of the energy profile of the MEP. The magnitude of ΔE scales with the length of the crack front. However, since this error is persistent throughout all the simulation results, a rigid shift of $\sim 2\%$ K_{Ic} applied to a set of energy barriers does not change the relative trends in E_{act} versus K_I .

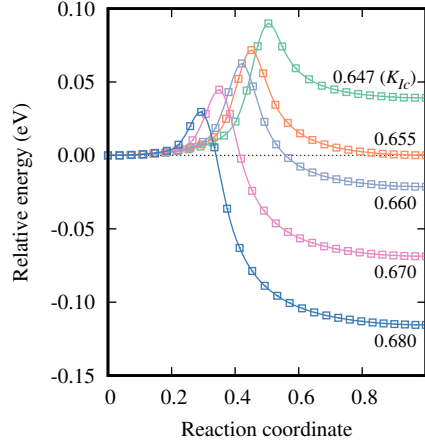


Figure 3.4: 2d cleavage energy profile of the NbTiZr (110) $[1\bar{1}0]$ crack orientation from NEB simulation at various K_I as labeled (in units of $\text{MPa}\sqrt{\text{m}}$).

For emission, the final state is a blunted crack tip with the emitted dislocation far from the crack tip (Fig. 3.3c). Since emission is not preferred ($K_{Ic} < K_{Ie}$) in many materials and orientations, the final blunted crack tip is created by using the minimum periodic length along the crack front, which artificially reduces the energy barrier for emission significantly, followed by a molecular dynamics simulation with atoms around the crack tip at temperature $T \gg 0$ to induce emission. The final $T = 0$ blunted crack tip is then obtained by cooling the specimen to $T = 0$ and replicating the structure along the crack line direction to create the full final-state 3d specimen for the NEB simulation. The Zhou et al. potential [1], for example, captures the the expected emission process in direct simulation under these specific conditions (i.e. where the barrier is much lower), so this physical path of emission can be probed accurately with a guided analysis despite the existence of lower-energy paths for the crack tip behavior (at higher loads, involving amorphization and other artifacts etc.).

The cleavage and emission processes are intrinsically 3d, as revealed by the NEB simulations. Again, using the model NbTiZr alloy to illustrate in Fig. 3.5a, cleavage involves the formation of a small section of decohered atoms just ahead of the original crack tip that then expands laterally along the entire (periodic) crack front, advancing the entire crack front line by one lattice spacing. The energy barrier at an applied K_I above K_{Ic} but below the zero lattice trapping barrier K_I corresponds to some critical length of decohered atoms. Dislocation nucleation below K_{Ie} is an instability due to the nucleation of a finite-sized loop on the slip plane that then expands out both laterally and ahead of the crack until a full dislocation line is formed, which then moves away from the crack tip (Fig. 3.6a). The energy barrier at an applied $K_I < K_{Ie}$ corresponds to some critical loop size. Since bcc dislocations do not dissociate into partials, the slipped region behind the emitting dislocation loop has the perfect bcc crystal structure. The two 3d processes of cleavage and emission thus require simulations on sufficiently thick specimens (crack front lengths) to capture the true 3d energy barrier. Figures 3.5b and 3.6b show the energy barriers for both cleavage and emission as a function of crack front length; only the asymptotic results at larger crack front lengths ($\sim 70\text{\AA}$ in depth) have physical meaning and are the only results quoted in the remainder of this thesis.

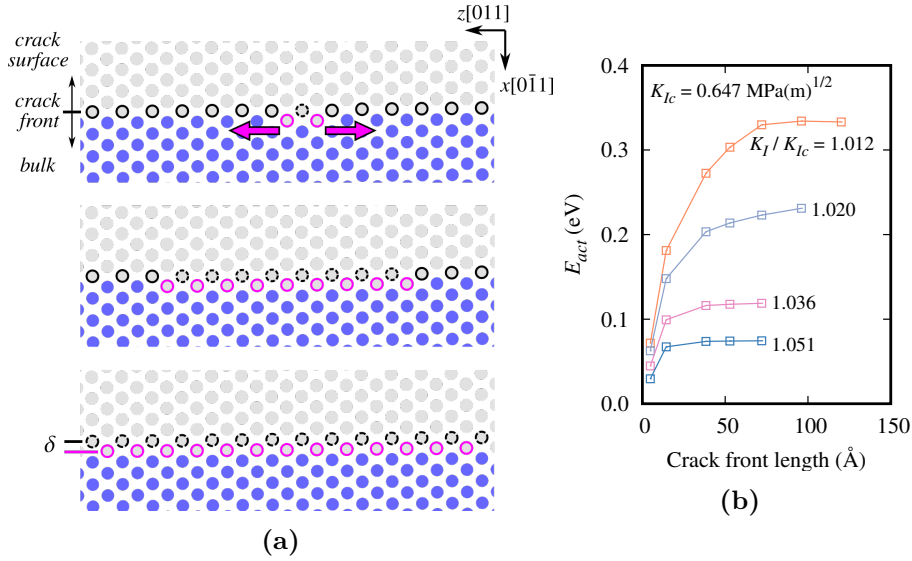


Figure 3.5: NEB simulation of the cleavage process in NbTiZr for the $(110) [\bar{1}\bar{1}0]$ crack orientation. (a) A small section of decohered atoms along the crack front (outlined in purple) expands laterally across the crack front until the crack front line has advanced by one periodic spacing δ . Atoms are colored by structure according to Common Neighbor Analysis: bcc (blue), non-bcc surface atoms (white). (b) The energy barrier versus crack front length at varying K_I (labels indicate K_I/K_{Ic}), showing the full 3d barrier to be achieved for a crack length of $\approx 70\text{\AA}$.

We proceed now to validate the LEFM theory for several model refractory HEAs using the set of Zhou et al. potentials [1]. These potentials are not quantitative for real materials but have well-defined alloy properties and so serve well as a set of model alloys.

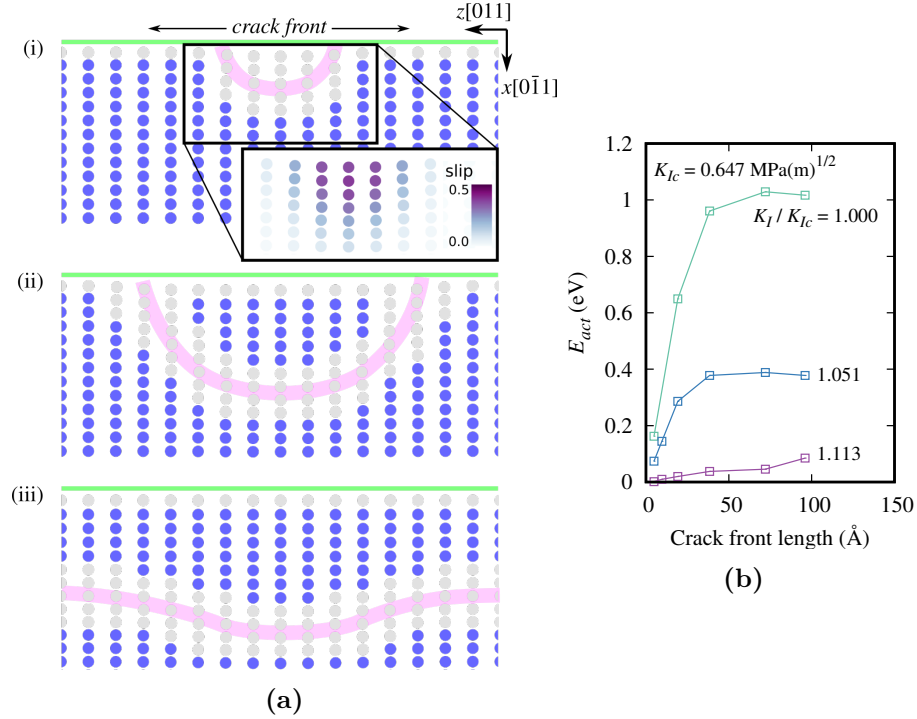


Figure 3.6: NEB simulation of the dislocation emission process in NbTiZr for the (110) $[1\bar{1}0]$ crack orientation. (a) Behavior of the emitting dislocation loop at $K_{Ic} = 0.647 \text{ MPa}\sqrt{\text{m}}$. Atoms are colored by structure according to Common Neighbor Analysis: bcc (blue), non-bcc atoms (white). A pink line is provided to show an approximate configuration of the dislocation loop. (i) The critical loop configuration is indicated by the white atoms. The slip inside the loop area (see inset) is less than the Burgers vector b . (ii) Unstable bow-out of the loop across the crack front after the critical configuration. (iii) An eventually straight dislocation moves away from the crack tip. (b) The energy barrier versus crack front length at varying K_I (labels indicate K_I/K_{Ic}) showing the full 3d barrier to be achieved for a crack length of $\approx 50 \text{ Å}$.

For each HEA, we use the average-atom potential [99] (see Chapter 4.3) constructed from the elemental Zhou et al. potentials because we wish to validate LEFM, which involves only the average material properties. So, we do not consider the actual random atomistic environments along the crack front that exist in the real random alloy, which is beyond the scope of LEFM.

The energy barriers for cleavage and emission versus K_I as computed using the free-end NEB method and the average-atom EAM potentials for four HEAs over a range of K_I are shown in Fig. 3.7 for a generally more-ductile orientation oriented for edge dislocation emission, i.e. (110) $[1\bar{1}0]$. The cleavage results show a fairly small lattice-trapping barrier (less than $\approx 0.5 \text{ eV}$) at the LEFM-predicted K_{Ic} . The cleavage barrier decreases quickly for $K_I > K_{Ic}$, reaching essentially zero at K_I less than $1.1K_{Ic}$. This behavior is due to the well-established lattice trapping phenomenon [37, 38]. Since there is some barrier for cleavage at K_{Ic} , cleavage can require slightly higher loads depending on temperature, time, and crack front length (cleavage can nucleate anywhere along a long crack front).

The emission barrier increases with decreasing $K_I < K_{Ie}$. The NEB results are limited to some maximum K_I above which the transition path exhibits behavior that invalidates the use of the computed barrier. At any K_I , however, the emission barrier is always larger than the cleavage barrier, and becomes insurmountably large ($2 - 3$ eV) at values of K_I still well above K_{Ic} . Therefore, for $K_I > K_{Ic}$, the rate of thermally-activated cleavage is always much higher than emission. Thermal activation therefore does not change the underlying brittleness of these refractory HEAs as represented by the model EAM potentials.

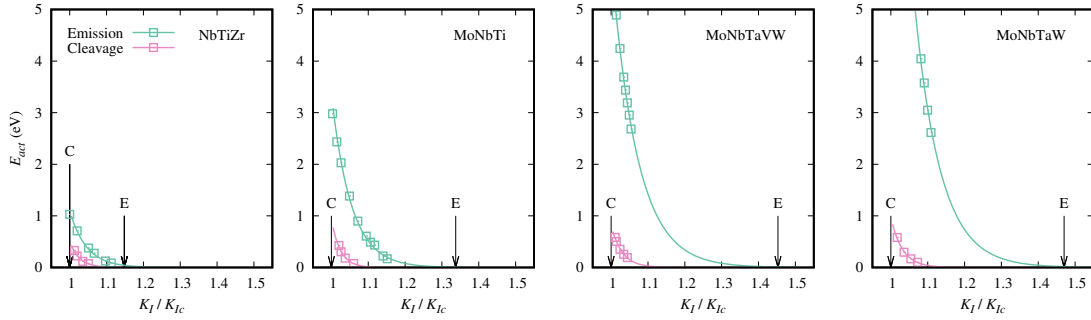


Figure 3.7: Energy barriers for cleavage and dislocation emission in the $(110) [\bar{1}\bar{1}0]$ crack orientation as a function of the applied load K_I . A fit of the form $E_{act} = b \exp(aK_I/K_{Ie})$ is shown (a and b are fitting coefficients). The extrapolated barrier becomes very small close to the LEFM prediction of K_{Ie} . The LEFM $T = 0$ K critical stress intensities are indicated by arrows and labels C= K_{Ic} and E= K_{Ie} .

There is no way to validate K_{Ie} in (intrinsically) brittle materials using direct K -test simulations because a crack will simply grow by cleavage at $K_{Ic} < K_{Ie}$ before reaching the higher value of K_{Ie} . The NEB results enable some validation of K_{Ie} for these bcc alloys, as follows however. The material properties entering into analytic theory (elastic constants, surface energy, and USF energy) are determined fully by the interatomic potential. The computed NEB energy barriers are fit to the functional form $E_{act} = b \exp(aK_I/K_{Ic})$ with a and b fitted parameters. The LEFM value of K_{Ie} does not enter into this fitting. Nonetheless, we find that the extrapolated emission barriers are indeed predicted to become very small (emission at essentially $T = 0$ K) quite close to the LEFM-predicted K_{Ie} (indicated in Fig. 3.7). In the presence of unphysical behavior, the LEFM predictions given the material properties would not quantitatively correspond to the simulated behavior. Thus, the NEB study demonstrates that the LEFM-predicted K_{Ie} is a good estimate of the zero-barrier emission load.

These results show that the $T = 0$ K LEFM values of K_{Ic} for cleavage and K_{Ie} for emission are accurate. These atomistic studies show that thermal-activation effects can be largely neglected because, for brittle alloys where $K_{Ic} < K_{Ie}$, the cleavage barriers for $K_I > K_{Ic}$ are small and the emission barriers for $K_I < K_{Ie}$ are usually much larger than the cleavage barriers.

4 Interatomic potentials for atomistic simulations of fracture

This chapter is in part extracted from the following publications

1. Mak, E., & Curtin, W. A. (2020). Intrinsic fracture behavior of Mg–Y alloys. *Modelling and Simulation in Materials Science and Engineering*, 28(3), 035012
2. Stricker, M., Yin, B., Mak, E., & Curtin, W. A. (2020). Machine learning for metallurgy II. A neural-network potential for magnesium. *Physical Review Materials*, 4(10), 103602

First-principles methods, e.g. Density Functional Theory (DFT), provide accurate understanding of the properties of isolated defects. Important macroscopic properties (e.g. yield strength, ductility, fracture toughness) depend on defect interactions and motion which operate at length- and time-scales far larger than what is currently accessible with DFT with current high performance computing. It is generally computationally prohibitive to directly study cracks with DFT due to the large system sizes, non-periodic geometry, incremental-type loading, etc. required for an accurate fracture study. Although there has been some development of multiscale methods [80, 100], most atomistic fracture simulations make use of classical semi-empirical potentials, e.g. Stillinger-Weber [70], Tersoff [101], Embedded Atom Method (EAM) [65], and Modified Embedded Atom Method (MEAM) [66], among others, which allow for Molecular Dynamics/Statics simulations of millions of atoms at timescales of nanoseconds.

The accuracy of the interatomic potential is paramount to the quality of the simulation results. Fracture is a particularly challenging system for any interatomic potential since it is a complex process involving large multiaxial stresses and a concentrated, highly non-linear region where atoms span from fully decohered to only moderately deformed. Generally, many physically-motivated potentials produce unphysical crack tip behavior despite good predictions for many material and defect properties. In this chapter we

describe the performance of several semi-empirical potentials, focusing on a MEAM-type potentials for pure magnesium (Mg) and the magnesium-yttrium (Mg-Y) system, and EAM-type potentials for various bcc elements which are used in the computational studies in Part II.

Semi-empirical potentials share a common trait of limited flexibility owing to fixed functional forms with limited number of adjustable parameters. The fitting process involves optimizing the accuracy/error over a range of properties, and the fixed functional form intrinsically limits the ability to accurately fit over many properties. As a result, the fitting process typically involves heuristic decisions as to which properties are most desirable. This motivates a discussion on recent advances in form-flexible machine learning interatomic potentials. A recent neural network-type machine learning potential for Mg is presented to illustrate the advantages of machine learning in the development of interatomic potentials.

4.1 Semi-empirical potentials for Mg and Mg-Y

Pure Mg has significant technological potential: it is lightweight and highly abundant in nature, and so is an attractive metal for structural applications, especially in the automotive and aerospace industries [102]. However, Mg has low ductility and low fracture toughness at low and moderate temperatures, and these properties limit its formability and suitability for fracture-critical and/or energy absorption applications, motivating study of its intrinsic fracture character.

The low ductility and limited formability of Mg are associated with the strong plastic anisotropy of the hexagonal close-packed (hcp) crystal structure, especially the difficulties in activating the pyramidal $\langle c + a \rangle$ slip modes [103] due to a thermally-activated transformation of the $\langle c + a \rangle$ dislocations to a sessile configuration [79]. The relatively brittle fracture behavior is equally complex, with multiple cleavage planes observed, especially at low temperatures [103].

Alloying of Mg with rare earth elements (Y, Ce, Tb, Gd, Dy, Ho) and other elements (Ca, Mn) at levels less than 1at% has been shown to enable good ductility, sufficient for forming Mg-based components [104–106]. The notable increase in ductility has been attributed to the ability of the alloying elements to greatly increase the pyramidal cross-slip rate [107], overcoming the fundamental immobilization of the pyramidal dislocations in pure Mg [79].

Many earlier EAM and MEAM potentials for Mg have difficulty capturing the complex slip and dislocation properties and show large disparity when compared against experiments and/or DFT. As evident from the continuum fracture theory, accurate surface energies, and generalized stacking fault (GSF) energies are important for intrinsic crack

tip nucleation mechanisms, and realistic core structures and accurate Peierls stresses for the subsequent dislocation glide. Accurate interatomic potentials are required to capture the closely competing intrinsic fracture behavior in Mg and to further understand the mechanisms that enhance the performance of Mg alloys such as Mg-Y relative to pure Mg.

4.1.1 EAM/MEAM potentials for Mg

Earlier EAM potentials fail in describing pyramidal dislocations [108], show unrealistic GSF energies [109, 110], Peierls barriers [111], $\langle c + a \rangle$ core structures [112], and also poor twin behavior in terms of unstable twin dislocation structures, unrealistic interface structures and surface energies [110]. Other potentials, e.g. [113, 114] were well-fit to bulk properties and GSF energies, but GSF energies alone are not sufficient to ensure good dislocation properties [2, 115]. As we see, no single classical EAM potential matches all the required properties to study Mg under general plastic strain [2].

Some second-nearest neighbor MEAM potentials (e.g. by Kim et al. [116] hereafter called the “Kim potential” and [110]) have the attractive ability to reproduce pyramidal core structures comparable to DFT [112], but are not widely tested and validated for other dislocation core structures and twin interfaces. The Kim potential unfortunately demonstrates very large and unphysical lattice trapping for metallic systems [37–40] which makes it particularly unsuitable for fracture studies [93].

A more recent MEAM potential by Wu et al. [2] (hereafter called the “Wu potential”) is quite good overall and generally improves on most of the problematic aspects of the Kim potential. It comprehensively demonstrates good agreement for basal cohesive separation and strength, GSF energies, dislocation core structures, and Peierls barriers over basal, prismatic, pyramidal, and tensile twin slip modes. Furthermore, the fracture behavior from direct K -test simulation shows minimal lattice trapping and is in very good agreement with continuum predictions when accounting for the step energy for emission [33, 48], for a set of edge-emission oriented cracks on basal, prismatic, pyramidal planes, and tensile twin boundaries.

The Wu potential does not accurately capture all of the important material properties due to compromises made in the fitting process. The accurate reproduction of the c/a ratio is very important for twinning deformation, but was obtained at the expense of reproducing slightly lower stacking fault energy. The basal $\langle a \rangle$ edge dislocation dissociation separation deviates somewhat from DFT partially due to deviations in the stable stacking fault (SSF) energy, and the structure of the edge dislocation can affect the emission behavior in mode I fracture. The USF energy, and to a lesser degree the SSF energy, are critical material parameters entering into the continuum theory. The good fracture behavior and agreement with the continuum theory is with respect to the ma-

terial parameters of the interatomic potential, but the potential itself is not an entirely DFT-accurate representation of Mg in reality.

The compromise required in the fitting is fundamentally due to the limited flexibility in the MEAM any other semi-empirical formulation, motivating the development of machine learning potentials with flexible functional forms. The neural network machine learning potential for Mg by Stricker et al. [94] (Sec. 4.4.2) captures the critical material properties for fracture (e.g. elastic constants, surface energies, and USF energies) much better overall than the MEAM Wu potential. It produces slightly more ductile fracture behavior which is likely more representative of the real material.

4.1.2 MEAM potential for Mg-Y

Yttrium (Y) is a particularly widely studied ductilizing element for Mg. The development of EAM /MEAM potentials for the Mg-Y system is a natural extension from the pure Mg system. An EAM potential by [113] was thoroughly studied for the generalized stacking faults for multiple slip systems, but stacking faults alone do not ensure good predictions of dislocation properties [2, 115]. The Mg Kim potential has a Mg-Y counterpart [117] which describes the structural and elastic properties of stable intermetallic compounds with reasonable agreement to experiments and DFT data, but predicts a significantly smaller Y misfit volume and a weaker effect of Y on basal and pyramidal I SSFs.

Ahmad et al. [118] present a MEAM-type potential for the Mg-Y system which combines the Wu Mg MEAM potential discussed above, which shows overall excellent agreement with DFT/experiments, with a MEAM potential for Y [119], which describes good structural and mechanical properties with respect to experimental data. We use this interatomic potential to study the fracture behavior of a model dilute alloy in Chapter 5. The fitting yields good agreement for the Y misfit volume and most solute-stacking fault interaction energies. The misfit volume is important for the solute-dislocation pressure field interactions dominating solute strengthening [120–122]. We find that the solute misfit also plays an important role providing an avenue for local energy dissipation and intrinsic toughening [33], so accurate misfit volume is an important material parameter for fracture simulations. We find that the continuum theory can capture even the subtle changes in intrinsic ductility arising from very small variations to the average material properties from a small (3at%) amount of Y.

The Mg-Y MEAM potential is also not a general-use interatomic potential. The application of this potential to strengthening is not completely validated as the solute-(edge) dislocation interactions was not fully examined over all slip systems. Like in the pure Mg system, we have good quantitative agreement between theory and atomistic simulation, but the interatomic potential is not an accurate representation of the real Mg-Y

material. The stacking fault energies are critical material properties for fracture, but one major deviation of the MEAM potential from DFT is the pyramidal I stacking fault. The surface energies are also critical properties, but their solute interactions are not explicitly studied by the authors. Small deviations in several properties makes the potential unsuitable for certain applications, one being assessing pyramidal cross-slip. We can still use the potential to assess select mechanisms with reasonable quantitative accuracy, but the capacity of the MEAM framework is exhausted beyond this point. Again, this points toward the development of machine learning potentials for more complex alloy systems.

4.2 EAM potentials for bcc elements and alloys

The use of body-centered cubic (bcc) materials, e.g. W and Fe, is widespread in engineering structural applications. The well-defined slip planes and planar dislocation cores of fcc structures encourage easy slip and well-behaved ductile behavior [123]. In comparison, the slip in bcc systems is more complex due to the non-planar behavior of the dislocations and also strong temperature effects of the dislocations.

Most bcc potentials available to date are for elements, although few show reasonable crack tip behavior to the best of our knowledge. Bcc α -Fe is a well-studied system in particular for fracture. Möller and Bitzek [98] compare the fracture performance of eight EAM-type potentials for bcc α -Fe in direct simulations of mode I fracture. The lattice constants, cohesive energy, and elastic constants for this set of potentials show overall good agreement to DFT/experiments, but it is standard to fit to these material properties. These potentials were not developed specifically for fracture, however, so the surface energies and stacking fault energies show wide deviations from DFT values, and also the GSF energy curves can take a different shape. No single potential was able to comprehensively reproduce the experimental fracture behavior in all crack systems, nor show complete quantitative agreement with the continuum theory. In addition, structural transformations (e.g. bcc \rightarrow fcc or bcc \rightarrow hcp) and planar faults developing at the crack tip and kinked crack extension were commonly observed behaviors, but these are possible artifacts likely arising from the potential. It remains unclear how to confidently separate artifacts of the potential from physical behavior.

At present, only a few very interatomic potentials are available for bcc alloys, but are limited in scope (e.g. a very recent MEAM-type for precipitates in the Hf-Nb-Ta-Ti-Zr family [124], machine learning potentials for phase stability [125] and grain boundaries [126] in the Mo-Nb-Ta-W family) and, to the best of our knowledge, none are tested for/show reasonable fracture behavior. In Chapters 6 and 7 we conduct simulations using a set of EAM-type interatomic potentials by Zhou et al. [1, 127] (hereafter called the “Zhou potentials”) for 16 elements which can be freely interalloyed. Our own studies show that the Zhou potentials suffer from similar problems as above in direct simulations

for both the bcc elements and their random alloys. However, the Zhou potentials have been reasonably validated for a number of complex HEA compositions (e.g. [8]) in terms of basic properties such as lattice constants, elastic constants, and also solute misfit volumes. While better potentials should and are being developed, we must find useful ways to proceed with existing available potentials in the meantime. The NEB method (Chapter 3.2.2) is one way to circumvent the problematic aspects of available interatomic potentials.

4.3 Average-atom approximation of random alloys

In alloys the underlying interactions between solutes and dislocations and other defects (e.g. precipitates, cracks, grain boundaries) control the mechanical behavior. The effect of solutes on material properties and solute-defect interactions and their dependence on composition is particularly interesting for alloy development. Complex HEAs are particularly challenging environments to study since they contain multiple principal components which obscures the conventional distinction between solvent and solute(s). The fluctuations in the local atomic chemical environment are very important, since the mechanistic origins of strengthening in random alloys arise from these fluctuations which control the detailed dislocation configurations and the plastic flow stress [99]. The concept of an “average-atom” (A -atom) interatomic potential (re-derived and validated by [99]) is highly valuable for the study of random alloys.

An arbitrary N -component alloy has an average concentration c_X of each constituent element X , with $\sum_{X=1}^N c_X = 1$. In a random alloy, the constituent atoms randomly occupy arbitrary sites in the system given the composition. The set of atomic sites i occupied by the individual atoms in the alloy is denoted by $\{s_i^X\}$, where the individual site occupation variables are

$$s_i^X = \begin{cases} 1 & \text{if type-}X \text{ atom sits on site } i \\ 0 & \text{otherwise} \end{cases} \quad (4.1)$$

The energy of a given configuration is

$$E(\{s_i^X\}) = \sum_{i,X} s_i^X F^X(\rho_i) + \frac{1}{2} \sum_{\substack{i,j \neq i \\ X,Y}} V_{ij}^{XY} s_i^X s_j^Y \quad (4.2)$$

containing the usual terms in the EAM formalism [65] as follows. Pairwise interactions between atoms X and Y are captured by V_{ij}^{XY} , and the factor of one half prevents double-counting the pairs. The embedding energy $F^X(\rho_i)$ for atom X at site i has local

4.3. Average-atom approximation of random alloys

electron density ρ_i at site i generated by the surrounding atoms, which is

$$\rho_i = \sum_{j \neq i, X} s_j^X \rho_{ij}^X \quad (4.3)$$

For a set of EAM interatomic potentials for a multicomponent system, an analytical average is performed over all possible random occupations of the atomic sites at the overall alloy composition – we direct the reader to [99] for the detailed process. The first-order approximate average energy is an analog to Eq. (4.2) and converts average occupations $\langle s_i^X \rangle$ to concentrations c_X , e.g.

$$\langle E \rangle = \sum_{i, X} c_X F^X(\bar{\rho}_i) + \frac{1}{2} \sum_{\substack{i, j \neq i \\ X, Y}} V_{ij}^{XY} c_X c_Y \quad (4.4)$$

where

$$\bar{\rho}_i = \sum_{j \neq i, X} c_X \rho_{ij}^X \quad (4.5)$$

Eq. (4.4) has form as the energy in the EAM formalism, so the A -atom potential represents a new atomic species which embeds the average properties of the random alloy.

The local lattice relaxations which exist in the true random alloy are eliminated in the “average-alloy” (A -alloy) system. Computed energies and forces are thus approximate, but the A -alloy shows very good agreement to the true random alloy for key bulk properties (e.g. lattice parameters, cohesive energies, and elastic constants) and planar defects (surface energies and stacking fault energies) which are relevant for fracture, dislocation structure, and plasticity (see Fig. 4.1). In particular, the agreement for elastic constants is very good, including C_{44} , which preserves the anisotropy entering into the continuum fracture theory. The A -alloy also shows excellent agreement for surface energies and small absolute differences for USF energies, which too enter into the theory. Finally, the A -atom capture the overall trends with alloy composition. We are thus able to use the A -alloy representation of the random system to distinguish which aspects of the mechanical behavior are controlled by the average material properties, and which by local compositional fluctuations in the random material.

Atomic volume misfit is an important feature in random alloys and in particular HEAs. The volume misfit between the elemental components cause atomic positions to deviate from their lattice positions, and these “microdistortions” have been shown to be connected to the high strength in HEAs [128, 129], e.g. through strengthening of screw dislocations [9]. The interaction between defect fields and solute misfit is a key quantity and seen in theories of solute strengthening [9, 130, 131]. However in HEAs the structure/fields of defects are affected by the stochastic compositional disorder, and furthermore the concept of a “solute” (from conventional alloying) is not so well-defined due to the many principal components, so characterizing the important composition-defect

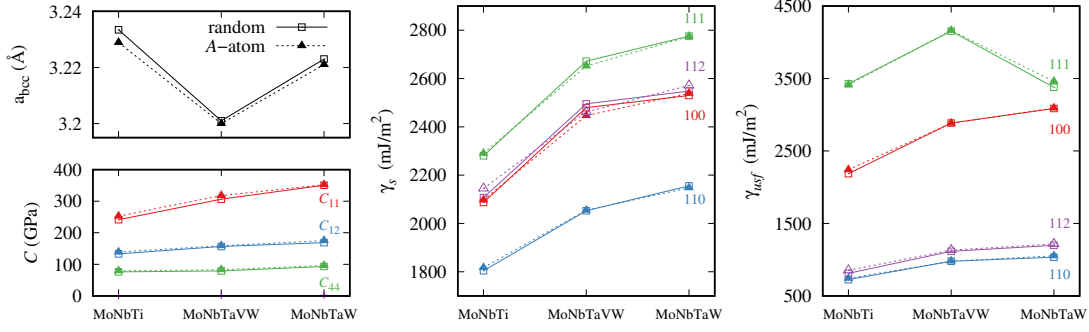


Figure 4.1: A-alloy vs. true random alloy material properties. The *A*-atom interatomic potential for three HEAs (based on the EAM-type Zhou et al. [1] family of potentials) reproduces the lattice parameter a , elastic constants C_{ij} , and various surface energies γ_s and unstable stacking fault energies γ_{usf} with good agreement to the true random system.

interactions is particularly challenging. The *A*-atom potential can be freely combined with any of the original elemental potentials, so it becomes possible to designate an explicit solute over a background of a homogenized *A*-alloy and study, for example, the much simpler interaction between this solute and an “average” defect. The *A*-atom method is thus a particularly invaluable tool for the study of HEAs.

The *A*-atom also allows for fast and accurate sampling for average bulk and defect properties since any random alloy collapses to a single homogeneous *A*-alloy representation. This facilitates large-scale studies over entire families of alloy compositions and is particularly advantageous for studying HEA families which span very large compositional spaces. It becomes computationally tractable to conduct parametric studies varying the element concentrations in order to identify average trends in material and mechanistic properties. We utilize the *A*-atom method to study HEA materials at specific alloy compositions and over the composition space of a family of alloys in Part II of this thesis.

Later in Chapter 6 we study several averaged HEAs using the *A*-atom derived from the elemental Zhou et al. [1] potentials. The new *A*-atom still retains the problematic aspects of the original potentials, but the problematic behavior is generally somewhat mitigated since the local lattice relaxations are eliminated by the averaging. Fig. 4.2) for example illustrates similar problematic fracture behavior in direct simulations from *A*-alloy representations of random alloys.

To study a crack in a random alloy, the uncracked simulation cell should be cut out of a very large random alloy “bulk” so that the atoms that become the boundary atoms are properly relaxed [132], and their relaxed positions are fixed in the *K*-test framework. In order to properly sample across different random alloy realizations, the boundary atoms should have different randomness, and this thus requires the relaxation of a very large “bulk” simulation cell for each new realization of the random alloy. Since the *A*-atom can be freely combined with any original atom, it is convenient and computationally

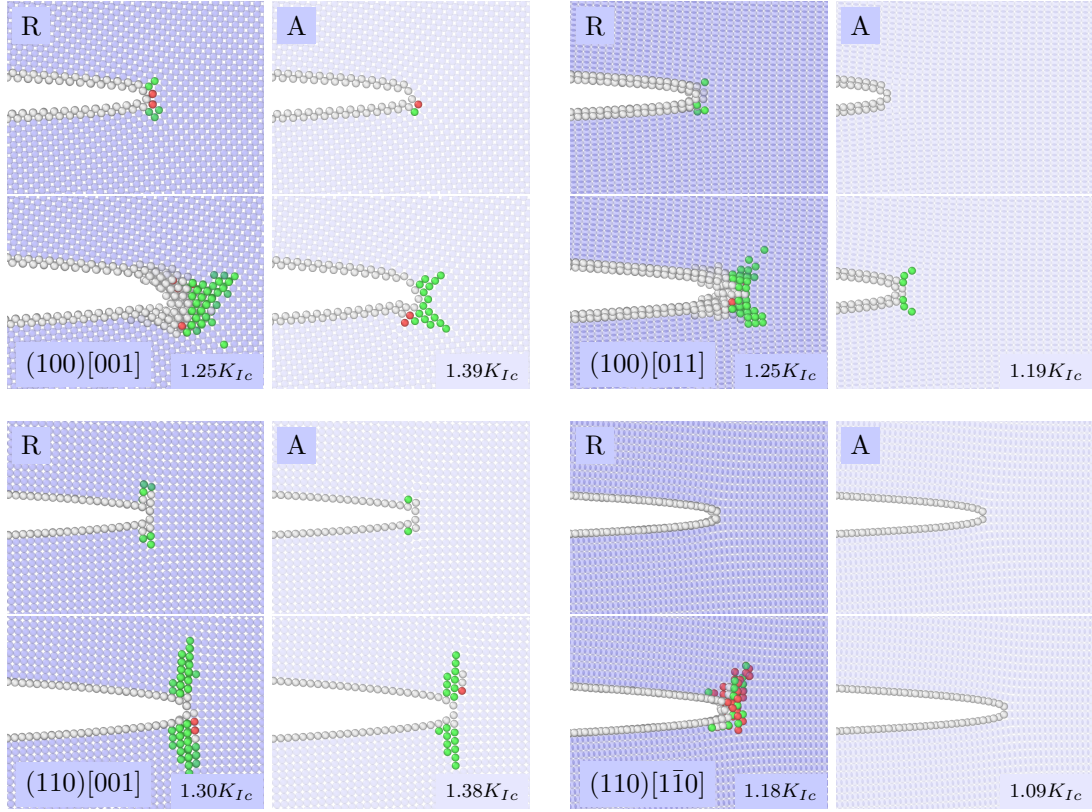


Figure 4.2: Crack tip behavior from direct K -test simulation for a random (R) and equivalent A -alloy (A) in the model $\text{Mo}_{20}\text{Nb}_{20}\text{Ta}_{20}\text{V}_{20}\text{W}_{20}$ system (Zhou potential [1]) for four crack orientations. Structural transformation/disorder is present at the crack tip in most cases at $\sim K_{Ic}$ (top row, A and R share the same K_{Ic}) and accumulates with further load increments (bottom row, load as labeled). Atoms are colored according to Common Neighbor Analysis according to structure: blue (bcc), green (fcc), red (hcp), and white (non-coordinated). Atoms are projected onto the x - y plane with transparency applied to the bulk (bcc) atoms.

efficient to instead create a homogeneous A -alloy boundary which is relaxed just once. The A -alloy boundary has no misfit volume since it is homogeneous and can be freely reused between realizations. Creation of different random realizations then only involves varying the randomness and relaxation of a much smaller cell containing the interior atoms. We use this method in Chapter 6 to create random realizations from a template “average” dislocation emission path.

We note here that mixing regions of A -alloy and (true) random alloy regions involves some care as the A -alloy and true random alloy have slightly different lattice constants and cohesive energies. The A -atom potential needs to be calibrated to reproduce the random alloy lattice constant, so the composition represented by the A -atom will be slightly different to the random alloy concentration. This involves some very small change in the elastic constants of the boundary atoms [132], but the boundary-interior interface should be sufficiently so the effect on the crack tip should be negligible. Additionally,

in the K -test setup, a minimum of 2 layers of “pad” atoms bridging between the fixed A -alloy boundary and the explicitly random system is recommended to prevent spurious behavior at the interface.

4.4 Machine learning potentials

Traditional semi-empirical potentials have fixed functional forms with limited number of fitting parameters that inherently limit their ability to accurately fit many properties. Due to this, user-decisions regarding the relative importance between material properties are often involved in their development process, since all desired properties cannot be achieved with sufficient accuracy, and the resulting potentials are often limited to specific applications where the most critical material properties are fit with high accuracy. There is a recent surge of interest in applications of machine learning (ML) methods [133–138] for interatomic potentials since no such restrictions to the functional form are imposed during the fitting of the potential energy surface.

Machine learning potentials developed to date assume that the total potential energy of a system of N atoms can be represented as a sum of the energies of each atom n , i.e.

$$E_{tot} = \sum_{n=1}^N E_n \quad (4.6)$$

where the energy of each atom E_n depends on the local environment around the atom. The geometric representation of the local atomic environment is known as the “descriptor”. The construction of a ML potential generally consists of the following steps. First, a suitable class of the descriptors is chosen to describe the local atom environments [139–143]. Then, a database of structures, energies, and forces, known as the “training dataset”, is developed using first-principles methods, e.g. DFT. A regression algorithm (e.g. neural network, kernel ridge regression) optimizes the parameters in the ML framework to best match the training set. The number of descriptors and parameters are unlimited, so the ML approach provides a parameter-rich space to capture the entirety of the training dataset well. It must be noted that ML is pure regression, so ML potentials are not suitable for extrapolation to structures that differ significantly from the training set.

The selection of the training dataset defines the mathematical optimization and thus has a strong influence on the resulting potential. Choosing too many similar structures, for example, implicitly steers the optimization toward favoring low error on those structures. A suitable training dataset is one that comprehensively spans the atomic environments encountered by a wide range of crystalline defects so that the resulting potential is well-suited to interpolate between those environments. The structures in the training dataset and the predicted material properties are generally associated with

the equilibrium geometry, the elastic response of the bulk, vibrational properties, vacancies, surfaces, liquid-state information, etc.. A “big data” approach may include many types of random structures, but may instead drive the ML toward capturing less-relevant structures.

In order to achieve broad accurate performance without overfitting, a balance must be struck between selecting an appropriately limited set of descriptors and fitting parameters and a sufficiently large and diverse training set. To this end, several semi-automated protocols (e.g. active learning [144], self-guided learning [145], on-the-fly methods [146], and hybrid approaches [136]) have been developed to curate an exhaustive training set while maintaining transferability. It is important to use well-converged and consistent DFT calculations for the atomic structures. The ML potential is only as accurate as the DFT, as any computational inconsistencies across the dataset are treated as real and translated into the resulting ML potential.

A critical limiting aspect of nearly all of the ML potentials created to date is that the training dataset and the fitness of the potential are mainly demonstrated on basic properties of the bulk crystalline material [147]. However, in order to create a potential for performing metallurgically useful studies of the behavior of metal defects, the structures need to be sufficient for an accurate representation of crystalline defects specifically. For example, the SSF energy, which is an important property for dislocation emission, is very poorly predicted by many ML methods (see [147]) because the nature of the training dataset did not include configurations near the stacking fault structure. Metallurgical knowledge can be incorporated by choosing relevant structures for mechanical properties [147].

In the following we discuss two ML potentials which incorporate defect structures in their training datasets. Previously developed interatomic potentials for W indicate that accurate depiction of dislocation core structure and mobility tend to yield simulation results that are more consistent with experimental predictions [148]. The Gaussian Approximation Potential (GAP) for bcc Fe [149] and W [150] include DFT-accurate dislocation structures, but we find them insufficient for fracture simulations. A more recent neural network (NN) type potential for hcp Mg [94] is also presented, which incorporates an extensive variety of metallurgically-relevant and fracture-geometry-relevant structures in its training data. It shows overall excellent performance for fracture, improving on the already quite good Wu MEAM potential, and has potential for further development into an accurate general-purpose potential.

4.4.1 Gaussian approximation potentials for bcc Fe and W

The bulk mechanical strength and ductility of bcc α -Fe and W are attributed to the stress- and temperature-dependent mobility of screw dislocations [151, 152]. Disloca-

tion mobility depends on the underlying mechanisms of nucleation of kink-pairs along a straight screw dislocation and its migration which advances the dislocation to the next Peierls valley yielding plastic slip of one Burgers vector. No conventional semi-empirical interatomic potential so far can (i) capture the kink-pair nucleation mechanism, (ii) reproduce the DFT-computed compact screw dislocation core, or (iii) display the expected Peierls potential [153], thus motivating development of a potentials which can accurately capture core structure and Peierls potential.

DFT-accurate interatomic potentials for bcc α -Fe [149] and W [150] were recently developed based on the Gaussian Approximation Potentials (GAP) framework [154, 155]. Since its inception, the GAP method has seen success with modeling defects [149], dislocations [153], grain boundaries [156], more recently to describe alloy phases [157]. GAP is based on machine learning over a large number of DFT atomic environments using kernel regression, e.g. the Smooth Overlap of Atomic Positions (SOAP), through invariant many-body representations of the neighbor environments of atoms [158]. The training in Fe and W SOAP-GAP utilizes atomic environments including pristine structures, stacking faults, free surfaces, vacancies, and interstitials. Fe GAP reproduces the bulk properties and also accurately portrays the key features associated with screw dislocations (core structure, slip behavior, Peierls potential, etc.) [148].

Despite the success with dislocation properties, Fe and W GAP dramatically fail when subjected to a typical fracture setup utilizing the QUIP/GAP packages [154, 158] as implemented in LAMMPS. Fig. 4.3 shows examples of both GAPs in a typical crack orientation of (110) $[1\bar{1}0]$. These cracks are predicted to be brittle and should cleave based on the material properties but do not cleave (or emit). The atomic planes directly ahead of the crack tip do not decohere, but rather distort the atoms and crystal structure on neighboring planes. GAP has slow evaluation speeds compared to conventional semi-empirical potentials (by three to four orders of magnitude [157]), which is expected, but also compared to other ML methods even with massive parallelization. For example, the moment tensor potential (MTP) [159] is another ML approach to learning the quantum-mechanical energy surfaces and is significantly faster than GAP due to its more-efficient polynomial basis of interatomic distances and angles [157]. A “sparse” version of the “full” Fe GAP is intended to increase the evaluation speed. Unsurprisingly, we see in Fig. 4.3b that this further degrades the performance in fracture. The crystal structure ahead of the crack tip transforms from bcc to a simple cubic arrangement, which is clearly an unphysical artifact of the potential.

ML potentials are not suitable for extrapolation outside of the training dataset, so the poor fracture performance indicates that the atomic configurations encountered in the fracture environment are well outside of the training set. The training dataset should be extended and the potential retrained. Inclusion of cuboidal structures as in the Mg Neural Network-type potential presented following is likely to improve the GAPs from their current form. While these DFT-accurate interatomic potentials can be a standard

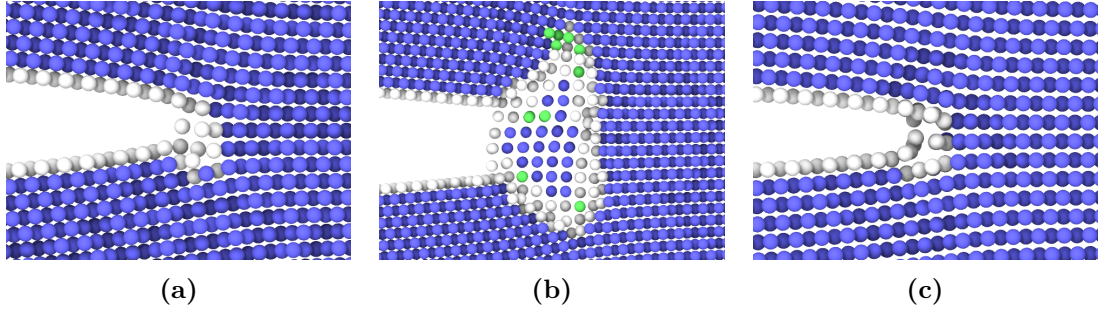


Figure 4.3: Examples of crack tip behavior obtained from GAP. (a) Fe GAP and (b) “sparse” version of Fe GAP [149], and (c) W GAP [150]. The simulation cell is periodic with minimum lattice dimensions in the out-of-plane direction. The cracks are oriented in the brittle (110) $[110]$ orientation and atoms are shown projected onto the x - y plane. Atoms are colored according to Common Neighbor Analysis [160] according to structure: blue (bcc), green (fcc), red (hcp), and white (non-coordinated).

used to judge the quality of interatomic potentials against ab initio data, their speed and thus range of applicability are still quite restricted.

4.4.2 Neural network potentials for Mg

Stricker et al. recently developed a family of Behler-Parinello neural network (NN) [139] ML potentials for pure Mg using the implementation for the library `n2p2` [161] which shows broadly superior performance compared to the MEAM-type potentials discussed above. The details and implementation of the NN method are well-presented in the recent literature and the reader is referred, e.g. Ref. [139, 161–164], but we review some major points following.

The Behler-Parinello NN potential formulation consists of the choice of the atomic structural representation, called “symmetry functions”, the number of hidden layers in the NN, and the number of hidden nodes per layer in the network. The so-called “weights” and “biases” are determined by fitting the total energy according to Eq. (4.6) to a training dataset of structures, total energies, and individual atomic force components. The structural representations of the atomic environment are dictated by radial and angular symmetry functions based on relative atomic distances and angles, respectively, a smooth cutoff function, and several predefined hyperparameters. The number of functions employed is a heuristic design choice based on goals of avoiding overfitting and having acceptable computational costs.

In order to choose a set of specific functions, a very large number of M of candidate symmetry functions is initially considered. A training dataset of atomic structures is specified with each atom in each structure having a local atomic environment. The M candidate symmetry functions centered on each atom in the training dataset is evaluated. An unsupervised selection algorithm based on a CUR matrix decomposition [165] determines the most valuable symmetry functions ($\ll M$), i.e. those with the highest

information content with respect to all the N environments in the training structures. This selection constitutes the input layer of the NN.

The employed NN consists of the input layer, hidden layers with a number of hidden nodes, and a final layer with one neuron representing the energetic contribution to the atomic environment. The chosen topology results in a large number of fitting parameters, which is the combined number of weights and biases of the network. The determination of the weights and biases is then done with supervised learning to minimize an error function Γ equal to the sum of the square of differences between the NN potential (NNP) and DFT energies and forces. The quality of the optimization is measured by separately evaluating the root-mean-square-errors (RMSE) of the energy and forces. The fitting (also called “training”) of NNPs is done with a Kalman filter [166] as implemented in `n2p2` for several hundred iterations corresponding to the gradient of the error function Γ becoming small while avoiding overfitting. The specific NN and training parameters for the Mg NNP are presented in detail in [94].

Rather than using a “big data” approach, Stricker et al. deliberately incorporate metallurgical knowledge into the training data set in order to accurately represent crystalline defects. The training data consists of the energy-volume curve, elastic constants, cohesive energy, and GSF energy curves, SSF energies, decohesion curves, and relaxed surface energies. The DFT training dataset used is relatively small and is nearly the same as prior MEAM-type potentials [2] and contains all of the critical material properties for fracture entering into the continuum theory. It is important to note that the same underlying data is used between the MEAM and NNPs, but the NNP is fit only with energies and forces, from which material properties are then derived. It is easy in the parameter-rich NNP framework to add further selected data in order to improve specific properties. For instance for fracture, the training dataset was extended to include additional rod and cuboidal structures containing corners and edges of several high symmetry planes to obtain physical behavior at atomically sharp crack tips. Compared to existing very good MEAM potentials [2, 167], the NNP generally performs better in reproducing many material properties and crystalline defects that are critical to mechanical performance. It is interesting to note that the vacancy formation and migration energies are in good agreement with DFT, along with the dislocation structures, despite not being in the training set.

The NNP predictions of the elastic constants, surface energies, and USF energies show overall much better accuracy than the performance of MEAM [2, 167]. These are the critical material parameters entering into the continuum theory so we can expect the NNP to be more realistic for assessing the fracture behavior of Mg. No anomalous or unphysical behavior is observed for any crack geometry when using the NNP, which is already a very positive result. Table 4.1 shows the predicted and observed results obtained using the NNP. In all cases, the observed or simulated behavior (see Fig. 4.4) coincides with the predicted behavior using the DFT material properties. The simulated

and predicted critical values differ slightly due to lattice trapping for cleavage and the non-exact theory for emission (Chapter 2). The only notable quantitative deviation between simulation and theory is for the pyramidal II orientation case where the simulated emission occurs at $0.82K_{Ic}$, i.e., much lower than the theoretical value. Nevertheless, overall, the NNP thus provides very good predictions for all fracture orientations studied. This study together with [33] and partially in [48] is one of the first validations of the Andric-Curtin theory [48] (e.g. Eq. (2.11) and (2.14)) compared to Rice theory [30] for non-fcc materials.

Table 4.1: Stress intensity factors K_I for cleavage and emission for various crack orientations as computed and simulated using Mg NNP and its material properties. The observed events using the Wu et al. MEAM potential [2] are also shown [168]. Critical K values in boldface indicate the predicted event. Cases where the MEAM event differs from the NNP-observed and DFT-predicted event are indicated in italics. Reproduced from [94].

Crack plane	Predicted critical K and event			Observed NNP		NNP vs. Pred	MEAM
	K_{Ic}	K_{Ie}	event	K_I	event	K^{NNP}/K^{pred}	event [168]
Basal I	0.265	0.284	cleavage	0.280	cleavage	1.06	cleavage
Basal II	0.265	0.291	cleavage	0.263	cleavage	0.99	cleavage
Prismatic I	0.297	0.253	emission	0.236	emission	0.93	<i>cleavage</i>
Prismatic II	0.307	0.282	emission	0.283	emission	1.00	<i>cleavage</i>
Pyramidal I	0.284	0.237	emission	0.250	emission	1.05	emission
Pyramidal II	0.302	0.286	emission	0.220	emission	0.82	<i>cleavage</i>

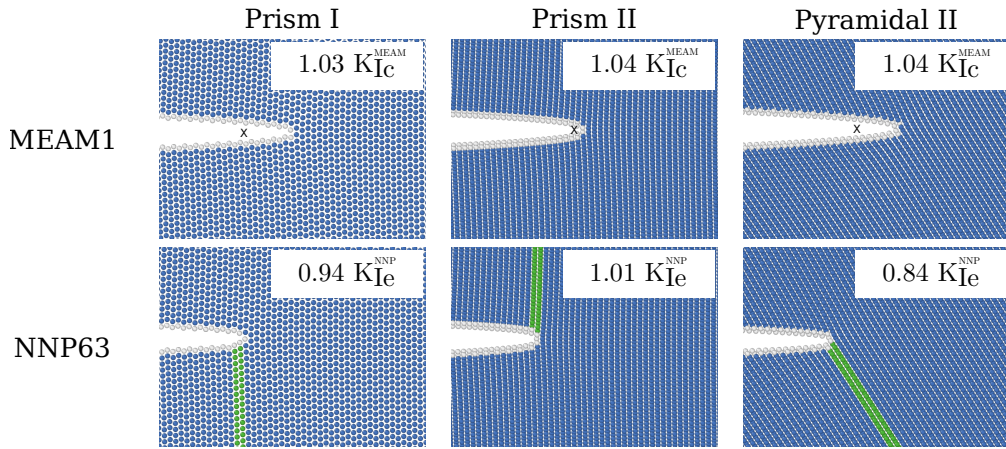


Figure 4.4: Cross sectional view of crack tips post fracture for prismatic I, prismatic II, and pyramidal II crack planes, as observed in simulations for MEAM [2] and NNP. The corresponding K values at each event are shown relative to K_{Ic} for the MEAM and K_{Ie} for NNP63 in the respective crack plane. Visualization used the Common Neighbor Analysis [160] (blue = hcp, green = fcc, gray = other) and the black “x” denotes the initial crack position for cleavage events. Reproduced from [94].

Comparing the fracture behavior from the NNP to the MEAM potentials, Mg is not as brittle as suggested by the studies based on the MEAM potential. The difference in intrinsic ductility is directly traceable to subtle differences in the underlying material properties. For example, the MEAM1 potential less accurately predicts the surface

energies and USF energies compared to the NNP, and this leads to different behavior in simulations. Furthermore, while both potentials predict the basal orientation to be brittle, the NNP predicts a much closer competition ($K_{Ic}/K_{Ic} \approx 1.07$) compared to the MEAM potential ($K_{Ic}/K_{Ic} \approx 1.38$ [33]). This suggests the possibility that dilute alloying could have a more important effect in mitigating brittle basal behavior than observed from the model Mg-Y alloy using an alloy MEAM potential [118] (Chapter 5).

This NNP is not yet a general-purpose Mg potential as there remains several points of improvement. For example, the pyramidal II screw dislocation structure is less than ideal. The important pyramidal I-II screw energy difference also requires improvement but accurate reference DFT data is not available and may remain challenging due to the very small energy difference; this is a problem of reference rather than fitting. Assessing the quality of a potential for metallurgical applications requires more than just the RMSE of the optimization. Further testing is required for more challenging structures, e.g. grain boundaries and interstitial atoms, to validate that the training dataset is sufficiently comprehensive. Nevertheless, the NNP is among the first to demonstrate the broad application of ML in capturing metallurgically relevant properties, structures, and behaviors, and clearly improves on existing optimized and quantitatively excellent semi-empirical potentials, namely MEAM [2]. These results are encouraging, not only for Mg, but also for the broader prospects for ML potentials. The improved performance comes at a cost – compared to the MEAM formalism as implemented in LAMMPS, the n2p2 implementation for BPNN is roughly $10\times$ more computationally expensive [161], but is still a fraction of the cost of DFT. Going forward, it appears likely that only ML potentials will reach sufficiently quantitative accuracy, approaching that of DFT, required to conduct realistic and large-scale atomistic studies of alloys.

The quality of a potential for metallurgical applications must not only be measured by the RMSE of the optimization. As we have seen, substantial tests outside of the training data set and/or to challenging but realistic structures (e.g., dislocations, crack tips) must be included. The performance comes at a cost. Compared to the MEAM formalism as implemented in LAMMPS, the n2p2 implementation [161] for BPNNs is $10\times$ more expensive computationally. Adding more elements to create interatomic potentials for alloys increases the cost significantly [92]. However, if the aim of atomistic studies is to be quantitatively correct for specific alloy compositions, then it is likely that only machine learning methods will provide an accuracy approaching that of DFT while at a tiny fraction of the computational cost, even if this cost significantly exceeds that of traditional potentials.

Although the NNP is not a general-purpose Mg potential, it is among the first to demonstrate the broad application of a machine learned potential to a cross section of metallurgically relevant properties, structures, and behaviors. The NNP clearly improves on existing traditional potentials that have been highly optimized and that are quantitatively among the best potentials among all those developed to date for pure metals.

These results are encouraging, not only for Mg, but also for the broader prospects for ML potentials.

Atomistic fracture in alloys **Part II**

5 Intrinsic fracture behavior of dilute Mg-Y alloys

This chapter is extracted from the following publication

1. Mak, E., & Curtin, W. A. (2020). Intrinsic fracture behavior of Mg-Y alloys. *Modelling and Simulation in Materials Science and Engineering*, 28(3), 035012

Pure magnesium (Mg) is lightweight and highly abundant in nature, and so is an attractive metal for structural applications, especially in the automotive and aerospace industries [102]. However, Mg has low ductility and low fracture toughness at low and moderate temperatures, and these properties limit its formability and suitability for fracture-critical and/or energy-absorption applications. The low ductility and limited formability of Mg are associated with the strong plastic anisotropy of the hexagonal close-packed (hcp) crystal structure, especially the difficulties in activating the pyramidal $\langle \mathbf{c} + \mathbf{a} \rangle$ slip modes [103] due to a thermally-activated transformation of the $\langle \mathbf{c} + \mathbf{a} \rangle$ dislocations to a sessile configuration [79]. The relatively brittle fracture behavior is equally complex, with multiple cleavage planes observed, especially at low temperatures [103]. Alloying of Mg with rare earth elements (Y, Ce, Tb, Gd, Dy, Ho) and other elements (Ca, Mn) at levels less than 1at% has been shown to enable good ductility, sufficient for forming Mg-based components [104–106]. The notable increase in ductility has been attributed to the ability of the alloying elements to greatly increase the pyramidal cross-slip rate [107], overcoming the fundamental immobilization of the pyramidal dislocations in pure Mg [79]. The ductilization, i.e. increased fracture strain, should enable toughening of the alloy due to greater plastic flow and dissipation around a crack tip, but it does not have any direct implications for the intrinsic fracture behavior of cracks in Mg. This motivates the present study of alloying effects on the intrinsic fracture behavior.

A previous atomistic study of Mg [93] showed that Mg is largely intrinsically brittle, i.e.

most orientations show brittle cleavage behavior. Cleavage on the basal plane is quite favorable, but the competition between cleavage and emission on many other planes is very delicate. Here, we investigate if alloying with Y, a particularly widely studied ductilizing element, can favorably alter the intrinsic ductility of the alloy relative to that of pure Mg using a model Mg-3at%Y random alloy.

The competition between ductile dislocation emission and brittle cleavage mechanisms at the crack tip can be evaluated within the framework of linear elastic fracture mechanics (LEFM) (see Chapter 1). The key material properties are the surface energies of the cleavage and emission planes, the unstable stacking fault on the emission plane, and the anisotropic elastic constants. Alloying can alter all of these quantities, and thus shift the behavior between ductile and brittle, especially for systems where cleavage and emission are in close competition in the pure metal. The random nature of the solid-solution alloying may also create additional local effects at the crack tip that cannot be directly evaluated within the continuum LEFM theories. Thus, atomistic simulations provide an avenue for investigating both continuum and local phenomena simultaneously.

As reported in detail below, we find that fracture resistance of Mg-3at%Y, a composition higher in Y than typical in experiments so as to exaggerate the solute effects, is generally increased relative to that of pure Mg. The cleavage/slip systems that are intrinsically brittle in pure Mg generally remain intrinsically brittle in the alloy, but can become tougher (higher critical mode I stress intensity at fracture) by a combination of local crack tip phenomena and statistical fluctuations allowing some dislocation emission. These effects lead to greater resistance to fracture, thus requiring higher applied loads and activating more far-field plasticity, which then conveys even higher macroscopic toughening; this is the so-called “Rice valve effect” [169]. Care must be taken when local crack tip effects occur, because these effects could be artifacts of the interatomic potential used in the simulations. However, the continuum trend alone is found to predict that cleavage is more difficult and emission less difficult in the alloy than in pure Mg. In this chapter we present the fracture results for various crack configurations and compare to LEFM, and then discuss the local crack tip phenomena.

5.1 Material properties and simulation details

We calculate the critical mode I stress intensities for cleavage K_{Ic} using Eq. (1.24) and emission K_{Ie} using Eq. (2.11), reiterating from Chapter 1 that the emission analysis is not limited to any crystal structure. The Andric-Curtin emission model was shown to capture the emission behavior in pure hcp Mg [48]. Specific values of the quantity Λ_{22} and the anisotropic parameter $o(\theta, \varphi)$ for the orientations studied here are provided for Mg and Mg-3at%Y in Appendix A.1.

For examining crack tip geometries, the Polyhedral template matching (PTM) algorithm

[170] with root-mean-square optimization (RSMD = 0.3 unless otherwise stated) is used for greater tolerance to the significant lattice distortions present at the crack tip.

Presently, Y is the only solute among the rare earth Mg-ductilizing elements for which a well-validated interatomic potential exists. This limits our study to the Mg-Y system, but comparison to general theory enables extension of the theory to other alloys. Specifically, we use a modified embedded-atom method (MEAM) interatomic potential for the binary Mg-Y system [118] based on the MEAM potential for pure Mg in [2] that provides a very good description of dislocations and fracture properties. The Mg-Y potential captures most key features of Y solutes in Mg, with the only notable deviation being an underprediction of the Y-concentration dependence of the pyramidal I stable stacking fault energy. Fortunately, the stable stacking fault energies, particularly for pyramidal I, are not crucial in the LEFM analysis, and so this Mg-Y potential is deemed sufficient for the present study.

In the fracture studies, we examine cracks on the basal, prismatic, pyramidal hcp planes, and on the tensile twin interface, consistent with the comprehensive study of Ref. [93]. To favor dislocation nucleation, the directions of the crack fronts are chosen such that possible dislocation slip planes intersect the crack plane along the entire crack front. The average surface and unstable stacking fault energies for pure Mg and Mg-3at%Y were determined for all of the relevant fracture and slip planes using large realizations of the random alloy configurations and standard methods [2]. Surface energies were determined using 10 trials of in-plane periodic samples having 1600 surface atoms. Unstable stacking fault energies were determined using 24 samples having 500 interface atoms on each side of the fault plane. Results are shown in Table. 5.1. In comparison to pure Mg, γ_s tends to increase by $\sim 5\%$ while γ_{usf} tends to decrease by $\sim 3\%$. These changes alone suggest a trend toward improving intrinsic ductility since $K_{Ic} \sim \sqrt{\gamma_s}$ and $K_{Ie} \sim \sqrt{\gamma_{usf}}$. Average elastic constants for the alloy are relatively unchanged compared to pure Mg (see Appendix A.1).

Crack geometries are created as described in Ref. [23]. Starting from a large perfect crystal sample using the lattice parameters of Mg, 3% of the atoms are randomly substituted for Y to create a random realization of the alloy. To accommodate the dilation due to the large misfit volume of Y ($\Delta V/V_0 = 0.593$), the simulation cell is then fully relaxed to zero stress before a crack is introduced. For homogeneous materials at $T = 0$ K, dislocation emission from a crack tip is independent of the simulation cell thickness, so the cell can have the minimum periodic length along the crack front direction (here, along the z -axis). Here, the depth of the simulation cell must be sufficiently large to ensure that the random solute concentration along the crack front is representative of the specified solute concentration. In addition, when there is dislocation emission, it is important that the cell dimension in the dislocation slip direction, typically in y , is large to limit boundary effects. Andric and Curtin [23] demonstrate that a $200 \times 200 \times 10$ Å ($x \times y \times z$) simulation cell is more than sufficient to produce converged results for mode

Chapter 5. Intrinsic fracture behavior of dilute Mg-Y alloys

Table 5.1: Crack tip cleavage and emission competition in Mg and Mg-3at%Y as predicted from linear elastic fracture mechanics. (\mathbf{n}) is the crack plane and $[\mathbf{l}]$ is the direction of the crack front. For orientations with multiple possible dislocation slip systems, the slip system with the lowest K_{Ie} is shown. Values of K_{Ie}^{trail} for trailing partial dislocation emission is shown for orientations where leading partial dislocation emission is observed.

Orientation (\mathbf{n}) $[\mathbf{l}]$	Comp.	Slip plane	γ_s (mJ m^{-2})	γ_{usf}^e	γ_s^e	K_{Ic}	K_{Ie}	K_{Ie}^{trail}	Predicted	MD
Basal I (0001)[1210]	Mg Mg-Y	Pyr. I	568 610	319 318	619 655	0.255 0.262	0.351 0.346	–	Cleavage	Cleavage
Basal II (0001)[1010]	Mg Mg-Y	Pyr. II	568 610	298 295	651 696	0.255 0.262	0.333 0.325	–	Cleavage	Cleavage
Prismatic I (1010)[1210]	Mg Mg-Y	Basal	582 624	125 118	568 610	0.252 0.258	0.254 0.255	– 0.353	Cleavage Basal $\langle \mathbf{a} \rangle$	Cleavage Basal $\langle \mathbf{a} \rangle$
Prismatic II (1210)[1010]	Mg Mg-Y	Basal	650 689	125 118	568 610	0.267 0.272	0.282 0.282	– ∞	Cleavage	Cleavage
Pyramidal I (1011)[1210]	Mg Mg-Y	Basal	615 655	125 118	568 610	0.262 0.266	0.239 0.240	0.352 0.332	Basal $\langle \mathbf{a} \rangle$	Basal $\langle \mathbf{a} \rangle$
Pyramidal II (1212)[1010]	Mg Mg-Y	Basal	651 696	125 118	568 610	0.269 0.275	0.270 0.269	– 0.215	Cleavage Basal $\langle \mathbf{a} \rangle$	Cleavage Basal $\langle \mathbf{a} \rangle$
Tensile twin I (1012)[1210]	Mg Mg-Y	Basal	661 701	125 118	568 610	0.256 0.262	0.3018 0.3020	–	Cleavage	Cleavage
Tensile twin II (1012)[1210]	Mg Mg-Y	Basal	661 701	125 118	568 610	0.256 0.262	0.778 0.775	–	Cleavage	Cleavage

I fracture simulations of homogeneous fcc materials. Consequently, we use a simulation cell size of $700 \times 700 \times 50\text{\AA}$ ($\sim 1 \times 10^6$ atoms) when dislocation emission is predicted, and $700 \times 350 \times 50\text{\AA}$ otherwise, with periodicity in the z direction.

We utilize the standard K -test methodology for direct simulation as described in Chapter 3.3. An atomically sharp crack is unstable to closure/opening when loaded below/above the Griffith value K_{Ic} and must often be artificially stabilized by “screening” or “blunting”. Here, $K_{Ie} \sim K_{Ic}$ so that the initial sharp crack tip is relatively stable to small perturbations around K_{Ic} , and so these adjustments are unnecessary. We simply apply an initial load slightly below (1-3%) the theoretical critical stress intensity and further load increments of $\Delta K_I^{\text{app}} = 5 \times 10^{-4} \text{MPa}\sqrt{\text{m}}$.

As the crack grows and moves from the center of the simulation cell, an updated crack tip position is determined for the current relaxed configuration via common neighbor analysis [171] in the vicinity of the previous crack tip position. The crack-tip position is estimated to within $\sim 10\text{\AA}$; this is sufficient for setting the stress intensity boundary conditions for large simulation cells [23]. Thus, the applied boundary conditions are always consistent with the *current* position of the crack tip. We record the applied stress intensity K_I^{app} , the crack tip position, and the positions of all previously-emitted dislocations, as crack tip phenomena (cleavage, emission, etc.) occur. The small increments in loading are useful for limiting crack extension events and for precise identification of

critical load levels at which phenomena occur.

5.2 Intrinsic ductility and fracture toughness

The first cleavage or emission event is indicative of the intrinsic ductility of a particular crack orientation, and is the main feature predicted by LEFM. The first event, as observed in the simulations, is compared against the LEFM prediction in Table 5.1 for all orientations for both pure Mg and the Mg-Y alloy. In all cases, the predicted behavior agrees with the observed behavior. However in most cases, the critical stress intensity for the first event differs by $\sim 10\%$ between theory and simulation. This quantitative discrepancy between theory and simulation suggests an underlying complexity of the crack tip in the alloy that is not accounted for in the continuum theory.

In pure Mg, seven of eight (all but pyramidal I) are intrinsically brittle. In the alloy, two of the brittle orientations (prismatic I, pyramidal II) become intrinsically ductile. The prismatic II orientation remains intrinsically brittle, but emits dislocations as will be discussed later. These changes in intrinsic behavior occur for those orientations where the brittle/ductile competition is quite subtle, so that even small average changes in relative material properties can change the intrinsic behavior. In spite of the delicate competition, the theory (Eqs. (1.24) and (2.11)) captures the changes due to alloying. For the basal and twin orientations, where K_{Ic} is well below K_{Ie} , the alloying cannot drive a change from brittle to ductile behavior.

Unlike pure Mg, fracture in the alloy is not entirely controlled by the first crack tip event because of the fluctuations of the local conditions along the crack front that influence crack behavior. Therefore, subsequent events and crack growth are necessary to characterize the overall fracture resistance of each crack orientation. In the presence of stable crack growth, fracture is characterized by the resistance curve (R-curve) defined as the applied far-field load K_I^{app} versus the crack extension Δa . In pure Mg, there is no R-curve for any orientation. The initial crack either cleaves and grows unstable at a critical applied load of K_{Ic} , or emits successive dislocations after K_{Ie} with no crack growth (except for an apparent crack extension due to the kinematics of the crack tip blunting, for example in pyramidal I).

As shown in Fig. 5.1, the R-curves of the alloy are generally characterized by two regimes. In the early stages of crack extension, an initial toughening of the stable crack tip is followed by additional toughening in steps. This toughening, which is discussed later, arises from local solute-induced phenomena at the crack tip in addition to dislocation shielding, and allows a crack to sustain higher applied loads without unstable crack extension. The intrinsically brittle twin crack configurations do not exhibit any toughening after alloying, behaving similarly to Mg. The behavior of the intrinsically ductile pyramidal I orientation also does not change appreciably upon alloying. The remaining intrinsically

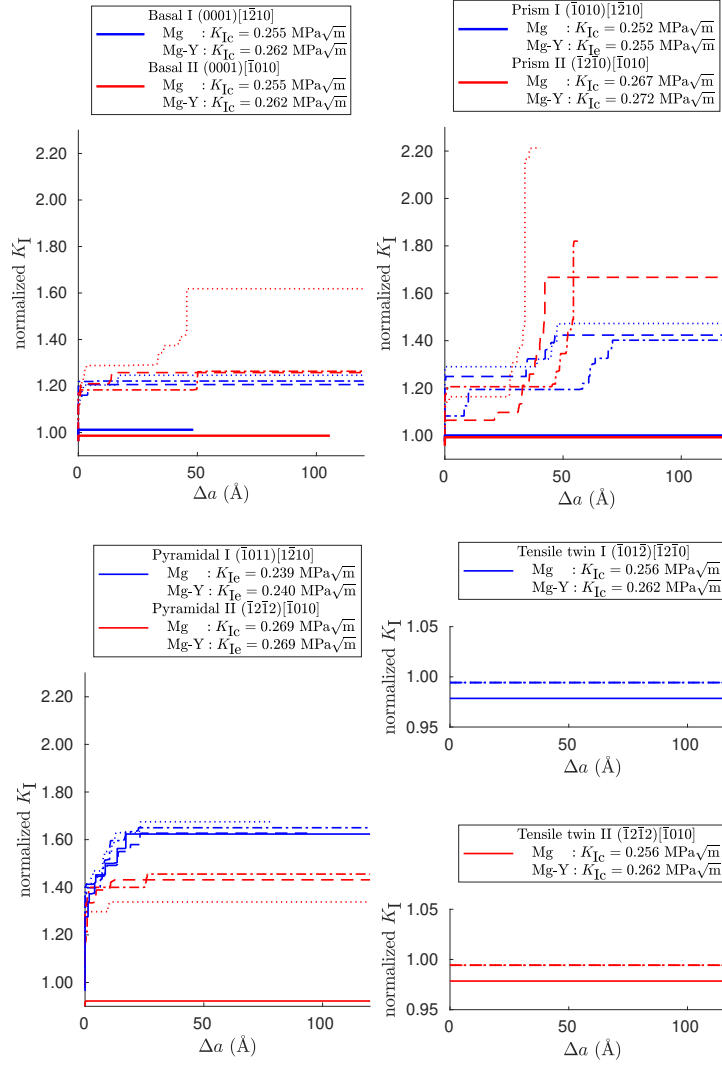


Figure 5.1: The resistance curve (R-curve) of the applied load K_I versus crack extension Δa . Three realizations per orientation of the random Mg-Y alloy (dashed lines) and a reference realization of Mg (solid line) are shown. Applied loading is normalized to the intrinsic critical stress intensity (K_{Ic} or K_{Ie}) of each crack orientation and composition as indicated.

brittle Mg orientations (basal and prismatic) however, show significant toughening after alloying. Where toughening and stable crack growth is observed, the critical applied load increases ($K_{I,crit} \approx 1.2 - 1.6 K_{Ic}$ or K_{Ie}) across the systems. At this load, the crack extends continuously, being able to overcome any dissipation mechanisms with no further increase in applied load.

Although there are some stochastic differences between different realizations of the same crack configuration due to the randomness of the alloy samples, phenomena are characteristic of each crack orientation because the crack tip/solute interactions are dominated by crack orientation rather than solute positions. We proceed to highlight the charac-

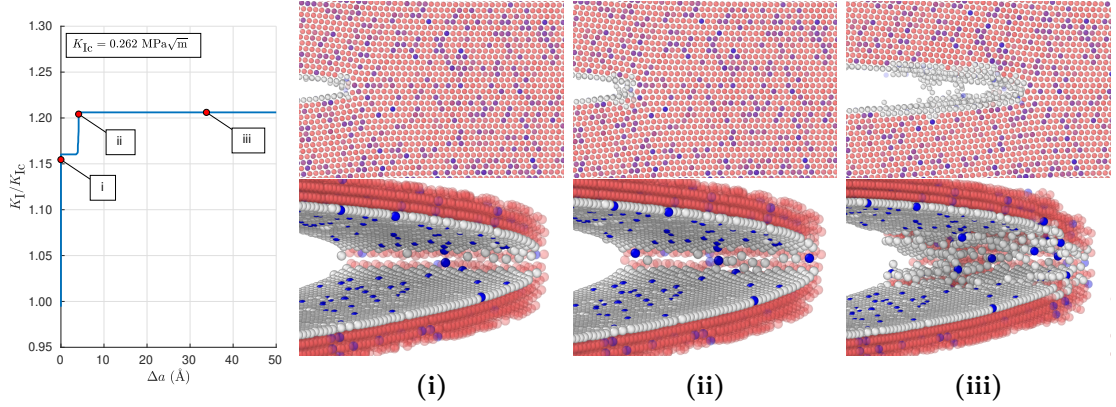


Figure 5.2: A basal I (0001)[$\bar{1}210$] orientation crack in a random Mg-Y alloy under mode I loading. Left-most: normalized R-curve with points of interest corresponding to (i)-(iii) indicated in red. In (i)-(iii): the plane projection (upper) and perspective view (lower) of the crack tip is provided. Bulk atoms in perspective view are removed for clarity. Atoms are colored according to composition and structure: hcp Mg (red), fcc Mg (green), non-coordinated Mg (white), and all solute Y atoms (blue).

teristic behavior of each crack orientation using the crack path of one representative realization of the random alloy.

5.2.1 Basal

Cracks in both basal orientations show fully brittle behavior with no dislocation emission (Fig. 5.2 and 5.3), as predicted by LEFM. However, some toughening is observed within the first 10\AA of crack extension, and this emerges from non-dislocation mechanisms. Along the crack front, there is increasing structural disorder with increasing applied load. The crack growth is not uniform, with intact ligaments bridging the crack tip, voids, and uneven crack surfaces. Both cracks eventually cleave and extend uninterrupted through the remainder of the samples at approximately $1.2K_{IC}$.

5.2.2 Prismatic

In both prismatic orientations, basal $\langle \mathbf{a} \rangle$ dislocation emission is observed to accompany crack cleavage. In the prismatic I orientation (Fig. 5.4), a partial dislocation is readily emitted from the initially stable crack tip. The crack eventually cleaves through the sample, interrupted only by an intermediate period of toughening ($\sim 20\% K_{IC}$) after $\sim 50\text{\AA}$ of crack extension. Dislocation emission normally produces a blunted crack tip due to the creation of a stacking fault. However, despite multiple emission events, the prismatic I crack tip remains very sharp with minimal structural disorder accumulated ahead of the crack tip.

In comparison, the prismatic II crack tip can initially cleave somewhat depending on

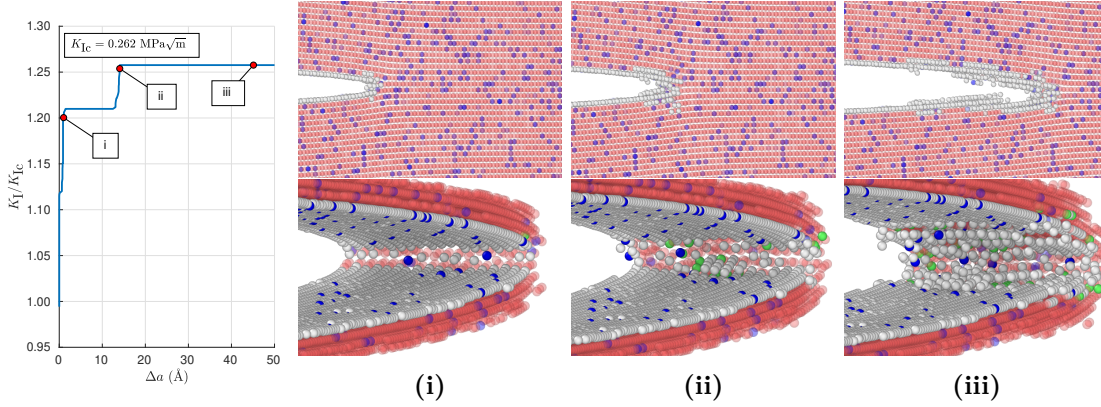


Figure 5.3: A basal II (0001)[$\bar{1}010$] orientation crack in a random Mg-Y alloy under mode I loading. Left-most: normalized R-curve with points of interest corresponding to (i)-(iii) indicated in red. In (i)-(iii): the plane projection (upper) and perspective view (lower) of the crack tip is provided. Bulk atoms in perspective view are removed for clarity. Atoms are colored according to composition and structure: hcp Mg (red), fcc Mg (green), non-coordinated Mg (white), and all solute Y atoms (blue).

the random crack tip environment, which for the particular case shown in Fig. 5.5 is $\sim 20\text{\AA}$. In general, multiple emission events concentrated at the crack tip quickly blunt and halt any initial crack extension. The crack significantly toughens ($\sim 60\%$ K_{Ic}) with some crack extension (partially due to the kinematics of the emission events at the crack tip) before it becomes unstable to growth at $\sim 50\text{\AA}$ of crack growth, which resharpens the crack tip. The new crack surfaces are rough and resemble the basal crack surfaces (Fig. 5.2 and 5.3).

In both prismatic orientations, dislocations emit as leading partials from the current crack tip position, rather than as trailing partials at a prior emission point in the crack history. This agrees with the LEFM prediction of $K_{Ie, trail} \gg K_{Ie}$. A sequence of alternating partials, emitted from both upper and lower crack surfaces, remain in the wake of an advancing crack as the partial dislocations are tethered to the crack by the stacking fault. This behavior is deemed quasi-brittle because it does not produce far-field plasticity.

A significant number of dislocations accumulate along the crack path of both prismatic orientations. However, it is the dislocations nearest to the current crack tip position that contribute most of the shielding; prior emission events left behind in the crack wake provide minimal toughening. The R-curves closely follow the computed shielded critical intensities at the crack tip (K_{Ic}^{tip} and K_{Ie}^{tip}), which are determined using the dislocation/crack tip configurations observed in the simulations. In the particular prismatic II case shown (Fig. 5.5), K_I^{app} briefly exceeds K_{Ic}^{tip} at $\sim 50\text{\AA}$, so neither crack tip mechanism is predicted to be energetically limited, yet the crack remains stable. This indicates the presence of additional dissipative mechanisms that are not quantitatively captured by the continuum theory, which will be discussed later.

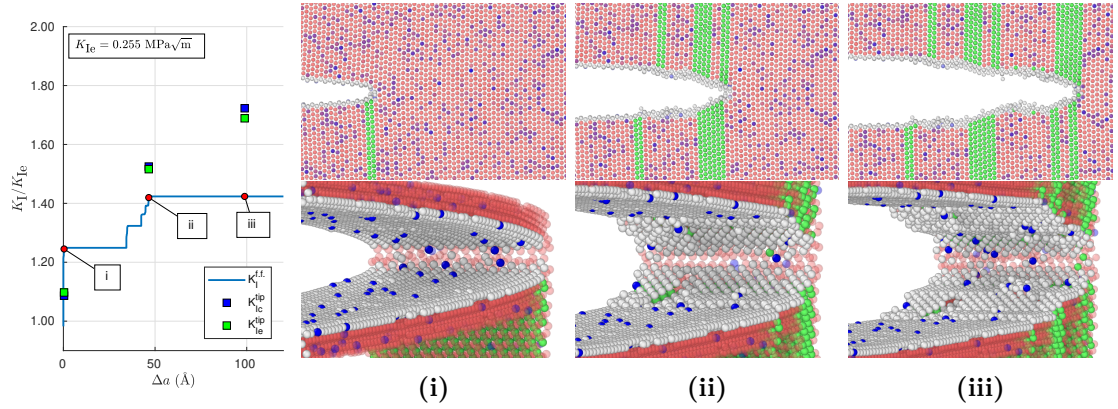


Figure 5.4: A prismatic I $(\bar{1}010)[1\bar{2}10]$ orientation crack in a random Mg-Y alloy under mode I loading. Left-most: normalized R-curve with points of interest corresponding to (i)-(iii) indicated in red. The shielded critical stress intensity factor at the crack tip is calculated for cleavage (K_{Ic}^{tip}) and emission of a leading partial (K_{Ie}^{tip}) for the observed dislocation/crack tip configuration at each point. In (i)-(iii): the plane projection (upper) and perspective view (lower) of the crack tip is provided. Bulk atoms in perspective view are removed for clarity. Atoms are colored according to composition and structure: hcp Mg (red), fcc Mg (green), non-coordinated Mg (white), and all solute Y atoms (blue).

In both orientations, the shielding is predominately mode I ($\sim 10\% K_I^{app}$) because the approximate symmetry of the dislocation configuration across the crack plane minimizes the mode II contribution ($\sim 2\% K_I^{app}$). Recalling Eq. (2.17), mode I shielding contributes equally to both cleavage and emission criteria, but mode II shielding only contributes to the emission criteria. Consequently, shielding should not drive changes between brittle and ductile intrinsic behavior unless the crack tip competition is close, i.e. on the order of mode II shielding, for example in prismatic I. Correspondingly, the relationship between the shielded stress intensities for prismatic I in Fig. 5.4 evolves over the crack path, with the crack tip competition $K_{Ie}^{tip} < K_{Ic}^{tip}$ first reversing to $K_{Ie}^{tip} > K_{Ic}^{tip}$ and then back again. In contrast, the intrinsic crack tip competition in prismatic II is not as subtle, and so no such reversal of the shielded crack tip competition is observed.

5.2.3 Pyramidal

The pyramidal orientations are the most ductile among the crack configurations studied here, emitting basal $\langle a \rangle$ dislocations. In the pyramidal I orientation (Fig. 5.6), partial dislocations are sequentially emitted in the same direction but on non-adjacent planes. The partial dislocations stay within the vicinity of the crack tip and create a growing array of partials with associated stacking faults, as also seen in pure Mg [93]. The region of stacking faults is fcc in character but does not form a twin structure across the inclined basal plane. This behavior does not produce far-field plasticity and so is deemed quasi-brittle. Each emission event corresponds to an increment of toughening in the R-curve (each approximately $0.25K_{Ie}$) over the first 20\AA of crack extension. The

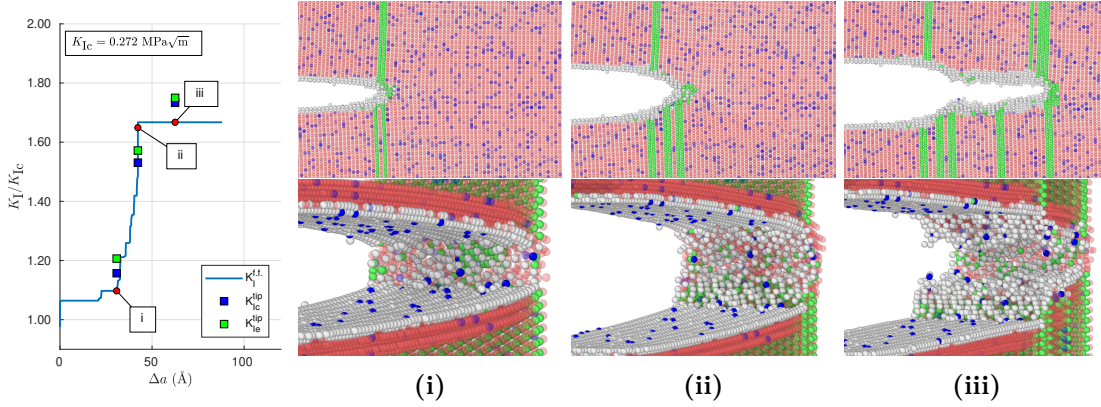


Figure 5.5: A prismatic II $(\bar{1}2\bar{1}0)[\bar{1}010]$ orientation crack in a random Mg-Y alloy under mode I loading. Left-most: normalized R-curve with points of interest corresponding to (i)-(iii) indicated in red. The shielded critical stress intensity factor at the crack tip is calculated for cleavage (K_{Ic}^{tip}) and emission of a leading partial (K_{Ie}^{tip}) for the observed dislocation-crack tip configuration at each point. In (i)-(iii): the plane projection (upper) and perspective view (lower) of the crack tip is provided. Bulk atoms in perspective view are removed for clarity. Atoms are colored according to composition and structure: hcp Mg (red), fcc Mg (green), non-coordinated Mg (white), and all solute Y atoms (blue).

crack front remains quite ordered throughout loading, as compared to the basal and prismatic orientations.

In the pyramidal I geometry, crack tip blunting associated with dislocation nucleation along one slip plane orientation generates a wedge-shaped tip geometry that promotes brittle behavior [97]. The crack in Fig. 5.6 finally extends through the sample at approximately $1.6K_{Ie}$, with the new crack plane becoming aligned with the c-axis following the wedge surface (Fig. 5.6-(iii)). The same reorientation of the crack plane is observed in pure Mg. However, this behavior may be a spurious, resulting from (i) uncertainty in applying the stress intensity and displacement fields for a sharp crack to the wedge geometry, and/or (ii) boundary effects interacting with the array of partials which will be discussed in the following. Nevertheless, the LEFM prediction determined before the crack reorientation (Fig. 5.6-(ii)) compared to after the crack reorientation (Fig. 5.6-(iii)), considering the dislocation shielding with respect to the reoriented crack plane, reflects the observed change from emission to cleavage behavior.

In the pyramidal II orientation (Fig. 5.7), the emission of trailing partial dislocations is observed, in agreement with the LEFM prediction of $K_{Ie, trail}^{tip} < K_{Ie}^{tip}$. The resulting full dislocations, untethered to the crack by the stacking fault, move far away from the crack tip and contribute to the far-field plasticity (which is not modeled here). This behavior is thus ductile. Larger increments of toughening in the R-curve (each approximately $0.5K_{Ie}$) correspond to the emission of full dislocations in the first 20\AA of crack extension. A mild wedge-shaped tip geometry arises from crack tip blunting. Although continued emission is predicted from LEFM, the crack instead extends uninterrupted through the

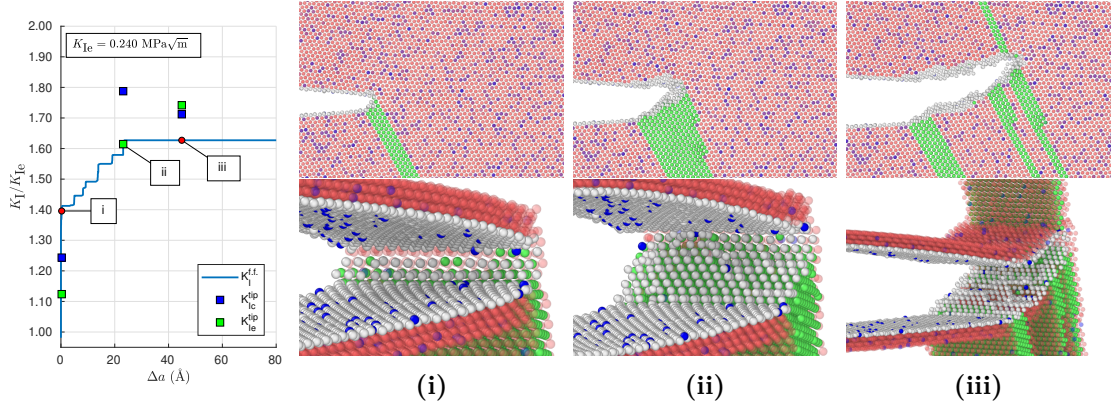


Figure 5.6: A pyramidal I $(\bar{1}011)[1\bar{2}10]$ orientation crack in a random Mg-Y alloy under mode I loading. Left-most: normalized R-curve with points of interest corresponding to (i)-(iii) indicated in red. The shielded critical stress intensity factor at the crack tip is calculated for cleavage (K_{Ic}^{tip}) and emission of a leading partial (K_{Ie}^{tip}) for the observed dislocation-crack tip configuration at each point. In (i)-(iii): the plane projection (upper) and perspective view (lower) of the crack tip is provided. Bulk atoms in perspective view are removed for clarity. Atoms are colored according to composition and structure: hcp Mg (red), fcc Mg (green), non-coordinated Mg (white), and all solute Y atoms (blue).

remainder of the sample at approximately $1.4K_{Ie}$, initiating at the lower wedge corner, with notably growing structural disorder at the crack tip.

Both pyramidal orientations are intrinsically ductile, with the eventual cleavage arising due to boundary effects. That is, continued emission and blunting is expected from these orientations but the movement of dislocations away from the crack tip artificially restricted by the simulation boundary. Pinning of the first dislocation at the boundary then leads to formation of a pile-up of dislocations as emission continues. The pile-up extends back toward the crack tip, changing the local stress intensity due to shielding.

Having dislocations closer to the crack tip should improve intrinsic ductility, as dislocations in the pyramidal orientations produce strong shielding in mode I and milder anti-shielding mode II, tilting the crack tip competition more in the favor of emission, i.e. $K_{Ie}^{tip}(\text{restricted}) < K_{Ie}^{tip}(\text{unrestricted}) < K_{Ic}^{tip}$. However, further emission events are suppressed by the pinned pile-up, which is controlled by the repulsive nature of the dislocations. Unlike in the infinite material, at some point the pile-up cannot move away from the crack tip to accommodate the addition of another dislocation. As a result, the material is observed to switch to cleavage fracture, which is spurious as these orientations are intrinsically ductile.

This boundary effect is stronger in the pyramidal II orientation, as emission occurs on the same slip plane and so the pile-up phenomena accumulates quickly. Increasing the simulation cell size, for example increasing the y -dimension to allow the full dislocations to move further away from the crack tip, does not appreciably change the R-curve. More

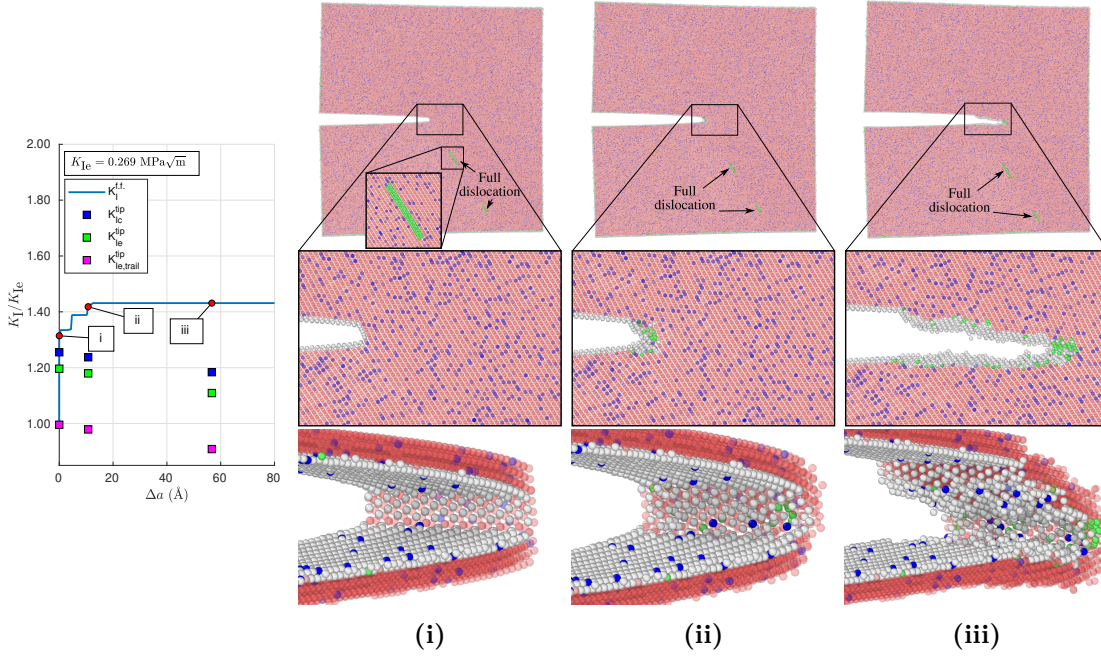


Figure 5.7: A pyramidal II $(\bar{1}\bar{1}2)[\bar{1}010]$ orientation crack in a random Mg-Y alloy under mode I loading. Left-most: normalized R-curve with points of interest corresponding to (i)-(iii) indicated in red. The shielded critical stress intensity factor at the crack tip is calculated for cleavage (K_{Ic}^{tip}), emission of a leading partial (K_{Ie}^{tip}), and emission of a trailing partial ($K_{Ie, trail}^{tip}$) for the observed dislocation-crack tip configuration at each point. In (i)-(iii): the plane projection of the simulation cell (upper), and plane projection (middle) and perspective view (lower) of the crack tip is provided. Bulk atoms in perspective view are removed for clarity. Atoms are colored according to composition and structure: hcp Mg (red), fcc Mg (green), non-coordinated Mg (white), and all solute Y atoms (blue).

dislocations are able to be emitted, resulting in a larger pile-up and more toughening of the R-curve, before the same switch to cleavage fracture. Thus, the far-field plasticity which is not modeled here is necessary to produce the expected ductile behavior. This is a limitation of the atomistic simulations presented in this study.

5.2.4 Tensile twin

Cracks in both tensile twin orientations show fully brittle behavior with no dislocation emission (Fig. 5.8 and 5.9), as predicted by LEFM. There is no predicted difference in the behavior between pure Mg and Mg-Y. The predicted K_{Ie} for the tensile twin II orientation is very high, and so there is little possibility that any solutes could inhibit brittle fracture of this configuration. In the simulations, unlike the basal orientations, no toughening is observed in either twin orientation during the early stages of crack extension despite some structural disorder at the crack tips. The crack growth is mostly uniform. The cracks extend through the sample along a relatively straight path closely following the twin boundary. Brittle fracture along twin interfaces thus remains among

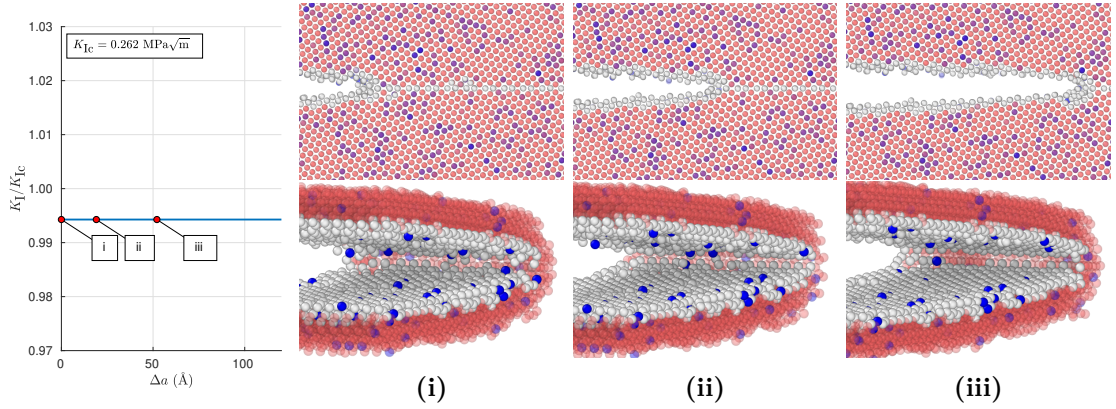


Figure 5.8: A tensile twin I $(\bar{1}01\bar{2})[\bar{1}2\bar{1}0]$ orientation crack in a random Mg-Y alloy under mode I loading. Left-most: normalized R-curve with points of interest corresponding to (i)-(iii) indicated in red. In (i)-(iii): the plane projection (upper) and perspective view (lower) of the crack tip is provided. Bulk atoms in perspective view are removed for clarity. Atoms are colored according to composition and structure (PTM=0.1): hcp Mg (red), fcc Mg (green), non-coordinated Mg (white), and all solute Y atoms (blue).

the most detrimental modes of fracture in Mg alloys.

5.3 Structural disorder of the crack tip

One of the key differences in the alloy compared to pure Mg is the delayed onset of crack growth or dislocation emission with respect to the intrinsic critical stress intensity K_{Ic} or K_{Ie} in almost all of the orientations studied. Toughening prior to dislocation activity, if any, is observed in the R-curves in Fig. 5.1, and this indicates the presence of additional energy-dissipative mechanisms from non-dislocation phenomena.

Recall in the setup of a K -test simulation that an initial relaxation of the system locally adjusts the lattice and relaxes the misfit fields, and then the system is relaxed again after the crack is opened. The random Y atoms on the surfaces of the opened crack are typically displaced outwards from the free surface, locally modulating the LEFM crack geometry. The positions of the neighboring Mg atoms are then modified as well to achieve stable mechanical equilibrium of all the atoms. The largest lattice distortions are observed in the immediate vicinity of the crack tip where the crack strain fields are also very large. The local distortions of the crack tip lattice is intrinsic to the alloy, and so are not present in any crack tip in pure Mg (e.g. in Ref. [93]).

In the initial opened crack configuration, the lattice distortions along the crack front include solute-induced interactions between atoms on opposing crack surfaces, which intrude upon the distinct separation between the atomic layers forming the crack tip (Fig. 5.10). As a result, the sharpness of the crack tip is effectively reduced, and the preferable decohesion pathways of the crack tip atoms are stochastically modified. Geo-

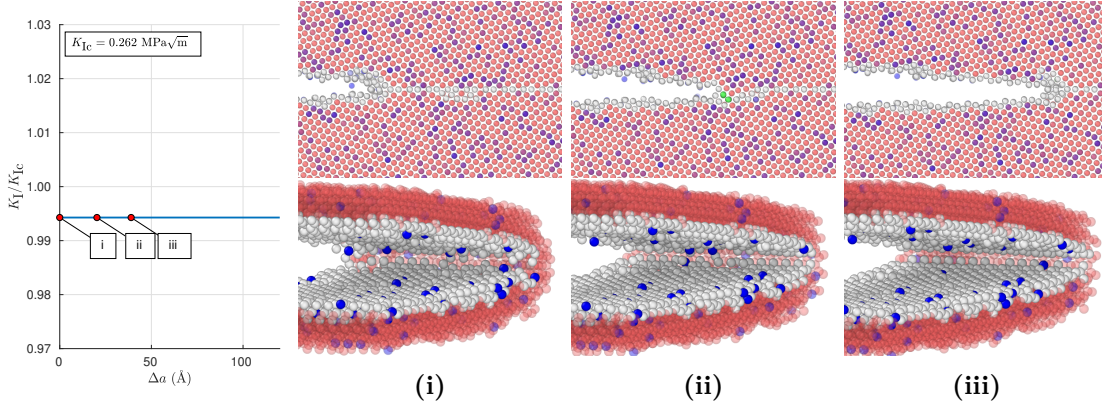


Figure 5.9: A tensile twin II $(10\bar{1}2)[1\bar{2}10]$ orientation crack in a random Mg-Y alloy under mode I loading. Left-most: normalized R-curve with points of interest corresponding to (i)-(iii) indicated in red. In (i)-(iii): the plane projection (upper) and perspective view (lower) of the crack tip is provided. Bulk atoms in perspective view are removed for clarity. Atoms are colored according to composition and structure: (PTM=0.1): hcp Mg (red), fcc Mg (green), non-coordinated Mg (white), and all solute Y atoms (blue).

metrically, the reduction of sharpness is beneficial for increasing fracture resistance [97]. The initial lattice distortion of the crack tip is strongest in the basal orientations. Comparatively, in the pyramidal orientations, as a dislocation is emitted from the initial crack tip at K_{Ie} , the resulting blunting increases the separation between the crack surfaces, forcing the full decohesion of any such interactions across the crack surfaces. Thus, dislocation emission typically minimizes the solute-induced structural disorder in the crack tip. This restoring effect is particularly demonstrated by pyramidal I (Fig. 5.6), where the structural disorder of the crack tip is minimal due to consecutive emission events.

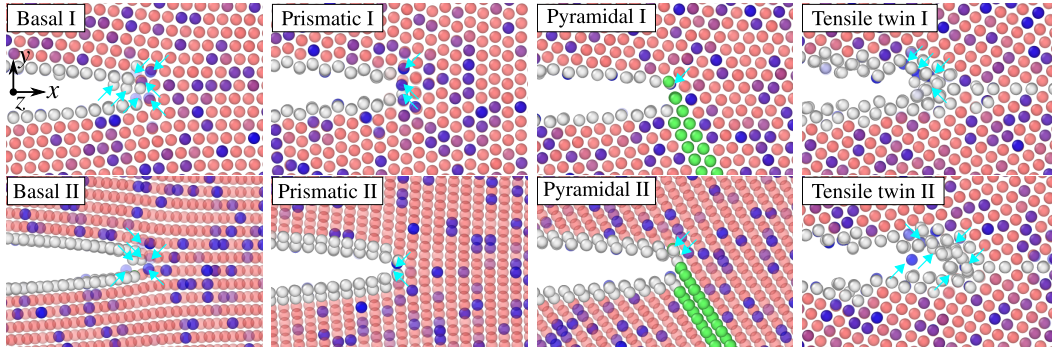


Figure 5.10: Plane projection (x - y) of crack tip configurations in Mg-Y around the intrinsic stress intensity K_{Ic} , K_{Ie} . Arrows guide the eye to the shifted atom positions distorting the lattice in the vicinity of the crack tip due to the presence of random solute atoms.

The structural disorder of a stable crack tip accumulates with further applied loading. In Fig. 5.11, new surface forms around the solute-induced interactions between atoms on opposing crack surfaces as the applied load is incremented in the simulation. A volume of the crack tip lattice rigidly displaces relative to its neighbors, resembling the slip

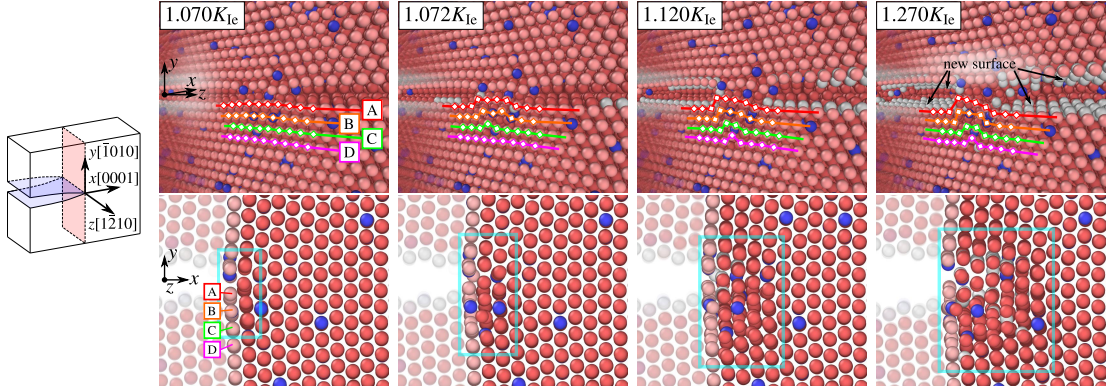


Figure 5.11: Plastic lattice disorder in the vicinity of the crack tip grows over $\Delta K_I = 0.20K_{Ic}$ ($K_{Ic} = 0.255 \text{ MPa}\sqrt{\text{m}}$) for a Mg-Y crack in the prismatic I ($\bar{1}010$)[$1\bar{2}10$] orientation. Shifting of atomic lines in the y - z plane (colored lines) result in change of atomic neighbors, providing an opportunity for atoms to shift in the x direction due to the offset in the lattice. The boxed region in the x - y plane is provided to guide the eye to the growing volume of lattice distortion ahead of the crack front. Atoms are colored according to composition and structure: hcp Mg (red), non-coordinated Mg (white), and all solute atoms (blue).

of a highly localized edge dislocation from the crack tip. The resulting changes of the atomic first-neighbors further modify the preferable decohesion pathways of the atoms in the distorted lattice, which in turn modify the behavior of the atoms at the boundary between the distorted and undistorted regions. The process iterates as the applied load is incremented, continuously affecting the atoms just beyond the expanding volume of distorted lattice. As a result, an irreversible region of structural disorder – an atomistic process zone – grows ahead of the crack front due to the response of the structural disorder to loading of the crack. This process is energy-dissipative, adding to the overall energy required to create new surface, and so produces toughening.

The structural disorder of the crack tip also leads to unpredictability in the cleavage path. Due to the stochastic changes to the preferable decohesion paths of the atoms in the distorted lattice, voids and intact ligaments bridging the crack tip are observed in the process of cleavage (Fig. 5.12). The crack tip follows alternative cleavage paths which emerge along the crack front. The resulting crack growth is non-uniform, evident from the rough surfaces typically left in the wake of a cleaving crack tip. At the macroscopic level, crack bridging and deflection are known sources of extrinsic toughening to brittle materials [172]. Crack deflection can produce significant shielding proportional to the roughness of the resulting crack surfaces, and has been shown to improve the macroscopic fracture toughness of brittle ceramics by up to 3 times [172]. A parallel can be drawn to similar behavior here at the atomistic level, contributing to the non-dislocation toughening observed in the alloy, particularly in the basal orientations. The twin boundary is a preferential cleavage path compared to the surrounding pyramidal-oriented bulk crystal, minimizing crack deflection. Although some structural disorder of the crack tip is present in both twin orientations, there is no obvious toughening of

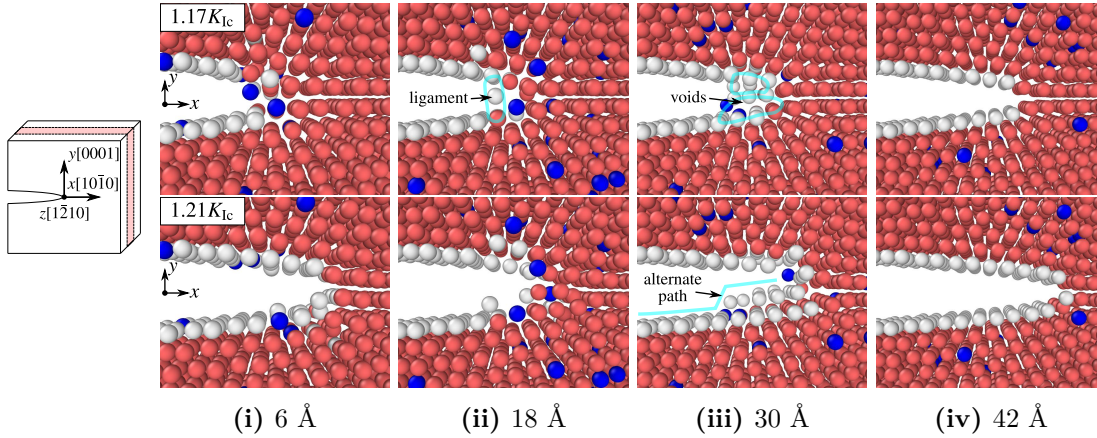


Figure 5.12: Evolution of the crack tip environment in a basal I (0001)[$\bar{1}210$] orientation over an increment of $\Delta K_I = 0.04K_{Ic}$ ($K_{Ic} = 0.262\text{MPa}\sqrt{\text{m}}$) illustrated using 12\AA thick slices centered at 6, 18, 20, and 42\AA along the crack front. Annotations in light blue are provided to guide the eye. Atoms are colored according to composition and structure: hcp Mg (red), non-coordinated Mg (white), and all solute atoms (blue).

the R-curve due to limited ability to disorder the boundary and explore other cleavage paths.

In pure Mg at $T = 0\text{ K}$, a single stacking fault, infinite in the periodic z dimension, instantaneously extends and the crack tip is blunted [93]. The structural disorder apparent in the alloy influences dislocation emission by distorting the geometry of emitted dislocations due to statistical fluctuations along the crack front. For example, instead of the emission of a single dislocation extending along the entire crack front, the simultaneous emission of multiple leading partials from a disordered crack tip is observed on occasion (Fig. 5.13). An emitting dislocation can also be partially pinned along a stretch of the crack front (Fig. 5.14) preventing instantaneous emission. In these cases, given sufficient increase of the applied load, either (i) the pinned dislocation can overcome the structural disorder, fully unpin from the crack front, and move away from the crack tip or (ii) the structural disorder amplifies the boundary effect by inhibiting dislocation emission and producing brittle crack behavior (for example, as seen in pyramidal II in Fig. 5.5).

The structural distortions at the crack tip could be due to artifacts in the interatomic potential. However, the misfit volume of Y in the lattice is large, and is captured accurately by the potential. Thus, large distortions introduced by Y atoms in the lattice, and near the surface and crack tips, can be expected to introduce distortions and local stress fields that can make the crack deviate from the ideal behavior. Thus, some effects here may be qualitatively realistic although quantitatively uncertain.

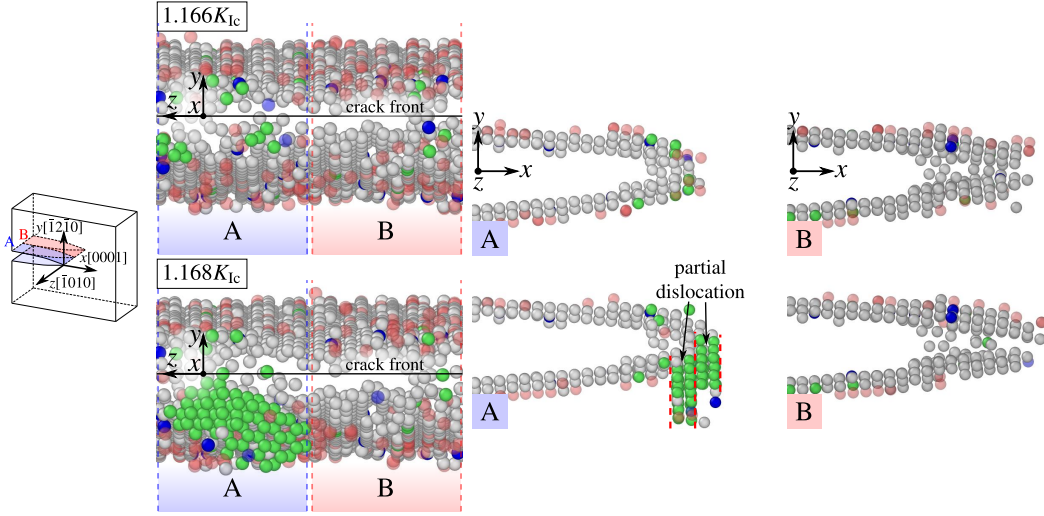


Figure 5.13: Dislocation emission from the disordered crack tip in a prismatic II $(\bar{1}2\bar{1}0)[\bar{1}010]$ orientation ($K_{Ic} = 0.272\text{MPa}\sqrt{\text{m}}$). Two leading partials are partially pinned along the crack front (section B). Bulk atoms are removed for clarity. Atoms are colored according to composition and structure: hcp Mg (red), non-coordinated Mg (white), fcc Mg (green), and all solute atoms (blue).

5.4 LEFM as a predictor of crack tip behavior

In spite of the stochastic complexity introduced at the crack tip due to the random solutes, LEFM remains quite a good predictor of the overall crack behavior of Mg-Y. Specifically, LEFM predicts an overall improvement of intrinsic ductility by alloying, showing good agreement with the atomistic simulations in all crack orientations by capturing even subtle changes ($< 5\%$) to the crack tip competition (Table 5.1).

The subsequent crack behavior observed in the simulations is also reasonably well-described by the relative values of the applied load K_I^{app} and the shielded stress intensities K_{Ic}^{tip} and K_{Ie}^{tip} . That is, the R-curves in Fig. 5.2 - 5.7 generally follow the evolution of the shielded critical stress intensities, i.e. toughening when K_I^{app} remains less than the critical stress intensity.

The stochastic solute-induced phenomena discussed previously cannot be directly evaluated with LEFM. They do not change the intrinsic behavior of the alloy but generally contribute some additional toughening. Most notably, the intrinsically brittle basal cracks, where there is no dislocation toughening, are initially toughened beyond the critical stress intensity predicted by LEFM by $10 - 20\% K_{Ic}$. In comparison, intrinsically ductile orientations are initially toughened up to $40\% K_{Ie}$, but mainly due to dislocation shielding consistent with LEFM predictions.

The performance of LEFM as a quantitative predictor is affected by the character of the crack tip. The structural complexity of the alloy crack tip violates a primary assumption

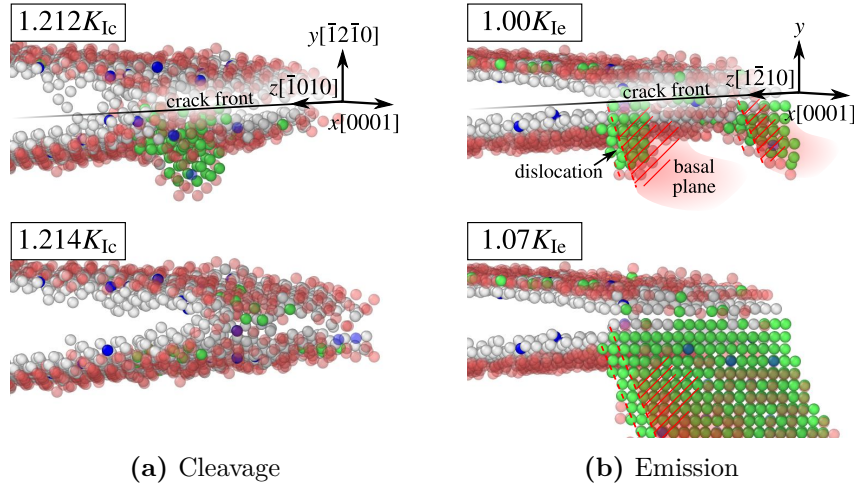


Figure 5.14: Response of a partially pinned dislocation nucleated from disordered crack tips in the Mg-Y alloy. (a) In the prismatic II $(\bar{1}2\bar{1}0)[\bar{1}010]$ orientation ($K_{Ic} = 0.272\text{MPa}\sqrt{\text{m}}$) cleavage occurs before dislocation can unpin. (b) In the pyramidal I orientation $(\bar{1}011)[1\bar{2}10]$ ($K_{Ie} = 0.240\text{MPa}\sqrt{\text{m}}$), dislocation can fully emit from the entire crack front on the basal plane. Bulk atoms are removed for clarity. Atoms are colored according to composition and structure: hcp Mg (red), fcc Mg (green), non-coordinated Mg (white), and all solute atoms (blue).

of the LEFM theory, which requires an atomistically sharp crack tip with a straight crack front. Instead, as seen in the simulation results in Sec. 5.2, the crack tip is generally disordered and crack growth is uneven compared to an ideal crack. Additionally, large geometric changes to the crack tip, for example in the pyramidal orientations (Fig. 5.6 and 5.7), affect the LEFM predictions due to a change of the crack tip singularity. Sharp corners act as alternative stress concentrators provoking crack initiation and/or reorientation [97] as is observed in the simulations, which is not considered in the LEFM theory. Nonetheless, LEFM captures the major trends of the crack tip behavior, and so remains an invaluable tool to assess alloy behavior.

5.5 Summary

We have studied the mode I fracture behavior of a random Mg-3at%Y alloy for a range of crack orientations using atomistic simulations to investigate the solute effect on fracture behavior. Alloying with Y changes the intrinsic ductility for several crack orientations from brittle to ductile, leading to significant toughening by dislocation emission. The stochastic crack tip environment leads to variance in the crack tip geometry, crack behavior, and the R-curve between different realizations of the same crack orientation. Solute-induced crack tip phenomena stochastically influence cleavage and dislocation emission mechanisms, providing additional toughening to the fracture resistance of the alloy. However, the solute effect does not change the intrinsic behavior of a given crack orientation. Although cleavage on several systems is largely prevented, Mg-Y alloys re-

main prone to brittle basal fracture and fracture along twin interfaces, since alloying does not fundamentally change the highly intrinsically brittle nature of these orientations.

The analysis and simulations presented here are conducted at $T = 0$ K. Material properties entering the fracture theory (elastic constants, surface and unstable stacking fault free energies) are temperature dependent, generally decreasing with increasing temperature. Whether these property changes, which decrease both K_{Ic} and K_{Ie} , lead to a change from brittle to ductile behavior requires detailed knowledge of the temperature dependence, which is beyond the scope of this paper. Dislocation nucleation is also a thermally activated process, and so can occur at finite rates at applied stress intensities below K_{Ie} . This makes intrinsic ductility more likely in cases where cleavage and emission conditions are close. However, such effects are unlikely to change the intrinsic behavior of basal plane fracture because K_{Ic} is far below ($> 30\%$) K_{Ie} at $T = 0$ K. Our overall conclusions here likely apply to Mg alloys at finite temperatures.

We have shown that alloying with Y improves fracture resistance, but it is unable to fully ductilize the highly brittle base Mg to a degree where it can be freely used as a structural material. The key to improving Mg fracture properties lies with the targeted ductilization of the brittle basal crack orientations. Large energetic changes are necessary to change the basal crack tip conditions from brittle to ductile. This poses a significant requirement on candidate solutes at low solute concentrations: the solute must increase the basal surface energy and/or decrease the pyramidal unstable stacking fault energies to promote emission. However, forthcoming work shows that while some solutes can transform Mg into a plastically ductile material, increasing the solute concentration beyond some limit can lead to a transition back to low ductility. Thus, better overall performance (plastic ductility and fracture toughness) may not be achievable simply by increasing solute concentrations. Nonetheless, other solute effects that provide modest toughening at the crack tip due to large misfit distortions may provide some improvement by increasing the operative K_{Ic} , enabling more far-field plasticity and higher toughness due to the “Rice valve effect”.

We have shown that LEFM is quite a good predictor of crack behavior in the alloy by predicting the intrinsic crack tip competition based only on the elastic constants, surface energies, and unstable stacking fault energies. These material properties can be accurately and relatively simply obtained using first-principles methods, e.g. Density Functional Theory. Thus, LEFM in conjunction with first-principles can be applied in a straightforward manner to other Mg-based systems, particularly those currently inaccessible due to lack of well-validated, if any, interatomic potentials. Our methodology streamlines the selection and analysis of potential alloying compositions from the vast composition space, and the continued systematic investigation of viable solute candidates to improve the fracture properties of Mg will be the subject of our future work.

6 A ductility criterion for bcc high entropy alloys

This chapter is extracted from the following publication

1. Mak, E., Yin, B., & Curtin, W. A. (2021). A ductility criterion for bcc high entropy alloys. *Journal of the Mechanics and Physics of Solids*, 152, 104389

The demand for metal alloys with superior structural and functional performance in industrial applications continues to increase, especially as the need for more-energy-efficient components becomes important. Recently, a new class of metal alloys has emerged, the High Entropy Alloys (HEAs) [4–6], which consist of many elemental components all at non-dilute concentrations and forming a single-phase polycrystalline material. Most HEAs studied to date are near-equiatomic and forming in fcc, bcc, or hcp crystal structures. One major classes of HEAs are the fcc late transition metal alloys in the Co-Cr-Fe-Mn-Ni-Cu family, with the original CoCrFeMnNi Cantor alloy being the most widely studied. Another major class of HEAs are the bcc refractory metal alloys in the Cr-Mo-Nb-Ta-V-W-Hf-Ti-Zr family. These bcc HEAs have high yield stresses at room temperature and some also have excellent strength retention up to high temperatures (1000 C or more) [173–178], making them attractive for high temperature applications. However, many of the alloys with impressive high temperature strength have low ductility at room temperature, limiting their formability and applications. While new theoretical advances are providing a quantitative understanding of the yield stress versus composition and temperature in these bcc HEAs [8–10], there is no understanding of the ductility of these alloys. The identification of novel alloy compositions with both high ductility at ambient temperatures and high strength at high temperatures is a goal that is driving current alloy development.

The bcc HEAs can have low ductility even in compression, suggesting that the failure is connected to fracture phenomena rather than traditional ductile failure mechanisms and necking failure according to the macroscopic Considère criterion. The refractory

bcc elements (Nb, V, Ta, Cr, Mo, W) also exhibit a relatively sharp brittle-to-ductile transition with increasing temperature, being quite brittle (low failure strain and low fracture toughness) at very low temperatures. Thus, the issue of ductility in bcc metals goes beyond the new class of HEAs. The brittle-to-ductile transition in the bcc elements has been attributed to rate-dependent plasticity effects and the shielding of a crack by surrounding dislocations [179, 180]. However, the brittle-to-ductile transition is quite abrupt whereas dislocation plasticity shows a smooth dependence on temperature and strain rate. In addition, there is no clear correlation between RT yield strengths and ductility. For instance, in W-Re the Ductile-Brittle Transition Temperature (BDTT) decreases steadily with increasing Re content, with a small tensile ductility at RT achieved at 25% Re, but the yield strength at 7 and 25% Re is comparable to or higher than pure W [181]. In the HEAs, MoNbTaW has very low ductility with a yield strength below 1 GPa [174] whereas MoNbTaTi has a yield strength above 1.2 GPa yet compression ductility of $\approx 25\%$ [182]. Examining stress levels beyond yield, the MoNbTaVW alloy supports a maximum stress of about 1.25 GPa at RT but has very low ductility [174] while NbTaTiW supports a stress of nearly 1.8 GPa at 20% strain [182]. It thus remains useful to pursue additional new lines of study to connect ductility to alloy composition.

Nearly all experimental studies of ductility of these bcc HEAs so far have been conducted in compression, in part due to the large sample sizes required for tensile testing, but also driven by an industrial interest in formability. We use compressive failure strains as a surrogate measure of the macroscopic ductility in the absence of available tensile data. There is some experimental evidence from very brittle HEAs (e.g. [174]) that the primary failure mode in compression is tensile rather than shear. The ductility in moderately ductile HEAs tends to be slip-dominated (e.g. [183]) and the eventual compression failure by fracture is generally an outcome of the interaction between the localization of the deformation, as expressed by macroscopic shear bands, and grain boundaries. The observed compressive ductility is thus related to an intrinsic resistance to tensile failure.

Here, we postulate that the ductility of bcc elements and alloys is controlled by the intrinsic fracture behavior at a sharp crack tip in the material. The intrinsic fracture behavior of a material is dictated by the competition between dislocation emission and brittle cleavage at an atomistically sharp crack tip. A material is intrinsically ductile if dislocation emission, occurring at a crack tip mode I stress intensity factor K_{Ie} , occurs prior to cleavage fracture, occurring at a crack tip mode I stress intensity factor K_{Ic} . Dislocation emission blunts the sharp crack tip and is the enabling mechanism for the subsequent onset of ductile failure mechanisms (void nucleation, growth, and coalescence ahead of the crack). Otherwise, a sharp crack remains sharp and propagates easily. Even if the crack remains sharp, the material can be deforming due to dislocation plasticity in the plastic zone around the crack tip, and this provides additional energy dissipation. The macroscopic toughness is thus higher than the Griffith cleavage value but remains far lower than the toughness achievable by ductile failure mechanisms.

Thus, the transition between high toughness (ductile mechanisms) and low toughness (cleavage plus surrounding plasticity) can be a sharp transition ultimately connected to the nanoscale crack tip behavior (cleavage or dislocation emission). Supporting this analysis approach, Ohr [46] reviewed TEM studies of crack tip deformation in Nb, Mo, and W at room temperature and reported extensive emission and blunting in Nb, moderate emission with cracking in Mo, and some emission with extensive cracking in W. While these experiments were not performed in pure mode I loading, with mixed mode loading argued to facilitate emission, the trend across these elements is consistent with the observed BDTT.

Based on the above postulate, we examine the intrinsic fracture behavior of refractory bcc elements and HEAs within the framework of Linear Elastic Fracture Mechanics (LEFM). The applicability of LEFM is first evaluated quantitatively using atomistic simulations on model HEAs alloys, putting the LEFM analysis on a firm quantitative foundation for bcc metals. We examine full dislocation emission only, neglecting twinning because it is not observed experimentally [46] and because the generalized fault surfaces for the metals studied here show no stable stacking faults that would enable twinning mechanisms. Through correlation of the intrinsic fracture behavior and the macroscopic ductility of elemental Mo, Nb, Ta, V, and W, we then establish a criterion for room temperature ductility in bcc metals and alloys. The LEFM theory is then applied to HEAs. The relevant material properties (elastic constants, surface energies, unstable stacking fault energies) are obtained from first-principles and appropriately scaled interatomic potentials. Predictions are then made for many single-phase alloys in the Cr-Mo-Nb-Ta-Ti-V-W family that have been studied experimentally, and results agree well with experimental trends. Finally, we extend the analysis across a large composition range in the Mo-Nb-Ta-V-W and Mo-Nb-Ti families to identify promising alloys for future investigation.

Recently, Li et al. [184] has performed a very similar LEFM-based analysis on five selected HEAs using a different (less-accurate but more-efficient) first-principles method. They computed the ratio of emission to cleavage stress intensities and reported a trend of increasing K_{Ie}/K_{Ic} versus alloy Valence Electron Count (VEC). The alloys with lower K_{Ie}/K_{Ic} are experimentally ductile and those with higher K_{Ie}/K_{Ic} are experimentally brittle (low ductility). However, Li et al. did not examine the bcc elements, did not make a detailed comparison with experiments, did not execute a broader study across the composition space, nor did they validate the use of LEFM; all of these aspects are features of the current work that are complementary to the study of Li et al.. Very new work by Hu et al. [185] also adopted the same general framework and computed the ratio (surface energy)/(unstable stacking fault energy) that is a major factor in determining K_{Ie}/K_{Ic} . They analyzed one crack orientation (denoted 110/110 below) and developed a very nice reduced order model trained on extensive (but less-stringent) first-principles Density Functional Theory (DFT) computations of the relevant energies. They showed a correlation of the energy ratio with compressive failure strain across a

number of HEAs and examined a broad composition space. However, Hu et al. did not validate the LEFM, did not directly address the quantity K_{Ie}/K_{Ic} that involves additional elasticity factors, and did not study multiple crack orientations. The current work is thus complementary to the work of Hu et al. in these respects.

In this chapter, we apply the LEFM theory to predict intrinsic ductility and assess these predictions against trends in experimental ductility, first for several refractory bcc elements in Section 6.2 and then for many HEAs in Section 6.3. In Section 6.4, we extend the analysis to predict ductility over a broad array of HEAs compositions.

6.1 Intrinsic ductility in bcc crystals: cleavage vs dislocation emission

The LEFM theory and the critical stress intensities K_{Ic} and K_{Ie} were presented in Chapters 1 and 2. Recalling Eq. (2.11), the emission theory including the energy of surface step creation [48] reduces to the Rice relationship when $\gamma_s^e < 3.45\gamma_{usf}$, where γ_s^e is the surface energy of the emission plane. This condition is satisfied by all the materials studied here and so the Rice condition is used here. We remark again that the values of both K_{Ic} and K_{Ie} are expected to decrease with increasing temperature since elastic constants, surface, and fault energies are all temperature dependent. The ratio between K_{Ie} and K_{Ic} is thus expected to be minimally dependent on temperature, especially at RT for the high-melting-point refractory alloys of interest here.

Andric et al. [186] later analyzed so-called tension-shear coupling, wherein the USF is proposed to be reduced by the high tension at the crack tip, facilitating emission. They showed that there is no tension dependence to the USF in several fcc and hcp metals, and that there is no effect of tension stresses on emission in ideal mode II loading where the Rice criterion is directly applicable, so that the original Rice condition remains valid. While the dependence of the USF on tension in bcc metals has not been studied to date, there is no a priori basis for assuming such an effect and so tension/shear coupling is neglected here. Finally, we reiterate that twinning is not considered since it is not observed nor expected based on the generalized stacking fault energy surfaces of metals studied here.

For bcc crystals, it is the $\{100\}$ and $\{110\}$ planes that are typically favored for cleavage [187]. The crack orientations on these planes that most-favor mode I nucleation of edge dislocations are shown in Fig. 6.1. Since growth of a crack requires crack extension in all in-plane directions, the crack must encounter these most-favorable orientations for emission, and so it is these orientations for which the intrinsic ductility analysis must be applied.

For clarity in later discussion in this chapter, we will refer to crack orientations in terms

6.1. Intrinsic ductility in bcc crystals: cleavage vs dislocation emission

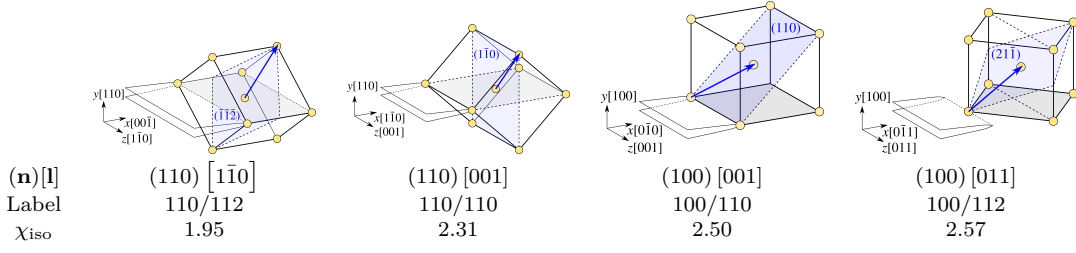


Figure 6.1: Geometry of crack orientations (n**)[**l**] favoring edge dislocation nucleation on the $a/2\langle 111 \rangle$ planes in mode I fracture.** (**n**) is the crack plane and [**l**] is the orientation of the crack front. For convenience, we label these orientations in terms of the cleavage and emission plane as indicated. For each orientation, the value of the elasticity parameter for an isotropic material χ_{iso} ($\nu = 0.33$) is also shown. Analysis reveals that the two orientations controlling ductility on the two cleavage planes are the 110/112 and 100/110 orientations.

of the cleavage and emission plane, e.g. orientation 110/112 refers to a crack on the $\{110\}$ (cleavage) plane and emission on the $\{112\}$ plane corresponding to a (110) $[\bar{1}\bar{1}0]$ crack front (see Fig. 6.1). The χ parameter in of the intrinsic ductility D (recall Eqs. (2.19) and (2.20)) is independent of the absolute value of the elastic constants, and only depends on the elastic anisotropy. For reference, Fig. 6.1 shows the isotropic value of χ for each orientation; note that the value for 110/112 is much lower than that for 110/110, making it intrinsically more favorable for emission. As we shall see, the 100/110 and 110/112 are the controlling orientations for ductile behavior in their respective crack planes. The degree of elastic anisotropy varies across the bcc materials considered here. For the 110/112 orientation, the effects of elastic anisotropy are weak so that $\chi/\chi_{\text{iso}} \sim 1$; the trends in intrinsic fracture behavior are then dominated by the surface and unstable stacking fault energies contained in $\tilde{\gamma}$. In contrast, for the 100/110 orientation, the effects of elastic anisotropy can increase χ up to $\chi/\chi_{\text{iso}} \sim 1.1$, which decreases the ductility relative to the isotropic limit. In general we consider full anisotropy in all results presented here.

In Chapter 3.4 we validated the theory using a set of EAM-type interatomic potentials by Zhou et al. [1]. These potentials are not quantitative for real materials but have well-defined alloy properties and so serve well as a set of model alloys. For each HEA, we use the average-atom potential [99] constructed from the elemental Zhou et al. [1] potentials because the LEFM only involves the average material properties. In this chapter, we do not yet consider the actual random atomistic environments along the crack front that exist in the real random alloy, which is beyond the scope of LEFM. Following in Chapter 7, for one of the averaged model alloys presented here, we consider the real random system and compare it to the average behavior studied here.

Direct K -test simulations of atomistic fracture commonly display unphysical behavior at the sharp crack tip. This is due to problems within the interatomic potentials despite producing reasonable and artifact-free material properties (elasticity, surface energy, usf energy) that control the crack tip phenomena of interest. This is particularly true for

bcc crystals, with bcc Fe well-studied in particular [98] and our own studies showing similar problems for the Zhou et al. family of potentials for both the bcc elements and their random alloys.

To overcome these difficulties, we use the Nudged-Elastic Band (NEB) method [89] to find the transition path and energy barrier between an initial sharp crack and a well-defined final state (either cleavage or dislocation emission) at an applied load K_I . In Chapter 3.4, we showed that over some range of applied K_I the transition path for both cleavage and emission is not influenced by the spurious crack tip behavior, and the evolving emission of a dislocation loop is very similar to that observed in other systems where there are no artifacts in the potentials. Thus, the physical emission path is separated from the spurious lower-energy paths by some energetic barriers such that the physical path can be studied without artifacts.

The energy barriers for cleavage and emission versus K_I as computed using the free-end NEB method and the average-atom EAM potentials for four HEAs over a range of K_I was shown in Fig. 3.7 for the most ductile orientation studied here, i.e. 110/112. Those results show that the $T = 0$ K LEFM values of K_{Ic} for cleavage and K_{Ie} for emission are accurate. The emission barrier is shown to always be larger than the cleavage barrier and is generally insurmountable even well-above K_{Ic} , so for $K_I > K_{Ic}$, the rate of thermally-activated cleavage is always much higher than emission. Thermal activation therefore does not change the underlying brittleness of these refractory HEAs as represented by the model EAM potentials. These atomistic studies show that thermal-activation effects can be largely neglected because, for brittle alloys where $K_{Ic} < K_{Ie}$, the cleavage barriers for $K_I > K_{Ic}$ are small and the emission barriers for $K_I < K_{Ie}$ are usually much larger than the cleavage barriers. The LEFM theory is thus used throughout the remainder of the work presented here.

6.2 Ductility criterion based on intrinsic fracture of bcc elements

The stable low temperature crystal structures of the refractory elements Mo, Nb, Ta, V, and W are bcc. The elements Ti and Zr that will later appear as constituents in various HEAs have an hcp structure at low temperatures and are only stable in the bcc structure at high temperatures or via alloying at low temperatures. We thus only consider Mo, Nb, Ta, V, and W here.

Fully-relaxed values of γ_s for the $\{100\}$ and $\{110\}$ surfaces and γ_{usf} for the $\{110\}$ and $\{112\}$ planes have been computed using DFT as implemented in VASP for the five elements of interest. Appendix A.3 provides important details about these computations. The elemental elastic moduli are also required, but it is well-established that the DFT-computed value of C_{44} is in poor agreement with experiments [188] (also see

6.2. Ductility criterion based on intrinsic fracture of bcc elements

Table 6.1: Material parameters of bcc refractory elements used in the LEFM analysis: the elastic constants C_{ij} , the relaxed surface energies γ_s and unstable stacking fault energies γ_{usf} . The Zener anisotropy ratio $a_r = 2C_{44}/(C_{11} - C_{12})$ is computed. The anisotropy parameter χ is also shown for all combinations of crack and emission planes, showing deviations relative to the isotropic values shown in Fig. 6.1.

Element	C_{11}	C_{12}	C_{44}	a_r	Plane	γ_s	γ_{usf}	χ	
	GPa					J/m ²	110	112	
Mo	450	173	125	0.90	100	3.250	–	2.416	2.433
					110	2.834	1.389	2.242	1.957
					112	–	1.390	–	–
Nb	253	133	31	0.52	100	2.310	–	2.233	2.287
					110	2.058	0.637	2.088	1.918
					112	–	0.752	–	–
Ta	266	158	87	1.62	100	2.490	–	2.715	2.827
					110	2.352	0.719	2.486	1.951
					112	–	0.829	–	–
V	238	122	47	0.81	100	2.381	–	2.233	2.282
					110	2.404	0.693	2.091	1.923
					112	–	0.793	–	–
W	533	241	199	1.37	100	4.026	–	2.529	2.576
					110	3.282	1.692	2.336	1.945
					112	–	1.714	–	–

Appendix A.2). Here, we therefore use the experimental elastic moduli [189–191]. The relevant material parameters are shown in Table 6.1.

As a first validation of the material parameters computed here, we compute the brittle fracture toughness of W in the 100/110 crack orientation to be $K_{Ic} = 1.950 \text{ MPa}\sqrt{\text{m}}$. The single-crystal fracture toughness data measured at 77 K, independent of the strain rate, is $(2.7 \pm 0.2) \text{ MPa}\sqrt{\text{m}}$ [3]. Extrapolating the fracture toughness data measured over many samples over a range of temperatures (see Fig. A.1) yields $K_{Ic} = 2.198 \text{ MPa}\sqrt{\text{m}}$. This agreement is good, well within the uncertainty of the extrapolation. Macroscopic experimental toughness also typically exceeds the theoretical K_{Ic} even in very brittle materials due to the formation of ledges/steps along the crack front and other defects. Such effects do not change the fundamental competition between cleavage and emission at the sharp crack tip, however.

Fig. 6.2a shows the computed K_{Ic} and K_{Ie} values for the 5 bcc elements studied here for all four orientations. The ductility index is $D = K_{Ie}/K_{Ic} > 1$ for all these metals over all four orientations (Fig. 6.2b). This is in agreement with the experimentally-established brittleness of all of these metals at very low temperatures. Each element has a brittle-to-ductile transition over a relatively narrow window of temperature typified by the Brittle-to-Ductile Transition Temperature (BDTT). We are interested in RT ductility, which is often characterized in terms of reduction of area at fracture. Ductile materials show a large reduction in the cross-sectional area prior to failure while brittle materials will fracture with little to no change in the area. In Fig. 6.2c, experiments at RT show

that Nb, V, and Ta reach an area of reduction at fracture of $> 90\%$ (BDTT $< \text{RT}$) [192]. These elements are considered fully ductile since they show area reductions similar to conventional ductile elements, e.g. Ni [193]. By the same measure, Mo becomes ductile around RT (BDTT $\sim \text{RT}$) and W is brittle at RT (BDTT $\gg \text{RT}$) [193]. Also shown in Fig. 6.2c are the deduced BDTT from other experiments [3, 194, 195], which are consistent with data on area reduction. The relative ductility as represented by the ductility index D computed from the DFT-based LEFM is $D(\text{Nb}) < D(\text{V}) \sim D(\text{Ta}) < D(\text{Mo}) < D(\text{W})$, which is qualitatively consistent with the RT experimental trends and the ordering of the BDTT values.

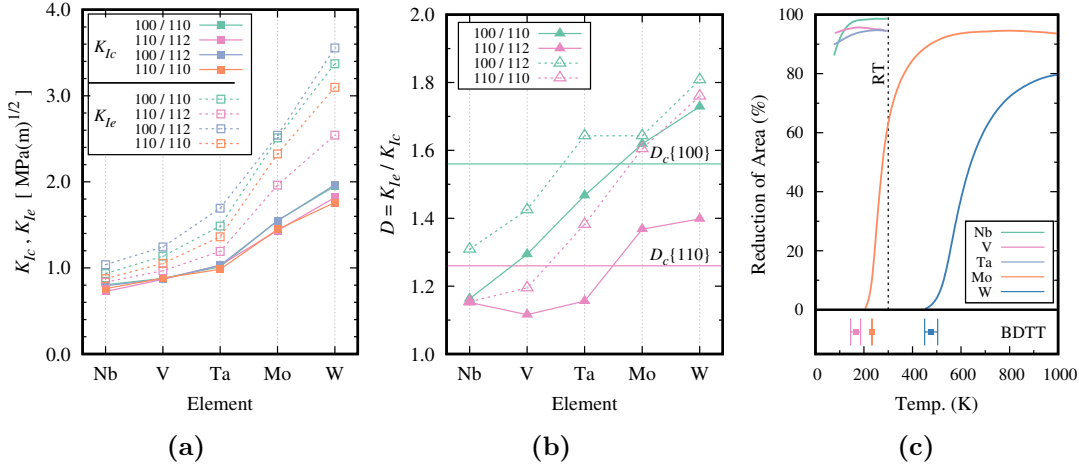


Figure 6.2: LEFM predictions of stress intensity and intrinsic ductility for 5 bcc elements and four crack orientations. (a) Predictions of K_{Ic} (solid lines) and K_{Ie} (dashed lines) using DFT-computed surface and USF energies and experimental elastic moduli. (b) Predicted ductility index $D = K_{Ie}/K_{Ic}$ for all cases. The proposed critical values $D_c\{110\} \approx 1.26$ and $D_c\{100\} \approx 1.56$ are also shown, selected to capture the experimental RT behavior (ductile or brittle); (c) Experimental reduction in cross-section area at tensile failure as a measure of RT ductility and the BDTT, from selected sources (see main text).

Our analysis shows that D is systematically lower (toward more ductile) for the 100/110 orientation on $\{100\}$ fracture plane and the 110/112 orientation on the $\{110\}$ fracture plane. Since any cleavage must be possible on the most ductile orientation of any fracture plane, it is the 100/110 and 110/112 orientations that control the ductility according to the intrinsic fracture criterion. In subsequent sections, we will therefore study these two orientations in depth.

We now address how we use the ductility index D computed at $T = 0$ K to understand ductility at RT. As noted, $D < 1$ is not satisfied by any of the elements, consistent with low- T experiments, but all elements do have a DBTT at higher temperatures. The ductility index does not predict a DBTT, and it is highly unlikely that the use of temperature-dependent material properties of refractory elements at RT will alter the K_{Ie}/K_{Ic} sufficiently to reach $D < 1$. To proceed, we therefore use the experimental observations of RT ductility to select a critical value of the ductility index D_c (one

6.2. Ductility criterion based on intrinsic fracture of bcc elements

value for each cleavage plane) that captures the experiments. From Fig. 6.2c, the RT experimental ductility observed in Nb, V, and Ta is clearly distinct from the absence of RT ductility in W. The ductility of Mo transitions around RT, but the exact conversion between the area of reduction to ductility is not well-defined. We conservatively select $D_c\{110\} \approx 1.26$ and $D_c\{100\} \approx 1.56$ to capture RT ductility in Nb, V, and Ta and relatively lower ductility in Mo and W, as shown in Fig. 6.2b. Ductility is only achieved if $D < D_c$ is satisfied for *both* fracture planes.

The selected RT D_c values represent a correlation only, and are larger than unity. The result of $D > 1$ for all the elements is consistent with very early estimates of Ohr [46]. There are several reasons why ductility (crack tip emission) could arise at finite T for $D > 1$ at $T = 0$ K. First, as discussed by Ohr, small amounts of mode II and/or mode III loading of the appropriate sign can facilitate emission relative to cleavage, reducing D . With isotropic elasticity, the effects of mode II and mode III loading can be assessed easily (also see Appendix A.4), and the ductility index of the mixed-mode loading D^{mix} derived as

$$\frac{D^{mix}}{D} = \frac{\sqrt{1 + (\frac{K_{II}}{K_I})^2 + \frac{1}{1-\nu}(\frac{K_{III}}{K_I})^2}}{1 \pm \frac{K_{II}}{K_I} \left(2 \csc \theta - 3 \tan \frac{\theta}{2}\right) \pm 2 \frac{K_{III}}{K_I} \csc \theta \tan \phi} \quad (6.1)$$

The ductility ratio still scales with the mode I ductility ratio, i.e. it still depends on the ratio of the USF energy and surface energy, but now also on the the magnitude and sign of the mixed mode components. Fig. 6.3 shows the fractional reductions in D for the most favorable signs of the mixed mode loadings for all four crack orientations in two cases ($K_{II}/K_I = \pm 0.1$; $K_{III} = 0$) and ($K_{II}/K_I = K_{III}/K_I = \pm 0.1$). In the latter case, $D_c\{110\}$ is reduced by $\approx 10\%$, bringing it close to unity while $D_c\{100\}$ is reduced by $\approx 30\%$, also bringing it close to unity. Particularly in polycrystals, this level of mode mixity for cracks best-oriented for mode I loading is modest. This would be the most likely explanation for ductility based on a purely mode I D_c . Second, some dislocation motion around the crack may also create additional mode II or mode III contributions, aiding ductility. Third, recent work on the double-kink nucleation barrier for screw dislocation motion in W has shown that anharmonic effects lower the barrier even at 400 – 600 K, and hence anharmonic effects may play a role in crack tip nucleation as well [196]. The latter two factors are beyond the scope of the present work. We show below that use of the selected values of D_c based on mode I analysis, although larger than unity, enables predictions of ductile and brittle behavior across a range of HEAs consistent with experimental observations to date.

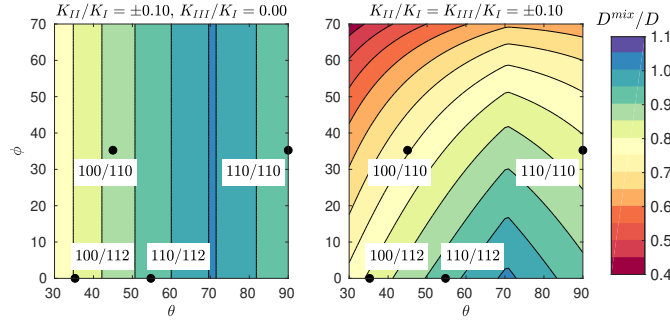


Figure 6.3: Mixed-mode isotropic ductility index normalized by the pure mode I ductility index for the various possible dislocation emission slip planes studied here (see Equation (6.1)). The kinks in the graphs arise due to changes in the signs of the mixed mode components that reduce the ductility index.

6.3 Ductility in High Entropy Alloys

6.3.1 Ductility of MoNbTaVW, MoNbTaW, and MoNbTi using first-principles inputs

For random HEAs, we use the same theoretical framework as applied to the elements but now using the average macroscopic properties of each alloy. Here, we first apply the LEFM theory to the equiatomic MoNbTaVW, MoNbTaW and MoNbTi HEAs using first-principles DFT material properties.

The theory requires the elastic constants, but in fact only requires the anisotropy ratio that enters the χ parameter. To our knowledge, there are no experimental studies of the elastic constants of these alloys beyond the polycrystalline averages, and hence no information on elastic anisotropy. As for the elements, DFT studies underestimate C_{44} [8]. The Zhou et al. EAM interatomic potentials were designed/fitted to the various bcc elements and so provide very good results for the alloys (see Appendix A.2). Specifically, the lattice constants agree well with experiments and both C_{11} and C_{12} agree well with DFT values. The C_{ij} including C_{44} obtained for the HEAs for the alloys are then also consistent with subsequent estimates of the polycrystalline moduli of the real alloys. We use the elastic constants predicted from these EAM potentials for the present HEAs, remembering that the predictions of D only depend on the elastic anisotropy and not on the absolute values of the elastic constants.

The theory also requires the surface and unstable stacking fault energies. We have computed the relaxed values for the various HEAs using first-principles DFT as implemented in VASP. We use large Special Quasi-random Structures (SQS) and examine several random realizations for some alloys. The computation of the unstable stacking fault energy requires some care due to the fact that atoms do not sit exactly on the ideal lattice sites in the bulk crystal. The details of our DFT methodology are discussed in Appendix A.3. Our results for the surface and USF energies are shown in Table A.5. Also shown are

recent results by [184] for two alloys obtained using the very different first-principles CPA-EMTO methodology that usually provides results in reasonable agreement with standard DFT implementations.

The DFT predictions for MoNbTaVW, MoNbTaW, and MoNbTi are shown in Fig. 6.4c. Classification of these HEAs as brittle or ductile according to our RT criterion $D_c\{100\}$ and $D_c\{110\}$ shows agreement with experimental ductility trends. MoNbTaVW and MoNbTaW are predicted to be brittle since $D > D_c$ for both orientations. Correspondingly, Senkov et al. [174] show that polycrystalline MoNbTaVW and MoNbTaW are quite brittle in RT compression with $< 3\%$ ductility. MoNbTi is predicted to be very close to the embrittlement criterion while experiments show moderate compression ductility. The predictions using the data of Li et al. [184] are also shown and are comparable, but higher than, our results for the 110/112 orientation but much lower for the 100/110 orientation, showing the need for standard DFT methods.

6.3.2 Ductility using scaled inputs from interatomic potentials

While the LEFM analysis requires only a few input parameters, the computational cost of fully-relaxed DFT studies on large SQS structures is significant and currently prohibitive for exploring many alloy compositions. Hence, here we seek an approximate approach that enables rapid assessment of many alloys. The approximate approach uses material parameters obtained by *scaling* the surface and USF energies predicted by the Zhou et al. EAM interatomic potentials [1] to our DFT results on several alloys. We then apply a scaling factor β to scale the EAM parameters for a much wider range of HEA compositions and make predictions of ductility using these scaled EAM inputs.

The Zhou et al. family of EAM potentials were fit to basic material properties (e.g. cohesive energy, lattice constants, elastic constants) but not to surface or USF energies. Thus, we first examine the predictions of these potentials for γ_s and γ_{usf} for the elements and for selected HEAs for which we have DFT data. Fig. 6.4a shows the ratio of fully-relaxed EAM to fully-relaxed DFT surface and USF energies for the elements Mo, Nb, Ta, V, and W. The EAM potential systematically underestimates the surface energies, with $\gamma_s^{\text{EAM}} \approx 0.8\gamma_s^{\text{DFT}}$. In contrast, the estimation of γ_{usf} by the EAM potential ranges from $0.8 - 1.2\gamma_{usf}^{\text{DFT}}$.

EAM results for the hcp elements Ti and Zr (not shown) deviate significantly from DFT for the $\{110\}$ surface energies ($\sim 40\%$) and USF energies ($\sim 80\%$). This is likely due to both inaccuracy of $T = 0$ K DFT for bcc Ti and Zr as well as inaccuracy of the EAM potentials that were fit to the hcp properties rather than to the bcc properties. We can thus expect that alloy compositions with high Ti and/or Zr content will be poorly described by the EAM potentials. With the exception of NbTiZr, we therefore avoid the study of alloys with Zr and restrict the Ti composition to 33.33% at most.

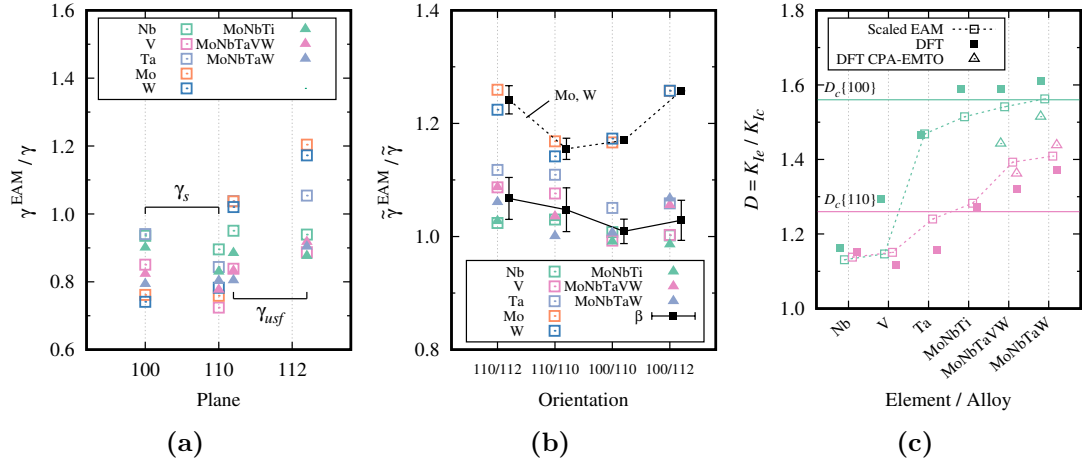


Figure 6.4: Fully-relaxed EAM material properties compared to fully-relaxed DFT material properties. (a) Ratio of EAM to DFT surface energy γ_s and USF energy γ_{usf} for several bcc elements and the MoNbTi, MoNbTaVW, and MoNbTaW HEAs. (b) Ratio of energies $\tilde{\gamma} = \sqrt{\gamma_{usf}/\gamma_s}$ entering the ductility analysis. The elements Mo and W stand out from among the other elements and the two HEAs due to the higher values of the USF for the EAM potential shown in (a). The average values for Nb, Ta, V, MoNbTi, MoNbTaVW, and MoNbTaW are shown, and are used as a scaling factor β (see text). (c) Comparison of scaled EAM ($\beta = 1.04$) versus DFT predictions of ductility for Nb, V, Ta, MoNbTi, MoNbTaVW, and MoNbTaW; some symbols slightly offset for visual clarity.

Fig. 6.4b shows the ratio of EAM to DFT values for the quantity $\tilde{\gamma}$ that enters the ductility condition. For the elements Nb, Ta, V, and HEAs MoNbTi, MoNbTaVW, and MoNbTaW, the ratios fall in a fairly narrow range. The ratios for elemental Mo and W are much higher, but these elemental deviations are not reflected in the values for the HEAs containing Mo and W up to 50% of the composition. Since even the MoNbTaVW and MoNbTaW alloys are observed and predicted to be brittle, alloys with higher Mo and W content are also likely to be quite brittle. We therefore consider scaling of EAM results to DFT results using the results for Nb, Ta, V, MoNbTi, MoNbTaVW, and MoNbTaW. For these materials, the energy ratio falls in a narrow range across all four orientations. We thus introduce a single scaling factor β relating the EAM energy ratio to the DFT energy ratio as

$$\beta = \frac{\sqrt{\gamma_{usf}^{EAM}/\gamma_{usf}}}{\sqrt{\gamma_{usf}^{EAM}/\gamma_s}} = \frac{\tilde{\gamma}^{EAM}}{\tilde{\gamma}} \quad (6.2)$$

averaged across all four orientations, leading to $\beta = 1.04 \pm 0.03$ with variations of $\pm 3\%$. The ductility index D for any alloy is then estimated using the EAM values for the alloy scaled by the factor β as

$$D = \frac{1}{\beta} D^{EAM} \quad (6.3)$$

Fig. 6.4c compares the estimated ductility indices using the scaled EAM data against

the actual DFT-based predictions for Nb, V, Ta, MoNbTaVW, and MoNbTaW. The agreement is generally good, preserving the ductility trends across these metals. As an aside, if the same β factor was applied to Mo and W, they would be predicted to be even less ductile than found using the DFT results.

We now apply the same procedure and scaling factor $\beta = 1.04 \pm 0.03$ to a wider range of HEA compositions. Fig. 6.5 shows the estimated ductility ratios for both orientations for a range of HEAs studied experimentally, with the $\pm 3\%$ uncertainty in β indicated. The available experimental data on ductility (maximum strain in compression) is also shown [178, 182, 183, 197–200], where arrows indicate experiments that were not continued until failure. The predictions across this scope of alloys fall into three categories: ductile ($D < D_c$ for both orientations), borderline ductile ($D \approx D_c$ for one orientation and $D < D_c$ for the other orientation) and brittle ($D > D_c$ for at least one orientation).

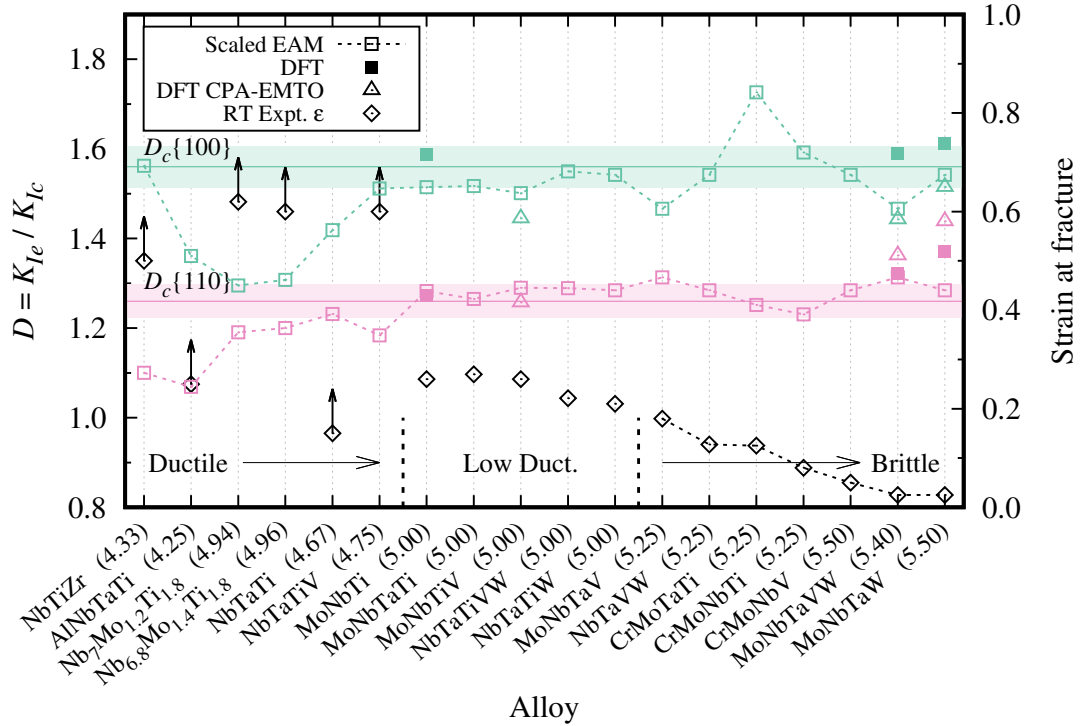


Figure 6.5: Predicted intrinsic ductility index $D = K_{Ie}/K_{Ic}$ and measured RT compression ductilities for selected HEA compositions. Experimental data with arrows indicates that tests were not carried out to the ductility limit. Predictions shown mainly use scaled EAM properties with the scaling factor $\beta = 1.04$, but results using fully-relaxed DFT properties and by CPA-EMTO DFT of [184] are shown where available. The RT ductility criterion for each cleavage plane is $D_c\{110\} \approx 1.26 \pm 3\%$ and $D_c\{100\} \approx 1.56 \pm 3\%$ as indicated. The alloy Valence Electron Count (VEC) is shown along with the alloy composition. Experimental data from [178] (NbTiZr), [182] (AlNbTaTi, NbTaTi, MoNbTaTi, NbTaTiW, CrMoTaTi, CrMoNbTi), [183] (Nb₇Mo_{1.2}Ti_{1.8}, Nb_{6.8}Mo_{1.4}Ti_{1.8}, MoNbTi), [197] (MoNbTiV), [198] (CrMoNbV), [199] (MoNbTaV), and [200] (NbTaTiV, NbTaTiVW, NbTaVW).

The Nb-rich alloys $\text{Nb}_7\text{Mo}_{1.4}\text{Ti}_{1.8}$, $\text{Nb}_{6.8}\text{Mo}_{1.4}\text{Ti}_{1.8}$, are all predicted and observed to be ductile (over 50% strain). The NbTiZr alloy is also ductile but the prediction is approaching the borderline for the 100/110 orientation due to an erroneous large USF energy predicted by the EAM potential that is $\sim 20\%$ higher than the *unrelaxed* DFT value; more accurate results should predict that this alloy is ductile, as observed. The alloys AlNbTaTi and NbTaTiV satisfy the ductility criteria and exhibit failure strains of over 25% and 50%, respectively. NbTaTi is also predicted to be ductile, but data extends only to 15% strain (but with no indication of impending failure). MoNbTi, MoNbTaTi, MoNbTiV, NbTaTiVW, NbTaTiW and MoNbTaV, with 25% or more of the brittle elements Mo and W, have failure strains of $\approx 25\%$ in compression and are predicted to be borderline ductile; their tensile ductility is likely low but not negligible. The 25% Cr alloys CrMoTaTi, CrMoNbTi, and CrMoNbV, which also contain 25% Mo, are predicted to be borderline or brittle, and exhibit fracture in compression at strains under 15%. The two Senkov et al. alloys MoNbTaVW and MoNbTaW are brittle as discussed earlier.

Our results above identify several general concepts. For the Senkov et al. alloys, the small differences between DFT and EAM-scaled results can put the alloys further or closer to the ductility limits. Thus, for alloys where the EAM-scaled results are close to the ductility criteria, more accurate DFT studies should be performed. Alloys predicted to be clearly ductile, i.e. those well below D_c for both orientations, are candidates for fabrication and testing. However, alloys near the ductility criteria, i.e. within the range of D_c , have uncertain ductility but may also be worth exploring if they are expected to have other attractive properties. Lastly, the ductility criteria D_c are not definitive, and hence improved correlations with experiments may emerge by using slightly different values for $D_c\{110\}$ and/or $D_c\{100\}$.

6.4 Identifying new ductile HEA compositions

In previous sections, we have shown that (i) the LEFM theory is validated by atomistic simulations, (ii) ductility criteria can be established based on first-principles versus experimental data on the refractory elemental metals, (iii) trends in ductility across a few alloys can be captured by first-principles material properties, and (iv) trends in ductility across even more HEAs studied to date can be reasonably captured by using the scaled EAM material properties. We can thus now use the LEFM theory, the ductility criteria, and the scaled EAM properties to make predictions for ductility across a much wider range of alloys with the goal of identifying promising new alloys for fabrication and testing.

Here, we investigate three families of alloys: Mo-Nb-Ti with $\text{Ti} \leq 33.33\%$, Mo-Nb-Ta-V-W with $\text{Mo} = 0.20$ to reduce the space of compositions, and Mo-Nb-Ta-W. Fig. 6.6 shows the predicted ductility indices versus alloy composition for these three families. The

6.4. Identifying new ductile HEA compositions

ductility index is normalized by the critical value for each orientation ($D\{110\}/D_c\{110\}$ and $D\{100\}/D_c\{100\}$). Using the uncertainty range in D_c of $\pm 3\%$ due to scaling, a ductile alloy has both normalized indices less than 0.97 (both entries colored green in Fig. 6.6).

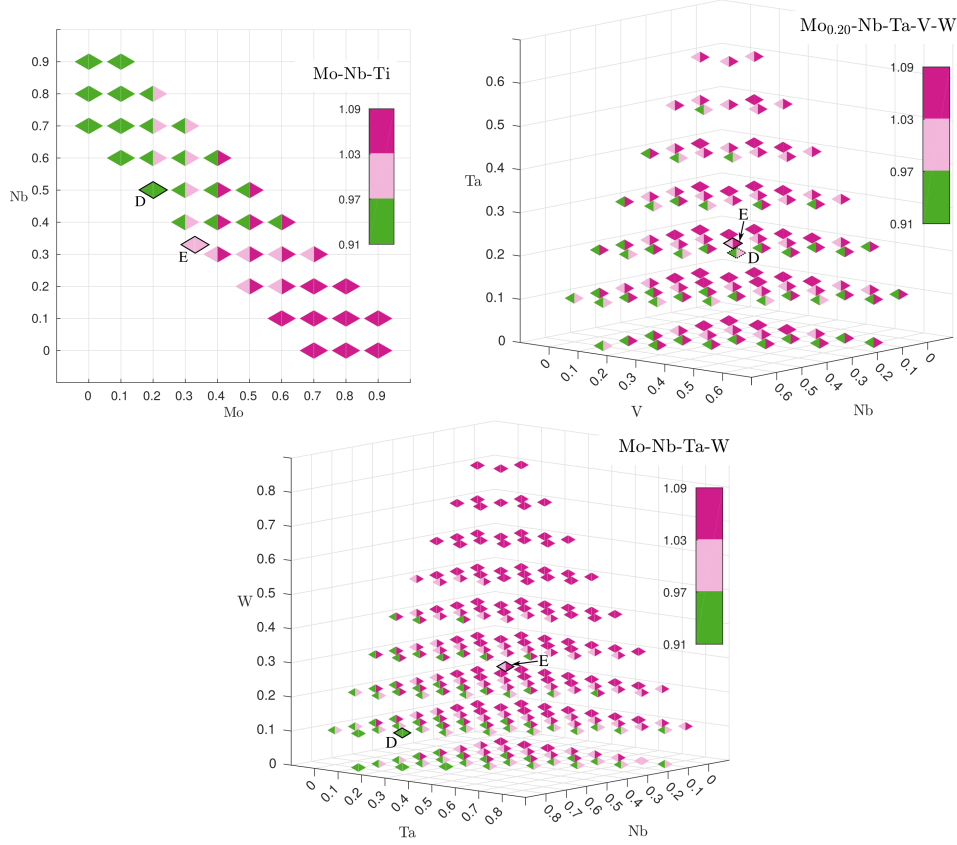


Figure 6.6: Ductility for three HEA families discretized at intervals of 10% concentration of each alloy constituent, using scaled EAM properties ($\beta = 1.04$). For each composition, the ductility of the 100/110 (\triangleleft symbols) and 110/112 (\triangleright symbols) orientations are normalized by the critical values $D_c\{100\}$ and $D_c\{110\}$, respectively. Light pink color corresponds to the borderline range of $D_c \pm 3\%$ as in Fig. 6.5. A RT ductile alloy has both normalized indices colored green. The equicomposition alloy and the closest ductile composition to it for each family are labeled “E” and “D”, respectively. For Mo-Nb-Ti, only compositions with $\text{Ti} \leq 33.33\%$ are shown.

Mo-Nb-Ti is predicted to be ductile when the Nb content is high ($\geq 50\%$) and the Mo content is low ($< 20\%$), and brittle when the Mo content is $\geq 30\%$, following the trends toward ductile Nb and brittle Mo (Fig. 6.2b). We do not show results for Ti content exceeding 33% but increasing Ti content decreases ductility in 100/110 but increases ductility in 110/112. The $\text{Mo}_{0.2}\text{Nb}_{0.5}\text{Ti}_{0.3}$ alloy might be an attractive candidate for preserving high strengths and achieving improved ductility over MoNbTi.

$\text{Mo}_{0.20}\text{-Nb-Ta-V-W}$ has no truly ductile domains, which is unfortunate since high strength retention at high T is most likely found in the Mo-Nb-Ta-V-W space. However, some

cases are borderline for sufficiently low W content and with higher Nb content tending toward ductility, consistent with Nb typically being the most ductile of the elements. For instance, $\text{Mo}_{0.2}\text{Nb}_{0.3}\text{Ta}_{0.3}\text{V}_{0.2}$ might be more attractive for ductility than MoNbTaVW. Similarly, Mo-Nb-Ta-W becomes ductile only as the Mo and W content is minimized (combined 20%) with the most ductile composition maximizing Nb, i.e. $\text{Mo}_{0.10}\text{Nb}_{0.70}\text{Ta}_{0.10}\text{W}_{0.10}$. Overall, the ductility of an alloy generally reflects the ductility of the constituent elements (i.e. from Fig. 6.2b) in rough proportion to their concentrations. However, we have found that rule-of-mixtures approaches to estimating material properties are not highly accurate.

The dimensionality of an N -component can be reduced to one generalized coordinate of the average valence electron count (VEC) of the alloy. Yang and Qi [201] have proposed that, in the context of binary W-Ta and W-Re alloys, D is maximized around $\text{VEC} = 5.8$. Li et al. [184] suggested that intrinsic ductilization, i.e. $D < 1.0$, may be possible on $\{110\}$ for $\text{VEC} < 4.2$. These are consistent with the trends here. We pursue this idea further here by recasting our results in Fig. 6.6 into the reduced space of D versus VEC as shown in Fig. 6.7 for the two critical orientations 110/112 and 100/110. For the 100/110 orientation, we find a wide range of D at fixed VEC for Mo-Nb-Ti (Ti < 0.33), $\text{Mo}_{0.20}$ -Nb-Ta-V-W, and Mo-Nb-Ta-W alloys, spanning above and below the critical D_c . Importantly, there is thus no distinct correlation between alloys with $D < D_c$ and any critical value of VEC. However, many alloys with $\text{VEC} < 5.25$ have $D < D_c$ for this orientation. For the 110/112 orientation, there is a much cleaner, roughly linear, correlation between D and VEC over the entire range of $4 < \text{VEC} < 6$. A similar linear trend for $\{110\}$ cracks is noted by Li et al. [184]. There remains a spread in D values at any VEC, but nearly all alloys with $\text{VEC} < 5.0$ fall into the ductile $D < D_c$ regime for this orientation.

According to Fig. 6.7, our RT ductility criteria appear to correlate with $\text{VEC} < 5.0$. In Fig. 6.6, the alloys with $\text{VEC} = 5.0$ are borderline whereas those with $\text{VEC} < 5.0$ are ductile. However, we predict (not shown) that NbTaV ($\text{VEC} = 5.0$) is ductile, which would not be surprising since the underlying elements Nb, Ta, and V are all ductile. The VEC alone thus does not appear sufficient to fully characterize ductility but we suggest use of $\text{VEC} < 5.0$ as a rapid first-screening for ductile compositions.

6.5 Discussion

Up to this point, we have neglected the effects of temperature. Material properties entering into the fracture theory (C_{ij} , γ_s , γ_{usf}) are temperature dependent. Generally they decrease with increasing temperature, so both K_{Ic} and K_{Ie} are expected to decrease with increasing temperature. Whether or not these property changes have a significant enough effect on the ratio K_{Ie}/K_{Ic} requires more detailed knowledge of the temperature dependence of the individual material properties, which is beyond the scope of this study.

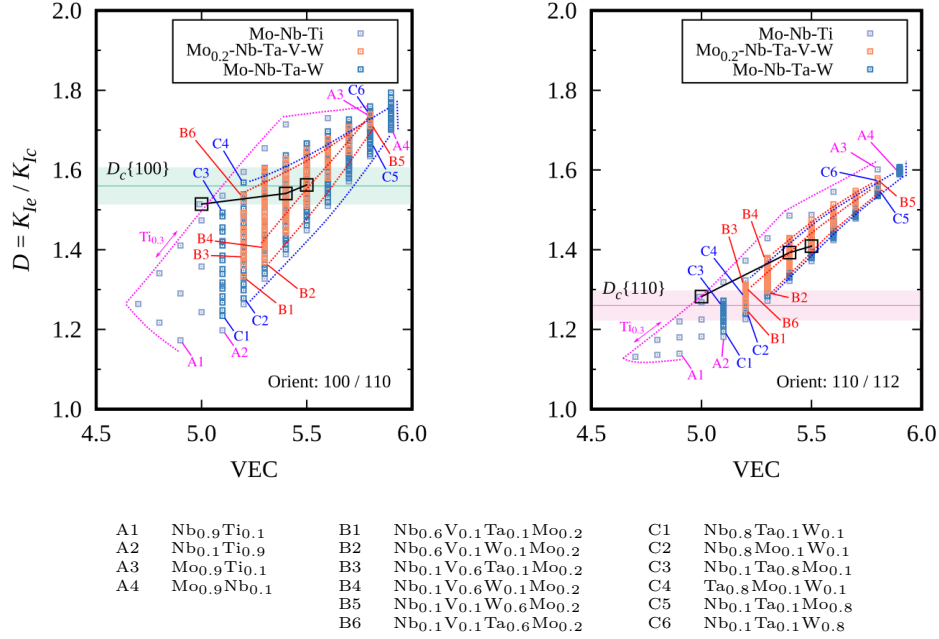


Figure 6.7: Ductility index $D = K_{Ie}/K_{Ic}$ versus the average valence electron count (VEC) per atom for three HEA families corresponding to Fig. 6.6, with the ductility criteria indicated, for each orientation. Equiatomic compositions are indicated by the solid black line. Colored dashed lines indicate various limiting compositions.

We have seen in a range of alloy compositions that K_{Ie}/K_{Ic} is generally rather greater than 1. Thus, we generally do not expect these property changes in refractory alloys to lead to a change from intrinsically brittle to ductile behavior at RT. Recalling the $T = 0$ energy barriers in Section 6.2, thermal activation also is generally not able to change the underlying brittleness if the emission barrier is much larger and insurmountable compared to the cleavage barrier around K_{Ic} . With increasing temperature however, the emission barrier is expected to decrease slightly due to thermal activation, which may enable a cross-over from brittle to ductile in some alloys.

The mechanical strength of bcc elements is controlled by the stress- and temperature-dependent mobility of screw dislocations [151]. Plastic flow up to moderate temperatures is dominated by the thermally-activated glide of screw dislocations. Even if a crack remains sharp, i.e. $D > D_c$, the surrounding material can be deforming due to dislocation plasticity. Dislocations in the plastic zone around a crack tip provide shielding, generally enabling a crack to support higher loads. Thus, the macroscopic fracture toughness can be significantly higher than the Griffith value even if the material remains subject to cleavage at the atomic scale. The transition to ductile behavior is here envisioned to be enabled by dislocation emission from the crack tip rather than dislocation plasticity away from the crack tip.

In HEAs, the high strength arises from strengthening mechanisms due to the random

solute environment on both screw and edge dislocation glide [8]. These high strengths will naturally reduce the size of the plastic zone around a crack, and reduce the macroscopic fracture toughness. Dislocations emitted from the crack tip will also be inhibited from moving far from the crack, and thus lead to shielding of subsequent emission and possibly increased anti-shielding for cleavage, both tending to make the alloy more brittle. Here, we do not include such stochastic effects of the true randomness of the alloy because we use the statistically-averaged representation of the random alloy. However, compositional variations along the crack front will also lead to local variations in γ_s and γ_{usf} , creating local environments that are both favorable and unfavorable for cleavage/emission with respect to the average behavior. Cleavage is thermodynamic, so such local variations cannot make overall cleavage easier or harder. In contrast, dislocation emission is a nucleation event, and so can be affected by the local environment. Dislocation emission can thus occur at loads below the average K_{Ic} at regions where the local composition can facilitate emission relative to the average. A moving crack encounters many local environments, and a single emission event somewhere along the crack front can lead to blunting. Thus, randomness can also possibly improve ductility compared to the average behavior; preliminary studies of true random MoNbTi suggests this to be the case. These aspects will be considered in future work.

6.6 Summary

Low compressive ductility displayed by some bcc elements and HEAs suggests that their ductility may be related to fracture phenomena. We have thus approached ductility by analyzing the nanoscale fracture competition between cleavage and dislocation emission at a sharp crack tip. We have validated the use of LEFM for assessing these two phenomena in selected model equiatomic HEAs described by EAM potentials. We have then used theory and experiments on bcc elements to develop a ductility criterion corresponding to critical values for the emission/cleavage ratio K_{Ie}/K_{Ic} for the two most-ductile crack orientations for bcc crystals. Application of this ductility criterion to various HEAs has then been made using material properties obtained from a validated scaling of EAM-potential properties. Generally good agreement for the predicted ductility was achieved across 15 different HEAs. The analysis was then extended to examine a much wider composition space. The same methodology can be applied to other alloy families. A correlation of ductility with Valence Electron Count was investigated as a very rapid but more-approximate assessment method. While further first-principles results will continually help refine our analysis here, such results are computationally intensive. We thus advocate application of the current methods in tandem with recent existing theories for yield strength [8, 9] to enable the computationally-guided design of strong, ductile, high temperature refractory HEAs.

7 Randomness and intrinsic ductility in bcc high entropy alloys

This chapter is extracted from the following publication

1. Mak, E., & Curtin, W. A. (2021). Randomness and intrinsic ductility in High Entropy Alloys. *Under preparation*

In Chapter 6, we observed that many refractory bcc HEAs (RHEAs) are likely intrinsically brittle ($D > 1$) and, when described by their average composition and average material properties, have very high and completely insurmountable energy barriers for emission compared to cleavage even well-above K_{Ic} so the rate of thermally-activated cleavage is always much higher than emission. [26]. Ductile behavior at low/ambient temperature is only possible the emission and cleavage barriers are comparable.

In the real random alloy system the composition fluctuates spatially throughout the material but the theory (Chapter 2.3) and predictions of D and D_c (Chapter 6) neglect the inherent randomness of the alloy environment. The material properties depend on the composition and so also fluctuate. When sampled locally they deviate from the average quantities of the system overall. Consequently, we expect the differences between local and average quantities of the material parameters entering into the theory (e.g. the elastic constants C_{ij} and anisotropy, the USF energy γ_{usf} , and the surface energy γ_s) to influence the fracture behavior. Additionally, structural “microdistortions” arise from the atomic misfit volumes of the elemental components.

Randomness provides the potential for variations in the local environment, which can be more/less favorable for cleavage or emission, i.e. the operating stress intensity is more/-less than K_{Ic} or K_{Ie} , respectively, relative to the average behavior of the alloy. Cleavage is a thermodynamic process, so local variations cannot make macroscopic cleavage easier or harder overall. Dislocation emission, however, is a nucleation event originating at a particular local environment. In alloys which have relatively comparable emission and

cleavage barriers on average, there is the potential for local environments in the random system to have lower emission barrier than cleavage barrier, enabling a *local* cross-over from brittle to ductile behavior. Emission occurring at a single emission-favorable local environment is sufficient for intrinsic ductility overall. So, the inherent randomness in the alloy can improve and not worsen ductility overall compared to the average behavior of the material.

One current goal in alloy development is to identify the alloy compositions in the family of RHEAs which have sufficient, if not high, RT ductility in addition to high strength. Compositions with borderline ductility may also be of interest if they possess other attractive properties. The first-estimate criterion for RT ductility $D_c > 1$ by [26] reasonably predicts the macroscopic ductility for a number of bcc HEAs. Screening with D_c can enable rapid and efficient identification of promising new ductile alloy compositions for fabrication and further testing, so it is advantageous to more accurately determine the values of D_c . No clear correlation has yet been established between RT yield strength and ductility with composition, but the properties of an alloy reflect a mixture of the properties of its constituent elements (see Chapter 6). Bcc RHEAs generally owe their attractive high strengths to high strength but brittle constituent elements, e.g. Mo and W, which only ductilize at temperatures above RT. Consequently, the alloy compositions of interest will likely have borderline ductility in the neighborhood of D_c . The contribution of randomness to the intrinsic ductility can have a significant impact on the ductility classification of compositions with borderline ductility and motivates this study.

We use a model equiatomic bcc MoNbTi HEA to study the effect of randomness on dislocation emission with atomistic simulations, although our observations generally apply to any random alloy system. Experimentally, MoNbTi achieves relatively high compressive ductility at RT ($\sim 25\%$) despite its high yield strength (~ 1.2 GPa) [183]. Randomness can potentially enable a local crossover from brittle to ductile behavior since the average intrinsic emission and cleavage barriers are at least comparable in the homogenized model system [26].

In this chapter, we apply the LEFM theory with atomistic simulations in Sec. 7.3 to semi-analytically identify the main energetic contributions of the emission process, including a balance of plastic slip and stress-work on an atomistic slip plane, and an elastic energy from stress change throughout the crack body. We obtain a distribution of possible emission pathways in the random alloy and observe the potential for significantly reduced local emission barriers compared to the average material. Local environments that are more-favorable for emission potentially enable local crossover from brittle to ductile behavior in a random system even if the material is brittle on average. Intrinsic/RT ductility criterion utilizing average material properties are effective for broad screening but yield conservative (more brittle) estimates of ductility. We begin to characterize the local environment for emission by studying fluctuations in material properties, par-

ticularly the USF energy γ_{usf} , which is the key material property for slip and emission according to conventional alloying wisdom. The average theory connects the energy barrier, stress intensity, and material properties for emission but small variations of local vs. average material properties do not directly reflect the variations in emission energy. The atomic misfit volume and its interaction with the crack fields is a critical energetic contribution to the emission process and introduces large variations to the emission energy. Large average misfit volume is proposed as a supplementary criterion for broad screening for ductility in HEAs.

7.1 Activated crack tip mechanisms in random environments

The Peierls concept-based Rice model [30] and dislocation emission as an activated process were introduced earlier in Chapter 2. The critical stress intensity K_{Ie} is the athermal critical load for instantaneous (2d) dislocation emission, but dislocation emission can occur at $K_I < K_{Ie}$ if thermal activation provides sufficient energy to overcome a finite energy barrier. The energy barrier ΔE_e associated with 3d emission approaches the zero-barrier for 2d emission as the load K_I increases toward the athermal critical K_{Ie} (e.g. black curve in Fig. 7.1b) corresponding to reaching the critical energy release rate $G_{Ie} = \gamma_{usf}$ [58, 60, 61]. The cleavage mechanism also experiences a small amount of lattice trapping [37, 38] corresponding to an energy barrier ΔE_c (e.g. dashed curve in Fig. 7.1b). The LEFM theory and nucleation models are formulated for a homogeneous continuum. The material properties of a homogeneous material entering into the theory (e.g. C_{ij} , γ_{usf} , γ_s) are constant and correspond to the critical stress intensities of the crack tip mechanisms (i.e. K_{Ic} , K_{Ie}) and their respective energy barriers which too are constant.

We can envision a random alloy system, which is inhomogeneous and has spatially varying material properties, sharing the same average material properties as a homogeneous system (see Fig. 7.1a). A single-atom A -atom species representing the model MoNbTi random alloy material statistically reproduces the average properties of the random material such that the resulting averaged-alloy (A -alloy) is the homogeneous representation of the random system. In the discussion following, we denote the averaged material properties of a true random system with an overhead bar ($\bar{\bullet}$) to distinguish from the constant properties of a homogeneous system, e.g. the homogenized A -alloy. By construction, the true random alloy and its A -alloy representation have equivalent average material properties, e.g. $\bar{C}_{ij} \equiv C_{ij}$, $\bar{\gamma}_{usf} \equiv \gamma_{usf}$, and $\bar{\gamma}_s \equiv \gamma_s$. Comparison of the random alloy to the A -alloy system enables us to identify the deviations from average crack behavior caused by phenomena due to randomness.

The model MoNbTi random alloy has equiatomic composition \bar{c} only when considering a sufficiently large volume of material, so the composition and thus the material properties

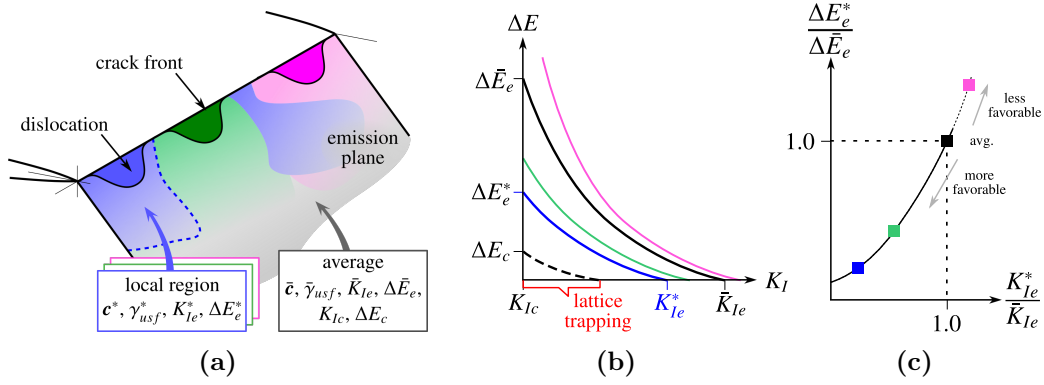


Figure 7.1: Schematic of local vs. average quantities in a random material. (a) Local composition c^* and material properties (denoted by \bullet^*), e.g. USF energy γ_{usf}^* , corresponding to a stress intensity for emission K_{Ie}^* and emission energy barrier ΔE_e^* deviates from the average material quantities (denoted by \bullet). (b) Energy barrier vs. stress intensity of loading shown schematically. Cleavage K_{Ic} (black dashed line) is associated with a small energy barrier ΔE_c and shows some lattice trapping but not influenced by deviations of the local environment. ΔE_e decreases toward the zero-barrier 2d emission limit corresponding to K_{Ie} . Local environments can be more favorable (blue/green lines) or less favorable (pink line) for emission than the material average (black line). (c) Deviations of the local emission barrier from the average barrier $\Delta E_e^*/\bar{\Delta E}_e$ corresponds to deviations of the local stress intensity for emission K_{Ie}^*/\bar{K}_{Ie} as shown schematically.

deviate from the system average when sampled locally (in a small volume). We denote these local quantities with a superscript asterisk, i.e. \bullet^* . Local variations in composition/material properties affect the crack tip behavior. Although these local variations could induce cleavage locally, they cannot make macroscopic cleavage easier/harder overall since cleavage is a global thermodynamic process. In contrast, dislocation emission is a nucleation event perceiving the local environment around the point of nucleation which depend on the variations in composition/material properties along the crack front and across the emission plane. From the theory we expect deviations of local USF energy γ_{usf}^* from the average $\bar{\gamma}_{usf}$ to be particularly critical for emission.

Suppose there exists a local region where the local USF is lower than average, i.e. $\gamma_{usf}^* < \bar{\gamma}_{usf}$. From theory, $K_{Ie} \sim \sqrt{\gamma_{usf}}$ so we expect lower local stress intensity, i.e. $K_{Ie}^* < \bar{K}_{Ie}$, which is more favorable for emission (e.g. comparing blue and black curves in Fig. 7.1). There can also be local regions that are less favorable for emission, i.e. where $\gamma_{usf}^* > \bar{\gamma}_{usf}$ (e.g. pink curve in Fig. 7.1). Emission will not occur there since the more favorable $\gamma_{usf}^* < \bar{\gamma}_{usf}$ regions are preferred, but this does not impact the ductility overall. The USF energy is also connected to the emission barrier, recalling from the continuum theory that the emission barrier partially depends on an energy of slip (Eq. (2.22)) that depends on a shear potential which scales with the USF energy (Eq. (2.2)). Based on the *average* theory, local reductions to the USF energy are conceptually connected to reductions to the local energy barrier, i.e. $\Delta E^*(\gamma_{usf}^*) < \bar{\Delta E}(\bar{\gamma}_{usf})$. However, we find in the following that the difference of local vs. global USF energy is not the key

factor behind the variations in random vs. average emission energy. The conceptual implications from the theory nonetheless still apply – a crossover from brittle to ductile behavior can occur locally if the local emission and cleavage barriers are comparable ($\Delta E_e^* \sim \Delta E_c$) even if the material is brittle on average. Only a single emission event is required for intrinsic ductility for the system overall, so the random alloy will be more ductile than predicted by theory.

7.2 Dislocation emission in random environments

Following the same methodology in Chapter 6, we simulate an atomistic crack with the K -test simulation framework and use the (free-end) NEB method [91] to circumvent the problems with the interatomic potentials present in the Zhou et al. [1] family of EAM-type potentials used here. We induce emission in thin specimens using finite temperature MD by artificially lowering the emission energy barrier (see Chapter 6) and replicate the resulting emitted configuration in the periodic direction to create 3d specimens. A simulation cell of $350 \times 350 \times 70 \text{ \AA}^3 (x \times y \times z)$, periodic in the out-of-plane z direction, is used to satisfy the in-plane convergence requirements for the K -test [23] and to capture the 3d emission barrier [26].

In order to save computational cost, we utilize the A -alloy emission behavior as a template to reconstruct random environments which we describe following. First, using the A -alloy, we identify the energy profile (Fig. 7.2) and transition path (\bar{P}) of emission between an initial sharp crack and a blunted crack tip with an emitted dislocation around Griffith K_{Ic} , which is the critical point for intrinsic ductility. The nucleation and bow-out of an incipient dislocation in the A -alloy is well-behaved (e.g. Fig. 7.2). The average emission pathway \bar{P} consists of replicas $\bar{P}^{(r)}$ and, since all local environments are equivalent in the A -alloy, the nucleation point along the A -alloy crack front in the simulation is arbitrary. The critical configuration of the dislocation is obtained at the saddle point of the energy profile, and the corresponding energy change is the energy barrier for emission $\Delta \bar{E}_e$ [58].

Using A -alloy atomic configurations in \bar{P} as a template, we then reconstruct random alloy environments by randomly designating the atoms in \bar{P} as one of the constituent elements, ensuring that the system has equiatomic composition, such that the A -alloy dislocation geometry sits in some random environment R . The dislocation geometry is then translated along the crack front, e.g. by $n = 1, 2, 3, \dots$ times the unit lattice spacing \bar{z} along the crack front as illustrated in Fig. 7.3. This process yields a set of N paths $\{P_n^R\}$ that have the A -alloy dislocation geometry centered at different points along a random crack front, thus sampling the local environments that random environment. These paths are given as the starting chain of replicas for a set of N number of NEB calculations corresponding to each environment R in order to sample the possible candidate emission pathways in R . These starting chain of replicas is much closer to the minimum energy

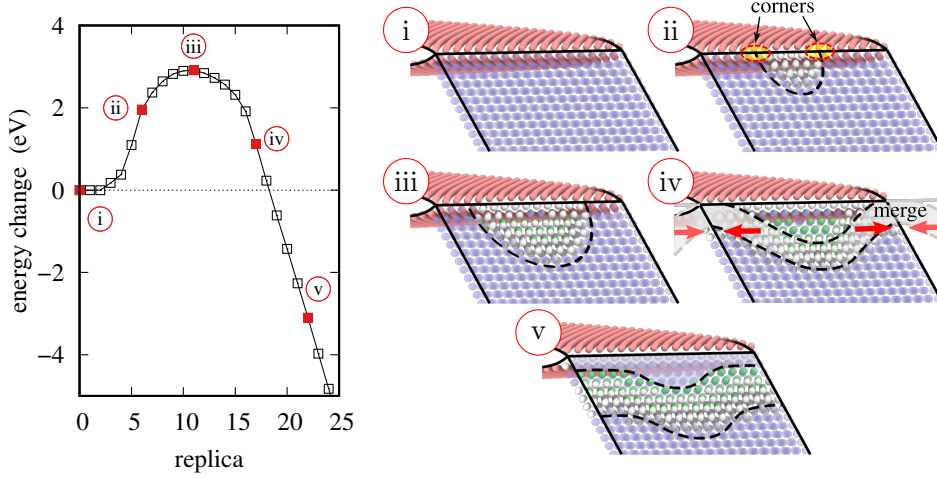


Figure 7.2: Model MoNbTi A-alloy emission energy along the NEB chain of replicas. Four dislocation configurations along the emission pathway as labeled and corresponding atomic configuration is shown. Black lines illustrate the crack front, emission plane, and dislocation loop. In (ii) two corners of the dislocation loop are at an angle with respect to the crack front early on; at (iv) they merge in the periodic crack to form a straight dislocation which moves away from the crack front (v). The atoms outside of the crack surface (red) and the slip plane have been removed for clarity. Slip plane atoms are colored blue (bcc), green (fcc), and white (non-bcc or fcc coordination) according to Common Neighbor Analysis.

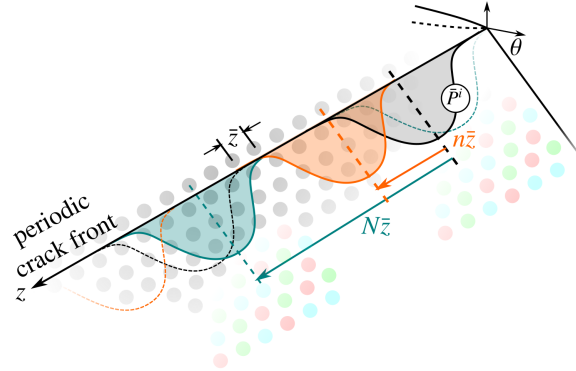


Figure 7.3: Creation of a set of starting chain of replicas for a random environment. The A-alloy dislocation loop geometry (P) is geometrically shifted along the periodic crack front direction (z) in a random environment by $n = 1, 2, \dots, N$ times the unit lattice spacing \bar{z} , where N is the number of lattice units in the simulation cell.

path (MEP) than a simple interpolation between the prescribed end-states, so the above template methodology saves a significant amount of computational cost.

7.2.1 Local emission energy barrier

We obtain the set of candidate pathways $\{P_n^R\}$ sampling the possible physical pathways taken for emission in 9 realizations of the random alloy. In each random environment, the

dislocation configurations resulting from adjacent starting paths are often quite similar geometrically, and the subtle variations between similar pathways are not entirely reliable since the energy landscape is very complex and there may be some influence from the interatomic potential. However, out of the set $\{P_n^R\}$ there are obvious “dominant” configurations, so we group the similar configurations together with some error in the geometry and corresponding energy barrier. Given the high computational cost of NEB calculation, sampling the local environment every three unit lattice spacings \bar{z} is sufficient to capture the dominant emission pathways in each random environment.

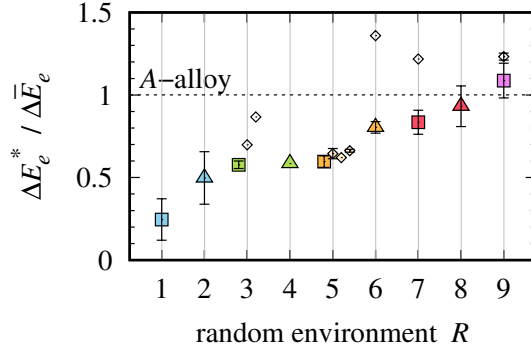


Figure 7.4: Emission energy barriers from 9 random environments, ordered approximately from lowest to highest energy overall. Energies ΔE_e^* are normalized by the A -alloy barrier $\Delta \bar{E}_e = 2.9$ eV. Error bars indicate initially adjacent pathways which that yield similar critical dislocation configurations but some variation in the energy. The lowest-energy pathway (solid colored markers) controls emission. Data points are slightly offset for clarity.

The energy barriers corresponding to the (grouped) set of candidate pathways for the random environments are shown in Fig. 7.4. The environments are ordered approximately from lowest to highest energy overall. The set of candidate pathways in each random environment correspond to different local environments from the random fluctuations in composition, and the differences between local environments correspond to variations in the (local) emission energy barrier and dislocation configuration. In general, each random crack front contains at least one, if not more, local environment and candidate pathway that corresponds to lower (local) emission energy than in the average A -alloy, i.e. $\Delta E_e^* < \Delta \bar{E}_e$. Each candidate pathway is the MEP for a given pair of end-states but is not necessarily the overall MEP for emission in environment R . The most-favorable pathway controlling emission in each environment has the lowest energy barrier; these pathways are indicated in Fig. 7.4 by solid colored markers for each environment. The remaining candidate pathways (unfilled markers) correspond to higher energy barriers and thus much slower nucleation rates. A key observation to be made at this point is that local environments that are more-favorable for emission, i.e. where emission in that environment corresponds to lower than average emission energy, are (i) easily found in the random system, and (ii) can be significantly less than the average $\Delta \bar{E}$. Some pathways follow a different emission mechanism, e.g. producing an energy profile with two saddle points, and they are excluded in the results shown. For

this reason only one pathway remains in environment 4 (no error bar). Unless otherwise noted, *we reference the lowest energy candidate pathway as the emission pathway for each random environment in all subsequent discussion.* Note for easy cross-referencing the numbering/color-coding of the random environments in Fig. 7.4 is carried throughout all subsequent discussion and figures.

The local environment has a strong effect on the geometry of the dislocation, e.g. Fig. 7.7 illustrates the large variation in the shape and size of the critical saddle point dislocation configurations from the random environments. Using one of the random environments to illustrate in Fig. 7.5, we make some general qualitative observations regarding the evolution of the incipient dislocation. Initial slip activity generally occurs at multiple locations along the crack, unlike in the homogeneous system where slip is confined to a single region through the entire emission process. Consequently in the random environment, we observe in simulation instances where two sufficiently isolated regions of slip are able to accumulate independently early on. The dislocation loops grow radially and laterally, as opposed to radial bow-out in the homogeneous material, so they tend not to be semi-circular. Very “flat” loops (e.g. environment 7 in Fig. 7.7) is a hallmark of the merging of multiple regions of slip. In all cases, the instability is achieved regardless of the dislocation geometry, and the dislocation eventually becomes straight and moves away from the crack front.

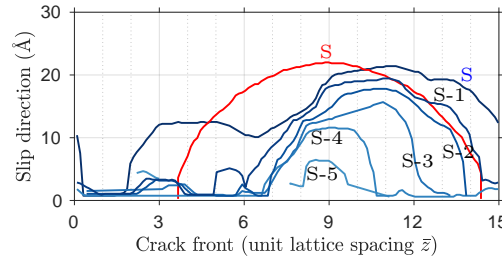


Figure 7.5: Expansion of an incipient dislocation in random environment 5. The dislocation loop as characterized by the $\Delta/b = 0.1$ slip contours on the slip plane is shown at the saddle point replica S and the preceding replicas $S - 1, S - 2, \dots$. The A-alloy saddle point dislocation geometry (red) is shown for reference.

7.2.2 Local environments on the slip plane

The exact dislocation geometry appearing in the random alloy is the expression of the complex interaction of the spatially fluctuating material properties with the dislocation loop and the crack tip. Capturing these relationships exactly is beyond the scope of this study, but in the following we begin to characterize the local environment in terms of local material properties. Discrete contours of Δ (schematically shown in Fig. 7.6), which bound a region A_Δ relative to the straight crack front, characterize a distribution of slip. The $\Delta/b = 0.5$ contour contains the atoms at or past the USF instability point and so delineates a critical region of slip of an incipient dislocation. Atoms on the slipping

layers of atoms but far away from this “core” region of the dislocation do not significantly contribute to the slip energy (e.g. Eq. (7.7)). For the set of random environments, the Δ contours, e.g. in Fig. 7.7, show the large variation in both area and distribution of slip, and the critical slip region occupies an area roughly $A_{\Delta/b \geq 0.5} \approx 250 \pm 125 \text{ \AA}^2$ over the slip plane.

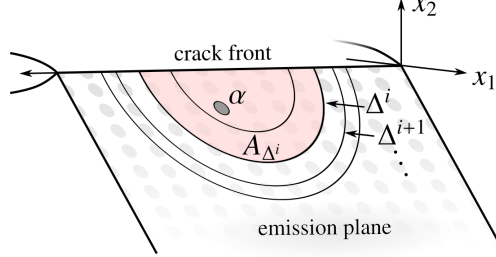


Figure 7.6: Schematic of a dislocation loop on its emission plane. Slip is characterized by contours Δ which bounds an area A^Δ relative to the straight crack front. The atoms $\alpha \in A_{\Delta^i}$ have slip $\Delta^\alpha \geq \Delta^i$.

The composition of the random alloy fluctuates spatially throughout the material so that the local composition \mathbf{c}^* deviates from the average “global” composition $\bar{\mathbf{c}}$. This deviation, i.e. $\|\mathbf{c}^* - \bar{\mathbf{c}}\|$, is roughly 7% of $\bar{\mathbf{c}}$ within an area of $\sim 250 \text{ \AA}^2$ (approximately the critical slip region) in a volume of slip plane atoms (see Appendix A.6). The local material properties (\bullet^*) deviate from the average material properties ($\bar{\bullet}$) due to the fluctuations in composition. The USF energy and the material anisotropy, and so indirectly the elastic constants, enter into the theory. As a result, the variations in γ_{usf}^* and C_{ij}^* are most likely to contribute to the variations observed in the local emission barrier compared to other material properties.

First, looking at the USF energy, only the close neighbors that are near the stacking fault of the slip plane atoms significantly contribute to γ_{usf}^* (see Appendix A.6). For each slip plane atom, its perceived γ_{usf}^* can vary up to $\pm 40\%$ of $\bar{\gamma}_{usf}$. Fig. 7.7 shows the field of varying atomic γ_{usf}^* in the set of random environments. Dislocation slip is driven by the USF energy over a region of the slip plane occupied by the dislocation loop and not directly by the USF energy of individual atoms, however. Based on the expected variation in composition corresponding to a critical slip region (e.g. 7%), the USF energy perceived by the dislocation loop and driving slip is expected to vary only $\pm 10\%$ from $\bar{\gamma}_{usf}$ in the model MoNbTi (see Fig. 7.9a).

From theory, the energy barrier is connected to the stress intensity, and the stress intensity scales with the USF energy. The relationship between ΔE and K_I for the MoNbTi A-alloy is well-fit to a decreasing exponential form and is thus very steep at the critical load of Griffith K_{Ic} [26] (see Fig. 7.10) – from that relationship very large reductions to the energy barrier are expected from modest reductions of the USF energy. Based on the average theory and the fit of [26], the USF energy for dislocation slip varying $\sim 10\%$

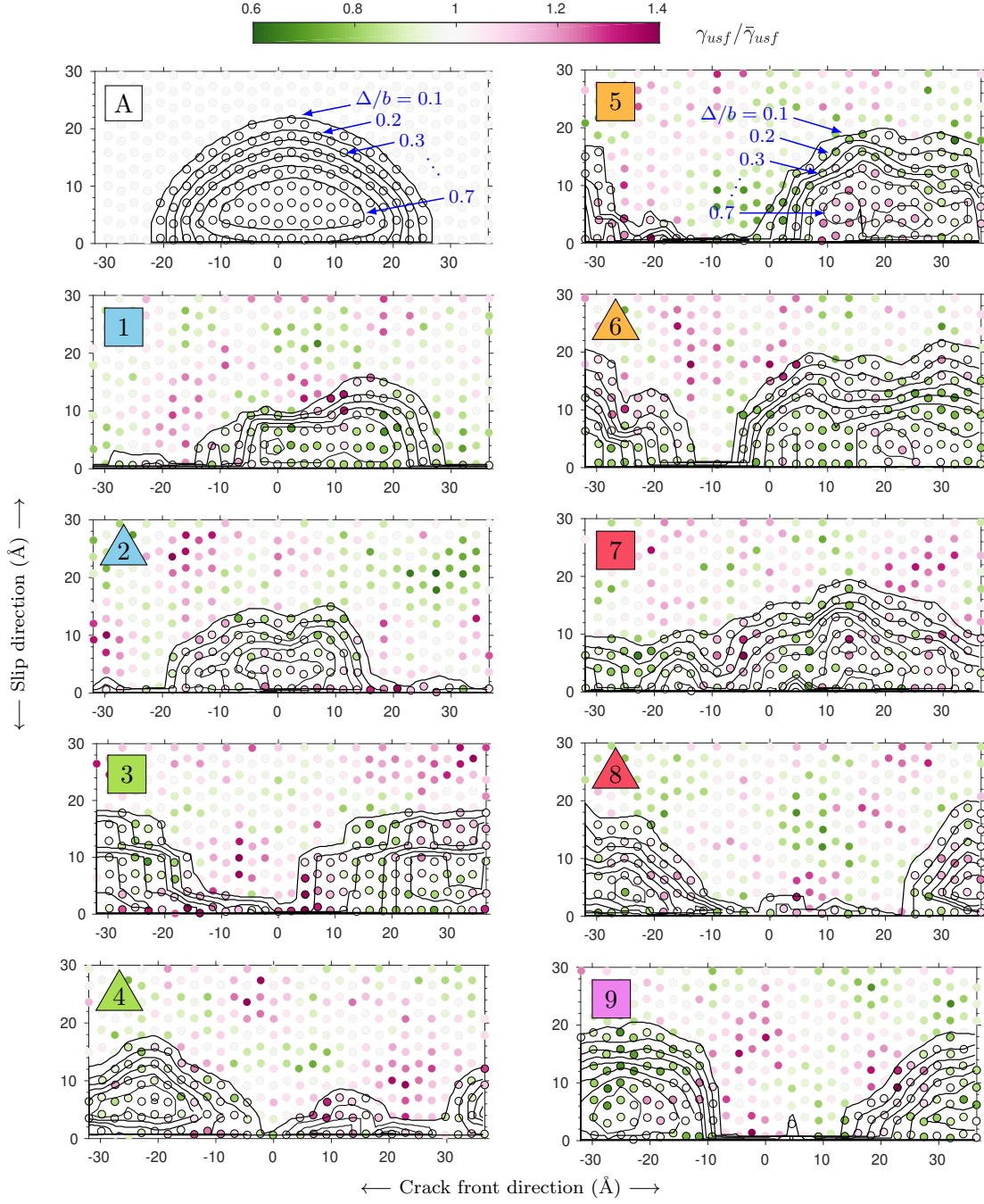


Figure 7.7: Saddle point dislocation slip contours and local unstable stacking fault (USF) energy of the slip plane atoms. Distribution of dislocation slip is characterized by slip contours Δ/b at increments of 0.1 for the A-alloy (labeled A) and 9 random environments (as numbered corresponding to Figure 7.4). The contour levels are indicated for environments A and 5 for reference. The outermost contour is $\Delta/b = 0.1$ but the number of contour levels varies between the environments. The projected positions of the slip plane atoms are indicated by circular markers which are colored according to the atomic USF energy γ_{usf}^* with respect to the A-alloy USF energy $\bar{\gamma}_{usf}$ (see colorbar).

7.2. Dislocation emission in random environments

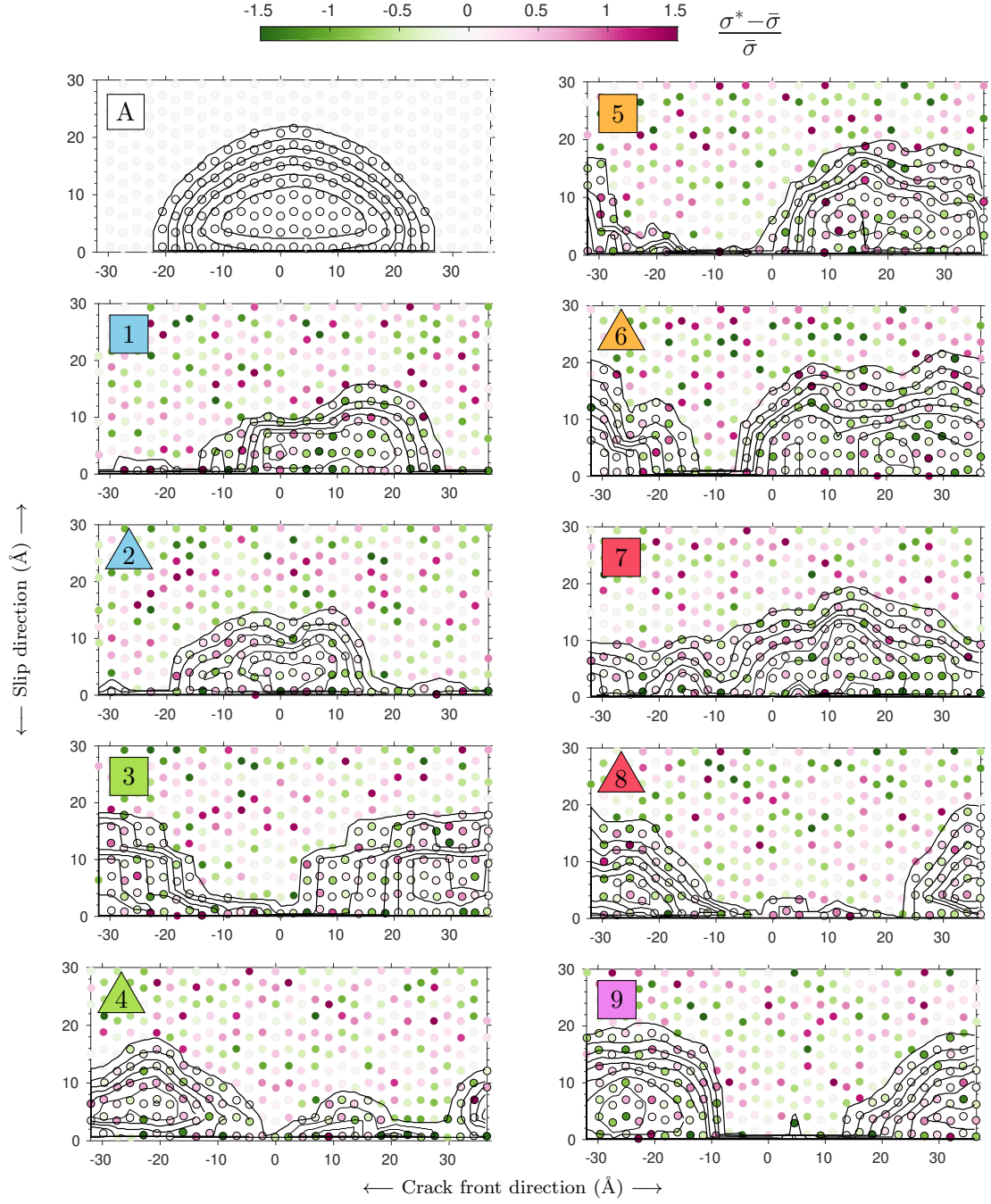


Figure 7.8: Saddle point dislocation slip contours and shear stress of the slip plane atoms. Distribution of dislocation slip is characterized by slip contours Δ/b at increments of 0.1 for the A-alloy (labeled A) and 9 random environments (as numbered corresponding to Figure 7.4). The outermost contour is $\Delta/b = 0.1$. The projected positions of the slip plane atoms are indicated by circular markers which are colored according to the difference in the atomic virial stress σ^* in the direction of slip with respect to the A-alloy stress field $\bar{\sigma}$ (see colorbar).

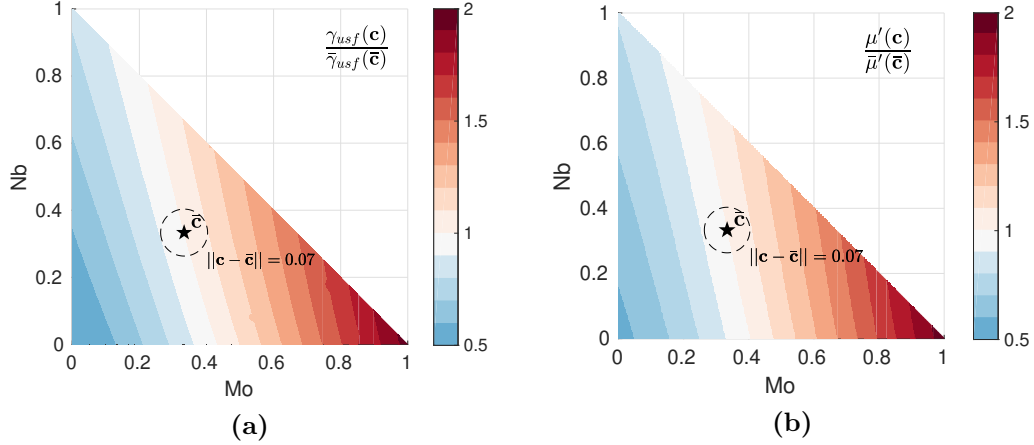


Figure 7.9: Similar variation of the unstable stacking fault (USF) energy γ_{usf} and stiffness μ' with composition in the A-alloy representation of the model Mo-Nb-Ti space of alloys. (a) The USF energy is normalized to the equiatomic quantity $\bar{\gamma}_{usf}(\bar{\mathbf{c}})$ (starred). The USF energy varies approximately 10% for a $\sim 7\%$ variation in composition, i.e. $\|\mathbf{c} - \bar{\mathbf{c}}\|$, delineated by the dashed circle. (b) The shear stiffness with respect to the slip plane $\mu' = (C'_{44} + C'_{55} + C'_{66})/3$ is normalized to the equiatomic quantity $\bar{\mu}'(\bar{\mathbf{c}})$. In the Mo-Nb-Ti composition space the shear stiffness varies very similarly with composition to the USF energy.

from $\bar{\gamma}_{usf}$ translates to $\sim 70\%$ reduction in the energy barrier, corroborating at least the magnitude the reduced local energy barriers obtained from atomistic simulations e.g. in Fig. 7.4. We deterministically obtain an average of the atomic γ_{usf}^* over $A_{\Delta/b \geq 0.5}$ as an estimate of the local USF energy driving slip for the set of random environments. Fig. 7.10 illustrates that ΔE_e does not depend solely on USF energy as described by the average theory. The observed simulated dislocations do not necessarily nucleate where the USF energy is lowest along a random crack front. That would not be the case if low USF energy were the sole criterion for ductility.

As seen in Fig. 7.9b, the shear stiffness with respect to the slip plane μ' (see Appendix A.6) in the Mo-Nb-Ti composition space specifically varies very similarly with composition to γ_{usf} . Consequently, we also expect about $\pm 10\%$ variation of the local shear stiffness compared to the average stiffness based on the variation of composition in a critical slip region. Atomic-scale variations of the material stiffness redistributes the crack fields. To illustrate, Fig. 7.8 shows the initial atomic (virial) shear stress (e.g. Eq. (7.6) discussed in the next section) across the slip plane in the random environments. In this system, regions of lower USF energy correspond to lower stiffness, and so conceptually the local regions which are easier to slip also carry less driving stress. The slip is associated with some energy cost connected to the fluctuating USF energy and driven by a stress-work across the slip fault plane connected to the fluctuating stiffness.

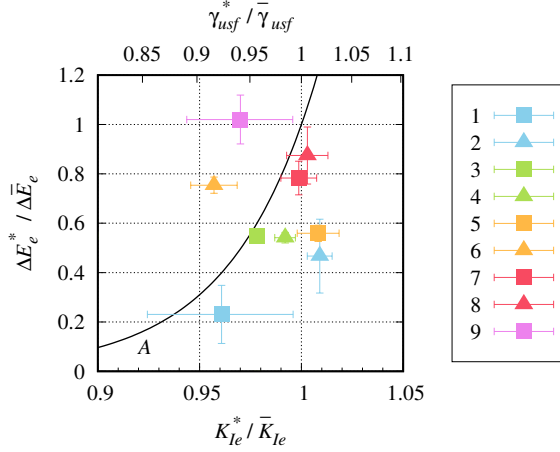


Figure 7.10: Variations of local USF energy γ_{usf}^* vs. variations of local energy barrier ΔE_e^* for the set of random environments. The average energy barrier $\Delta \bar{E}$ is connected to the average stress intensity for emission K_{Ie} based on an exponential functional form derived from fitting the *A*-alloy [26] (labeled *A*), and the average USF energy $\bar{\gamma}_{usf}$ scales with K_{Ie} according to the theory. Local γ_{usf}^* obtained for the critical slip region $A_{\Delta/b=0.5}$ for the set of random environments (error bars for the group of dominant pathways) and does not directly scale with variations in ΔE_e^* . Marker types and colors correspond to Fig. 7.7.

7.3 Energy of emission in the atomistic system

In the following we attempt to account for the total energy cost of emission through a semi-analytical approach combining nucleation theory and atomic quantities (e.g. slip and stress) obtained from simulation. First taking a step back, we return to the *A*-alloy system to identify and quantify the major energetic contributions of the emission process in the average system. The fluctuations in composition/material properties in the random alloy can affect the balance of these contributions or introduce additional contributions to the total system energy.

Chapter 2 introduced approximate continuum models for dislocation emission, e.g. the cohesive-type Rice [30] model based on the Peierls concept. The continuum slip plane is a mathematical cut plane of zero-thickness, and in the theory the incipient dislocation is a distribution of shear displacement δ across this cut plane [30]. In comparison, in the atomistic system two planes of atoms slide relative to one another creating a planar stacking fault (an “atomistic slip plane”), and the incipient dislocation “loop” is the distribution of relative shear displacement Δ of the atoms relative to their lattice positions. The slip/slip plane of the atomistic system is not directly equivalent to the continuum definition, and there is no general consensus on how to (best) equate the discrete system to the approximate continuum models. The relative atomic displacements Δ includes an elastic contribution to the slip Δ_{el} associated with the discrete lattice [30], i.e.

$$\Delta = \delta + \Delta_{el} \quad (7.1)$$

Detailed analysis of 2d emission by Andric and Curtin [48] show that using atomistic Δ reduces the atomistic generalized stacking fault (GSF) quantities to the Rice results for K_{Ie} when the step energy is small, which is the case here. The energy barrier for emission, which is captured by NEB simulations, is the net excess energy from the contributions of various processes involved in the nucleation mechanism, and this requires more detailed partitioning the atomic slip/stress/energy into elastic and plastic contributions.

For dislocation emission from the crack tip, the accumulation of slip of the incipient dislocation is superimposed over the crack and its elastic fields. The slip is fundamentally connected to the USF instability and the GSF curve. We direct the reader to Appendix A.5 for detailed discussion of the atomistic energetic balance in the pure stacking fault scenario but review the key points following. The concept of the USF is conceptually derived from the shearing of one half of a rigid block relative to its other half along a slip plane (also discussed in Chapter 2). The energy of slip is an integral of the shear resistance over the slip (Eq. (2.2)), and the shear resistance exerted by one half-block on the other half-block for slip is equivalent to a traction \mathcal{T}_Δ over the fault plane. There is a balance between the slip energy U_Δ [30] and a stress-work $W_\Delta(\mathcal{T}_\Delta)$ over the fault surface, i.e.

$$\Pi_\Delta = U_\Delta - W_\Delta \quad (7.2)$$

In the continuum, the quantities of slip and work in Eq. (7.2) are confined to a mathematical plane discontinuity. In contrast, in the discrete system they involve the slip of “slip plane atoms”, which are the two slipping layers directly above and below the atomistic slip plane and are notated 0^+ and 0^- , respectively, for all subsequent discussion. The discrete form of the slip energy is written as a sum over the slip plane atoms, i.e.

$$U_\Delta = \sum_{\alpha \in 0^+, 0^-} U_\Delta^\alpha = \frac{1}{2} \sum_{\alpha \in 0^+, 0^-} A^\alpha \gamma_{usf} \sin^2 \left(\frac{\pi \Delta^\alpha}{b} \right) \quad (7.3)$$

where A^α is the area occupied by atom α on its layer so the surface area of the slip plane is $A = \frac{1}{2} \sum_{\alpha \in 0^+, 0^-} A^\alpha$, and the USF energy γ_{usf} is constant over A in the A -alloy. The stress-work is the work of the shear traction \mathcal{T}_Δ over A in the direction Δ , i.e.

$$W_\Delta = A \int \mathcal{T}_\Delta d\Delta \quad (7.4)$$

and for the stacking fault scenario \mathcal{T}_Δ is approximated by the atomic virial shear stress τ_Δ of the slip plane atoms in the direction Δ corresponding to the Burgers vector, i.e.

$$W_\Delta = \sum_{\alpha \in 0^+, 0^-} W_\Delta^\alpha \approx \sum_{\alpha \in 0^+, 0^-} A^\alpha \int \tau_\Delta^\alpha d\Delta \quad (7.5)$$

7.3. Energy of emission in the atomistic system

For atom α , τ_Δ^α is the shear stress component corresponding to slip Δ in the virial stress tensor σ^α (see Appendix A.5) and is written

$$\tau_\Delta^\alpha = \frac{1}{A^\alpha} \left[\frac{1}{2} \sum_{\substack{\beta \\ \beta \neq \alpha}} f_\Delta^{\alpha\beta} \cdot \tilde{r}_\perp^{\alpha\beta} \right] \quad (7.6)$$

where $f_\Delta^{\alpha\beta}$ is the component of the force pair-interaction of atom β on atom α in the direction of slip, h is the spacing of the atomic layers in the direction normal to the slip plane, $\tilde{r}_\perp^{\alpha\beta}$ is the number of atomic layers from β to α , and $A^\alpha = V^\alpha/h$ is the slip plane surface area occupied by atom α with volume V^α .

In Eq. (7.1), Δ includes an elastic part Δ_{el} associated with the discrete lattice. By the same token, the slip energy U_Δ includes an elastic part $U_{\Delta_{el}}$ [30], and the remaining plastic part U_δ is written

$$\begin{aligned} U_\delta &= U_\Delta - U_{\Delta_{el}} \\ &= \sum_{\alpha \in 0^+, 0^-} U_\delta^\alpha = \frac{1}{2} \sum_{\alpha \in 0^+, 0^-} A^\alpha \gamma_{usf}^\alpha \sin^4 \left(\frac{\pi \Delta^\alpha}{b} \right) \end{aligned} \quad (7.7)$$

The plastic counterpart of the energy balance in Eq. (7.2) is then

$$\Pi_\delta = U_\delta - W_\delta \quad (7.8)$$

where W_δ is a portion of the stress-work that balances U_δ by construction. W_δ comes from a portion of the traction $\mathcal{T}_\delta = \mathcal{T}_\Delta - \mathcal{T}_{\Delta_{el}}$ (i.e. removing the elastic part $\mathcal{T}_{\Delta_{el}}$) that comes from a portion of the atomic stress $\tau_\delta = \tau_\Delta - \tau_{\Delta_{el}}$, i.e.

$$\begin{aligned} W_\delta &= W_\Delta - W_{\Delta_{el}} = A \int \mathcal{T}_\delta d\Delta \\ &= \sum_{\alpha \in 0^+, 0^-} W_\delta^\alpha \approx \sum_{\alpha \in 0^+, 0^-} A^\alpha \int \tau_\delta^\alpha d\Delta \end{aligned} \quad (7.9)$$

In the pure stacking fault problem, the slip energy is perfectly balanced by the stress-work so $W_\delta = U_\delta$, i.e. $\Pi_\delta = 0$ in Eq. (7.8), and by taking the derivative of that expression, the part of the shear stress of each atom α required to satisfy the equality is

$$\begin{aligned} \sum_{\alpha \in 0^+, 0^-} A^\alpha \frac{d}{d\Delta} \left[\int \tau_\delta^\alpha d\Delta \right] &= \sum_{\alpha \in 0^+, 0^-} \frac{1}{2} A^\alpha \frac{d}{d\Delta} \left[\gamma_{usf}^\alpha \sin^4 \left(\frac{\pi \Delta^\alpha}{b} \right) \right] \\ \implies \tau_\delta^\alpha \Big|_{\Pi_\delta=0} &= \frac{\pi}{b} \gamma_{usf}^\alpha \sin^2 \left(\frac{\pi \Delta^\alpha}{b} \right) \sin \left(\frac{2\pi \Delta^\alpha}{b} \right) \end{aligned} \quad (7.10)$$

Following from Eq. (7.8), the *change* in the plastic slip plane energy balance of a slipped crack configuration r (e.g. an NEB replica) relative to the unslipped state 0 (e.g. the

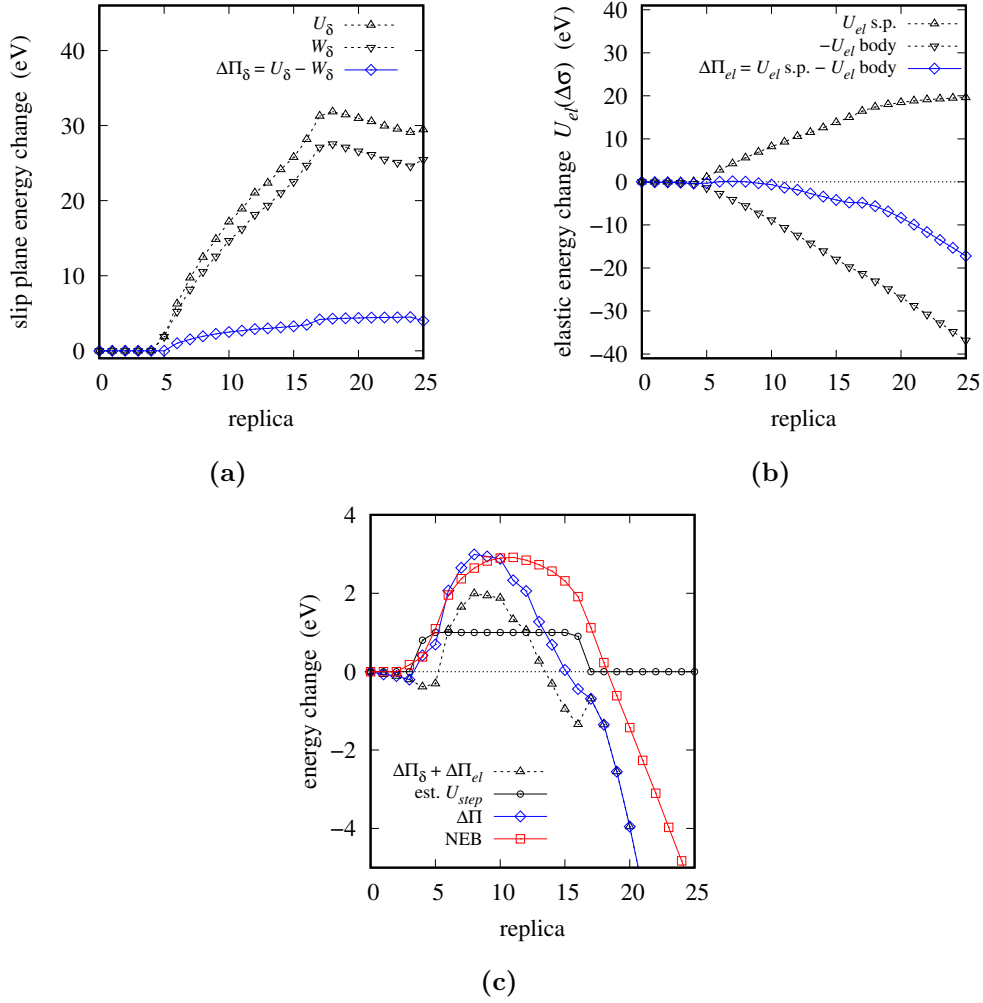


Figure 7.11: Emission energy contributions along NEB chain of replicas in the model MoNbTi A-alloy. (a) Slip plane energy contributions include the plastic slip energy U_δ and stress-work W_δ , and the balance $\Delta\Pi_\delta = U_\delta - W_\delta$ is Eq. (7.11). (b) Elastic energy contributions from the stress change in the slip plane (s.p.) atoms (Eq. (7.12)) and the rest of the crack body (Eq. (7.14)) relative to the unslipped configuration; the net contribution is $\Delta\Pi_{el}$ (Eq. (7.16)). (c) An estimated step energy U_{step} smooths the step drop in energy shown by $\Delta\Pi_\delta + \Delta\Pi_{el}$. The expression $\Delta\Pi = \Delta\Pi_\delta + \Delta\Pi_{el} + U_{step}$ (Eq. (7.17)) shows reasonable correspondence with the NEB energy profile.

initial NEB state) is

$$\begin{aligned} \Delta\Pi_\delta^{(r)} &= \Delta\Pi_\delta^{(r)} - \Delta\Pi_\delta^{(0)} \\ &= \sum_{\alpha \in 0^+, 0^-} U_\delta^{\alpha(r)} - W_\delta^{\alpha(r)} \end{aligned} \quad (7.11)$$

where $U_\delta^{\alpha(r)}$ and $W_\delta^{\alpha(r)}$ are Eq. (7.7) and Eq. (7.9) and (7.10) evaluated for the atomic slips $\Delta^{\alpha(r)}$ in configuration r , respectively. We obtain a smooth displacement field $u^{0^+}(\mathbf{x})$ and $u^{0^-}(\mathbf{x})$ over layers 0^+ and 0^- , respectively, by interpolating the atomic displacements

7.3. Energy of emission in the atomistic system

on each layer over the atomic positions. A smooth slip field $\Delta(\mathbf{x}) = u^{0+}(\mathbf{x}) - u^{0-}(\mathbf{x})$ is obtained for the atomistic slip plane and evaluated at the atomic positions for the atomic slip, i.e. $\Delta^\alpha = \Delta(\mathbf{x}^\alpha)$.

For dislocation emission from the crack tip, the slip of the emission interacts with the crack field and so is not the pure stacking fault scenario. The presence of slip and the stacking fault implies some balance between U_δ and W_δ as in Eq. (7.11). These two quantities are evaluated for the *A*-alloy in Fig. 7.11a, and we see they are both individually very large and track each other along emission pathway. Their difference, i.e. $\Delta\Pi_\delta$, is relatively small in comparison, on the order of the emission energy, and is non-zero due to the slip-crack interaction. A part of the excess energy in the system, i.e. a part of the emission energy barrier, thus originates from the slip-crack interaction.

The slip is also associated with changes to the stress fields around the crack tip, and these changes contribute to the elastic energy. The atomic virial stress (tensor) $\boldsymbol{\sigma}$ as extracted from atomistic simulation corresponds to the total combined behavior of all plastic and elastic processes. Thus, only some *part* of its shear component τ is τ_δ – to reiterate, τ_δ corresponds to the amount of traction which balances the plastic slip. The remaining amount of shear, $\tau - \tau_\delta$, together with the other components of $\boldsymbol{\sigma}$ contribute elastically to the energy. For an atom with extracted virial stress $\boldsymbol{\sigma}^\alpha$ and slip Δ^α , the amount $\tau_\delta(\Delta^\alpha)$ (Eq. (7.10)) is removed from the corresponding shear component of $\boldsymbol{\sigma}^\alpha$ – this is denoted $(\boldsymbol{\sigma}^\alpha - \tau_\delta)$ – and the elastic strain energy is obtained for that adjusted tensor. The elastic energy contribution from the slip plane atoms is written

$$\sum_{\alpha \in 0^+, 0^-} U^{el}(\boldsymbol{\sigma}^\alpha - \tau_\delta(\Delta^\alpha)) \quad (7.12)$$

where the notation U^{el} denotes

$$U^{el}(\boldsymbol{\sigma}^\alpha) = V^\alpha \int \boldsymbol{\sigma}^\alpha(\Delta) : d\boldsymbol{\epsilon}^\alpha(\Delta) = V^\alpha \cdot \frac{1}{2} S_{ij} \sigma_i^\alpha \sigma_j^\alpha \quad (7.13)$$

for a tensor $\boldsymbol{\sigma}$ and the elastic compliance \mathbf{S} expressed in contracted Voigt notation. The atoms outside of the slipping layers also experience a stress change due to the slip. Their contribution to the system energy is entirely elastic thus no partitioning as above is required and the strain energy is obtained from the full stress tensor, i.e.

$$\sum_{\alpha \notin 0^+, 0^-} U^{el}(\boldsymbol{\sigma}^\alpha) \quad (7.14)$$

The net elastic energy of the system has contributions from the slip plane atoms (Eq. (7.12)), which is associated with the slip, and from rest of the crack body (Eq. (7.14)), i.e.

$$\Pi_{el} = \sum_{\alpha \in 0^+, 0^-} U^{el}(\boldsymbol{\sigma}^\alpha - \tau_\delta(\Delta^\alpha)) - \sum_{\alpha \notin 0^+, 0^-} U^{el}(\boldsymbol{\sigma}^\alpha) \quad (7.15)$$

If atoms α in the unslipped configuration 0 have stresses $\sigma^{\alpha(0)}$, the stress change of configuration r relative to the unslipped state is $\Delta\sigma^{\alpha(r)} = \sigma^{\alpha(r)} - \sigma^{\alpha(0)}$. Following from Eq. (7.15), the *change* in elastic energy of a slipped crack configuration r relative to the unslipped state 0 is then

$$\begin{aligned}\Delta\Pi_{el}^{(r)} &= \Pi_{el}^{(r)} - \Pi_{el}^{(0)} \\ &= \sum_{\alpha \in 0^+, 0^-} U^{el} \left(\Delta\sigma^{\alpha(r)} - \tau_\delta(\Delta^\alpha) \right) - \sum_{\alpha \notin 0^+, 0^-} U^{el} \left(\Delta\sigma^{\alpha(r)} \right)\end{aligned}\quad (7.16)$$

The two elastic terms in Eq. (7.16) are shown for the *A*-alloy in Fig. 7.11b. The slip plane contains a relatively small amount of atoms but those atoms are associated with a large amount of elastic energy. More importantly, the atoms in the crack body also have a large cumulative contribution to the elastic energy. Although the stress change and thus energy change associated with each individual atom is very small, the cumulative energy over the large number of atoms is large. This has major implications for the random alloy environment since there will be an additional interaction of the solute misfit volumes with the crack fields. Collectively the misfit over the entire crack body will likely have a significant impact on the net elastic contribution. We return to this point in Sec. 7.3.1

If the plastic slip contribution in Eq. (7.11) and the net elastic strain energy in Eq. (7.16) completely account for the total system energy, then their sum $\Delta\Pi_\delta + \Delta\Pi_{el}$ as shown in Fig. 7.11c (blue curve) should recover the smooth energy profile of the NEB simulation (red curve). There, $\Delta\Pi_{pl} + \Delta\Pi_{el}$ is smooth except for a step drop in energy for the stretch of the pathway between replicas 5 and 16, which indicates there is a step-like contribution not yet included. Replica 5 roughly corresponds to the initial appearance of the dislocation loop, the two corners of which are at an angle with respect to the straight crack front (conceptually shown in Fig. 7.2(ii)). These “kinks” are likely associated with some energetic cost, which results in a rapid rise in the energy early on in the emission process, persisting through subsequent lateral bow-out of the loop. The corners of the loop eventually meet and self-annihilate in the periodic crack front (e.g. Fig. 7.2(iv)) so that the original energy cost (of formation) is recovered and the energy rapidly decreases in response. A straight dislocation configuration (e.g. Fig. 7.2(v)) is observed around replica 16 at the end of the energy drop in Fig. 7.11c. This energy cost/recovery is conceptually step-like, so we approximate a smooth step function $U_{step} = 1$ eV by inspection so that the resulting sum $\Delta\Pi = \Delta\Pi_\delta + \Delta\Pi_{el} + U_{step}$ is relatively smooth and the curve resembles the NEB energy profile. Since U_{step} is on the order of the emission barrier, it requires further study to accurately quantify but is outside the scope of this study.

7.3. Energy of emission in the atomistic system

Including U_{step} , we then have a semi-analytical expression estimating the change in system energy using atomistic quantities which is written

$$\begin{aligned}\Delta\Pi^{(r)} &= \Delta\Pi_{\delta}^{(r)} + \Delta\Pi_{el}^{(r)} + U_{step} \\ &= \sum_{\alpha \in 0^+, 0^-} U_{\delta}^{\alpha(r)} - W_{\delta}^{\alpha(r)} + U^{el} \left(\Delta\sigma^{\alpha(r)} - \tau_{\delta}(\Delta^{\alpha}) \right) \\ &\quad - \sum_{\alpha \notin 0^+, 0^-} U^{el} \left(\Delta\sigma^{\alpha(r)} \right) + U_{step}\end{aligned}\tag{7.17}$$

For the *A*-alloy, Eq. (7.17) does not perfectly reproduce the NEB energy as we see in Fig. 7.11c. The uphill part of the estimated energy shows reasonable correspondence to the NEB, and we recover a similar magnitude in the energy barrier using the maximum of $\Delta\Pi$, which is in the neighborhood of the NEB saddle point.

There are several sources of error in Eq. (7.17) which we describe following. $\Delta\Pi$ is semi-analytical and so depends on the processing of atomic quantities. For example, there is error associated with converting the atomistic displacements into Δ , e.g. here using interpolation, which determines where each atom is precisely along its GSF curve, so there is uncertainty if the magnitudes of U_{δ} , W_{δ} , etc. map exactly to that atomic configuration. The GSF curve itself is a global quantity and due to the atomic interactions over some distance, but we have interpreted it locally, so there could be differences due atomic-scale gradients in the slip. In Fig. 7.11c, the atomic configuration before the saddle point yields the maximum of the $\Delta\Pi$ curve so we have overestimated Δ somewhat. There is also some geometric change associated with blunting which reduces the apparent Δ when the dislocation is well past the instability and thus lowers the energies obtained with Δ beyond the saddle point (note the dip in the energy plateau after replica 17 in Fig. 7.11a). Furthermore, the individual quantities of U_{δ} , W_{δ} , and also the elastic energies are generally an order of magnitude larger than the energy barrier we are hoping to capture. We use the differences between large numbers, e.g. $U_{\delta} - W_{\delta}$ and $U_{el}|_{\alpha \in 0^+, 0^-} - U_{el}|_{\alpha \notin 0^+, 0^-}$, so this generally does not give very high resolution/accuracy.

All in all, Eq. (7.17) does not exactly reproduce the NEB energy given the atomistic configuration but nevertheless captures the major energetic contributions to the emission process which, to summarize, include (i) a balance between plastic slip and stress-work, (ii) the elastic strain energy inside vs. outside the slip plane, and (iii) some remaining energy likely associated with the dislocation loop-crack interaction. We are presently verifying these energy contributions of the emission process in the random system as we have done for the *A*-alloy.

7.3.1 Misfit volume/crack interaction

The misfit volume of the elemental components in an alloy causes atomic positions to deviate from their exact lattice positions [130]. Atomic misfit volume is a particularly important feature in HEAs since these “microdistortions” have been shown in DFT studies to be connected with strength [128, 129]. Misfit volume is also a key quantity appearing in solute strengthening models (e.g. [9, 130, 131]), where the interaction between an element n solute with misfit volume ΔV_n , and a defect (e.g. a dislocation) associated with pressure field $p(x_1, x_2)$ produces an elastic contribution $-p(x_1, x_2)\Delta V$ in addition to a chemical interaction. Misfit volumes in HEAs are most accurately determined by first-principles methods e.g. DFT, but Maresca and Curtin [8] show for MoNbTaW and MoNbTaVW that DFT-computed misfit volumes closely follow Vegard’s law, $\Delta V_n = V_n - \bar{V}$ where V_n are the element n atomic volumes, $\bar{V} = \sum_n c_n V_n$ is the alloy atomic volume, and $\sum_n c_n \Delta V_n = 0$ by construction. Misfit volumes for the model MoNbTi alloy (based on the EAM-type Zhou et al. [1] family of interatomic potentials) estimated following Vegard’s law are shown in Table. 7.1.

Table 7.1: Misfit volume following Vegard’s law for the model MoNbTi HEA.

n	c_n	V_n (Å ³)	ΔV_n (Å ³)
Mo	0.33	15.630	-1.515
Nb	0.33	17.967	0.823
Ti	0.33	17.830	0.692
\bar{V}		17.145	

The atoms in a cracked HEA system have misfit volumes and are in a stressed state due to the crack tip fields. The fields corresponding to the initial unslipped crack configuration for load K_I evolve with accumulating dislocation slip over the emission pathway as seen in the A -alloy (e.g. Fig. 7.11b showed U_{el} from changes in virial stress). Drawing a parallel from solute strengthening theory, there is an elastic contribution from the interaction between the atomic misfits and the crack pressure field. The *change* in misfit energy of a slipped configuration r relative to the unslipped state 0 is

$$\Delta U_{mis}^{(r)} = U_{mis}^{(r)} - U_{mis}^{(0)} = \sum_{\alpha} -\Delta p^{\alpha(r)} \Delta V_n^{\alpha} \quad (7.18)$$

where $\Delta p^{\alpha(r)} = p^{\alpha(r)} - p^{\alpha(0)}$ is the crack pressure change of n -type atom α ’s throughout the system.

Previously for the A -alloy in Sec. 7.3, we separated the elastic strain energy contribution of the slip plane atoms from the rest of the crack body. The stress change of each individual atom outside of the slip plane/immediate vicinity of the crack tip is generally very small, but the cumulative contribution of the many atoms in the system is a large and significant energy contribution to the emission process and comparable to the contribution from the slip plane atoms. In Eq. (7.18), pressure is the hydrostatic part

7.3. Energy of emission in the atomistic system

of the stress σ , so we expect the atomic misfit-crack pressure interaction will also be non-negligible.

As a preliminary result, in Fig. 7.12 misfit energies are obtained by combining the pressure field from the A -atom emission pathway with the configurations of atomic misfit volumes corresponding to the random alloy environments. Recalling Sec. 7.2, the set of starting chain of replicas $\{P_n^R\}$ for the NEB simulations for each random environment R contains the A -alloy crack/dislocation geometry within a random configuration of atom element types. For each random environment, Fig. 7.12 shows the misfit energy of the *starting* pathway of the dominant configuration (which produces the lowest emission energy in that random environment). There are thus not exactly the misfit energy for the random emission pathways, but we can nevertheless make some preliminary observations.

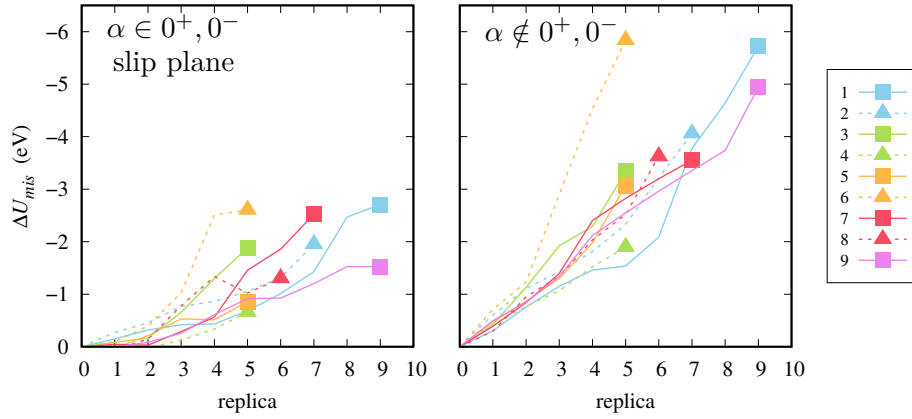


Figure 7.12: The misfit energy ΔU_{mis} of the A -atom emission pathway with random configurations of atomic misfit volume. ΔU_{mis} of the slip plane atoms ($\alpha \in 0^+, 0^-$) and for the remaining crack body ($\alpha \notin 0^+, 0^-$) is obtained from the A -alloy pressure field along the chain of replicas (truncated at the saddle point) and the atomic misfit volumes for the random environments corresponding to Fig. 7.4. The saddle point energy is denoted by the filled markers.

This "mixed" misfit energy is generally negative and likely reduces the excess (total) energy of the system, which is qualitatively consistent with the reduction of the emission energy barriers observed in the random systems relative to the A -alloy. Recalling Eq. (7.17) which contains the major energy contributions for emission in the average system, ΔU_{mis} is an additional term on the right-hand side that is completely exclusive to alloys since homogeneous systems fundamentally do not have atomic misfit. Here in Fig. 7.12, the variation in ΔU_{mis} (standard deviation ~ 2 eV) by varying only the random environment and not the pressure field is comparable to the emission energy barrier itself (~ 3 eV), and so ΔU_{mis} is likely an important energy contribution to the emission barrier. In the real random environment, the system will find an emission pathway such that the total energy includes the variation in ΔU_{mis} , and this energy change also competes with the variations of the other contributions (e.g. slip energy, stress-work) due to

the random environment. At this point, the misfit energy and its variation appears to be the key factor behind the large variations in the emission energy barrier. Part of the ongoing work is to characterize the distribution of ΔU_{mis} , first numerically using a large number of random environments, and then statistically to incorporate into an eventual theory.

7.4 Discussion

Bcc refractory HEAs are desirable as structural materials due to their high strengths and excellent high temperature strength retention but are generally quite brittle and intrinsically brittle as well. The refractory elements (Nb, V, Ta, Cr, Mo, W) are quite brittle at low temperatures (low fracture toughness and failure strain) but exhibit a relatively sharp brittle-to-ductile transition (BDT) with increasing temperature. While more ductile elements (e.g. Nb and V) ductilize at low/ambient temperatures, the more brittle elements providing high strength (e.g. Mo and W) only ductilize above room temperature (RT), and the BDT of the alloys is a mixture of the elemental behavior. Identification of new alloy compositions with high strength and high temperature strength retention but also good RT ductility is one current goal driving alloy development. In the very large composition spaces of HEAs especially, efficient broad screening is necessary to identify candidate ductile compositions for fabrication and further testing. The athermal intrinsic ductility criterion $D < 1$ is poorly suited to screen for low/ambient temperature ductility of brittle HEAs. For this reason, initial efforts have been made to identify a criterion for RT ductility with a critical value of $D_c > 1$ [26]. The compositions of interest likely have borderline ductility, since strength and ductility are generally inversely related, so it is important to refine the screening criterion as best as possible.

Many bcc HEAs are intrinsically brittle and have very large and completely insurmountable emission barriers $\Delta \bar{E}_e$ compared to cleavage barriers $\Delta \bar{E}_c$ based on their average properties. From atomistic simulation we observe that (i) a true random system can likely find many more-favorable than average pathways for emission, and (ii) many of these pathways correspond to significantly lower than average energy barriers. Despite brittle behavior on average, the local emission barrier ΔE_e^* can be lower than the cleavage barrier ΔE_c , thus enabling a local cross-over from brittle to ductile behavior. Less-favorable local environments do not negatively impact ductility since the average behavior still limits the ductility. Noting that only a single emission event is required for intrinsic ductility overall, and a real moving crack tip likely encounters many locally emission-favorable environments, the variations in the random system always improves ductility relative to average behavior or in a homogeneous system. Theory predictions of ductility in HEAs and random alloys in general using average material properties, e.g. average USF $\bar{\gamma}_{usf}$, will always be conservative (i.e. material is more ductile than predicted).

The exact atomic configuration of an incipient dislocation depends on the interaction between spatially varying material properties and the crack tip fields. The slip, which is connected to the USF energy, and the stress, which is connected to the stiffness, are closely interlinked since the material properties themselves are connected by the underlying composition. The true random alloy shows relatively small variations ($\sim 10\%$) of critical material properties (γ_{usf} , μ , etc.) at the scale of the dislocation loop. In the average theory, variations in the USF are directly connected to the energy barrier, but in simulation, variations in local ΔE_e^* do not scale solely with variations to local γ_{usf}^* (e.g. Fig. 7.10). The conceptual relationship between USF energy and emission barrier does not transfer to a local scale of the fluctuations, and the fluctuations of γ_{usf}^* is not the key feature behind the reduced energy barriers in the random vs. average material. We are unable to definitely predict the improved ductility in the random system based on local γ_{usf}^* unfortunately. Predictions with average properties, e.g. with $\bar{\gamma}_{usf}$, nonetheless remain an effective broad-screening criterion.

The atomic misfit volume is an inherent feature of HEAs which is known to be connected to strengthening. Other than the misfit volume, the homogeneous A -alloy and the random alloy studied here are otherwise equivalent in terms of average material properties. The interaction between misfit volume and crack fields is a critical aspect of the emission process in random HEAs since its energy contribution shifts the energy balance in the average system so that large changes to the excess energy, which is the emission barrier, are possible. It is very important that misfit volume is captured accurately by alloy interatomic potentials, which is important point to note when selecting a potential for alloy fracture simulations or when developing new potentials. Variations in the misfit energy are key to improving ductility – the atomic compositional configurations producing misfit energies which reduce the emission barrier improve ductility overall. Variations in the misfit energy are maximized by maximizing the amount of misfit. Suppose two HEA compositions produce the same average material properties ($\bar{\gamma}_{usf}$ and \bar{C}_{ij} , for example) but have different average volume misfit, i.e.

$$\langle \Delta V \rangle = \frac{1}{n} \sum_n |\Delta V_n| \quad (7.19)$$

for n number of constituent elements. We expect the one with larger average misfit relative to the average alloy atomic volume, i.e. $\langle \Delta V \rangle / \bar{V}$, to produce more variation in the possible misfit energy and so producing emission behavior that deviates more strongly from the A -alloy behavior. A possible supplementary criterion for screening or design is thus for large average misfit volume.

We have showed some preliminary connections between the fluctuating composition and local material properties, e.g. γ_{usf}^* . However, in order to develop a fully analytic theory capturing the variation/reduction of the energy barrier in the random alloy relative to the average material, we need to stochastically connect the compositional disorder

to variations in the material properties, and then to variations in the major energetic contributions – this is part of our ongoing work.

7.5 Summary

In HEAs the compositional disorder produces spatial variations in the material properties, and structural “microdistortions” arise from the atomic volume misfit of the elemental components. From atomistic simulation of a model random MoNbTi HEA system, we observe deviations in local emission behavior compared to the average behavior which improve ductility overall. Local emission-favorable environments along a random crack front correspond to potentially large reductions to the local emission barrier, enabling possible local crossover from brittle to ductile behavior even if the material is brittle on average. The USF energy, stress intensity for emission, and emission energy barrier are conceptually connected by the average theory, but these same connections do not translate to the scale of the fluctuations and cannot relate variations in the USF energy to variations in the local emission energy. The emission energy consists of a balance of plastic slip energy and stress-work, and the elastic strain inside vs. outside of the atomistic slip plane. Interaction between atomic misfit volume and the crack fields is key to introducing large variations to the emission energy. Identification of new HEA compositions with attractive strength properties but also good low/ambient temperature ductility is one current goal driving alloy development. Theory predictions based on average behavior/material properties remain very effective for broad screening but will always be conservative (i.e. materials are more ductile). Part of the ongoing work is quantifying the stochastic variations of the energy contributions as a function of the compositional disorder and is necessary to develop an analytic theory to predict the deviations of the emission energy, which is the random effect on intrinsic ductility. A supplementary screening criterion for large average misfit volume can potentially provide more detailed screening in the meantime.

8 Conclusion

Complex alloys such as the class of HEAs can possess very desirable mechanical properties (e.g. high strength and excellent high temperature strength retention) which make them attractive as structural materials if not their poor fracture properties. We have only just recently begun to understand the connections between strength, temperature, and composition in these complex systems. The connections between composition and fracture properties, e.g. ductility and fracture toughness, are not well-understood, but this knowledge is critical to develop this class of materials for industrial applications. The macroscopic ductility and toughness of a crack is connected to an atomistic competition between brittle cleavage and ductile dislocation emission crack tip mechanisms. In this thesis we have studied the atomistic crack tip in three model alloy environments of increasing complexity: first in a random but dilute “conventional” Mg-Y alloy, then in averaged (*A*-alloy) representations of complex HEAs, and finally in a true random HEA system. We reiterate some of the key observations presented earlier and discuss the future outlook in this avenue of research.

The cleavage and dislocation emission crack tip mechanisms are thermally activated and correspond to load- and temperature-dependent energy barriers of activation. The crack tip competition is captured by intrinsic ductility $D = K_{Ie}/K_{Ic}$ based on the critical stress intensities for emission and cleavage, K_{Ie} and K_{Ic} , respectively, where the stress intensities correspond to the zero-energy barriers. Intrinsic ductility can thus also be expressed as a competition between the magnitude of the energy barriers for emission and cleavage (at K_{Ic}), and a cross-over from brittle to ductile behavior is possible through reduction of the emission barrier. Intrinsic ductility represents the ability of an atomistic crack tip to emit a dislocation, which is the necessary precursor for subsequent ductile mechanisms producing macroscopic ductility.

In the Mg-Y system, the solutes introduce distinct local deviations to the base material, e.g. structural distortions and local stress fields, due to their volume misfit so that cracks deviate from the ideal behavior even with only a dilute amount of solutes. Although

this can lead to significant toughening by dislocation emission, the atomistic simulations reveal that dilute alloying is unlikely to fundamentally change the fracture nature of the majority base material, especially that of highly brittle materials such as Mg. This illustrates the main constraint of conventional alloys to the behavior of the principal base material.

In contrast, the new class of HEAs which have multiple principal components cover a broad composition space and have the potential for a large spectrum of material properties and behavior. Many refractory HEAs are very strong but generally brittle and also intrinsically brittle with very large and completely unsurmountable energy barriers for emission compared to energy barriers for cleavage on average. In a random system, variations between local vs. average material properties arise from compositional disorder, and structural “microdistortions” are produced from the atomic misfit volume of the elemental components. Dislocation emission is by nature a nucleation event and thus perceives local environments within a random system. Significant reductions in local emission energy (compared to average emission energy) are possible in the random system, signifying the potential for local crossover from brittle to ductile behavior at local emission-favorable environments even if an alloy is brittle based on its average properties. The average theory conceptually connects emission energy, critical stress intensity, and material properties, but these connections do not translate to the scale of the atomic fluctuations. The misfit volume, which is also connected to strengthening in HEAs, plays a critical role in introducing variations to the emission energy.

Identification of new alloy compositions with attractive structural properties (e.g. high strength, high temperature strength retention) but also good RT ductility remains a challenge, especially in broad compositional space of HEAs. Intrinsic ductility D has been proposed as a broad screening criterion for ductility since it is a straightforward criterion requiring only a few material properties (C_{ij} , γ_{usf} , γ_s) which can be accurately and relatively simply obtained using first-principles methods, e.g. DFT. One notable observation is that LEFM is quite a good qualitative predictor of the crack behavior in alloys even if the interatomic potentials are not entirely quantitative, and this enables us to extract trends in the relative ductility between similar alloys comparable to experimental observations. We show that scaling of interatomic potential properties to DFT requires some additional effort up front, but then can be used to harness cheaper methods such as MD/MS to quantitatively approximate the material properties and predict D over entire alloy families. Extending from D , we also propose a room temperature criterion D_c which is more effective for screening for low/ambient temperature ductility of the generally brittle refractory HEAs. The theory only accommodates for the average chemistry from average material properties and yield conservative (i.e. more brittle) predictions of ductility for random alloys. Nevertheless, application of the criterion D and D_c can broadly identify candidate ductile alloy compositions for fabrication, testing, and further study in an efficient manner.

There are several necessary extensions to the presented studies. We have semi-analytically identified the major energetic contributions to the emission process and have deterministically showed preliminary connections between fluctuating composition and local material properties. Our ongoing work involves connecting the stochastic compositional disorder, first to the variations in local material properties, and then to the variations in the energy contributions. This is necessary to develop a fully analytic theory describing the energy variations associated with the inherent randomness in a system. The interaction of misfit energy and the crack (pressure) fields is a particularly critical piece of this analysis, and we can draw from recently developed solute strengthening theories where the misfit-defect interaction is also a key energetic quantity. Another point of extension is the detailed study of the temperature-dependence of the critical material properties, which may lead to a change from brittle to ductile behavior and so can be important to capture the subtleties in alloy compositions with borderline ductility. Augmenting the current D and D_c criterion by including the random effect and temperature dependence is necessary to refine the screening criterion and accurately classify alloy compositions even with borderline ductility.

The accuracy of the interatomic potentials is paramount for any atomistic simulation. The development of accurate and general-purpose interatomic potentials, e.g. with machine learning methods, is ongoing work. Some excellent potentials for metal elements and simple alloys have been produced recently (e.g. Mg [94], Al-Cu [92]) or are in late stages of development (e.g. Zr [203]). We still lack good potentials for complex alloy systems but machine learning appears to be one of the most likely avenues for developing comprehensive and high accuracy interatomic potentials for complex alloys. In the meantime, we can utilize the current methods, e.g. the NEB methodology presented in this thesis, to circumvent some of the problematic aspects of the presently available interatomic potentials. The NEB calculations conducted in this thesis utilize standard NEB methodology as implemented in LAMMPS as a proof of concept. The 3d crack calculations are quite computationally expensive so if they are to be conducted in larger quantities, e.g. to fully validate stochastic effects, optimization of the NEB calculations would be beneficial. Improvements include, for example, optimization of the reaction path to improve MEP convergence or refining the saddle point search using for example the Dimer method [204]. Overall, we can apply these methods in tandem with recent existing methods for yield strength [8, 9], considering also the thermodynamic properties (e.g. with computer calculation of phase diagrams (CALPHAD) methodology [205]), to enable the computationally-guided design of strong and ductile alloys.

Appendix

These appendices are extracted from the following publications

1. Mak, E., & Curtin, W. A. (2020). Intrinsic fracture behavior of Mg–Y alloys. *Modelling and Simulation in Materials Science and Engineering*, 28(3), 035012
2. Mak, E., Yin, B., & Curtin, W. A. (2021). A ductility criterion for bcc high entropy alloys. *Journal of the Mechanics and Physics of Solids*, 152, 104389
3. Mak, E., & Curtin, W. A. (2021). Randomness and intrinsic ductility in High Entropy Alloys. *Under preparation*

A.1 Material properties and anisotropic elastic parameters of Mg and Mg-Y

Average elastic constants were determined with 50 random realizations of a 256-atom periodic cell (Table. A.1). Component C_{44} softens by 4% compared to Mg, with the remaining components relatively unchanged ($< 1\%$).

Table A.1: Elastic constants calculated for Mg and Mg-Y.

(GPa)	Mg	Mg-Y
C_{11}	64.27	63.68
C_{12}	25.45	26.40
C_{13}	20.86	20.26
C_{33}	70.93	70.15
C_{44}	18.02	17.29

The quantities of Λ_{22} , used to determine the K_{Ic} (Eq. 1.24), and the anisotropic parameter $o(\theta, \varphi)$, used to determine K_{Ie} and K_{Ie}^{trail} (Eq. 2.11, 2.15) are presented in Table. A.2.

Appendix

Table A.2: Anisotropic elastic properties for Mg and Mg-Y. Quantities for Mg-Y based on the average elastic constants.

Orientation	Comp.	Λ_{22}	$o(\theta, \varphi)$
Basal I	Mg	0.01742540	55.44598236
	Mg-Y	0.01780702	54.21698990
Basal II	Mg	0.01742540	56.63453325
	Mg-Y	0.01780702	55.42777703
Prism I	Mg	0.01829787	54.65117664
	Mg-Y	0.01868975	53.50525576
Prism II	Mg	0.01829787	50.33182938
	Mg-Y	0.01868975	49.10509913
Pyramidal I	Mg	0.01810451	54.65117664
	Mg-Y	0.01849412	53.50525576
Pyramidal II	Mg	0.01805779	50.33182938
	Mg-Y	0.01844685	49.10509913
Tensile twin I	Mg	0.01788996	57.38747914
	Mg-Y	0.01827705	56.15762787
Tensile twin II	Mg	0.01788996	57.38747914
	Mg-Y	0.01827705	56.15762787

A.2 Material parameters of bcc refractory elements and alloys

The elastic moduli of selected bcc refractory elements (Mo, Nb, Ta, V, W) are shown in Table A.3. We compare the Zhou et al. [1] EAM interatomic potential against first-principles/DFT studies and experimental literature from various sources as indicated. The $T = 0$ K experimental moduli are used in Section 6.2. The Zener anisotropy ($a_r = 2C_{44}/(C_{11} - C_{12})$) is calculated from the reported elastic moduli. For these elements, there is reasonable correspondence between EAM, DFT, and experiments. However, the DFT C_{44} is consistently underestimated; this is historically well-known [188]. Thus, the EAM potential provides a better description of the material anisotropy. Elements Ti and Zr, also shown in Table A.3, are hcp at low temperatures but bcc at high temperatures. It is likely that the EAM potentials that are fit to hcp properties yield spurious large anisotropy for alloys with high Ti and/or Zr content.

A similar comparison of the elastic moduli is presented for MoNbTaW, MoNbTaVW, and NbTiZr HEAs in Table A.4. The DFT value of C_{44} is also likely an underestimate for these alloys. Since the elastic moduli of the bcc refractory elements (Mo, Nb, Ta, V, W) from the EAM potential are accurate, the EAM elastic constants of MoNbTaW and MoNbTaVW are also likely accurate and supported by good comparisons of C_{11} and C_{12} versus DFT [8]. In contrast, as for Ti and Zr, the EAM-predicted anisotropy

A.2. Material parameters of bcc refractory elements and alloys

Table A.3: Elastic moduli and the Zener anisotropy of selected bcc refractory elements obtained from the EAM potential, and selected First-principles/Density Functional Theory (FP/DFT) and experimental (Expt.) literature.

Element	Data	a Å	C_{11} GPa	C_{12} GPa	C_{44} GPa	a_r
Mo	EAM	3.150	457	167	113	0.78
	FP/DFT [109, 188, 206]		469	162	101	0.66
	Expt. ($T = 300$ K) [207–210]		466	163	109	0.72
	Expt. ($T = 0$ K) [189]		450	173	125	0.90
Nb	EAM	3.300	262	125	36	0.52
	FP/DFT [109, 188, 206, 211, 212]		246	136	15	0.27
	Expt. ($T = 300$ K) [207, 213–215]		246	133	28	0.51
	Expt. ($T = 0$ K) [190]		253	133	31	0.52
Ta	EAM	3.303	263	158	82	1.57
	FP/DFT [188, 216, 217]		271	161	76	1.40
	Expt. ($T = 300$ K) [189, 207, 214]		265	160	82	1.57
	Expt. ($T = 0$ K) [189]		266	158	87	1.62
V	EAM	3.026	264	119	38	0.52
	FP/DFT [188, 206, 211, 212]		268	139	21	0.32
	Expt. ($T = 300$ K) [191, 207, 213, 214, 218–220]		230	120	43	0.78
	Expt. ($T = 0$ K) [191]		238	122	47	0.81
W	EAM	3.165	523	204	161	1.01
	FP/DFT [188, 221]		508	206	143	0.95
	Expt. ($T = 300$ K) [189, 207, 208, 222, 223]		524	204	160	1.00
	Expt. ($T = 0$ K) [189]		533	241	199	1.37
Ti (bcc)	EAM	3.292	120	109	77	13.82
	FP/DFT [206, 211, 212]		91	114	40	-3.62
	Expt. ($T > 1200$ K) [224]		110	93	36	4.27
Zr (bcc)	EAM	3.590	113	101	65	10.98
	FP/DFT [206, 211, 212]		83	92	32	-7.21
	Expt. ($T > 1200$ K) [225]		100	82	38	4.86

of NbTiZr is likely too large.

Table A.4: Elastic moduli and the Zener anisotropy of the selected HEAs obtained from the EAM potential and selected First-principles/Density Functional Theory (FP/DFT) literature.

Alloy	Data	a Å	C_{11} GPa	C_{12} GPa	C_{44} GPa	a_r
MoNbTaW	EAM	3.221	352	174	96	1.08
	FP/DFT [8]	3.237	374	163	64	0.61
	DFT CPA-EMTO [184]		412	185	71	0.63
MoNbTaVW	EAM	3.200	310	158	83	1.10
	FP/DFT [8]	3.192	338	164	51	0.59
	DFT CPA-EMTO [184]		371	178	52	0.54
NbTiZr	EAM	3.396	148	111	61	3.36
	FP/DFT [226]	3.390	143	96	29	1.23

Giannattasio and Roberts [3] investigated the fracture toughness of single-crystal W (see Fig. A.1). For the $\{100\}\langle 001 \rangle$ crack orientation, i.e. 100/110, a linear extrapolation of

the available data ($\ln K_I$ versus T) to $T = 0$ K yields an athermal cleavage toughness of $2.198 \text{ MPa}\sqrt{\text{m}}$. In Section 6.2, we obtain a prediction of $K_{Ic} = 1.950$ for W in this orientation based on DFT energies and athermal experimental elastic moduli.

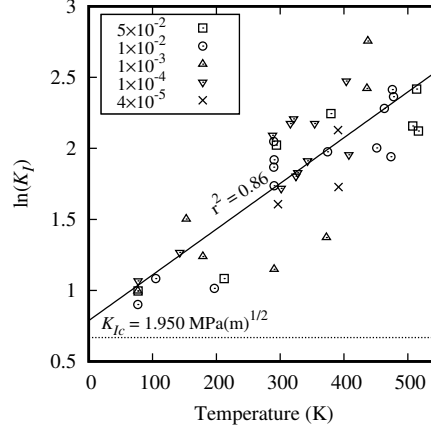


Figure A.1: Brittle fracture toughness K_I versus temperature of W in the $\{100\}\langle 001 \rangle$ crack orientation at varying strain rates [3]. An athermal cleavage toughness of $2.198 \text{ MPa}\sqrt{\text{m}}$ estimated by linear extrapolation to $T = 0$ K (solid line) shows good correspondence to the DFT-based LEFM prediction of $K_{Ic} = 1.950 \text{ MPa}\sqrt{\text{m}}$ (dashed line).

A.3 DFT methodology for bcc HEAs

DFT computations¹ as implemented in the VASP code [227] are performed using the PBE functional [228]. The core electrons are replaced by the projector augmented wave (PAW) pseudopotentials [229]. The valence-electron eigenstates are expanded using a plane-wave basis set with a cutoff energy of 550 eV. In reciprocal space, a Γ -centered Monkhorst–Pack [230] k-mesh is used with line density consistent across all geometries. The interval between the neighboring k-points along each reciprocal lattice vector is $0.04\pi \text{ \AA}^{-1}$. The first-order Methfessel–Paxton [231] method is used to smear the single-particle eigenstates, with a smearing parameter of 0.2 eV. Ionic forces are relaxed to $< 3 \text{ meV \AA}^{-1}$.

To construct the HEA supercells, we first use special quasi-random structures (SQSs) [232] (~ 100 atoms per SQS) to determine the average lattice constant a_{alloy} of the HEA. Then we use the a_{alloy} to construct the HEA bcc bulk structures with larger dimensions (360 atoms per supercell) with the plane of interest, i.e. for the stacking fault or surface, as the a_1 - a_2 plane.

¹The DFT computations presented in work were performed by Dr. Binglun Yin who at the time was a postdoctoral researcher in the Laboratory for Multiscale Mechanics Modeling at EPFL, Switzerland.

A.4. Mixed-mode ductility criterion

The calculations of planar defects always requires fixing the in-plane lattice dimensions (a_1 , a_2) during relaxation. Given that (i) the supercell is quite large, and (ii) the USF energy and surface energy are not very sensitive to the in-plane lattices constants, we thus hold the in-plane lattices at the pristine bcc value a_{alloy} . Therefore, in the relaxation of the bulk HEA, we relax only the out-of-plane lattice a_3 to release the σ_{3j} stress components, while all atoms positions are fully relaxed. The USF and surface structures are then created based on this relaxed bulk structure.

The USF structure is created by tilting the a_3 supercell vector by the desired USF fault vector while keeping the atoms fixed in the relaxed Cartesian coordinates. Then a_3 and all the atoms are relaxed only in the direction normal to the SF plane such that $\sigma_{33} = 0$, which is needed to account for inelastic displacements associated with the SF [186, 233]. The free surface structure is created by extending a_3 in the direction normal to the surface, introducing a vacuum layer. Again, all the atoms are fixed to the relaxed Cartesian coordinates. The supercell vectors are fixed and all the atoms are fully relaxed. Our surface energies and USF energies determined according to this methodology are presented in Table A.5 along with recent results by Li et al. [184].

Table A.5: Surface energies γ_s and USF energies γ_{usf} used in the LEFM analysis of four equiatomic HEAs. Energies are reported in units of J/m².

Alloy		DFT	DFT unrelaxed	DFT CPA-EMTO [184]	EAM
NbTiZr	γ_s 100	–	1.841	–	1.767
	γ_s 110	–	1.795	–	1.531
	γ_{usf} 110	–	0.346	–	0.463
	γ_{usf} 112	–	0.415	–	0.526
MoNbTi	γ_s 100	2.317	2.568	–	2.087
	γ_s 110	2.174	2.245	–	1.804
	γ_{usf} 110	0.820	0.893	–	0.725
	γ_{usf} 112	0.927	0.977	–	0.812
MoNbTaVW	γ_s 100	3.012	3.393	3.477	2.479
	γ_s 110	2.645	2.673	2.909	2.053
	γ_{usf} 110	1.176	1.337	1.448	0.979
	γ_{usf} 112	1.215	1.581	1.447	1.115
MoNbTaW	γ_s 100	3.188	3.577	3.667	2.530
	γ_s 110	2.684	2.776	2.943	2.156
	γ_{usf} 110	1.286	1.555	1.584	1.034
	γ_{usf} 112	1.325	1.738	1.602	1.198

A.4 Mixed-mode ductility criterion

The addition of mode II and/or mode III shear loading affects the critical stress intensities for cleavage and emission. The thermodynamics in mixed-mode cleavage considers

the total energy release rate of the mixed-mode loading, i.e.

$$G \equiv \frac{(1 - \nu)(K_I^2 + K_{II}^2) + K_{III}^2}{2\mu} \quad (8.1)$$

in the isotropic case, which is balanced by the critical energy for surface creation, i.e. $G = G_c = 2\gamma_s$. The mixed-mode critical stress intensity for cleavage, compared to the mode I-only stress intensity (K_{Ic}), is

$$\frac{K_{Ic}^{mix}}{K_{Ic}} = \left[1 + \left(\frac{K_{II}}{K_I} \right)^2 + \frac{1}{1 - \nu} \left(\frac{K_{III}}{K_I} \right)^2 \right]^{-1/2} \quad (8.2)$$

Using the constrained path approximation, Rice [30] provides the isotropic formulation for emission on an inclined slip plane at $\theta > 0$ with the Burgers vector angled at ϕ with respect to the crack front normal. The mixed-mode critical stress intensity for emission, compared to the mode I-only stress intensity (K_{Ie}), is

$$\frac{K_{Ie}^{mix}}{K_{Ie}} = \left[1 \pm \frac{K_{II}}{K_I} \left(2 \csc \theta - 3 \tan \frac{\theta}{2} \right) \pm 2 \frac{K_{III}}{K_I} \csc \theta \tan \phi \right]^{-1} \quad (8.3)$$

From Equation (8.2), the decrease in the critical stress intensity for cleavage by mixed-mode loading scales $\sim 1/s^2$, where s is the amount of shear. In comparison, from Equation (8.3), the scaling is $\sim 1/s$. Consequently, we generally expect mixed-mode loading to improve ductility, since the critical stress intensity for emission decreases faster than for cleavage. The mixed-mode ductility index, compared to the mode I-only index (D), is

$$\frac{D^{mix}}{D} = \frac{K_{Ie}^{mix}}{K_{Ie}} \left[\frac{K_{Ic}^{mix}}{K_{Ic}} \right]^{-1} = \frac{\sqrt{1 + \left(\frac{K_{II}}{K_I} \right)^2 + \frac{1}{1 - \nu} \left(\frac{K_{III}}{K_I} \right)^2}}{1 \pm \frac{K_{II}}{K_I} \left(2 \csc \theta - 3 \tan \frac{\theta}{2} \right) \pm 2 \frac{K_{III}}{K_I} \csc \theta \tan \phi} \quad (8.4)$$

which is illustrated in Fig. 6.3 for the crack orientations studied.

A.5 Atomistic energy in rigid block shear

Rice [30] describes the scenario where one half-block of material is rigidly sheared relative to the other half-block along a slip plane forming a stacking fault (see Fig. A.2a). In the atomistic system, the relative displacement between two layers of atoms spaced at distance h is Δ , and Δ includes an elastic contribution Δ_{el} associated with the discrete lattice [30], i.e.

$$\Delta = \delta + \Delta_{el} \quad (8.5)$$

where δ is the shear displacement across a continuum cut plane of zero-thickness associated with the stacking fault. The shear resistance to the sliding is τ and is periodic according to the Peierls concept [49] – and the simplest approximation of τ is the Frenkel sinusoid (Eq. (2.1)). The shear potential is an integral of the shear resistance over the slip, i.e. $\Psi(\Delta) = \int \tau d\Delta$, and the energy of slip for a slip surface of area A and USF energy γ_{usf} is [30]

$$U_{\Delta} = A\Psi(\Delta) = A\gamma_{usf} \sin^2 \left(\frac{\pi\Delta}{b} \right) \quad (8.6)$$

where b is the Burgers vector, and Δ is the relative slip of the two half-blocks. The total energy change of the system in rigid shear is purely from slip and the creation of a stacking fault and so is the generalized stacking fault (GSF) energy and is approximated by U_{Δ} in Eq. (8.6) (see Fig. A.2b (bottom)).

The discrete form of U_{Δ} sums the contributions from the atoms α on the layers of slip plane atoms directly adjacent to the stacking fault (notated as 0^+ , 0^- , also see Fig. A.2a) since the atoms in the rigidly displacing parts of the block do not experience relative slip. The potential energy is connected to the atomic forces, recalling Eq. (3.1)). U_{Δ} is *exactly* obtained from the atomic forces, e.g.

$$U_{\Delta} = - \sum_{\alpha \in 0^+} \int f_{\Delta}^{\alpha}(\Delta) d\Delta \equiv - \sum_{\alpha \in 0^+, 0^-} \int f_{\Delta}^{\alpha}(\Delta) d(\Delta/2) \quad (8.7)$$

where f_{Δ}^{α} is the component in the direction of slip of the force vector \mathbf{f}^{α} for atom α . In the above, considering the bottom half-block as fixed and prescribing a shear displacement of Δ to the top half-block, the force (per unit displacement) of the atoms in the upper block (i.e. $\alpha \in 0^+$) is integrated over Δ . Equivalently, if Δ is shared between the two half-blocks, i.e. both blocks each displace $\Delta/2$, yields the right-most term in Eq. (8.7). The discrete counterpart of Eq. (8.6) requires atomic slip Δ^{α} (rather than displacements). The slip of top half- relative to the bottom half-block is equivalent to the slip of the bottom half- to the top half-block, i.e. $\Delta = \Delta^{0+} = \Delta^{0-}$. The discrete form of Eq. (8.6) is

$$U_{\Delta} = \frac{1}{2} \sum_{\alpha \in 0^+, 0^-} A^{\alpha} \gamma_{usf} \sin^2 \left(\frac{\pi\Delta^{\alpha}}{b} \right) \quad (8.8)$$

where $A^{\alpha}/2$ is projected area of both 0^+ and 0^- layers onto an atomistic slip plane corresponding to the stacking fault, and $A = \sum_{\alpha \in 0^+, 0^-} A^{\alpha}/2$ recovers the area of the slip surface.

Now consider a free-body diagram of the top half-block – the shear resistance exerted by the bottom half-block on the cut surface (of the top half-block) is equivalent to a shear traction \mathcal{T}_{Δ} (see Fig. A.2a). The work of \mathcal{T}_{Δ} over the area of the slip plane A is

$$W_{\Delta} = A \int \mathcal{T}_{\Delta} d\Delta \quad (8.9)$$

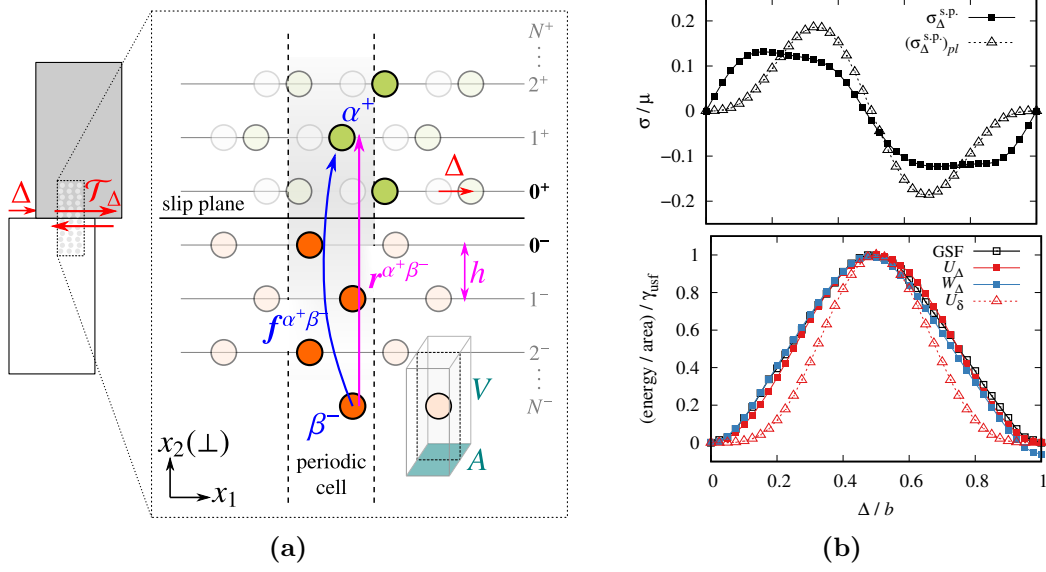


Figure A.2: Rigid shift of one half-block relative to another by Δ forming a stacking fault at the slip plane. (a) Layers of atoms above and below the slip plane are spaced at h and are labeled $0, 1, \dots, N^\pm$. Atoms have undeformed volume V and occupy an area A over the slip plane. The sum of all interaction forces between every atom in the lower block (β^- 's) with every atom in the upper block (α^+ 's), i.e. $\sum \mathbf{f}^{\alpha^+\beta^-}$, is equivalent to traction τ_Δ over the fault surface. In the minimum periodic cell, $\mathbf{f}^{\alpha^+\beta^-}$ represents the interaction between the layer corresponding to atom β^- and α^+ . (b) U_Δ approximates the GSF energy and balances W_Δ . Numerical integration of the virial stress (top) results in a small error for W_Δ . The plastic part of the stress $(\sigma_\Delta^{s.p.})_{pl}$ and work W_δ are approximated.

This traction represents the resistance of the bottom block, and is equivalent to a “block interaction force” \mathcal{F}_Δ exerted by the atoms in the bottom block resolved over A , i.e.

$$\mathcal{T}_\Delta = \mathcal{F}_\Delta / A \quad (8.10)$$

In the atomistic system, the interaction of the bottom half-block on the top half-block consists of the force interactions between every atom β^- in the lower block with every atom α^+ in the upper block, i.e.

$$\mathcal{F}_\Delta = \sum_{\alpha^+}^{N^+} \sum_{\beta^-}^{N^-} f_\Delta^{\alpha^+\beta^-} \quad (8.11)$$

for N^+ and N^- layers of atoms above and below the fault plane, respectively. To be precise, $f_\Delta^{\alpha\beta}$ here is the component of the force interaction in the direction of slip between a single atom α and a *layer* of atoms represented by a single atom β , i.e.

$$f_\Delta^{\alpha\beta} = \sum_n f_\Delta^{\alpha n} \quad (8.12)$$

where n are the images of β on the same layer in the (minimum) periodic cell.

To relate atomic forces and stresses, we use a Cauchy-like atomistic virial stress tensor [63] without kinetic terms, i.e.

$$\boldsymbol{\sigma}^\alpha = \frac{1}{V^\alpha} \left[\frac{1}{2} \sum_{\substack{\beta \\ \beta \neq \alpha}} \mathbf{f}^{\alpha\beta} \otimes \mathbf{r}^{\alpha\beta} \right] \quad (8.13)$$

where $\mathbf{f}^{\alpha\beta}$ is the pair force interaction vector between atoms α and those represented by β , $\mathbf{r}^{\alpha\beta}$ is their separation (see Eq. (3.2)), and V^α are the atomic volumes. Note we use undeformed volumes instead deformed volumes typically associated with the continuum Cauchy stress which lead to unbalanced momentum and violation of equilibrium. We refer the reader to Ref. [234], for example, for a dissection of the continuum-atomistic equivalence for virial stress. For periodic systems, Eq. (8.13) holds using the minimum image convention. Following from Eq. (8.13), the component of shear in the direction of slip corresponding to the Burgers vector is

$$\tau_\Delta^\alpha = \frac{1}{A^\alpha} \left[\frac{1}{2} \sum_{\substack{\beta \\ \beta \neq \alpha}} f_\Delta^{\alpha\beta} \cdot \tilde{r}_\perp^{\alpha\beta} \right] \quad (8.14)$$

where $\tilde{r}_\perp^{\alpha\beta} = (\tilde{r}_2^\beta - \tilde{r}_2^\alpha)/h$ is the number of atomic layers from β to α in the direction normal to the slip plane (\perp), h is the lattice spacing in the normal x_2 -direction, and $A^\alpha = V^\alpha/h$ is the slip plane surface area of the atom (see Fig. A.2a for schematic).

Substituting Eq. (8.11) and (8.14) back into Eq. (8.10), we obtain the expression for the traction for the rigid shear scenario in terms of atomic forces/stresses as

$$\mathcal{T}_\Delta = \left(\tau_\Delta^{0+} + \tau_\Delta^{0-} \right) + \frac{1}{A^\alpha} \underbrace{\left[\sum_{n=2}^N f_\Delta^{0+n-} \cdot (n-1) - \sum_{n=1}^N f_\Delta^{0+n+} \cdot n - \sum_{m=1}^N \sum_{n=1}^N f_\Delta^{m+n-} \right]}_{\approx 0} \approx 2\tau_\Delta^{0+} \quad (8.15)$$

where τ_Δ^{0+} and τ_Δ^{0-} are the stresses of the slip plane atom above and below the slip plane in the minimum periodic cell, respectively. The traction of the slip plane includes some contributions from forces of the atoms outside of the slip plane due to the virial stress definition and the multibody potential. However these contributions, which is the square-bracketed term on the right-hand side of Eq. (8.15) is very small. In the pure stacking fault scenario we also have $\tau_\Delta^{0+} = \tau_\Delta^{0-}$. The discrete form of Eq. (8.9) is then approximately

$$W_\Delta \approx \sum_{\alpha \in 0^+, 0^-} A^\alpha \int \tau_\Delta^\alpha d\Delta \quad (8.16)$$

noting the stress contribution from two layers of atoms corresponding to a single slip plane surface. The traction \mathcal{T}_Δ and resulting W_Δ (approximate) are shown in Fig. A.2b with some error since the additional forces are neglected.

The slip energy U_Δ and the stress-work of the traction W_Δ of the slip plane atoms form a balance, i.e.

$$\Pi_\Delta = U_\Delta - W_\Delta \quad (8.17)$$

and for the creation of the pure stacking fault, $\Pi_\Delta = 0$.

A.6 Local material properties in random alloys

The composition of a random alloy spatially fluctuates throughout the material, and as a result the material properties vary spatially. The average composition of the alloy (at the system level) is $\bar{\mathbf{c}}$, but the local composition \mathbf{c}^* varies somewhat. The elastic constants and USF energy critical properties for emission entering into the theory and they vary with the composition.

The USF energy connected to dislocation slip concerns the composition of the alloy in the neighborhood of the two layers of slipping atoms creating the stacking fault. The composition of the alloy far away from the fault will have minimal influence on the USF energy for slip. For each atom α on the layer above and below the fault, we define a cluster around the atom containing its 16-nearest neighbors within ± 1 atomic planes which has a composition $\mathbf{c}^\alpha = [c_1, c_2, c_3]$ (see Figure A.3a). We assign the USF energy for the central atom γ_{usf}^α as the *A*-alloy USF energy given the composition of its neighbor-cluster \mathbf{c}^α , i.e. $\gamma_{usf}^\alpha = \bar{\gamma}_{usf}(\mathbf{c}^\alpha)$ (Figure A.3b). Fig. 7.9a maps the *A*-alloy USF energies over the composition space of the model MoNbTi family.

We now proceed to demonstrate that γ_{usf}^α is a reasonable characterization of the local USF energy using the model MoNbTi system. Random alloy samples are oriented as if to assess the $\{112\}$ stacking fault (i.e. $\{112\}$ is a horizontal plane) corresponding to slip on an emission plane. The cell dimension in the direction normal to the plane is large so that each sample has an equiatomic average composition $\bar{\mathbf{c}}$ overall. The $\{112\}$ planar dimensions are small and approximately contains one neighbor-cluster configuration with minimal periodicity (see *x*-axis in Fig. A.3c). First, we obtain the USF energy for the periodic sample using standard methods. Here the “local” composition/USF energy (within the minimum cell) is equivalent to the “global” composition/USF energy (with periodicity). So, if the neighbor-clusters are a suitable representation of the local environment, their USF should correspond to these periodic quantities.

Due to the periodicity, 8 unique neighbor-clusters (with different central atoms) are possible within the minimum cell. As above, each cluster has a composition and is mapped to the *A*-alloy behavior to obtain γ_{usf}^α . The USF of the possible neighbor clusters

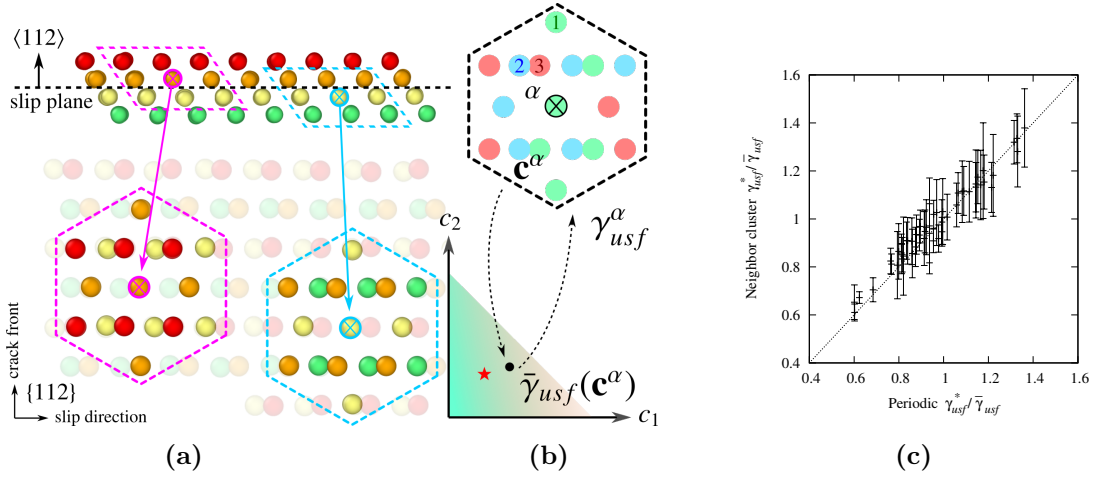


Figure A.3: Local USF energy of a slip plane atom. (a) Local neighbor volume for a slip plane atom above and below the slip plane. Each volume contains 16 atoms within ± 1 layer of atoms of the central atom (indicated by \otimes). (b) The neighbor volume for each central atom α has local concentration $\mathbf{c}^\alpha = [c_1, c_2, c_3]$ and local USF energy mapped from the A-alloy for that concentration, i.e. $\gamma_{usf}^\alpha = \bar{\gamma}_{usf}(\mathbf{c}^\alpha)$. (c) Periodic vs. neighbor-cluster USF energies normalized to the equiatomic A-alloy quantity $\bar{\gamma}_{usf}(\bar{\mathbf{c}})$.

for that fault plane has an average and standard deviation (see y -axis in Fig. A.3c). In Fig. A.3c, the neighbor-cluster definition well-describes the local environment. The energies are shown normalized against the average equiatomic quantity, i.e. $\bar{\gamma}_{usf}(\bar{\mathbf{c}})$, and we see the atoms perceive a USF energy that can vary up to 40% from the average.

The elastic constants C_{ij} also enter into theory through the anisotropy and they depend on the composition of the material around the slip plane. For the same lattice orientation as above, we now consider a planar volume 3 atom layers in thickness and varying in size in the $\{112\}$ dimensions. This simulates one layer of slipping atoms its ± 1 layers and varying the in-plane dimensions simulates the varying size of the local region. Again for the model MoNbTi system, the composition of such a volume \mathbf{c}^* varies somewhat from $\bar{\mathbf{c}}$. The scalar norm $\|\mathbf{c} - \bar{\mathbf{c}}\| = \sqrt{(c_1 - \bar{c}_1)^2 + (c_2 - \bar{c}_2)^2}$ indicates the magnitude in the variation and is determined varying the planar area. The variation increases as the planar area and the number of atoms in the sample decreases and is a statistical problem. Numerically, for a volume with planar area of 250 \AA^2 , which is roughly the size of the critical dislocation slip region, variation in composition is roughly 7% from $\bar{\mathbf{c}}$.

Dislocation slip involves the shearing of the material containing the slipping layers of atoms which creates the stacking fault of the slip plane. There an initial elastic part shear resistance from the lattice material [30]. We rotate the elastic constants C_{ij} to align the basis with the slip plane for C'_{ij} . The average shear stiffness in the direction of slip is estimated as $\mu' = (C'_{44} + C'_{55} + C'_{66})/3$. Fig. 7.9b maps the A-alloy stiffness over the composition space of the model MoNbTi family. For this material, the variation of stiffness with composition is very similar to that of USF energy with composition.

Bibliography

- [1] Zhou, X. W., Wadley, H. N. G., Johnson, R. A., Larson, D. J., Tabat, N., Cerezo, A., Petford-Long, A. K., Smith, G. D. W., Clifton, P. H., Martens, R. L., & Kelly, T. F. (2001). Atomic scale structure of sputtered metal multilayers. *Acta Materialia*, 49(19), 4005–4015.
- [2] Wu, Z., Francis, M. F., & Curtin, W. A. (2015). Magnesium interatomic potential for simulating plasticity and fracture phenomena. *Modelling and Simulation in Materials Science and Engineering*, 23(1), 015004.
- [3] Giannattasio, A., & Roberts, S. G. (2007). Strain-rate dependence of the brittle-to-ductile transition temperature in tungsten. *Philosophical Magazine*, 87(17), 2589–2598.
- [4] Miracle, D., Miller, J., Senkov, O., Woodward, C., Uchic, M., Tiley, J., Miracle, D. B., Miller, J. D., Senkov, O. N., Woodward, C., Uchic, M. D., & Tiley, J. (2014). Exploration and development of high entropy alloys for structural applications. *Entropy*, 16(1), 494–525.
- [5] Miracle, D. B., & Senkov, O. N. (2017). A critical review of high entropy alloys and related concepts. *Acta Materialia*, 122, 448–511.
- [6] Gorsse, S., Miracle, D. B., & Senkov, O. N. (2017). Mapping the world of complex concentrated alloys. *Acta Materialia*, 135, 177–187.
- [7] Tsai, M.-H., & Yeh, J.-W. (2014). High-Entropy Alloys: A critical review. *Materials Research Letters*, 2(3), 107–123.
- [8] Maresca, F., & Curtin, W. A. (2020). Mechanistic origin of high strength in refractory BCC high entropy alloys up to 1900K. *Acta Materialia*, 182, 235–249.
- [9] Maresca, F., & Curtin, W. A. (2020). Theory of screw dislocation strengthening in random BCC alloys from dilute to “High-Entropy” alloys. *Acta Materialia*, 182, 144–162.
- [10] Rao, S. I., Woodward, C., Akdim, B., Antillon, E., Parthasarathy, T. A., & Senkov, O. N. (2019). Estimation of diffusional effects on solution hardening at high temperatures in single phase compositionally complex body centered cubic alloys. *Scripta Materialia*, 172, 135–137.
- [11] Hirth, J. P., & Lothe, J. (1982). *Theory of Dislocations*. John Wiley & Sons.
- [12] Launey, M. E., & Ritchie, R. O. (2009). On the fracture toughness of advanced materials. *Advanced Materials*, 21(20), 2103–2110.

Bibliography

- [13] Cotterell, B. (2002). The past, present, and future of fracture mechanics. *Engineering Fracture Mechanics*, 69(5), 533–553.
- [14] Griffith, A. A. (1921). The phenomena of rupture and flow in solids. *Phil. Trans. R. Soc. Lond. A*, 221(582-593), 163–198.
- [15] Irwin, G. R. (1947). Fracture dynamics. *Fracturing of Metals*.
- [16] Irwin, G. R. (1957). Analysis of stresses and strains near the end of a crack traversing a plate. *Journal of Applied Mechanics*, 24(3), 361–364.
- [17] Orowan, E. (1949). Fracture and strength of solids. *Reports on Progress in Physics*, 12(1), 185–232.
- [18] Westergaard, H. M. (1939). Bearing pressures and cracks. *Journal of Applied Mechanics*, 6, A49–53.
- [19] Rice, J. R. (1968). A path independent integral and the approximate analysis of strain concentration by notches and cracks. *Journal of Applied Mechanics*, 35(2), 379–386.
- [20] Ting, T. T. C. (1996). *Anisotropic Elasticity: Theory and Applications*. Oxford Engineering Science Series. Oxford, New York: Oxford University Press.
- [21] Sun, C. T., & Jin, Z.-H. (2012). *Fracture mechanics*. Waltham, MA: Academic Press.
- [22] Anderson, T. L. (2017). *Fracture Mechanics: Fundamentals and Applications*. Boca Raton: CRC Press, 3 ed.
- [23] Andric, P., & Curtin, W. A. (2019). Atomistic modeling of fracture. *Modelling and Simulation in Materials Science and Engineering*, 27(1), 013001.
- [24] Muskhelishvili, N. I. (1977). *Some Basic Problems of the Mathematical Theory of Elasticity*. Springer Netherlands.
- [25] Sih, G. C. (1966). On the Westergaard method of crack analysis. *International Journal of Fracture Mechanics*, 2(4), 628–631.
- [26] Mak, E., Yin, B., & Curtin, W. A. (2021). A ductility criterion for bcc high entropy alloys. *Journal of the Mechanics and Physics of Solids*, 152, 104389.
- [27] Stroh, A. N. (1958). Dislocations and cracks in anisotropic elasticity. *Philosophical Magazine*, 3(30), 625–646.
- [28] Liebowitz, H., & Sih, G. C. (1968). Mathematical theories of brittle fracture.
- [29] Andric, P. (2019). *The mechanics of crack-tip dislocation emission and twinning*. Ph.D. thesis, École polytechnique fédérale de Lausanne, Lausanne, Switzerland.
- [30] Rice, J. R. (1992). Dislocation nucleation from a crack tip: An analysis based on the Peierls concept. *Journal of the Mechanics and Physics of Solids*, 40(2), 239–271.
- [31] Rice, J. R. (1968). Mathematical analysis in the mechanics of fracture. *Fracture: an advanced treatise*, 2, 191–311.
- [32] Sun, Y., & Beltz, G. E. (1994). Dislocation nucleation from a crack tip: A formulation based on anisotropic elasticity. *Journal of the Mechanics and Physics of Solids*, 42(12), 1905–1932.

-
- [33] Mak, E., & Curtin, W. A. (2020). Intrinsic fracture behavior of Mg–Y alloys. *Modelling and Simulation in Materials Science and Engineering*, 28(3), 035012.
- [34] Rice, J. R., & Wang, J.-S. (1989). Embrittlement of interfaces by solute segregation. *Materials Science and Engineering: A*, 107, 23–40.
- [35] Chung, Y. (2014). Validity of Caltrans’ environmental hydrogen embrittlement tests on grade BD anchor rods in the SAS span. Tech. rep.
- [36] Rice, J. R., & Thomson, R. (1973). Ductile vs brittle behavior of crystals. Tech. Rep. COO–3084-22, 4403224.
- [37] Thomson, R., Hsieh, C., & Rana, V. (1971). Lattice trapping of fracture cracks. *Journal of Applied Physics*, 42(8), 3154–3160.
- [38] Curtin, W. A. (1990). On lattice trapping of cracks. *Journal of Materials Research*, 5(7), 1549–1560.
- [39] Bernstein, N., & Hess, D. W. (2003). Lattice trapping barriers to brittle fracture. *Physical Review Letters*, 91(2), 025501.
- [40] Zhu, T., Li, J., & Yip, S. (2006). Atomistic characterization of three-dimensional lattice trapping barriers to brittle fracture. *Proceedings of the Royal Society A: Mathematical, Physical and Engineering Sciences*, 462(2070), 1741–1761.
- [41] Argon, A. S. (1987). Brittle to ductile transition in cleavage fracture. *Acta Metallurgica*, 35(1), 185–196.
- [42] Armstrong, R. W. (1966). Cleavage crack propagation within crystals by the Griffith mechanism versus a dislocation mechanism. *Materials Science and Engineering*, 1(4), 251–254.
- [43] Kelly, A., Tyson, W. R., & Cottrell, A. H. (1967). Ductile and brittle crystals. *The Philosophical Magazine: A Journal of Theoretical Experimental and Applied Physics*, 15(135), 567–586.
- [44] Schoeck, G. (1991). Dislocation emission from crack tips. *Philosophical Magazine A*, 63(1), 111–120.
- [45] Thomson, R. (1978). Brittle fracture in a ductile material with application to hydrogen embrittlement. *Journal of Materials Science*, 13(1), 128–142.
- [46] Ohr, S. (1985). An electron microscope study of crack tip deformation and its impact on the dislocation theory of fracture. *Materials Science and Engineering*, 72(1), 1–35.
- [47] Lin, I. H., & Thomson, R. (1986). Cleavage, dislocation emission, and shielding for cracks under general loading. *Acta Metallurgica*, 34(2), 187–206.
- [48] Andric, P., & Curtin, W. A. (2017). New theory for Mode I crack-tip dislocation emission. *Journal of the Mechanics and Physics of Solids*, 106, 315–337.
- [49] Peierls, R. (1940). The size of a dislocation. *Proceedings of the Physical Society*, 52(1), 34–37.
- [50] Ritchie, R. (1988). Mechanisms of fatigue crack propagation in metals, ceramics and composites: Role of crack tip shielding. *Materials Science and Engineering: A*, 103(1), 15–28.

Bibliography

- [51] Andric, P., & Curtin, W. (2018). New theory for crack-tip twinning in fcc metals. *Journal of the Mechanics and Physics of Solids*, 113, 144–161.
- [52] Rice, J. R. (1985). Conserved integrals and energetic forces. In *Fundamentals of Deformation and Fracture (Eshelby Memorial Symposium)*, (pp. 33–56). University Press.
- [53] Zhu, T., Li, J., & Yip, S. (2004). Atomistic study of dislocation loop emission from a crack tip. *Physical Review Letters*, 93(2).
- [54] Zhu, T., Li, J., Samanta, A., Leach, A., & Gall, K. (2008). Temperature and Strain-Rate Dependence of Surface Dislocation Nucleation. *Physical Review Letters*, 100(2).
- [55] Gordon, P. A., Neeraj, T., & Luton, M. J. (2008). Atomistic simulation of dislocation nucleation barriers from cracktips in α -Fe. *Modelling and Simulation in Materials Science and Engineering*, 16(4), 045006.
- [56] Tadmor, E. B., & Hai, S. (2003). A Peierls criterion for the onset of deformation twinning at a crack tip. *Journal of the Mechanics and Physics of Solids*, 51(5), 765–793.
- [57] Schoeck, G., & Püschl, W. (1991). The formation of dislocation loops at crack tips in three dimensions. *Philosophical Magazine A*, 64(4), 931–949.
- [58] Rice, J. R., & Beltz, G. E. (1994). The activation energy for dislocation nucleation at a crack. *Journal of the Mechanics and Physics of Solids*, 42(2), 333–360.
- [59] Xu, G., & Ortiz, M. (1993). A variational boundary integral method for the analysis of 3-D cracks of arbitrary geometry modelled as continuous distributions of dislocation loops. *International Journal for Numerical Methods in Engineering*, 36(21), 3675–3701.
- [60] Xu, G., Argon, A. S., & Ortiz, M. (1995). Nucleation of dislocations from crack tips under mixed modes of loading: Implications for brittle against ductile behaviour of crystals. *Philosophical Magazine A*, 72(2), 415–451.
- [61] Schoeck, G. (1996). Dislocation emission from crack tips as a variational problem of the crack energy. *Journal of the Mechanics and Physics of Solids*, 44(3), 413–437.
- [62] Curtin, W. (2017). The X-mechanics toolbox to solve Y-mechanics problems. *Procedia IUTAM*, 21, 2–10.
- [63] Tadmor, E. B., & Miller, R. E. (2011). *Modeling materials: continuum, atomistic, and multiscale techniques*. Cambridge ; New York: Cambridge University Press.
- [64] Finnis, M. (2003). *Interatomic Forces in Condensed Matter*. OUP Oxford.
- [65] Daw, M. S., & Baskes, M. I. (1984). Embedded-atom method: Derivation and application to impurities, surfaces, and other defects in metals. *Physical Review B*, 29(12), 6443–6453.
- [66] Baskes, M. I. (1992). Modified embedded-atom potentials for cubic materials and impurities. *Physical Review B*, 46(5), 2727–2742.

-
- [67] Plimpton, S. (1995). Fast parallel algorithms for short-range molecular dynamics. *Journal of Computational Physics*, 117(1), 1–19.
- [68] Stukowski, A. (2010). Visualization and analysis of atomistic simulation data with OVITO—the Open Visualization Tool. *Modelling and Simulation in Materials Science and Engineering*, 18(1), 015012.
- [69] Honeycutt, J. D., & Andersen, H. C. (1987). Molecular dynamics study of melting and freezing of small Lennard-Jones clusters. *The Journal of Physical Chemistry*, 91(19), 4950–4963.
- [70] Stillinger, F. H., & Weber, T. A. (1985). Computer simulation of local order in condensed phases of silicon. *Physical Review B*, 31(8), 5262–5271.
- [71] Vineyard, G. H. (1957). Frequency factors and isotope effects in solid state rate processes. *Journal of Physics and Chemistry of Solids*, 3(1-2), 121–127.
- [72] Weiner, J. H. (2012). *Statistical Mechanics of Elasticity*. Courier Corporation.
- [73] Ahmad, R. (2020). *Atomic Scale Investigations into the Origins of Ductility in Mg Alloys*. Ph.D. thesis, EPFL, Lausanne, Switzerland.
- [74] Eyring, H. (1935). The activated complex in chemical reactions. *The Journal of Chemical Physics*, 3(2), 107–115.
- [75] Rodney, D. (2007). Activation enthalpy for kink-pair nucleation on dislocations: Comparison between static and dynamic atomic-scale simulations. *Physical Review B*, 76(14), 144108.
- [76] Hirel, P., Godet, J., Brochard, S., Pizzagalli, L., & Beauchamp, P. (2008). Determination of activation parameters for dislocation formation from a surface in fcc metals by atomistic simulations. *Physical Review B*, 78(6), 064109.
- [77] Nguyen, L. D., Baker, K. L., & Warner, D. H. (2011). Atomistic predictions of dislocation nucleation with transition state theory. *Physical Review B*, 84(2), 024118.
- [78] Vegge, T., Rasmussen, T., Leffers, T., Pedersen, O. B., & Jacobsen, K. W. (2000). Determination of the of rate cross slip of screw dislocations. *Physical Review Letters*, 85(18), 3866–3869.
- [79] Wu, Z., & Curtin, W. A. (2015). The origins of high hardening and low ductility in magnesium. *Nature*, 526(7571), 62–67.
- [80] Warner, D., & Curtin, W. (2009). Origins and implications of temperature-dependent activation energy barriers for dislocation nucleation in face-centered cubic metals. *Acta Materialia*, 57(14), 4267–4277.
- [81] Ryu, S., Kang, K., & Cai, W. (2011). Predicting the dislocation nucleation rate as a function of temperature and stress. *Journal of Materials Research*, 26(18), 2335–2354.
- [82] Kocks, U. F., Argon, A. S., & Ashby, M. F. (1975). *Thermodynamics and kinetics of slip*. Oxford, Pergamon Press.
- [83] Warner, D. H., Curtin, W. A., & Qu, S. (2007). Rate dependence of crack-tip processes predicts twinning trends in f.c.c. metals. *Nature Materials*, 6(11), 876–881.

- [84] Mills, G., & Jónsson, H. (1994). Quantum and thermal effects in H₂ dissociative adsorption: Evaluation of free energy barriers in multidimensional quantum systems. *Physical Review Letters*, 72(7), 1124–1127.
- [85] Mills, G., Jónsson, H., & Schenter, G. K. (1995). Reversible work transition state theory: application to dissociative adsorption of hydrogen. *Surface Science*, 324(2-3), 305–337.
- [86] E, W., Ren, W., & Vanden-Eijnden, E. (2002). String method for the study of rare events. *Physical Review B*, 66(5), 052301.
- [87] Jónsson, H., Mills, G., & Jacobsen, K. W. (1998). Nudged elastic band method for finding minimum energy paths of transitions. In B. J. Berne, G. Ciccotti, & D. F. Coker (Eds.) *Classical and Quantum Dynamics in Condensed Phase Simulations*, (p. 385). Singapore: World Scientific.
- [88] Henkelman, G., & Jónsson, H. (2000). Improved tangent estimate in the nudged elastic band method for finding minimum energy paths and saddle points. *The Journal of Chemical Physics*, 113(22), 9978–9985.
- [89] Henkelman, G., Uberuaga, B. P., & Jónsson, H. (2000). A climbing image nudged elastic band method for finding saddle points and minimum energy paths. *The Journal of Chemical Physics*, 113(22), 9901–9904.
- [90] Zhu, T., Li, J., & Yip, S. (2013). Atomistic reaction pathway sampling: The nudged elastic band method and nanomechanics applications. In *Nano and Cell Mechanics*, (pp. 311–338). John Wiley & Sons, Ltd.
- [91] Zhu, T., Li, J., Samanta, A., Kim, H. G., & Suresh, S. (2007). Interfacial plasticity governs strain rate sensitivity and ductility in nanostructured metals. *Proceedings of the National Academy of Sciences*, 104(9), 3031–3036.
- [92] Marchand, D., Jain, A., Glensk, A., & Curtin, W. A. (2020). Machine learning for metallurgy I. A neural-network potential for Al-Cu. *Physical Review Materials*, 4(10), 103601.
- [93] Wu, Z., & Curtin, W. (2015). Brittle and ductile crack-tip behavior in magnesium. *Acta Materialia*, 88, 1–12.
- [94] Stricker, M., Yin, B., Mak, E., & Curtin, W. A. (2020). Machine learning for metallurgy II. A neural-network potential for magnesium. *Physical Review Materials*, 4(10), 103602.
- [95] Khosrownejad, S. M., & Curtin, W. A. (2017). Crack growth and fracture toughness of amorphous Li-Si anodes: Mechanisms and role of charging/discharging studied by atomistic simulations. *Journal of the Mechanics and Physics of Solids*, 107, 542–559.
- [96] Neogi, A., Alam, M., Hartmaier, A., & Janisch, R. (2020). Anisotropic failure behavior of ordered intermetallic TiAl alloys under pure mode-I loading. *Modelling and Simulation in Materials Science and Engineering*, 28(6), 065016.
- [97] Gumbsch, P. (1995). An atomistic study of brittle fracture: Toward explicit failure criteria from atomistic modeling. *Journal of Materials Research*, 10(11), 2897–2907.

-
- [98] Möller, J. J., & Bitzek, E. (2014). Comparative study of embedded atom potentials for atomistic simulations of fracture in α -iron. *Modelling and Simulation in Materials Science and Engineering*, 22(4), 045002.
- [99] Varvenne, C., Luque, A., Nöhling, W. G., & Curtin, W. A. (2016). Average-atom interatomic potential for random alloys. *Physical Review B*, 93(10).
- [100] Lu, G., Tadmor, E. B., & Kaxiras, E. (2006). From electrons to finite elements: A concurrent multiscale approach for metals. *Phys. Rev. B*, 73, 024108.
- [101] Tersoff, J. (1986). New empirical model for the structural properties of silicon. *Physical Review Letters*, 56(6), 632–635.
- [102] Pollock, T. M. (2010). Weight loss with magnesium alloys. *Science*, 328(5981), 986–987.
- [103] Bhattacharya, B., & Niewczas, M. (2011). Work-hardening behaviour of Mg single crystals oriented for basal slip. *Philosophical Magazine*, 91(17), 2227–2247.
- [104] Agnew, S. R., Senn, J. W., & Horton, J. A. (2006). Mg sheet metal forming: Lessons learned from deep drawing Li and Y solid-solution alloys. *JOM*, 58(5), 62–69.
- [105] Sandlöbes, S., Zaefferer, S., Schestakow, I., Yi, S., & Gonzalez-Martinez, R. (2011). On the role of non-basal deformation mechanisms for the ductility of Mg and Mg–Y alloys. *Acta Materialia*, 59(2), 429–439.
- [106] Sandlöbes, S., Pei, Z., Friák, M., Zhu, L. F., Wang, F., Zaefferer, S., Raabe, D., & Neugebauer, J. (2014). Ductility improvement of Mg alloys by solid solution: Ab initio modeling, synthesis and mechanical properties. *Acta Materialia*, 70, 92–104.
- [107] Wu, Z., Ahmad, R., Yin, B., Sandlöbes, S., & Curtin, W. A. (2018). Mechanistic origin and prediction of enhanced ductility in magnesium alloys. *Science*, 359(6374), 447–452.
- [108] Nogaret, T., Curtin, W., Yasi, J., Hector, L., & Trinkle, D. (2010). Atomistic study of edge and screw $\langle c + a \rangle$ dislocations in magnesium. *Acta Materialia*, 58(13), 4332 – 4343.
- [109] Liu, Z., & Shang, J. (2011). First principles calculations of electronic properties and mechanical properties of bcc molybdenum and niobium. *Rare Metals*, 30(1), 354–358.
- [110] Sun, D. Y., Mendelev, M. I., Becker, C. A., Kudin, K., Haxhimali, T., Asta, M., Hoyt, J. J., Karma, A., & Srolovitz, D. J. (2006). Crystal-melt interfacial free energies in hcp metals: A molecular dynamics study of Mg. *Physical Review B*, 73(2), 024116.
- [111] Yasi, J. A., Nogaret, T., Trinkle, D. R., Qi, Y., Hector, L. G., & Curtin, W. A. (2009). Basal and prism dislocation cores in magnesium: comparison of first-principles and embedded-atom-potential methods predictions. *Modelling and Simulation in Materials Science and Engineering*, 17(5), 055012.
- [112] Ghazisaeidi, M., Hector, L., & Curtin, W. (2014). First-principles core structures of edge and screw dislocations in Mg. *Scripta Materialia*, 75, 42–45.

- [113] Pei, Z., Zhu, L.-F., Friák, M., Sandlöbes, S., Pezold, J. v., Sheng, H. W., Race, C. P., Zaeferrer, S., Svendsen, B., Raabe, D., & Neugebauer, J. (2013). Ab initio and atomistic study of generalized stacking fault energies in Mg and Mg–Y alloys. *New Journal of Physics*, 15(4), 043020.
- [114] Jelinek, B., Groh, S., Horstemeyer, M. F., Houze, J., Kim, S. G., Wagner, G. J., Moitra, A., & Baskes, M. I. (2012). Modified embedded atom method potential for Al, Si, Mg, Cu, and Fe alloys. *Physical Review B*, 85(24), 245102.
- [115] Nogaret, T., Curtin, W. A., Yasi, J. A., Hector, L. G., & Trinkle, D. R. (2010). Atomistic study of edge and screw $\langle c+a \rangle$ dislocations in magnesium. *Acta Materialia*, 58(13), 4332–4343.
- [116] Kim, Y.-M., Kim, N. J., & Lee, B.-J. (2009). Atomistic modeling of pure Mg and Mg–Al systems. *Calphad*, 33(4), 650–657.
- [117] Kim, K.-H., Jeon, J. B., & Lee, B.-J. (2015). Modified embedded-atom method interatomic potentials for Mg–X (X=Y, Sn, Ca) binary systems. *Calphad*, 48, 27–34.
- [118] Ahmad, R., Groh, S., Ghazisaeidi, M., & Curtin, W. A. (2018). Modified embedded-atom method interatomic potential for Mg–Y alloys. *Modelling and Simulation in Materials Science and Engineering*, 26(6), 065010.
- [119] Ko, K.-J., Cha, P.-R., Srolovitz, D., & Hwang, N.-M. (2009). Abnormal grain growth induced by sub-boundary-enhanced solid-state wetting: Analysis by phase-field model simulations. *Acta Materialia*, 57(3), 838–845.
- [120] Yasi, J. A., Hector, L. G., & Trinkle, D. R. (2010). First-principles data for solid-solution strengthening of magnesium: From geometry and chemistry to properties. *Acta Materialia*, 58(17), 5704–5713.
- [121] Leyson, G. P. M., Curtin, W. A., Hector, L. G., & Woodward, C. F. (2010). Quantitative prediction of solute strengthening in aluminium alloys. *Nature Materials*, 9(9), 750–755.
- [122] Leyson, G., Hector, L., & Curtin, W. (2012). Solute strengthening from first principles and application to aluminum alloys. *Acta Materialia*, 60(9), 3873–3884.
- [123] Weinberger, C. R., Boyce, B. L., & Battaile, C. C. (2013). Slip planes in bcc transition metals. *International Materials Reviews*, 58(5), 296–314.
- [124] Huang, X., Liu, L., Duan, X., Liao, W., Huang, J., Sun, H., & Yu, C. (2021). Atomistic simulation of chemical short-range order in HfNbTaZr high entropy alloy based on a newly-developed interatomic potential. *Materials & Design*, 202, 109560.
- [125] Kostiuchenko, T., Körmann, F., Neugebauer, J., & Shapeev, A. (2019). Impact of lattice relaxations on phase transitions in a high-entropy alloy studied by machine-learning potentials. *npj Computational Materials*, 5(1), 1–7.
- [126] Li, X.-G., Chen, C., Zheng, H., Zuo, Y., & Ong, S. P. (2020). Complex strengthening mechanisms in the NbMoTaW multi-principal element alloy. *npj Computational Materials*, 6(1), 1–10.

-
- [127] Zhou, X. W., Johnson, R. A., & Wadley, H. N. G. (2004). Misfit-energy-increasing dislocations in vapor-deposited CoFe/NiFe multilayers. *Physical Review B*, 69(14).
- [128] Wang, P., Wu, Y., Liu, J., & Wang, H. (2017). Impacts of atomic scale lattice distortion on dislocation activity in high-entropy alloys. *Extreme Mechanics Letters*, 17, 38–42.
- [129] Chen, H., Kauffmann, A., Laube, S., Choi, I.-C., Schwaiger, R., Huang, Y., Lichtenberg, K., Müller, F., Gorr, B., Christ, H.-J., & Heilmaier, M. (2018). Contribution of lattice distortion to solid solution strengthening in a series of refractory high entropy alloys. *Metallurgical and Materials Transactions A*, 49(3), 772–781.
- [130] Nöhring, W. G., & Curtin, W. A. (2019). Correlation of microdistortions with misfit volumes in High Entropy Alloys. *Scripta Materialia*, 168, 119–123.
- [131] Nag, S., Varvenne, C., & Curtin, W. A. (2020). Solute-strengthening in elastically anisotropic fcc alloys. *Modelling and Simulation in Materials Science and Engineering*, 28(2), 025007.
- [132] Nag, S., Junge, T., & Curtin, W. A. (2019). Atomistic-continuum coupling of random alloys. *Modelling and Simulation in Materials Science and Engineering*, 27(7), 075004.
- [133] Bartók, A. P., Kondor, R., & Csányi, G. (2013). On representing chemical environments. *Phys. Rev. B*, 87, 184115.
- [134] Behler, J. (2014). Representing potential energy surfaces by high-dimensional neural network potentials. *Journal of Physics: Condensed Matter*, 26(18), 183001.
- [135] Kobayashi, R., Giofré, D., Junge, T., Ceriotti, M., & Curtin, W. A. (2017). Neural network potential for al-mg-si alloys. *Phys. Rev. Materials*, 1, 053604.
- [136] Pun, G. P., Batra, R., Ramprasad, R., & Mishin, Y. (2019). Physically informed artificial neural networks for atomistic modeling of materials. *Nature communications*, 10, 2339.
- [137] Wang, H., Zhang, L., Han, J., & E, W. (2018). Deepmd-kit: A deep learning package for many-body potential energy representation and molecular dynamics. *Computer Physics Communications*, 228, 178 – 184.
- [138] Dickel, D., Francis, D., & Barrett, C. (2020). Neural network aided development of a semi-empirical interatomic potential for titanium. *Computational Materials Science*, 171, 109157.
- [139] Behler, J., & Parrinello, M. (2007). Generalized neural-network representation of high-dimensional potential-energy surfaces. *Phys. Rev. Lett.*, 98, 146401.
- [140] Rogers, D., & Hahn, M. (2010). Extended-connectivity fingerprints. *J. Chem. Inf. Model.*, 50(5), 742–754.
- [141] Montavon, G., Rupp, M., Gobre, V., Vazquez-Mayagoitia, A., Hansen, K., Tkatchenko, A., Müller, K.-R., & von Lilienfeld, O. A. (2013). Machine learning

- of molecular electronic properties in chemical compound space. *New Journal of Physics*, 15(9), 095003.
- [142] Bartók, A. P., & Csányi, G. (2015). Gaussian approximation potentials: A brief tutorial introduction. *International Journal of Quantum Chemistry*, 115(16), 1051–1057.
 - [143] Faber, F. A., Hutchison, L., Huang, B., Gilmer, J., Schoenholz, S. S., Dahl, G. E., Vinyals, O., Kearnes, S., Riley, P. F., & von Lilienfeld, O. A. (2017). Prediction errors of molecular machine learning models lower than hybrid dft error. *Journal of chemical theory and computation*, 13(11), 5255–5264.
 - [144] Zhang, L., Lin, D.-Y., Wang, H., Car, R., & E, W. (2019). Active learning of uniformly accurate interatomic potentials for materials simulation. *Phys. Rev. Materials*, 3, 023804.
 - [145] Bernstein, N., Csányi, G., & Deringer, V. L. (2019). De novo exploration and self-guided learning of potential-energy surfaces. *npj Computational Materials*, 5(1), 99.
 - [146] Jinnouchi, R., Karsai, F., & Kresse, G. (2019). On-the-fly machine learning force field generation: Application to melting points. *Phys. Rev. B*, 100, 014105.
 - [147] Zuo, Y., Chen, C., Li, X., Deng, Z., Chen, Y., Behler, J., Csányi, G., Shapeev, A. V., Thompson, A. P., Wood, M. A., & Ong, S. P. (2020). Performance and cost assessment of machine learning interatomic potentials. *J. Phys. Chem. A*, 124(4), 731–745.
 - [148] Bonny, G., Terentyev, D., Bakaev, A., Grigorev, P., & Neck, D. V. (2014). Many-body central force potentials for tungsten. *Modelling and Simulation in Materials Science and Engineering*, 22(5), 053001.
 - [149] Dragoni, D., Daff, T. D., Csányi, G., & Marzari, N. (2018). Achieving dft accuracy with a machine-learning interatomic potential: Thermomechanics and defects in bcc ferromagnetic iron. *Phys. Rev. Materials*, 2, 013808.
 - [150] Szlachta, W. J., Bartók, A. P., & Csányi, G. (2014). Accuracy and transferability of gaussian approximation potential models for tungsten. *Phys. Rev. B*, 90, 104108.
 - [151] Argon, A. S. (2008). *Strengthening Mechanisms in Crystal Plasticity*. Oxford University Press.
 - [152] Gumbsch, P. (1998). Controlling factors for the brittle-to-ductile transition in tungsten single crystals. *Science*, 282(5392), 1293–1295.
 - [153] Maresca, F., Dragoni, D., Csányi, G., Marzari, N., & Curtin, W. A. (2018). Screw dislocation structure and mobility in body centered cubic Fe predicted by a Gaussian Approximation Potential. *npj Computational Materials*, 4(1), 1–7.
 - [154] Bartók, A. P., Payne, M. C., Kondor, R., & Csányi, G. (2010). Gaussian Approximation Potentials: The Accuracy of Quantum Mechanics, without the Electrons. *Physical Review Letters*, 104(13), 136403.

-
- [155] Bartók, A. P., & Csányi, G. (2015). Gaussian approximation potentials: A brief tutorial introduction. *International Journal of Quantum Chemistry*, 115(16), 1051–1057.
- [156] Rosenbrock, C. W., Homer, E. R., Csányi, G., & Hart, G. L. W. (2017). Discovering the building blocks of atomic systems using machine learning: application to grain boundaries. *npj Computational Materials*, 3(1), 1–7.
- [157] Rosenbrock, C. W., Gubaev, K., Shapeev, A. V., Pártay, L. B., Bernstein, N., Csányi, G., & Hart, G. L. W. (2021). Machine-learned interatomic potentials for alloys and alloy phase diagrams. *npj Computational Materials*, 7(1), 1–9.
- [158] Bartók, A. P., Kondor, R., & Csányi, G. (2013). On representing chemical environments. *Physical Review B*, 87(18), 184115.
- [159] Shapeev, A. V. (2016). Moment tensor potentials: A class of systematically improvable interatomic potentials. *Multiscale Modeling & Simulation*, 14(3), 1153–1173.
- [160] Stukowski, A. (2012). Structure identification methods for atomistic simulations of crystalline materials. *Modelling and Simulation in Materials Science and Engineering*, 20(4), 045021.
- [161] Singraber, A., Behler, J., & Dellago, C. (2019). Library-based lammmps implementation of high-dimensional neural network potentials. *J. Chem. Theory Comput.*, 15(3), 1827–1840.
- [162] Behler, J. (2015). Constructing high-dimensional neural network potentials: A tutorial review. *International Journal of Quantum Chemistry*, 115(16), 1032–1050.
- [163] Singraber, A. (2018). *Designing and training neural network potentials for molecular dynamics simulations: Application to water and copper sulfide*. Ph.D. thesis, Universität Wien.
- [164] Singraber, A., Morawietz, T., Behler, J., & Dellago, C. (2019). Parallel multistream training of high-dimensional neural network potentials. *J. Chem. Theory Comput.*, 15(5), 3075–3092.
- [165] Imbalzano, G., Anelli, A., Giofré, D., Klees, S., Behler, J., & Ceriotti, M. (2018). Automatic selection of atomic fingerprints and reference configurations for machine-learning potentials. *The Journal of Chemical Physics*, 148(24), 241730.
- [166] Witkoskie, J. B., & Doren, D. J. (2005). Neural network models of potential energy surfaces: Prototypical examples. *Journal of Chemical Theory and Computation*, 1(1), 14–23.
- [167] Ahmad, R., Wu, Z., & Curtin, W. (2020). Analysis of double cross-slip of pyramidal I $\langle c+a \rangle$ screw dislocations and implications for ductility in Mg alloys. *Acta Materialia*, 183, 228 – 241.
- [168] Mak, E., & Curtin, W. A. (2020). Intrinsic fracture behavior of Mg–Y alloys. *Modelling and Simulation in Materials Science and Engineering*, 28(3), 035012.
- [169] Rice, J. R. (1966). Plastic yielding at a crack tip. In T. Yokobori, T. Kawasaki, & J. L. Swedlow (Eds.) *Proceedings of the 1st International Conference on*

- Fracture, Sendai, 1965*, vol. Vol. I, (pp. 283–308). Japanese Society for Strength and Materials, Tokyo.
- [170] Larsen, P. M., Schmidt, S., & Schiøtz, J. (2016). Robust structural identification via polyhedral template matching. *Modelling and Simulation in Materials Science and Engineering*, 24(5), 055007.
 - [171] Faken, D., & Jónsson, H. (1994). Systematic analysis of local atomic structure combined with 3D computer graphics. *Computational Materials Science*, 2(2), 279–286.
 - [172] Ritchie, R. (1999). Mechanisms of fatigue-crack propagation in ductile and brittle solids. *International Journal of Fracture*, 100(1), 55–83.
 - [173] Senkov, O. N., Wilks, G. B., Miracle, D. B., Chuang, C. P., & Liaw, P. K. (2010). Refractory high-entropy alloys. *Intermetallics*, 18(9), 1758–1765.
 - [174] Senkov, O. N., Wilks, G. B., Scott, J. M., & Miracle, D. B. (2011). Mechanical properties of Nb₂₅Mo₂₅Ta₂₅W₂₅ and V₂₀Nb₂₀Mo₂₀Ta₂₀W₂₀ refractory high entropy alloys. *Intermetallics*, 19(5), 698–706.
 - [175] Senkov, O., Scott, J., Senkova, S., Miracle, D., & Woodward, C. (2011). Microstructure and room temperature properties of a high-entropy TaNbHfZrTi alloy. *Journal of Alloys and Compounds*, 509(20), 6043–6048.
 - [176] Senkov, O. N., Scott, J. M., Senkova, S. V., Meisenkothen, F., Miracle, D. B., & Woodward, C. F. (2012). Microstructure and elevated temperature properties of a refractory TaNbHfZrTi alloy. *Journal of Materials Science*, 47(9), 4062–4074.
 - [177] Senkov, O., Senkova, S., & Woodward, C. (2014). Effect of aluminum on the microstructure and properties of two refractory high-entropy alloys. *Acta Materialia*, 68, 214–228.
 - [178] Senkov, O., Rao, S., Chaput, K., & Woodward, C. (2018). Compositional effect on microstructure and properties of NbTiZr-based complex concentrated alloys. *Acta Materialia*, 151, 201–215.
 - [179] Hirsch, P. B., & Roberts, S. G. (1991). The brittle-ductile transition in silicon. *Philosophical Magazine A*, 64(1), 55–80.
 - [180] Gumbsch, P. (2003). Brittle fracture and the brittle-to-ductile transition of tungsten. *Journal of Nuclear Materials*, 323(2-3), 304–312.
 - [181] Raffo, P. (1969). Yielding and fracture in tungsten and tungsten-rhenium alloys. *Journal of the Less Common Metals*, 17(2), 133–149.
 - [182] Coury, F. G., Kaufman, M., & Clarke, A. J. (2019). Solid-solution strengthening in refractory high entropy alloys. *Acta Materialia*, 175, 66–81.
 - [183] Senkov, O., Rao, S., Butler, T., & Chaput, K. (2019). Ductile Nb alloys with reduced density and cost. *Journal of Alloys and Compounds*, 808, 151685.
 - [184] Li, X., Li, W., Irving, D. L., Varga, L. K., Vitos, L., & Schönecker, S. (2020). Ductile and brittle crack-tip response in equimolar refractory high-entropy alloys. *Acta Materialia*, 189, 174–187.

-
- [185] Hu, Y.-J., Sundar, A., Ogata, S., & Qi, L. (2021). Screening of generalized stacking fault energies, surface energies and intrinsic ductile potency of refractory multicomponent alloys. *Acta Materialia*, (p. 116800).
- [186] Andric, P., Yin, B., & Curtin, W. A. (2019). Stress-dependence of generalized stacking fault energies. *Journal of the Mechanics and Physics of Solids*, 122, 262–279.
- [187] Tyson, W., Ayres, R., & Stein, D. (1973). Anisotropy of cleavage in B.C.C. transition metals. *Acta Metallurgica*, 21(5), 621–627.
- [188] Koči, L., Ma, Y., Oganov, A. R., Souvatzis, P., & Ahuja, R. (2008). Elasticity of the superconducting metals V, Nb, Ta, Mo, and W at high pressure. *Physical Review B*, 77(21), 214101.
- [189] Featherston, F. H., & Neighbours, J. R. (1963). Elastic constants of tantalum, tungsten, and molybdenum. *Physical Review*, 130(4), 1324–1333.
- [190] Carroll, K. J. (1965). Elastic constants of niobium from 4.2° to 300°K. *Journal of Applied Physics*, 36(11), 3689–3690.
- [191] Bolef, D. I., Smith, R. E., & Miller, J. G. (1971). Elastic Properties of Vanadium. I. Temperature Dependence of the Elastic Constants and the Thermal Expansion. *Physical Review B*, 3(12), 4100–4108.
- [192] Spitzig, W., & Owen, C. (1987). Effect of the nitrogen-to-hydrogen ratio on the mechanical behavior of vanadium, niobium and tantalum. *Materials Science and Engineering*, 91, 97–104.
- [193] Northcott, L. (1961). Some features of the refractory metals. *Journal of the Less Common Metals*, 3(2), 125–148.
- [194] Joseph, T., Tanaka, M., Wilkinson, A., & Roberts, S. (2007). Brittle–ductile transitions in vanadium and iron–chromium. *Journal of Nuclear Materials*, 367–370, 637–643.
- [195] Roberts, S. G., Hirsch, P. B., Booth, A. S., Ellis, M., & Serbena, F. C. (1993). Dislocations, cracks and brittleness in single crystals. *Physica Scripta*, T49B, 420–426.
- [196] Swinburne, T. D., & Marinica, M.-C. (2018). Unsupervised calculation of free energy barriers in large crystalline systems. *Physical Review Letters*, 120(13).
- [197] Chen, S., Yang, X., Dahmen, K., Liaw, P., & Zhang, Y. (2014). Microstructures and Crackling Noise of AlxNbTiMoV High Entropy Alloys. *Entropy*, 16(2), 870–884.
- [198] Liaw, P. (2020). Private communication.
- [199] Yao, H., Qiao, J.-W., Gao, M., Hawk, J., Ma, S.-G., & Zhou, H. (2016). MoNbTaV Medium-Entropy Alloy. *Entropy*, 18(5), 189.
- [200] Yao, H., Qiao, J., Gao, M., Hawk, J., Ma, S., Zhou, H., & Zhang, Y. (2016). NbTaV-(Ti,W) refractory high-entropy alloys: Experiments and modeling. *Materials Science and Engineering: A*, 674, 203–211.
- [201] Yang, C., & Qi, L. (2018). Ab initio calculations of ideal strength and lattice instability in W-Ta and W-Re alloys. *Physical Review B*, 97(1), 014107.

Bibliography


- [202] Mak, E., & Curtin, W. A. (2021). Randomness and intrinsic ductility in High Entropy Alloys. *Under preparation*.
- [203] Liyanage, M., & Curtin, W. A. (2021). A machine learning potential for Zr. *Under preparation*.
- [204] Henkelman, G., & Jónsson, H. (1999). A dimer method for finding saddle points on high dimensional potential surfaces using only first derivatives. *The Journal of Chemical Physics*, 111(15), 7010–7022.
- [205] Kaufman, L., & Bernstein, H. (1970). Computer calculation of phase diagrams. With special reference to refractory metals.
- [206] Ikehata, H., Nagasako, N., Furuta, T., Fukumoto, A., Miwa, K., & Saito, T. (2004). First-principles calculations for development of low elastic modulus Ti alloys. *Physical Review B*, 70(17), 174113.
- [207] Katahara, K. W., Manghnani, M. H., & Fisher, E. S. (1979). Pressure derivatives of the elastic moduli of BCC Ti-V-Cr, Nb-Mo and Ta-W alloys. *Journal of Physics F: Metal Physics*, 9(5), 773–790.
- [208] Bolef, D. I., & De Klerk, J. (1962). Elastic constants of single-crystal Mo and W between 77° and 500°K. *Journal of Applied Physics*, 33(7), 2311–2314.
- [209] Dickinson, J. M., & Armstrong, P. E. (1967). Temperature dependence of the elastic constants of molybdenum. *Journal of Applied Physics*, 38(2), 602–606.
- [210] Davidson, D. L., & Brotzen, F. R. (1968). Elastic constants of molybdenum-rich rhenium alloys in the temperature range -190°C to +100°C. *Journal of Applied Physics*, 39(12), 5768–5775.
- [211] Shang, S., Saengdeejing, A., Mei, Z., Kim, D., Zhang, H., Ganeshan, S., Wang, Y., & Liu, Z. (2010). First-principles calculations of pure elements: Equations of state and elastic stiffness constants. *Computational Materials Science*, 48(4), 813–826.
- [212] Liao, M., Liu, Y., Cui, P., Qu, N., Zhou, F., Yang, D., Han, T., Lai, Z., & Zhu, J. (2020). Modeling of alloying effect on elastic properties in BCC Nb-Ti-V-Zr solid solution: From unary to quaternary. *Computational Materials Science*, 172, 109289.
- [213] (1969). III - elastic constants. In S. Allard (Ed.) *Metals*, (pp. 72–90). Pergamon.
- [214] Bolef, D. I. (1961). Elastic constants of single crystals of the bcc transition elements V, Nb, and Ta. *Journal of Applied Physics*, 32(1), 100–105.
- [215] Walker, E., & Peter, M. (1977). Elastic constants of the bcc phase in niobium-zirconium alloys between 4.2 and 300 K. *Journal of Applied Physics*, 48(7), 2820–2826.
- [216] Nagasako, N., Jahnátek, M., Asahi, R., & Hafner, J. (2010). Anomalies in the response of V, Nb, and Ta to tensile and shear loading: *Ab initio* density functional theory calculations. *Physical Review B*, 81(9), 094108.
- [217] Söderlind, P., Eriksson, O., Wills, J. M., & Boring, A. M. (1993). Theory of elastic constants of cubic transition metals and alloys. *Physical Review B*, 48(9), 5844–5851.

-
- [218] Alers, G. A. (1960). Elastic moduli of vanadium. *Physical Review*, 119(5), 1532–1535.
- [219] Fisher, E. S., Westlake, D. G., & Ockers, S. T. (1975). Effects of hydrogen and oxygen on the elastic moduli of vanadium, niobium, and tantalum single crystals. *physica status solidi (a)*, 28(2), 591–602.
- [220] Magerl, A., Berre, B., & Alefeld, G. (1976). Changes of the elastic constants of V, Nb, and Ta by hydrogen and deuterium. *physica status solidi (a)*, 36(1), 161–171.
- [221] Bercegeay, C., & Bernard, S. (2005). First-principles equations of state and elastic properties of seven metals. *Physical Review B*, 72(21), 214101.
- [222] Lowrie, R., & Gonas, A. M. (1967). Single-crystal elastic properties of tungsten from 24° to 1800°C. *Journal of Applied Physics*, 38(11), 4505–4509.
- [223] Ayres, R. A., Shannette, G. W., & Stein, D. F. (1975). Elastic constants of tungsten-rhenium alloys from 77 to 298 °K. *Journal of Applied Physics*, 46(4), 1526–1530.
- [224] Ledbetter, H., Ogi, H., Kai, S., Kim, S., & Hirao, M. (2004). Elastic constants of body-centered-cubic titanium monocrystals. *Journal of Applied Physics*, 95(9), 4642–4644.
- [225] Heiming, A., Petry, W., Trampenau, J., Alba, M., Herzig, C., Schober, H. R., & Vogl, G. (1991). Phonon dispersion of the bcc phase of group-IV metals. II. bcc zirconium, a model case of dynamical precursors of martensitic transitions. *Physical Review B*, 43(13), 10948–10962.
- [226] Rao, S. I., Akdim, B., Antillon, E., Woodward, C., Parthasarathy, T. A., & Senkov, O. N. (2019). Modeling solution hardening in BCC refractory complex concentrated alloys: NbTiZr, Nb_{1.5}TiZr_{0.5} and Nb_{0.5}TiZr_{1.5}. *Acta Materialia*, 168, 222–236.
- [227] Kresse, G., & Furthmüller, J. (1996). Efficient iterative schemes for *ab initio* total-energy calculations using a plane-wave basis set. *Physical Review B*, 54(16), 11169–11186.
- [228] Perdew, J. P., Burke, K., & Ernzerhof, M. (1996). Generalized gradient approximation made simple. *Physical Review Letters*, 77(18), 3865–3868.
- [229] Kresse, G., & Joubert, D. (1999). From ultrasoft pseudopotentials to the projector augmented-wave method. *Physical Review B*, 59(3), 1758–1775.
- [230] Monkhorst, H. J., & Pack, J. D. (1976). Special points for Brillouin-zone integrations. *Physical Review B*, 13(12), 5188–5192.
- [231] Methfessel, M., & Paxton, A. T. (1989). High-precision sampling for Brillouin-zone integration in metals. *Physical Review B*, 40(6), 3616–3621.
- [232] Zunger, A., Wei, S.-H., Ferreira, L. G., & Bernard, J. E. (1990). Special quasirandom structures. *Physical Review Letters*, 65(3), 353–356.
- [233] Yin, B., Wu, Z., & Curtin, W. A. (2017). Comprehensive first-principles study of stable stacking faults in hcp metals. *Acta Materialia*, 123, 223–234.

Bibliography

- [234] Zhou, M. (2003). A new look at the atomic level virial stress: on continuum-molecular system equivalence. *Proceedings of the Royal Society of London. Series A: Mathematical, Physical and Engineering Sciences*, 459(2037), 2347–2392.

Eleanor Mak

CONTACT INFORMATION	<p>Ph.D. Candidate Laboratory for Multiscale Mechanics Modeling Institute of Mechanical Engineering Ecole Polytechnique Fédérale de Lausanne 1015 Lausanne, Switzerland</p>	<p>✉ eleanor.mak@epfl.ch eleanormak92@gmail.com  www.linkedin.com/in/eleanormak</p>
RESEARCH INTERESTS	Computational mechanics of materials, atomistic simulations of fracture, random alloys, magnesium, high entropy alloys, intrinsic ductility, dislocation emission, dislocation dynamics	
EDUCATION	<p>Ecole Polytechnique Fédérale de Lausanne (EPFL), Lausanne, Switzerland Ph.D. in Mechanical Engineering Sept 2017 – Present <i>Thesis:</i> Atomic scale investigations of fracture in metal alloys <i>Advisor:</i> Prof. W. A. Curtin</p> <p>University of Waterloo, Waterloo, Canada M.A.Sc. in Civil Engineering Sept 2015 – Jun 2017 <i>Thesis:</i> Dislocation Dynamics for High Strain-Rate Plasticity: Inertial and Thermal Effects <i>Advisor:</i> Prof. R. Gracie</p> <p>B.A.Sc. in Civil Engineering (Honours), Co-operative Education Sept 2010 – Jun 2015 <i>with distinction, Dean's Honours List</i></p>	
PUBLICATIONS	<p>Mak, E., & Curtin, W. A. (2021). Intrinsic contribution of randomness to ductility in high entropy alloys. <i>In preparation</i>.</p> <p>Mak, E., Yin, B. & Curtin, W. A. (2021). A ductility criterion for bcc high entropy alloys. <i>J. Mech. Phys. Solids</i>, 104389.</p> <p>Stricker, M., Yin, B., Mak, E. & Curtin, W. A. (2020). Machine learning for metallurgy II. A neural network potential for magnesium. <i>Phys. Rev. Mater.</i> 4 (10), 103602.</p> <p>Mak, E. & Curtin, W. A. (2020). Intrinsic fracture behavior of Mg–Y alloys. <i>Model. Simul. Mat. Sci. Eng.</i> 28(3), 035012.</p>	
CONFERENCES/ SUMMER SCHOOLS	<p>Mak, E., Curtin, W. A. (2018). Strain Hardening and Crack Growth in ‘2.5D’ Discrete Dislocation Dynamics. <i>13th World Congress in Computational Mechanics</i>, New York, USA.</p> <p>Mak, E., Gracie, R. (2017). Dislocation Dynamics at High Strain-Rate – Inertial and Thermal Effects. <i>14th U.S. National Congress for Computational Mechanics</i>, Montreal, Canada.</p> <p>Mak, E., Skiba, O., & Gracie, R. (2016). Inertial effects on a thermomechanical dislocation dynamics model for plastic deformation. <i>24th International Congress of Theoretical and Applied Mechanics</i>, Montreal, Canada.</p> <p>The Art of Modeling in Computational Solid Mechanics (2019). International Centre for Mechanical Sciences (CISM), Udine, Italy.</p> <p>Multi-scale and micromechanics (2018). Dutch Engineering Mechanics Graduate School, Eindhoven, The Netherlands.</p>	

TEACHING EXPERIENCE	Teaching assistant, EPFL	
	• Solid mechanics	Winter semester 2018, 2019, 2020
	Teaching assistant, University of Waterloo	
	<ul style="list-style-type: none"> • Finite element analysis • Advanced mechanics of solids • Mechanics of solids • Structural analysis • Statics and solid mechanics • Advanced calculus 	Winter semester 2017 Fall semester 2016 Spring semester 2016 Winter semester 2016 Fall semester 2012 Fall semester 2012
HONORS AND AWARDS	Course development, University of Waterloo	
	• Statics and solid mechanics	Fall semester 2015
	The Natural Sciences and Engineering Research Council of Canada (NSERC)	
	<ul style="list-style-type: none"> • Postgraduate scholarship • Alexander Graham Bell Canada graduate scholarship 	Sept 2017 – Aug 2020 Sept 2015 – Aug 2016
RELEVANT COURSES	Government of Ontario, Canada	
	<ul style="list-style-type: none"> • Graduate scholarship • Queen Elizabeth II scholarship 	Sept 2016 – Aug 2017 Sept 2010 – Aug 2015
	University of Waterloo	
	<ul style="list-style-type: none"> • President's graduate scholarship • President's undergraduate scholarship • Jacques Lamarre Scholarship in civil engineering 	Sept 2015 – Aug 2017 Sept 2010 – Aug 2011 Sept 2010 – Aug 2011
PROFESSIONAL EXPERIENCE	Read Jones Christoffersen Consulting Engineers, Toronto, Canada Structural engineering professional trainee	
	May – Aug 2013, Jan – Apr & Sept – Dec 2014	
	Ministry of Transportation of Ontario (Traffic Head Office), St. Catharines, Canada Traffic engineering professional trainee	
	May - Aug 2011	

